



U.S. DEPARTMENT OF
ENERGY

PNNL-18160

Prepared for the U.S. Department of Energy
Under Contract DE-AC05-76RL01830

2008 Annual Report

Summer Research Institute Interfacial and Condensed Phase Chemical Physics

BC Garrett, BES Lead
RGTonkyn, SRI Coordinator
NB Avery, SRI Administrator

November 2008



Pacific Northwest
NATIONAL LABORATORY

DISCLAIMER

This report was prepared as an account of work sponsored by an agency of the United States Government. Neither the United States Government nor any agency thereof, nor Battelle Memorial Institute, nor any of their employees, makes **any warranty, express or implied, or assumes any legal liability or responsibility for the accuracy, completeness, or usefulness of any information, apparatus, product, or process disclosed, or represents that its use would not infringe privately owned rights.** Reference herein to any specific commercial product, process, or service by trade name, trademark, manufacturer, or otherwise does not necessarily constitute or imply its endorsement, recommendation, or favoring by the United States Government or any agency thereof, or Battelle Memorial Institute. The views and opinions of authors expressed herein do not necessarily state or reflect those of the United States Government or any agency thereof.

PACIFIC NORTHWEST NATIONAL LABORATORY
operated by
BATTELLE
for the
UNITED STATES DEPARTMENT OF ENERGY
under Contract DE-AC05-76RL01830

Printed in the United States of America

**Available to DOE and DOE contractors from the
Office of Scientific and Technical Information,
P.O. Box 62, Oak Ridge, TN 37831-0062;
ph: (865) 576-8401
fax: (865) 576-5728
email: reports@adonis.osti.gov**

**Available to the public from the National Technical Information Service,
U.S. Department of Commerce, 5285 Port Royal Rd., Springfield, VA 22161
ph: (800) 553-6847
fax: (703) 605-6900
email: orders@ntis.fedworld.gov
online ordering: <http://www.ntis.gov/ordering.htm>**



This document was printed on recycled paper.

(9/2003)

2008 Annual Report

Summer Research Institute Interfacial and Condensed Phase Chemical Physics

Bruce Garrett, BES Lead
Russ Tonkyn, SRI Coordinator
Nikki Avery, SRI Administrator

November 2008

Prepared for
the U.S. Department of Energy
under Contract DE-AC05-76RL01830

Pacific Northwest National Laboratory
Richland, Washington 99352

Executive Summary

For the fifth year, the Pacific Northwest National Laboratory in Richland, Washington, invited graduate students, postdoctoral fellows, university faculty, and students entering graduate school from around the world to participate in the Summer Research Institute in Interfacial and Condensed Phase Chemical Physics. The institute offers participants the opportunity to gain hands-on experience in top-notch research laboratories while working along internationally respected mentors.

Of the 38 applicants, 20 were accepted for the 8- to 10-week program. The participants came from universities as close as Seattle and Portland and as far away as Germany and Singapore. At Pacific Northwest National Laboratory, the 20 participants were mentored by 13 scientists. The mentors tailored the work in their lab to meet the needs of the participants. Further, the mentors provided guidance on experimental and theoretical techniques, research design and completion, and other aspects of scientific careers in interfacial and condensed phase chemical physics.

The research conducted at the institute can result in tangible benefits for the participants. For example, many have co-authored papers that have been published in peer-reviewed journals, including top-rated journals such as *Science*. Also, they have presented their research at conferences, such as the Gordon Research Conference on Dynamics at Surfaces and the AVS national meeting. Beyond that, many of the participants have started building professional connections with researchers at Pacific Northwest National Laboratory, connections that will serve them well during their careers.

TABLE OF CONTENTS

EXECUTIVE SUMMARY	iii
ACKNOWLEDGMENTS	vii
INTRODUCTION.....	1
Participants and Institute Structure.....	1
Benefits.....	14
New in FY 2008	14
Measures of Success	14
TECHNICAL REPORTS	33
<u>Abramov, Alexander</u> , Prof. Maciej Gutowski, Greg Schenter, Shawn Kathmann "Intermolecular Interactions in Ammonia Borane – Hydrogen Systems Rock Salt and Zinc Blende Structures of Ammonium Borohydride"	35
<u>Athavan, Nadarajah</u> , Shutthanadan Vaithiyalingam "Implanting C in TiO ₂ and Investigate the Location of C and Damage/Damage Recovery in TiO ₂ as a Function of Annealing Temperature"	51
<u>Bateman, Adam</u> , <u>Nizkorodov, Sergey</u> , Alex Laskin, Julia Laskin "Photochemical Aging of Secondary Organic Aerosol"	55
<u>Cain, Jeremy</u> , Hai Wang, Alexander Laskin "Analysis of Ethylene Soot Produced by a Flat Flame Burner"	59
<u>Chua, Yong Shen</u> , S Thomas Autrey, Wendy J Shaw, Abhi Karkamkar, Ping Chen "Application of In-situ NMR in Studying Structure and Dynamics of Condensed Phase H-storage Materials"	63
<u>Edie, Michael</u> , Prof. Maciej Gutowski, and Donald Camaioni "Structure and Energetics of Diammoniate of Diborane: A Computational Study in the Solid State"	67
<u>Gabdoulline, Razif</u> , Rebecca Wade, TP Straatsma "Computer Simulations on Biomolecular Systems, using QM/MM, MD and Free Energy Methodologies"	71
<u>Gupta, Shilpi</u> , S.V.N.T. Kuchibhatla, M.H. Engelhard, V. Shutthanandan, P. Nachimuthu, W. Jiang, L.V. Saraf, S.Thevuthasan, S. Prasad "Influence of Samaria Doping on the Resistance of Ceria Thin Films and its Implications to the Planar Oxygen Sensing Devices"	75

<u>Gutowski, Maciej</u> , Sotiris Xantheas, Gregory Schenter, Donghai Mei, Donald Camaioni, Jun Li "Computational Studies: Materials for Hydrogen Storage, Molecular Electronegativities, Catalytic Properties of Surfaces of WO ₃ and ReO ₃	101
<u>Kim, Hyunjeong</u> , Nancy J. Hess, Wendy J. Shaw, Abhi Karkamkar, S. Thomas Autrey "Investigating Ammonia Borane (NH ₃ BH ₃) Nanocomposites in Mesoporous Silica MCM-41"	105
<u>Ling, Sanliang</u> , Donghai Mei, Maciej Gutowski "Hydrogen Adsorption on Surfaces of Pure MO ₃ (M=W or Re) and Their Interface Structures: A Comparative Study"	109
<u>Liu, Dawei</u> , Chongmin Wang, Jun Liu "The Learning of Transmission Electronic Microscope" Fabrication of TiO ₂ One Dimensional Nanostructures Which Could be Used as Anode for Lithium Ion Intercalation" and "Study of Electlyte Used for Lithium Ion Batteries"	123
<u>Maerzke, Katie</u> , Garold Murdachaew, Christopher Mundy, Gregory Schenter, J. Ilja Siepmann "Self-consistent Polarization Density Functional Theory: Application to Argon"	125
<u>Miara, Lincoln</u> , Srikanth Gopalan, Larry Pederson "Micro-Fabrication of: Patterned LCM and LSCF Cathodes on YSZ Electrolyte and Oriented LCM Thin-films on Single Crystals by PLD"	159
<u>Moffet, Ryan</u> , Mary Gilles, Nancy Marley, Jeffrey Gaffney, Alex Laskin, Julia Laskin "A High Resolution Mass Spectrometry Study of Organic Particulate Matter Aging in an Urban Environment"	165
<u>Olanrewaju, Babajide</u> , Thomas Orlando, Nikolai Petrik, Greg Kimmel "Photoionization of Liquid Water and Aqueous Solutions"	171
<u>Tsuchyia, Masaru</u> , Shriram Ramanathan, Vaithiyalingam Shutthanandan, Mark H. Engelhard "Effect of Ultraviolet Photon Irradiation on Oxygen Stoichiometry in Ultra-thin Zirconia and Ceria Films"	177
<u>Whiteside, Alexander</u> , Maciej Gutowski "Electronegativities of Groups and Molecular Ions"	181
<u>Yamada, Tomonori</u> , Misako Aida, Michel Dupuis "Calculation of Quantum Vibrational Spectra by Means of ab initio Centroid Molecular Dynamics"	189

Acknowledgments

The Summer Research Institute would not happen without the commitment of the U.S. Department of Energy's Office of Basic Energy Sciences and Pacific Northwest National Laboratory. The U.S. Department of Energy's Office of Basic Energy Sciences provided guidance to initiate the Summer Research Institute in Interfacial and Condensed Phase Chemical Physics.

At Pacific Northwest National Laboratory, our thanks go to the many staff within the Science and Engineering Education Office. They handled a myriad of details associated with appointments, including awards, agreements, and disbursements. Also, our thanks go to Cynthia A. Irwin and Susan M. Finch for providing financial and budgetary support. In addition, our thanks go to Susan Widener for maintaining the institute's website.

Of course, the real stars of the Interfacial and Condensed Phase Chemical Physics Research Institute were our participants. The remainder of this document is largely devoted to the fiscal year 2008 participants.

Dr. Russell Tonkyn
Coordinator

and

Ms. Nikki B. Avery
Administrator

October 2008

Introduction

Pacific Northwest National Laboratory's (PNNL's) Management and Operations Contract with the U.S. Department of Energy (DOE)¹ Office of Science identified an Office of Basic Energy Sciences (BES) Mission Stretch Goal: "To establish PNNL in a national leadership role in the area of theoretical and experimental condensed phase and interfacial chemical physics research." Successful achievement of a national leadership role was measured by: "Establishment of a summer school (at least two weeks in duration) to educate graduate students and young scientists in state-of-the-art theory, simulation, and experimental measurement, with a total attendance of at least 60 over the contract period." Although the stretch goal was completed at the end of the 2007, the value and impact of the SRI provided the incentive to continue this activity.

Interfacial and condensed phase chemical physics is important in nearly every scientific discipline. Technology and engineering in today's world depend to one degree or another on our ability to understand and manipulate condensed phases and interfacial processes.

The guidance from DOE's Office of Science gave PNNL considerable latitude in implementing the Summer Research Institute (SRI), which focuses on graduate students, postdoctoral fellows, and university faculty. The SRI caters more to graduate students and early career scientists than generally accommodated by PNNL's summer internship programs. The best education people at this level can receive is to conduct research relevant to their own career development goals. To accomplish this objective, SRI puts different requirements on its participants than other internship programs. Perhaps the best overall description of the institute is a "visiting scientist program for early career researchers." In this spirit, each scientist's particular program is individually tailored. The descriptions given in this report are generally true for most of the scientists but may not apply to any particular individual.

Participants and the Institute Structure

Prospective participants applied at the Summer Research Institute's website: <http://www.pnl.gov/si/>. Submission of applications, screening, and correspondence were all handled online. This greatly facilitated the review and screening process as well as recordkeeping. Preliminary screening was handled by the SRI Administrator, in consultation with the Coordinator. The Administrator acknowledged receipt of the applications and informed the candidates of any additional information or actions that were necessary to complete the application process. A number of candidates were unsuited to participate in the institute, and they were informed as quickly as that determination could be made. Reasons for rejection included the following:

- Candidate's area of interest was outside of the scope of the program
- Prospective PNNL hosts were already committed or unavailable
- Candidate was looking for employment
- Candidate failed to finish the application process.

¹ Appendix H of Contract Number: DE-AC06-76RL01830, Modification M375.

Candidates who passed this first series of hurdles and who identified a willing PNNL host were then required to submit a summary of proposed research or activity that they would conduct at PNNL during the summer. Normally, this proposal was prepared with the assistance of both the PNNL host and the candidate's academic advisor (as appropriate). Once the application deadline had passed, all completed applications were reviewed to ensure program eligibility. Individual acceptance and rejection letters were prepared and distributed by the SRI Administrator. Table 1 provides some statistics on applications and acceptances.

Table 1. 2008 Participant Numbers

Applications and inquiries	38
Acceptances	20
Participants	20
Graduating Seniors	0
Graduate Students	15
Postdoctoral Fellows	3
Junior Faculty	2
Senior Researchers	0
US Citizens/Foreign Nationals	6/14
PNNL Hosts	13

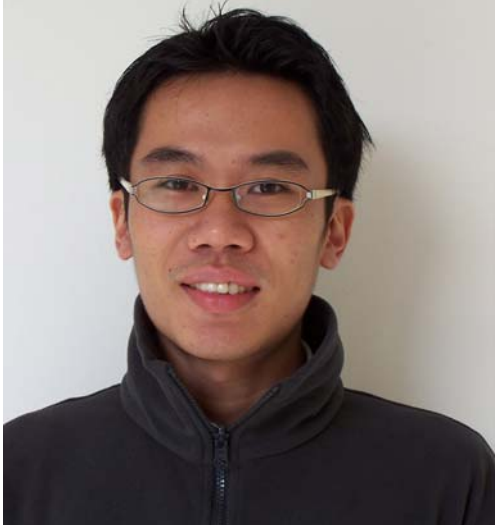
The application and acceptance procedure required participation from all concerned parties: the PNNL mentors, the participants, and the participants' supervisors at his or her home institution (if applicable). Further, PNNL mentors ensured all necessary resources were available to accomplish the proposed work. The participants bore the bulk of the application responsibility to come to PNNL for an extended stay. The participants' supervisors were expected to continue financial support during this visit to PNNL as the SRI only covers travel to and from PNNL and partial living expenses.

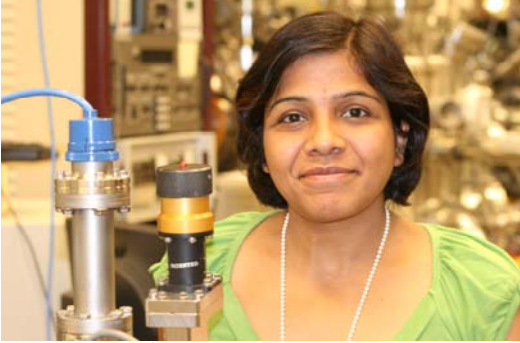
Each participant had a specific program tailored around his or her schedule and research goals. To accommodate individual schedules, the 2008 summer appointments began in late April and the final appointment concluded in September. Before their arrival, each participant was paired with a PNNL host and worked out a research program for the visit. All of this activity was coordinated with the participant's supervisor. Most often, the participant was playing a role in a collaboration or prospective collaboration between the PNNL host and his or her supervisor. Table 2 lists the SRI participants, PNNL hosts, and home institution supervisors. Table 3 shows the university statistics.

Table 2. Summer Research Institute Participants, Academic Advisors, and Hosts

<p style="text-align: center;">Alexander Abramov</p> 	<p>Chemistry, PhD Heriot Watt University Edinburgh, Scotland ava3@hw.ac.uk</p> <p>University Advisor: Prof. Maciej Gutowski M.Gutowski@hw.ac.uk</p> <p>PNNL Host: Dr. Greg Schenter, FCSD gregory.schenter@pnl.gov</p>
<p style="text-align: center;">Dr. Nadarajah Athavan</p> 	<p>Physics, PhD Portland State University Portland, OR nadaraja@pdx.edu</p> <p>University Advisor: Prof. Rolf Koenenkamp rkoe@pdx.edu</p> <p>PNNL Host: Dr. Thevuthasan, EMSL theva@pnl.gov</p>
<p>EMSL = Environmental Molecular Sciences Laboratory EED = Energy & Environment Directorate FCSD = Fundamental & Computational Sciences Directorate</p>	

Adam Bateman	
	<p>Chemistry, PhD University of California, Irvine Irvine, CA abateman@uci.edu</p> <p>University Advisor: Dr. Sergey Nizkorodov nizkorod@uci.edu</p> <p>PNNL Hosts: Dr. Alexander Laskin, EMSL alexander.laskin@pnl.gov</p> <p>Dr. Julia Laskin, FCSD julia.laskin@pnl.gov</p>
Jeremy Cain	
	<p>Mechanical Engineering, PhD University of Southern California Los Angeles, CA jcain@usc.edu</p> <p>University Advisor: Prof. Hai Wang haiw@usc.edu</p> <p>PNNL Host: Dr. Alexander Laskin, EMSL alexander.laskin@pnl.gov</p>

Yong Shen Chua	
	<p>Physical Chemistry, PhD National University of Singapore Singapore g0601155@nus.edu.sg</p> <p>University Advisor: Assistant Prof. Dr Chen Ping chmchenp@nus.edu.sg</p> <p>PNNL Host: Dr. S. Thomas Autrey, FCSD tom.autrey@pnl.gov</p>
Michael Edie	
	<p>Chemistry, PhD Heriot Watt University Edinburgh, Scotland m.j.edie@hw.ac.uk</p> <p>University Advisor: Prof. Maciej Gutowski M.Gutowski@hw.ac.uk</p> <p>PNNL Host: Dr. Don Camaioni, FCSD donald.camaioni@pnl.gov</p>

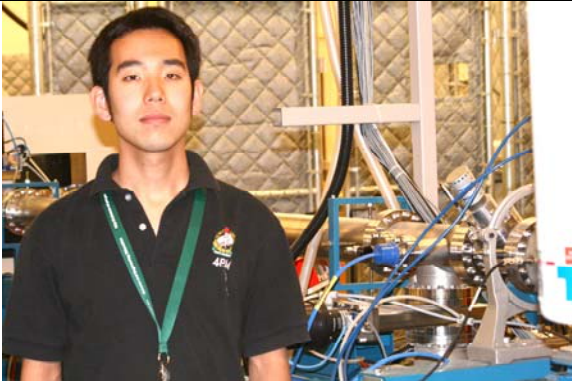
<p>Dr. Razif Gabdoulline</p>	
	<p>Theoretical and Mathematical Physics, PhD BIOMS (Center for Modeling and Simulation in the Biosciences) Fellow, University of Heidelberg, Germany Heidelberg, Germany razif.gabdoulline@bioquant.uni-heidelberg.de</p> <p>PNNL Host: Dr. Tjerk Straatsma, FCSD tp.straatsma@pnl.gov</p>
<p>Shilpi Gupta</p>	
	<p>Electrical, MS Portland State University Portland, OR shilpigupta23@gmail.com</p> <p>University Advisor: Prof. Shalini Prasad sprasad@pdx.edu</p> <p>PNNL Host: Dr. Thevuthasan, EMSL theva@pnl.gov</p>

Prof. Dr. Maciej Gutowski	
	<p>Physical Chemistry, PhD Heriot Watt University Edinburgh, Scotland M.Gutowski@hw.ac.uk</p> <p>PNNL Host: Dr. Sotiris Xantheas, FCSD sotiris.xantheas@pnl.gov</p>
Dr. Hyunjeong Kim	
	<p>Experimental Condensed Matter Physics, PhD Lujan Neutron Scattering Center Los Alamos National Laboratory Los Alamos, NM hjkim@lanl.gov</p>

<p style="text-align: center;">Sanliang Ling</p> 	<p>Chemistry, PhD Heriot Watt University Edinburgh, Scotland sl160@hw.ac.uk</p> <p>University Advisor: Prof. Maciej Gutowski M.Gutowski@hw.ac.uk</p> <p>PNNL Host: Dr. Donghai Mei, FCSD donghai.mei@pnl.gov</p>
<p style="text-align: center;">Dawei Liu</p> 	<p>Materials Science and Engineering, PhD University of Washington Seattle, WA daweiliu@u.washington.edu</p> <p>University Advisor: Prof. Guozhong Cao gzcao@u.washington.edu</p> <p>PNNL Host: Dr. Chongmin Wang, EMSL Chongmin.wang@pnl.gov</p>

<p style="text-align: center;">Katie Maerzke</p> 	<p>Chemistry, PhD University of Minnesota Minneapolis, MN maerz001@umn.edu</p> <p>University Advisor: Prof. J. Ilja Siepmann siepmann@chem.umn.edu</p> <p>PNNL Host: Dr. Christopher Mundy, FCSD chris.mundy@pnl.gov</p>
<p style="text-align: center;">Lincoln Miara</p> 	<p>Manufacturing Engineering, PhD Boston University Brookline, MA lmira@bu.edu</p> <p>University Advisor: Prof. Srikanth Gopalan sgopalan@bu.edu</p> <p>PNNL Host: Dr. Lax Saraf, EMSL laxmikant.saraf@pnl.gov</p> <p>Dr. Larry Pederson, EED larry.pederson@pnl.gov</p>

<p style="text-align: center;">Dr. Ryan Moffet</p> 	<p>Chemistry, PhD Lawrence Berkeley National Laboratory Berkeley, CA rcmoffet@lbl.gov</p> <p>PNNL Host: Dr. Alexander Laskin, EMSL alexander.laskin@pnl.gov</p>
<p style="text-align: center;">Dr. Sergey Nizkorodov</p> 	<p>Chemistry, PhD University of California, Irvine Irvine, CA nizkorod@uci.edu</p> <p>PNNL Host: Dr. Alexander Laskin, EMSL alexander.laskin@pnl.gov</p> <p>Dr. Julia Laskin, FCSD julia.laskin@pnl.gov</p>

Babajide Olanrewaja	
	<p>Chemistry, PhD Georgia Tech Atlanta, GA boalanre@gatech.edu</p> <p>University Advisor: Thomas Orlando Thomas.orlando@chemistry.gatech.edu</p> <p>PNNL Host: Dr. Gregory Kimmel, FCSD gregory.kimmel@pnl.gov</p>
Masaru Tsuchiya	
	<p>Applied Degree Harvard University Cambridge, MA tsuchiya@fas.harvard.edu</p> <p>University Advisor: Prof. Shriram Ramanathan shriram@seas.harvard.edu</p> <p>PNNL Host: Dr. Shutthanandan shuttha@pnl.gov</p>

<p style="text-align: center;">Alexander Whiteside</p> 	<p>Chemistry, PhD Heriot Watt University Edinburgh, Scotland aw95@hw.ac.uk</p> <p>University Advisor: Prof. Maciej Gutowski M.Gutowski@hw.ac.uk</p> <p>PNNL Host: Sotiris Xantheas, FCSD sotiris.xantheas@pnl.gov</p>
<p style="text-align: center;">Tomonori Yamada</p> 	<p>Chemistry, PhD Hiroshima University Hiroshima, Japan tomonori-y@hiroshima-u.ac.jp</p> <p>University Advisor: Prof. Misako Aida maida@hiroshima-u.ac.jp</p> <p>PNNL Host: Michel Dupuis, FCSD Michel.dupuis@pnl.gov</p>

Table 3. 2008 University Statistics	
Boston University	1
Georgia Institute of Technology	1
Harvard University	1
Heriot-Watt University, Edinburgh, Scotland	5
Hiroshima University, Japan	1
Lawrence Berkeley National Laboratory	1
Lujan Neutron Scattering Center, LANL	1
National University of Singapore	1
Portland State University	2
University of California, Irvine	2
University of Heidelberg, Germany	1
University of Minnesota	1
University of Southern California	1
University of Washington	1
Total	20

Benefits

The SRI offered several benefits to the participants and to the PNNL staff who mentored them. For the participants, the institute offered the opportunity to

- work on projects tailored to their research interests while gaining a fuller understanding of interfacial and condensed phase sciences
- conduct research alongside internationally respected scientists
- use advanced theoretical and experimental techniques.

For the PNNL staff, working with the institute provided the opportunity to encourage the next generation of scientists and receive additional assistance on a research project. Further, the staff benefited from the participant's inquisitiveness, creativity, and energy.

New in FY 2008

In FY 2008, Russell Tonkyn of PNNL took over the role of SRI coordinator. At PNNL, his research involves fundamental investigations of NO_x storage and release (NSR) catalysts for the treatment of NO_x emissions from lean burn gasoline and light-duty diesel engines. The goal is a 90 percent chemical reduction of nitrogen oxide to nitrogen in light-duty diesel exhaust with less than a 5 percent fuel penalty. His other research projects include the investigation of the liquid water-vacuum interface and the development of a quantitatively accurate database of liquid infrared spectra. For more information about his career, see http://www.pnl.gov/science/staff/staff_info.asp?staff_num=5515.

Measures of Success

This is an educational project within a research enterprise. As such, sustained success becomes apparent only in the following years or decade. However, on a shorter time scale, success can and must also be measured. We can point, for example, to early successes in FY 2008. All of the candidates, PNNL mentors, and academic advisors expressed enthusiasm about the institute at the outset and were generally more enthusiastic by the end of the summer appointments. In several cases, plans are being readied for return visits to PNNL, independent of the summer program. Numerous presentations and manuscripts are being readied for submission to peer-reviewed journals.

2004 Follow-up

As of November 2008, 47 papers, listed in Table 4, have been submitted, are in press, or published in the peer-reviewed literature. At least 17 presentations for national or international meetings were also produced (see Table 5). In addition, internal PNNL reports have been generated.

The author lists from 2004 through 2008 (see Tables 4 and 5) also point to an additional and somewhat unexpected benefit of SRI. Those visitors doing laboratory research in the U.S. Department of Energy's Environmental Molecular Sciences Laboratory (EMSL), a national scientific user facility located at PNNL, were extremely facile in harnessing internal collaborative opportunities. Thus, many of the papers included unanticipated participation by non-host PNNL staff members.

Table 4. Peer-Reviewed Publications from 2004 Work through October 2008.
<u>Alexandrova, A. N.</u> ^a , <u>Boldyrev, A. I.</u> ^b , Fu, Y. J., Yang, X., Wang, X. B., Wang, L. S. (2004). "Structure of the Na _x Cl _{x+1-} (x=1-4) clusters via ab initio genetic algorithm and photoelectron spectroscopy." <i>Journal of Chemical Physics</i> 121 (12): 5709-5719.
<u>Alexandrova, A. N.</u> ^a , <u>Boldyrev, A. I.</u> ^b , Zhai, H. J., & <u>Wang, L. S.</u> ^c (2004). "Sigma-aromaticity in clusters of boron, lithium and magnesium." <i>Abstracts of Papers of the American Chemical Society</i> , 227 : U1517-U1517.
<u>Alexandrova, A. N.</u> ^a , <u>Boldyrev, A. I.</u> ^b , Zhai, H. J., & <u>Wang, L. S.</u> ^c (2004). "Electronic structure, isomerism, and chemical bonding in B-7(-) and B-7." <i>Journal of Physical Chemistry A</i> 108 (16): 3509-3517.
<u>Alexandrova, A. N.</u> ^a , Zhai, H. J., <u>Wang, L. S.</u> ^c & <u>Boldyrev, A. I.</u> ^b , (2004). "Molecular wheel B-8(2-) as a new inorganic ligand. Photoelectron spectroscopy and ab initio characterization of LiB8." <i>Inorganic Chemistry</i> 43 (12): 3552-3554.
<u>Alexandrova, A. N.</u> ^a , <u>Boldyrev, A. I.</u> ^b , Zhai, H. J., & <u>Wang, L. S.</u> ^c (2005). "Photoelectron spectroscopy and ab initio study of the doubly antiaromatic B-6(2-) dianion in the LiB6- cluster." <i>Journal of Chemical Physics</i> 122 (5): 8.
<u>Alexandrova, A. N.</u> ^a , <u>Boldyrev, A. I.</u> ^b , Zhai, H. J., & <u>Wang, L. S.</u> ^c (2005). "Cu3C4-: A new sandwich molecule with two revolving C-2(2-) units." <i>Journal of Physical Chemistry A</i> 109 (4): 562-570.
<u>Alexandrova, A. N.</u> ^a , <u>Boldyrev, A. I.</u> ^b , Zhai, H. J., & <u>Wang, L. S.</u> ^c (2006). "All-boron aromatic clusters as potential new inorganic ligands and building blocks in chemistry." <i>Coordination Chemistry Reviews</i> 250 (21-22): 2811-2866.
Zubarev, D. Y., <u>Alexandrova, A. N.</u> ^a , <u>Boldyrev, A. I.</u> ^b , Cui, L. F., Li, X., & <u>Wang, L. S.</u> ^c (2006). "On the structure and chemical bonding of Si-6(2-) and Si-6(2-) in NaSi6- upon Na+ coordination." <i>Journal of Chemical Physics</i> 124 (12): 13.
Gologan, B., <u>Green, J. R.</u> ^a , <u>Alvarez, J.</u> ^a , <u>Laskin, J.</u> ^c , & <u>Cooks, R. G.</u> ^b (2005). "Ion/surface reactions and ion soft-landing." <i>Physical Chemistry Chemical Physics</i> . <i>PCCP</i> 7 : 1490-1500.
<u>Alvarez, J.</u> ^a , <u>Cooks, R. G.</u> ^b , Barlow, S. E., Gaspar, D. J., Futrell, J. H., & <u>Laskin, J.</u> ^c (2005). "Preparation and in situ characterization of surfaces using soft landing in a Fourier transform ion cyclotron resonance mass spectrometer." <i>Analytical Chemistry</i> 77 (11): 3452-3460.
<u>Alvarez, J.</u> ^a , Futrell, J. H., & <u>Laskin, J.</u> ^c (2006). "Soft-landing of peptides onto self-assembled monolayer surfaces." <i>Journal of Physical Chemistry A</i> 110 (4): 1678-1687.

Table 4. Peer-Reviewed Publications from 2004 Work through October 2008.

Laskin, J. ^c , Wang, O., Hadjar, O., Futrell, J. H., Alvarez, J. ^a , & Cooks, R. G. ^b (2007). "Charge retention by peptide ions soft-landed onto self-assembled monolayer surfaces." <i>International Journal of Mass Spectrometry</i> 265 (2-3): 237-243.
Bera, D. ^a , Kuchibhatla, S., S, A., Saraf, L. V., Wang, C., Shutthanandan, V., McCready, D. E., Engelhard, M., Marina, O. A., Baer, D. R. ^c , Seal, S. ^b , and Thevuthasan, S. (2008). "Growth and characterization of highly oriented gadolinia-doped ceria (111) thin films on zirconia (111)/sapphire (0001) substrates." <i>Thin Solid Films</i> 516 (18): 6088-6094.
Chang, H. S. ^a , Korshin, G. V., et al. (2006). "Adsorption of uranyl on gibbsite: A time-resolved laser-induced fluorescence spectroscopy study." <i>Environmental Science & Technology</i> 40 (4): 1244-1249.
Korshin, G. V. ^b , Chang, H. S. ^a , Wang, Z. M. ^c , & Zachara, J. M. (2005). "Speciation of uranyl adsorbed on gibbsite: A time-resolved laser-induced fluorescence spectroscopic study." <i>Geochimica Et Cosmochimica Acta</i> 69 (10): A619-A619.
Du, Y. ^a , Atha, S., Hull, R., Groves, J. F. ^b , Lyubinetsky, I. ^c , & Baer, D. R. (2004). "Focused-ion-beam directed self-assembly of Cu2O islands on SrTiO3(100)." <i>Applied Physics Letters</i> 84 (25): 5213-5215.
Du, Y. ^a , Groves, J. F. ^b , Lyubinetsky, I. ^c , & Baer, D. R. (2006). "Formation of Cu2O quantum dots on SrTiO3 (100): Self-assembly and directed self-assembly." <i>Journal of Applied Physics</i> 100 (9): Art. No. 094315.
Yu, Z., Wang, C. M., Du, Y. ^a , Thevuthasan, S., Lyubinetsky, I. ^c , (2006). "Reproducible tip fabrication and cleaning for UHV STM." <i>Ultramicroscopy</i> 108 (9): 873-877.
Groves, J. F. ^b , Y. Du, Y. ^a , Lyubinetsky, I. ^c , Baer, D. R. (2007). "Focused ion beam directed self-assembly (Cu2O on SrTiO3): FIB pit and Cu2O quantum dot evolution." <i>MRS Proceedings, "Superlattices and Microstructures"</i> .
Du, Y. ^a , Deskins, N. A., Zhang, Z., Dohnalek, Z., Dupuis, M., Lyubinetsky, I. ^c (2008). "Imaging "elusive" HO2 and terminal OH species during O2 reaction with hydroxylated TiO2(110)." <i>Journal of Physical Chemistry C</i> . In press .
Du, Y. ^a , Deskins, N. A., Zhang, Z., Dohnalek, Z., Dupuis, M., Lyubinetsky, I. ^c (2008). "Imaging consecutive steps of O2 reaction with hydroxylated TiO2(110): Identification of HO2, and terminal OH intermediates." <i>Journal of the American Chemical Society</i> . In press
Du, Y. ^a , Z. Dohnalek, Z., Lyubinetsky, I. ^c (2008). "Transient mobility of oxygen adatoms upon O2 dissociation on reduced TiO2 (110)." <i>Journal of Physical Chemistry C</i> 112 (7): 2649-2653.
Du, Y. ^a , Zhang, Z., Dohnalek, Z., Lyubinetsky, I. ^c (2008). "Direct observation of O2 dissociation on Ti rows of reduced TiO2(110) surface." <i>Journal of the American Chemical Society</i> .
Ohsawa, T., Lyubinetsky, I., Du, Y. ^a , Henderson, M. A., Rousseau, R. J., Shutthanandan, V., Chambers, S. A. (2008). "Crystallographic dependence of visible-light-induced photochemistry in nitrogen-doped titanium dioxides." <i>Science</i> .
Li, S.-C., Zhang, Z., Sheppard, D. Kay, B. D., White, J. M., Du, Y. ^a , Lyubinetsky, I. ^c , Henkelman, G. A., Dohnalek, Z., (2008). "Intrinsic diffusion of hydrogen on rutile TiO2(110)." <i>Journal of the American Chemical Society</i> 130 (28): 9080-9088.
Zhang, Z., Du, Y. ^a , Petrik, N. G., Kimmel, G. A., Lyubinetsky, I. ^c , Dohnalek, Z., (2008). "Water as a catalyst: Imaging reactions of O2 with partially and fully hydroxylated TiO2(110) Surfaces." <i>Journal of Physical Chemistry C</i> . Submitted
Elliott, B. ^a , Koyle, E., Boldyrev, A. I. ^b , Wang, X. B., & Wang, L. S. ^c (2005). "MX3-superhalogens (M=Be, Mg, Ca; X=C1, Br): A Photoelectron spectroscopic and ab initio theoretical study." <i>Journal of Physical Chemistry A</i> 109 (50): 11560-11567.
Elliott, B. ^a , Boldyrev, A. I. ^b , Alexandrova, A. N. ^a , Zhai, H. J., Yang, X., Wang, X. B., & Wang, L. S. ^c (2005). "Oxygen rich species: Areas of growth and advancement." <i>Amer Chemical Soc</i> .

Table 4. Peer-Reviewed Publications from 2004 Work through October 2008.
<u>Lagutschenkov, A.</u> ^a , <u>Fanourgakis, G. S.</u> , <u>Niedner-Schatteburg, G.</u> ^b , & <u>Xantheas, S. S.</u> ^c (2005). "The spectroscopic signature of the "all-surface" to "internally solvated" structural transition in water clusters in the n=17-21 size regime." <i>Journal of Chemical Physics</i> 122 (19): 9.
<u>Xantheas, S. S.</u> ^c , <u>Fanourgakis, G. S.</u> , <u>Kowalski, K.</u> , <u>Lagutschenkov, A.</u> ^a , & <u>Niedner-Schatteburg, G.</u> ^b . (2005). "Structural, spectral and excited state features of water hydrogen bonding networks: Results of ab-initio calculations and interaction potentials." <i>Abstracts of Papers of the American Chemical Society</i> , 229: U706-U707.
<u>Pankewitz, T.</u> , <u>Lagutschenkov, A.</u> ^a , <u>Niedner-Schatteburg, G.</u> ^b , <u>Xantheas, S. S.</u> ^c , & <u>Lee, Y. T.</u> (2007). "Infrared spectrum of NH ₄ ⁺ (H ₂ O): Evidence for mode specific fragmentation." <i>Journal of Chemical Physics</i> 126 (7): 14.
<u>Joly, A. G.</u> ^c , <u>Williams, J. R.</u> , <u>Chambers, S. A.</u> , <u>Xiong, G.</u> , <u>Hess, W. P.</u> , & <u>Laman, D. M.</u> ^a (2006). "Carrier dynamics in alpha-Fe ₂ O ₃ (0001) thin films and single crystals probed by femtosecond transient absorption and reflectivity." <i>Journal of Applied Physics</i> 99 (5): 6.
<u>Henager, C. H.</u> , <u>Le, E. A.</u> ^a , <u>Jones, R. H.</u> (2004). "A Model Stress Analysis of Swelling in SiC/SiC Composites as a Function of Fiber Type and Carbon Interphase Structure." 11th International Conference on Fusion Reactor Materials in <i>Journal of Nuclear Materials</i> , Amsterdam, Netherlands, Elsevier. vol. 329-333, no. Pt A, ed. Kohyama, A., pp. 502 - 506. Elsevier, Amsterdam, Netherlands.
<u>Ou, F. S.</u> ^a , <u>Saraf, L. V.</u> , & <u>Baer, D. R.</u> (2006). "Patterned regions of porous silicon through trapped hydrogen bubbles." <i>Applied Physics Letters</i> 88 (14): 3.
<u>Ou, F. S.</u> ^a , <u>Saraf, L. V.</u> ^c , & <u>Baer, D. R.</u> (2006). "Site-specific Formation of Nanoporous Silicon on Micro-fabricated Silicon Surfaces." <i>Mater. Res. Soc. Symp. Proc.</i> Vol. 829 © 2005 Materials Research Society
<u>Lloyd, J. A.</u> , <u>Spraggins, J. M.</u> ^a , & <u>Johnston, M. V.</u> ^b (2006). "Peptide ozonolysis: Product structures and relative reactivities for oxidation of tyrosine and histidine residues." <i>Journal of the American Society for Mass Spectrometry</i> 17 (9): 1289-1298.
<u>Spraggins, J. M.</u> ^a , <u>J. M.</u> , <u>Lloyd, J. A.</u> , <u>Laskin, J.</u> ^c , <u>Johnston, M. V.</u> ^b <u>Ridge, D. P.</u> (2008). "Fragmentation Mechanisms of Oxidized Peptides Elucidated by SID, RRKM Modeling and Molecular Dynamics." <i>Journal of the American Chemical Society</i> Submitted .
<u>Tait, S. L.</u> ^a , <u>Dohnalek, Z.</u> ^c , <u>Campbell, C. T.</u> ^b , & <u>Kay, B. D.</u> (2005). "Methane adsorption and dissociation and oxygen adsorption and reaction with CO on Pd nanoparticles on MgO(100) and on Pd(111)." <i>Surface Science</i> 591 (1-3): 90-107.
<u>Tait, S. L.</u> ^a , <u>Dohnalek, Z.</u> ^c , <u>Campbell, C. T.</u> ^b , & <u>Kay, B. D.</u> (2005). "n-Alkanes on MgO(100). I. Coverage-dependent desorption kinetics of n-butane." <i>Journal of Chemical Physics</i> 122 (16): 9.
<u>Tait, S. L.</u> ^a , <u>Dohnalek, Z.</u> ^c , <u>Campbell, C. T.</u> ^b , & <u>Kay, B. D.</u> (2005). "n-Alkanes on MgO(100). II. Chain length dependence of kinetic desorption parameters for small n-alkanes." <i>Journal of Chemical Physics</i> 122 (16): 13.
<u>Tait, S. L.</u> ^a , <u>Dohnalek, Z.</u> ^c , <u>Campbell, C. T.</u> ^b , & <u>Kay, B. D.</u> (2006). "n-alkanes on Pt(111) and on C(0001)/Pt(111): Chain length dependence of kinetic desorption parameters." <i>Journal of Chemical Physics</i> 125 (23): 15.
<u>Wang, Y.</u> ^a , <u>Zhang, L. G.</u> , <u>Fan, Y.</u> , <u>Luo, J.</u> , <u>McCready, D. E.</u> , <u>Wang, C. M.</u> ^c , & <u>An, L. A.</u> ^b (2005). "Synthesis, characterization, and optical properties of pristine and doped yttrium aluminum garnet nanopowders." <i>Journal of the American Ceramic Society</i> 88 (2): 284-286.
<u>Wang, Y. G.</u> ^a , <u>An, L. A.</u> ^b , <u>Fan, Y.</u> , <u>Zhang, L. G.</u> , <u>Burton, S.</u> , & <u>Gan, Z. H.</u> (2005). "Oxidation of polymer-derived SiAlCN ceramics." <i>Journal of the American Ceramic Society</i> 88 (11): 3075-3080.
<u>Wang, Y.</u> ^a , <u>Wang, C. M.</u> ^c , & <u>Yang, B.</u> (2006). "Synthesis of P(MMA-b-MAA) amphiphilic block copolymer and its self-organization behavior in solvent." <i>Chemical Journal of Chinese Universities-Chinese</i> , 27 (4): 758-760.

Table 4. Peer-Reviewed Publications from 2004 Work through October 2008.
Wang, Y. G. ^a , Fan, Y., Zhang, L. G., Zhang, W. G., & An, L. A. ^b (2006). "Polymer-derived SiAlCN ceramics resist oxidation at 1400 degrees C." <i>Scripta Materialia</i> , 55 (4): 295-297.
Wang, Y. G. ^a , Fei, W. F., & An, L. A. ^b (2006). "Oxidation/corrosion of polymer-derived SiAlCN ceramics in water vapor." <i>Journal of the American Ceramic Society</i> , 89 (3): 1079-1082.
Wang, Y. G. ^a , Saraf, L. V., Wang, C. M., Shutthanandan, V., McCready, D. E., Thevuthasan, S., (2007). "Fabrication and characterization of alternating-multilayer structures of gadolinia-doped ceria and zirconia grown by sputter-deposition." <i>Solid State Ionics</i> , Submitted .
Liu, Y., Yang, Z. ^a , Dessiaterik, Y., Gassman, P., Wang, H. ^b , & Laskin, A. ^c (2008). "Hygroscopic behavior of substrate-deposited particles studied by micro-FT-IR spectroscopy and complementary methods of particle analysis." <i>Analytical Chemistry</i> 80 (3): 633-642.

^aParticipant; ^bMentor; ^cPNNL Host

Table 5. Presentations/Conference Papers from 2004 Work though August 2007.
Laskin, J. ^c , Alvarez, J. ^a , Cooks, R. G. ^b , Futrell, J. H., & Barlow, S. E. (2005). "Collisions of Peptide Ions with Surfaces Studied Using FT-ICR MS." Presented at the 53rd ASMS Conference on Mass Spectrometry in San Antonio, TX.
Laskin, J. ^c , Hadjar, O., Wang, P., Futrell, J. H., Alvarez, J. ^a , Green, J. R. ^a , & Cooks, R. G. ^b (2006). "Soft Landing of Peptide Ions on Surfaces." Presented by Julia Laskin (Invited Speaker) at Isolated Biomolecules and Biomolecular Interactions (IBBI), Trest Castle, Czech Republic on May 10, 2006.
Laskin, J. ^c , Wang, P., Futrell, J. H., Alvarez, J. ^a and Cooks, R. G. ^b (2007). "Soft-Landing of Large Ions on Self-Assembled Monolayer Surfaces." Presented by Julia Laskin (Invited Speaker) at 18th International Conference on Ion Surface Interactions ISI-2007, Zvenigorod, Russian Federation on August 25, 2007
Deskins, N., Langell, M., Dupuis, M., Lyubinetsky, I. ^c , Du, Y. ^a , & Henderson, M. (2007). "Unique Hydrogen Configuration on TiO ₂ (110) upon Carboxylic Acid Dissociation" 2007 AIChE Annual Meeting, Salt Lake City, UT
Deskins, N., Langell, M., Dupuis, M., Lyubinetsky, I. ^c , Du, Y. ^a , and Henderson, M. (2008). "Carboxylic Acid Dissociation over Rutile TiO ₂ (110)." Presented by N. Aaron Deskins at 2008 Symposium of the Pacific Northwest Chapter of the AVS, Richland, WA on September 18, 2008.
Fanourgakis, G. S., Lagutschenkov, A. ^a , Niedner-Schatteburg, G. ^b , & Xantheas, S. S. ^c (2005). "Structural and spectral features of size selected water clusters in the n=7-21 regime: Results from electronic structure calculations and empirical potentials" Presented by Sotiris Xantheas (Invited Speaker) at Symposium on Size Selected Clusters, Brand, Austria on February 28, 2005.
Fanourgakis, G. S., Lagutschenkov, A. ^a , Kowalski, K., Niedner-Schatteburg, G. ^b , & Xantheas, S. S. ^c (2005). "Structural, spectral and excited state features of water hydrogen bonding networks: Results of ab-initio calculations and interaction potentials," Presented by Sotiris S. Xantheas (Invited Speaker) at American Chemical Society, San Diego, CA on March 13, 2005.
Lagutschenkov, A., Fanourgakis, G. S., Niedner-Schatteburg, G. ^b , & Xantheas, S. S. ^c (2005). "The Spectroscopic Signature of the "All-Surface" to "Internally Solvated" Structural Transition in Water Clusters in the n=17-21 Size Regime." Presented by Sotiris s. Xantheas (Invited Speaker) at EMSI International Workshop on Ions and Molecules at Aqueous Interfaces, Prague, Czech Republic on June 27, 2005.
Joly, A. G. ^c , Hess, W. P., Xiong, G., Laman, D. M. ^a , Williams, J. R., & Chambers, S. A. (2005). "Carrier Lifetimes and Dynamics in Epitaxial Grown Fe ₂ O ₃ /Cr ₂ O ₃ Thin Films Measured by Femtosecond Transient Reflectivity and Absorption" Presented by Gang Xiong (Invited Speaker) at APS Meeting, Los Angeles, CA on March 21, 2005.

Table 5. Presentations/Conference Papers from 2004 Work though August 2007.
Henager CH, JR, <u>EA Le</u> , and RH Jones. (2004). "A Model Stress Analysis of Swelling in SiC/SiC Composites as a Function of Fiber Type and Carbon Interphase Structure ." Presented by Charles H. Henager, Jr. at 5th International Conference on High-Temperature Ceramic Matrix Composites (HTCMC 5), Seattle, WA on September 12, 2004.
<u>Ou, F. S.^a</u> , <u>Saraf, L. V.^c</u> , & Baer, D. R. (2004). "Site-Specific Formation of Nanoporous Silicon on Micro-fabricated Silicon Surfaces". Presented by Fung Suong Ou at MRS 2004 Fall Meeting, Boston, MA on December 1, 2004.
<u>Ou, F. S.^a</u> , <u>Saraf, L. V.^c</u> , Baer, D. R., Wang, Z., & Engelhard, M. (2004). "Use of Hydrogen Reactivity During Chemical Etching to Achieve Site-Specific Nano-Porosity. " Presented by Don Baer at Micro Nano Breakthrough Conference, Portland, OR on July 28, 2004.
<u>Ou, F. S.^a</u> , <u>Saraf, L. V.^c</u> , & Baer, D. R. (2006). "Site-specific Formation of Nanoporous Silicon on Micro-fabricated Silicon Surfaces." Paper presented at the Materials Research Society Symposium.
<u>Spraggins, J. M.^a</u> , <u>Laskin, J.^c</u> & <u>Johnston, M. V.^b</u> (2005). "Ozonated Peptides: Insight Into Structure and Fragmentation Energetics Using SID FT-ICR MS. " Presented at the 53rd ASMS Conference on Mass Spectrometry in San Antonio, TX on June 08, 2005.
Liu Y, <u>Yang, Z.</u> , Gassman, P., <u>Wang, H.^b</u> , & <u>Laskin, A.^c</u> (2006). "Probing Deliquescence, Efflorescence and Hygroscopic Growth of Aerosols Using Micro-FTIR Spectroscopy." Presented by Yong Liu at AGU Meeting, San Francisco, CA on December 12, 2006.
Liu, Y., <u>Yang, Z.^a</u> , Gassman, P., <u>Wang, H.^b</u> , & <u>Laskin, A.^c</u> (2007). "Probing Hygroscopic Properties of Atmospheric Particles Using Complementary Methods of Micro FTIR Spectroscopy and Micro Analyses. " Presented by Yong Liu at AAAR 2007 Meeting, Reno, NV on September 27, 2007.

^aParticipant; ^bMentor; ^cPNNL Host

2005 Follow-up

Work from the summer of 2005 has already produced 21 refereed publications (Table 6) and 37 presentations (Table 7).

Table 6. Peer Reviewed Publications from 2005 Work through August 2007.
<u>Laskin, J.^c, Futrell, J. H., & Chu, I.^a (2007). Is Dissociation of Peptide Radical Cations an Ergodic Process? <i>Journal of the American Chemical Society</i> 129(31): 9598-9599.</u>
<u>Laskin, J.^c, Yang, Z., Lam, C., & Chu, I.^a (2007). Charge-Remote Fragmentation of Odd-Electron Peptide Ions <i>Analytical Chemistry</i> 79(17): 6607-6614.</u>
<u>Laskin, J.^c, Yang, Z., & Chu, I.^a (2008). "Energetics and dynamics of electron transfer and proton transfer in dissociation of metalIII(salen)-peptide complexes in the gas phase." <i>Journal of the American Chemical Society</i> 130(10): 3218-3230.</u>
<u>Yang, Z., Lam, C., & Chu, I.^a; Laskin, J.^c, (2008). "The effect of the secondary structure on dissociation of peptide radical cations: Fragmentation of angiotensin III and its analogues." <i>Journal of Physical Chemistry B</i> 112(39): 12468-12478.</u>
<u>Fister, T.^a, Vila, F., Seidler, G.^b, Svec, L., Linehan, J. C.^c (2008). "Local electronic structure of dicarba-closo-dodecaboranes C₂B₁₀H₁₂." <i>Journal of the American Chemical Society</i> 130(3): 925-932.</u>
<u>Fister, T.T.^a, Seidler, G.T.^b, Shirley, E.L., Vila, F.D., Nagle, K.P., Rehr, J. J., Linehan, J. C.^c Cross, J. O., (2008). "The local electronic structure of $\hat{1}\pm$-Li₃N." <i>Journal of Chemical Physics</i> 129(4): 345-352.</u>
<u>Bera, D., Kuchibhatla, S.^a, S, A., Saraf, L. V., Wang, C., Shutthanandan, V., McCready, D. E., Engelhard, M., Marina, O. A., Baer, D. R.^c, Seal, S.^b, & Thevuthasan, S. (2007). "Growth and characterization of highly oriented gadolinia-doped ceria (111) thin films on zirconia (111)/sapphire (0001) substrates" <i>Thin Solid Films</i>. In Press.</u>
<u>Baer, D. R.^c, Amonette, J. E., Engelhard, M. H., Gaspar, D. J., Karakoti, A. S., Kuchibhatla, S.^a, Nachimuthu, P., Nurmi, J. T., Qiang, Y., Sarathy, V., Baer, D. R.^c, Sharma, A., Tratnyek, P. G., Wang, C. M. (2008). "Characterization challenges for nanomaterials." <i>Surface and Interface Analysis</i> 40(3-4): 529-537.</u>
<u>Karakoti, A. S., Kuchibhatla, S.^a, Baer, D. R.^c, Thevuthasan, S., Sayle, D. C., Baer, D. R.^c, (2008). "Self-assembly of cerium oxide nanostructures in ice molds." <i>Small</i> 4(8): 1210-1216.</u>
<u>Gutowska, A., Li, L. Y., Shin, Y. S., Wang, C. M. M., Li, X. H. S., Linehan, J. C., Smith, R. S., Kay, B. D., Schmid, B.^a, Shaw, W., Gutowski, M., & Autrey, T.^c (2005). "Nanoscaffold mediates hydrogen release and the reactivity of ammonia borane". <i>Angewandte Chemie-International Edition</i>, 44(23): 3578-3582.</u>
<u>Stowe, A. C., Shaw, W. J., Linehan, J. C., Schmid, B.^a, & Autrey, T.^c (2007). "In situ solid state B-11 MAS-NMR studies of the thermal decomposition of ammonia borane: mechanistic studies of the hydrogen release pathways from a solid state hydrogen storage material". <i>Physical Chemistry Chemical Physics</i>, 9(15): 1831-1836.</u>
<u>Wei, W.^a, Xiong, G. Sun, Y., Joly, A. G., Beck, K. M., White, J. M.^b Hess, W. P.^c (2007). "In Materials, technology and reliability of low-k dielectrics and copper interconnects". <i>Materials Research Society Symposium Proceedings</i>; 2006; <i>Material Research Society</i>: Warrendale, PA, 2007; Vol. 914, p 185-190 (Paper no. 0914-F05-07).</u>
<u>Wei, W.^a, Parker, S. L., Sun, Y. M., White, J. M.^b, Xiong, G., Joly, A. G., Beck, K. M., & Hess, W. P.^c (2007). "Study of copper diffusion through a ruthenium thin film by photoemission electron microscopy". <i>Applied Physics Letters</i> 90(11): 3.</u>
<u>Dhamne, A., Xu, W. X.^a, Fookes, B. G., Fan, Y., Zhang, L. G., Burton, S.^c, Hu, J. Z., Ford, J., & An, L. A.^b, (2005). "Polymer-ceramic conversion of liquid polyaluminasilazanes for SiAlCN ceramics". <i>Journal of the American Ceramic Society</i>, 88(9): 2415-2419.</u>

Table 6. Peer Reviewed Publications from 2005 Work through August 2007.
<u>White, J. M.^b, Henderson, M., Dohnalek, Z.^c, & Zhang, Z.^a, (2006). "Surface chemistry on single crystal titania". <i>Abstracts of Papers of the American Chemical Society</i>. 231.</u>
<u>Zhang, Z.^a, Bondarchuk, O., Kay, B. D., White, J. M.^b, & Dohnalek, Z.^c, (2006). "Imaging water dissociation on TiO₂(110): Evidence for inequivalent geminate OH groups." <i>Journal of Physical Chemistry B</i> 110(43): 21840-21845.</u>
<u>Zhang, Z. R.^a, Bondarchuk, O., White, J. M.^b, Kay, B. D., & Dohnalek, Z.^c. (2006). "Imaging adsorbate O-H bond cleavage: Methanol on TiO₂(110)." <i>Journal of the American Chemical Society</i> 128(13): 4198-4199.</u>
<u>Zhang, Z. R.^a, Bondarchuk, E., Kay, B. D., White, J. M.^b, & Dohnalek, Z.^b. (2007). "Direct visualization of 2-butanol adsorption and dissociation on TiO₂(110)." <i>Journal of Physical Chemistry C</i> 111(7): 3021-3027.</u>
<u>Williams, R., Mancevski, V., McClure, P., Zhang, Z. R.^a, Li, S., Dohnalek, Z.^b, & Stevenson, K. J. (2008). "Simultaneous Fabrication of Carbon Nanotube Atomic Force Microscopy and Scanning Tunneling Microscopy Tips Via Localized Chemical Vapor Deposition and Nanomanipulation." <i>ACS Nano Submitted</i>.</u>
<u>Zhang, Z. R.^a, Ge, Q., Li, S., White, J. M.^b, Kay, B. D., & Dohnalek, Z.^b. "Imaging intrinsic diffusion of bridge-bonded oxygen vacancies on TiO₂(110)." <i>Physical Review Letters</i> 99(12): 4.</u>
<u>Zhang, Z. R.^a, Rousseau R.J. Gong, J., Kay, B. D., Ge, Q., White, J. M.^b, & Dohnalek, Z.^b. (2008). "Vacancy Assisted Diffusion of Alkoxy Species on Rutile TiO₂(110)." <i>Physical Review Letters</i> 101(15): art no. 156103.</u>

^aParticipant; ^bMentor; ^cPNNL Host

Table 7. Presentations/Conference Papers from 2005 Work though August 2007.
<u>Futrell, J. H., Laskin, J.^c, & Chu, I.^a (2006). "Surface-induced Collisional Activation and Dissociation of Even- and Odd-Electron Peptide Ions". 4th International UPPSALA Conference on ECD/ETD Mass Spectrometry. Ustron, Poland.</u>
<u>Futrell, J. H., Laskin, J.^c, & Chu, I.^a (2006). "Studies in Tandem Mass Spectrometry: Collisional Activation and Dissociation of Even- and Odd-Electron Peptide Cations". Presented by Jean H. Futrell (Invited Speaker) at WSU, Pullman, WA on November 3, 2006.</u>
<u>Lam, C.^a, Orlova, G., Laskin, J.^c, & Chu, I.^a (2006). "Facile Generation and Characterization of Cationic Radical Peptides: Ligand Effect and Peptide Structures" Presented by Julia Laskin at ASMS Conference on Mass Spectroscopy, Seattle, WA on May 29, 2006.</u>
<u>Laskin, J.^c, Yang, Z., Lam, C.^a, & Chu, I.^a (2007). "Energetics and Dynamics of Electron Transfer and Proton Transfer in Dissociation of Metal III (Salen)-Peptide Complexes in the Gas-Phase". Presented by Julia Laskin at 55th ASMS Conference on Mass Spectrometry, Indianapolis, IN on June 6, 2007.</u>
<u>Futrell, J. H., Yang, Z., Laskin, J.^c, & Chu, I.^a (2007). "Collisional Activation and Dissociation of Even- and Odd-electron Peptide Ion". Presented by Julia Laskin at the 25th Informal Meeting on Mass Spectrometry, Nyiregyhaza-Sosto, Hungary.</u>
<u>Yang, Z., Lam, C.^a, Chu, I.^a & Laskin, J.^c, (2008). Surface-Induced Dissociation of Peptide Radical Cations Presented by Julia Laskin (Invited Speaker) at ASMS Conference, in Denver CO on February 5, 2008</u>
<u>Laskin, J.^c, Yang, Z., Wang, P., Cooks, R.G.^b & Chu, I.^a (2008). Ion-Surface Interactions in Mass Spectrometry in Annapolis, MD on March 14, 2008</u>
<u>Dyer, M.^a, El-Azab, A.^c, & Gao, F.^c (2006). "Interfacial Structure and Point Defects in Ceria/Zirconia Superlattices". MRS Fall 2006, Symposium AA.</u>

Table 7. Presentations/Conference Papers from 2005 Work though August 2007.
Hadjar, O., Dessiaterik, Y., Futrell, J. H., Lea, A., <u>Green, J. R.^a</u> , <u>Cooks, R. G.^b</u> , & <u>Laskin, J.^c</u> (2006). "Design and Performance of a Novel Instrument for Soft-Landing of Biomolecular Ions on Surfaces". Presented by Omar Hadjar at ASMS Conference on Mass Spectrometry, Seattle, WA on May 30, 2006.
<u>Baer, D. R.^c</u> , Engelhard, Lea, A. S., Gaspar, D. J., Pecher, K. H., Wang, C. M., Amonette, J. E., El-azab, A. A. <u>Kuchibhatla, S.^a</u> and <u>Seal, S.^b</u> , (2005). "The Secret Life of Nanoparticles: characteristics of nanoparticles and nanostructured materials that are frequently forgotten or ignored". San Antonio, TX
<u>Kuchibhatla, S.^a</u> , Marina, O.A., Wang, C.M. Arey, B.W., Shutthanandan, V., Engelhard, M.H. Saraf, L.V., Matson, D.W., <u>Seal, S.^b</u> , <u>Baer, D. R.^c</u> , and Thevuthasan, S. (2005). "Fabrication of Gadolinia and Samaria Doped Ceria and Zirconia Vertical Layered Nanostructures for Solid Oxide Fuel Cell Applications". Boston, MA,
Bauder, L. M., Thevuthasan, S., <u>Kuchibhatla, S.^a</u> and Kim, Y. J. (2006). "Growth and Characterization of Samaria Doped Ceria for the Application of Fuel Cell Electrolytes". Richland, WA.
<u>Baer, D. R.^c</u> , Engelhard, M. H., Amonette, J. E., Wang, C. M. <u>Kuchibhatla, S.^a</u> , (2007). "Characterization challenges for nanomaterials." Surface and Interface Analysis Brussels, Belgium
<u>Kuchibhatla, S.^a</u> , Z. Yu, V. Shutthanandan, P. Nachimuthu, W. Jiang, C. M. Wang, S. Thevuthasan, C. H. Henager and S. K. Sundaram (2008). "Growth and characterization of cuprous oxide nanoclusters on strontium titanate (100) surface". Richland, WA.
Sundaram, S. K., <u>Kuchibhatla, S.^a</u> , Yu, Z., Nachimuthu, P, Engelhard, M. H., Shutthanandan, V., Thevuthasan, S. and Henager, C. H. (2008). "Copper Oxide Nano-clusters: Growth "Morphology" Chemistry". ETB/Wenatchee River Room, PNNL, WA.
Vasil, C., <u>Kuchibhatla S.^a</u> , Shutthanandan, V., Engelhard, M. H., Nachimuthu, P, Thevuthasan, S., and Singh, P., (2008). "Understanding the Initial Oxide Scale Formation and Growth on Haynes 214 Alloy". Richland, WA.
Smith, R. D., Adkins, J. N., Anderson, D. J., Auberry, K. J. Belov, M. E., Callister, S. J., Clauss, T. R. W., Fredrickson J. K., Du, X., Hixson, K. K., Jaitly, N., Kiebel, G. R., Lipton, M. S., Livesay, E. A., <u>Mayampurath, A. M.^a</u> , Monroe, M. E., Moore, R. J., Mottaz, H. M., Nicora, C. D., Norbeck, A. D., Orton, D., Pasa-Tolic, L., Petritis, K., Prior, D. C., Purvine, S. O., Shen, Y., <u>Shukla, A. K.^b</u> , Tolmachev, A. V., Tolic, N., Udseth, H. R. Zhang, R., and Zhao, R., (2006). "High Throughput Comprehensive and Quantitative Microbial and Community Proteomics". Bethesda, MD.
Hartl, M. A., Daemen, L. L., <u>Autrey, T.^c</u> , Linehan, J. C., Hess, N. J., Stowe, A. C., Gutowski, M., Brown, C. M., Mamontov, E., & <u>Schmid, B.^a</u> (2005). "Methyl torsion dynamics in methyl borate: An inelastic neutron scattering study". Abstracts of Papers of the American Chemical Society, 230: U411-U412.
Shaw, W. J., Brown, C. M., Daemen, L. L., Mamontov, E., Scott Smith, R., Kay, B. D., Shaw, W. J., Linehan, J. C., <u>Schmid, B.^a</u> , Stowe, A. C., Gutowski, M., & <u>Autrey, T.^c</u> (2005). "Spectroscopic studies of hydrogen formation from amineborane complexes". Abstracts of Papers of the American Chemical Society, 230: U1651-U1652.
Smith, R. S., Kay, B. D., Li, L. Y., <u>Schmid, B.^a</u> , Hess, N. J., Gutowski, M., & <u>Autrey, T.^c</u> (2005). "Mechanistic studies of hydrogen formation from amineborane complexes". Abstracts of Papers of the American Chemical Society, 229: U858-U858. Presenter: Julia Laskin
Smith, R. S., <u>Schmid, B.^a</u> , Hess, N.J., Kay, B. D. and <u>Autrey, T.^c</u> (2005). "Mechanistic studies of molecular hydrogen formation from borane ammonia complexes". Honolulu, HI

Table 7. Presentations/Conference Papers from 2005 Work though August 2007.
<u>Schmid, B.</u> ^a , Gutowska, M. A. Li, L., Shaw, W. J., Linehan, J. C., Hess, N.J., Daemen, L. L., Brown, C., Mamontov, E. and <u>Autrey, T.</u> ^c (2005). "Novel hybrid materials for hydrogen storage: using mesoporous scaffolds to enhance the reactivity and selectivity of hydrogen release from ammonia borane". Honolulu, HI
Smith, R. S., Kay, B. D., Daemen, L. L., Brown, C., Mamontov, E., Hess, N.J., Shaw, W. J., Linehan, J. C., <u>Schmid, B.</u> ^a , Stowe, A. C., Gutowski, M.S., and <u>Autrey, T.</u> ^c (2005). "Spectroscopic Studies of Hydrogen Formation From Amineborane Complexes". Washington, DC,
Bauder, L. M., Kemmitt, T., Shaw, W. J., Hess, N. J., Linehan, J. C., Gutowski, M. S., <u>Schmid, B.</u> ^a and <u>Autrey, T.</u> ^c (2005). "Mechanistic Studies of Hydrogen Release from Solid Amine Borane Materials". San Francisco, CA.
Shaw, W. J., Linehan, J. C., <u>Schmid, B.</u> ^a , Stowe, A. C., and <u>Autrey, T.</u> ^c (2005). "In situ NMR studies of amine boranes. Dynamics and mechanisms of hydrogen formation". San Francisco, CA.
Li, L., <u>Schmid, B.</u> ^a , Smith, R.S., Kay, B.D., Linehan, J. C., Shaw, W. J., Hess, N. J., Stowe, A. C., Gutowski, M. S., and <u>Autrey, T.</u> ^c (2005). "Hydrogen Storage in HNBH Systems". San Francisco, CA.
<u>Autrey, T.</u> ^c , Bowden, M., Kemmitt, T. Shaw, W. J., Shaw, W. J., Linehan, J. C., Gutowski, M. and <u>Schmid, B.</u> ^a (2006). "Mechanistic Studies of Hydrogen Release from Solid Amine Borane Materials". San Francisco, CA.
<u>Wei, W.</u> ^a , Sun, Y., <u>White, J. M.</u> ^b , Xiong, G., Joly, A. G., Beck, K. M., and <u>Hess, W. P.</u> ^c (2005). "In Situ Study of Cu Diffusion Through Ru Thin Film by Photoelectron Emission Microscopy (PEEM)". San Francisco, CA.
Xiong, G., Joly, A. G., Beck, K. M., and <u>Hess, W. P.</u> ^c , Cai, M., Dickinson, J. T., <u>Wei, W.</u> ^a and <u>White, J. M.</u> ^b (2006). "Research Applications of Photoelectron Emission Microscopy". Denver, CO.
<u>Zhang, Z.</u> ^a , O. Bondarchuk, J. M. White, J. Kim, B. D. Kay and Z. Dohnalek (2006). "Surface Reactions of Alcohols on TiO ₂ (110) Investigated by in situ Scanning Tunneling Microscopy". San Francisco, CA.
<u>Zhang, Z.</u> ^a , Kay, B. D., Ge, Q., <u>White, J. M.</u> ^b , & <u>Dohnalek, Z.</u> ^c . (2006). "Diffusion of Bridge-Bonded Oxygen Vacancies on TiO ₂ (110) " Presented by Zhenrong Zhang at AVS 53rd International Symposium and Exhibition, San Francisco, CA on November 13, 2006.
<u>Dohnalek, Z.</u> ^c , Kay, B. D., <u>White, J. M.</u> ^b , Bondarchuk, O., Kim, J., Kim, Y., Li, S., & <u>Zhang, Z.</u> ^a (2007). "Structure and Catalytic Activity of Model Oxide Systems". Presented by Zdenek Dohnalek (Invited Speaker) at DOE BES Catalysis Contractors' Meeting, Washington DC, on May 24, 2007.
<u>Zhang, Z.</u> ^a , Li, S., Ge, Q., Kay, B. D., <u>White, J. M.</u> ^b , & <u>Dohnalek, Z.</u> ^c (2007). "Diffusion of Bridge-Bonded Oxygen Vacancies and Hydrogen on TiO ₂ (110) ". Presented by Zhenrong Zhang; Gordon Research Conference on Dynamics at Surfaces, Andover, NH on August 16, 2007.
<u>Zhang, Z.</u> ^a , Li, S., <u>White, J. M.</u> ^b , & <u>Dohnalek, Z.</u> ^c (2007). "Defect and Adsorbate Dynamics on TiO ₂ (110) ". Presented by Zdenek Dohnalek (Invited Speaker) at University of California, Santa Barbara, Santa Barbara, CA on September 26, 2007.
<u>Zhang, Z.</u> ^a , Kay, B. D., Ge, Q., <u>White, J. M.</u> ^b , & <u>Dohnalek, Z.</u> ^c (2007). "Diffusion of Bridge-Bonded Oxygen Vacancies on TiO ₂ (110) ". Presented by Zhenrong, Zhang at National AVS Conference, Seattle, WA on October 16, 2007.
Zhang, Z., R. J. Rousseau, J. Gong, S.-C. Li, B. D. Kay, Q. Ge, J. M. White and Z. Dohnalek (2008). "Diffusion and Rotation of Alkoxy Species on Rutile TiO ₂ (110)". Philadelphia, PA.

^aParticipant; ^bMentor; ^cPNNL Host

2006 Follow-up

Work from the summer of 2006 has already produced 35 peer-reviewed publications as well as 1 submitted (Table 8) and 32 presentations (Table 9).

Table 8. Peer Reviewed Publications from 2006 Work through August 2007.
Liu, Y., <u>Cain, J. P.</u> ^a , <u>Wang, H.</u> ^b , & <u>Laskin, A.</u> ^c (2007). "Kinetic Study of Heterogeneous Reactions of Deliquesced NaCl Particles with Gaseous HNO ₃ Using Particle-on-Substrate Stagnation Flow Reactor Approach". <i>Journal of Physical Chemistry A</i> . 111(40): 10026-10043.
Liu, Y., Gibson, E. R., <u>Cain, J. P.</u> ^a , <u>Wang, H.</u> ^b , Grassian, V. H., & <u>Laskin, A.</u> ^c 2008. "Kinetics of Heterogeneous Reaction of CaCO ₃ Particles with Gaseous HNO ₃ Over a Wide Range of Humidity". <i>Journal of Physical Chemistry A</i> . 112(7): 1561-1571.
<u>Zelenyuk, A.</u> ^c , Imre, D., & <u>Cuadra-Rodriguez, L. A.</u> ^a (2006). "Evaporation of water from particles in the aerodynamic lens inlet: An experimental study". <i>Analytical Chemistry</i> , 78(19): 6942-6947.
<u>Chang, C.L.</u> ^a , Shutthanandan, V., Singhal, S. C., & Ramanathan, S. (2007). "In situ ion scattering and x-ray photoelectron spectroscopy studies of stability and nanoscale oxidation of single crystal (100)". <i>Applied Physics Letters</i> , 90(20): 3.
<u>Chang, C.L.</u> ^a , Shutthanandan, V., Singhal, S. C., & Ramanathan, S. (2007). "On the stability and oxidation of single crystal (100), <i>Electrochemical Society Transactions, Physics and Technology of High-k Gate Dielectrics</i> 11(4), 409.
<u>Chang, C.L.</u> ^a , Shutthanandan, V., Singhal, S. C., & Ramanathan, S. (2007). "In situ studies on stoichiometry and structure of thin film yttria-stabilized zirconia under thermal processing". <i>Materials Research Society Symposium Proceedings, San Francisco, CA</i> . 1023-JJ01-07
<u>Chang, C.L.</u> ^a , Engelhard, M. H., Ramanathan, S., (2008), "Superior Nanoscale Passive Oxide Layers Synthesized Under Photon Irradiation for Environmental Protection", <i>Appl. Phys. Lett.</i> , 92(26): 263103, 1-3
Sarathy, V., Tratnyek, P. G., Nurmi, J. T., <u>Baer, D. R.</u> ^c , Amonette, J. E., <u>Chun, C. L.</u> ^a , Penn, R. L., Reardon, E. J., (2008), "Aging of iron nanoparticles in aqueous solution: Effects on structure and reactivity", <i>J. Phys. Chem. C</i> , 112(7): 2286
<u>Du, S.</u> ^a , <u>Francisco, J. S.</u> ^b , <u>Schenter, G. K.</u> ^c , Iordanov, T. D., Garrett, B. C., Dupuis, M., & Li, J. (2006). "The OH Radical-H ₂ O Molecular Interaction Potential". <i>Journal of Chemical Physics</i> 124(22):
<u>Francisco, J. S.</u> ^b , Kathmann, S. M., <u>S Schenter, G. K.</u> ^c , Dang, L. X., Xantheas, S. S., Garrett, B. C., <u>Du, S.</u> ^a , Dixon, D. A., Bianco, R., Wang, S., Hynes, J. T., Morita, A., Peterson, K. A., (2006), "A Computational Approach to Understanding Aerosol Formation and Oxidant Chemistry in the Troposphere", PNNL Report
<u>Du, S.</u> ^a , <u>Francisco, J. S.</u> ^b , <u>Schenter, G. K.</u> ^c , & Garrett, B. C. (2007). "Ab initio and analytical intermolecular potential for ClO-H ₂ O". <i>Journal of Chemical Physics</i> , 126(11): 146-155.
<u>Du, S.</u> ^a , <u>Francisco, J. S.</u> ^b , <u>Schenter, G. K.</u> ^c , & Garrett, B. C. (2008). "Many-Body Decomposition of the Binding Energies for OH ₂ (H ₂ O) ₂ and OH ₂ (H ₂ O) ₃ " Complexes. <i>Journal of Chemical Physics.</i> , 128(8):
<u>Dutta, D.</u> ^a , <u>Sundaram, S. K.</u> ^c , Teeguarden, J. G., Riley, B. J., Fifield, L. S., Jacobs, J. M., Addleman, S. R., Kaysen, G. A., Moudgil, B. M., Weber, T. J. (2007). "Adsorbed Proteins Influence the Biological Activity and Molecular Targeting of Nanomaterials". <i>Toxicological Sciences</i> , 100(1): 303-315.
<u>Zhang, Y.</u> ^c , Milbrath, B. D., Weber, W. J., <u>Elfman, M.</u> ^a , & Whitlow, H. J. (2007). "Radiation detector resolution over a continuous energy range". <i>Applied Physics Letters</i> , 91(09): 1-3.

Table 8. Peer Reviewed Publications from 2006 Work through August 2007.
Zhang, Y. ^c , Elfman, M. ^a , Milbrath, B. D., Weber, W. J., (2008), "Evaluate Scintillation Response Over a Continuous Energy Region", IEEE Transactions on Nuclear Science,55(3): 1097-1101
Lins Neto, R. D. ^c , Vorpapel, E. R., Guglielmi, M. ^a , & Straatsma, T., (2008), "Computer Simulation of Uranyl Uptake by the Rough Lipopolysaccharide Membrane of Pseudomonas aeruginosa", Biomacromolecules,9(1): 29-35
Hopkins, R. J. ^a , Lewis, K. M., Dessiaterik, Y., Wang, Z., Tivanski, A., Arnott, W. P., Laskin, A. ^c , & Gilles, M. K. ^b (2007). "Correlations between optical, chemical and physical properties of biomass burn aerosols". Geophys. Res. Lett., 34(18).
Hopkins, R. J. ^a , Tivanski, A., Dessiaterik, Y., Tyliczszak, T., Laskin, A. ^c , & Gilles, M. K. ^b (2007). "Chemical Speciation of Sulfur in Marine Cloud Droplets and Particles: 2. Partitioning of Methanesulfonate and Non-Sea Salt Sulfate in Individual Sea Salt Particles". Journal of Geophysical Research. D. (Atmospheres). Submitted.
Doran, J. C., Fast, J. D., Barnard, J. C., Laskin, A. ^c , Dessiaterik, Y., Gilles, M. K. ^b , & Hopkins, R. J. ^a (2008). "Applications of Lagrangian Dispersion Modeling to the Analysis of Changes in the Specific Absorption of Elemental Carbon". Atmospheric Chemistry and Physics. 8(5): 1377-1389.
Hopkins, R. J. ^a , Tivanski, A., Dessiaterik, Y., Tyliczszak, T., Laskin, A. ^c , & Gilles, M. K. ^b (2008). "Chemical Speciation of Sulfur in Marine Cloud Droplets and Particles: 1. Analysis of Individual Particles from Marine Boundary Layer Over the California Current". Journal of Geophysical Research. D. (Atmospheres). 113(D4).
Moffet, R. C., Desyaterik, Y., Hopkins, R. J. ^a , Tivanski, A. V., Gilles, M. K. ^b , Wang, Y., Shutthanandan, V., Molina, L. T., Abraham, R. G., Johnson, K. S., Mugica, V., Molina, M. J., Laskin, A. ^c , Prather, K. A., (2008), "Characterization of aerosols containing Zn, Pb, and Cl from an industrial region of Mexico City", Environ. Sci. Technol.,42(19): 7091-7097
Johnson, K. S., de Foy, B., Zuberi, B., Molina, L. T., Molina, M. J. ^b , Xie, Y., Laskin, A. ^c , & Shutthanandan, V. (2006). "Aerosol composition and source apportionment in the Mexico City Metropolitan Area with PIXE/PESA/STIM and multivariate analysis". Atmospheric Chemistry and Physics, 6: 4591-4600.
Salcedo, D., Onasch, T. B., Dzepina, K., Canagaratna, M. R., Zhang, Q., Huffman, A. J., DeCarlo, P., Jayne, J., Mortimer, P., Worsnop, D. R., Kolb, C. E., Johnson, K. S. ^a , Zuberi, B., Marr, L., Volkamer, R. M., Molina, L. T., Molina, M. J. ^b , Cardenas, B., Bernabe, R., Marquez, C., Gaffney, J. S., Marley, N. A., Laskin, A. ^c , Shutthanandan, V., Xie, Y., Brune, W. H., Leshner, R., Shirley, T., & Jimenez, J. L. (2006). "Characterization of Ambient Aerosols in Mexico City during the MCMA-2003 Campaign with Aerosol Mass Spectrometry. Results from the CENICA Supersite". Chemistry and Physics, 6: 925-946.
San Martini, F. M., Dunlea, E. J., Volkamer, R., Onasch, T. B., Jayne, J. T., Canagaratna, M. R., Worsnop, D. R., Kolb, C. E., Shorter, J. H., Herndon, S. C., Zahniser, M. S., Salcedo, D., Dzepina, K., Jimenez, J. L., Ortega, J. M., Johnson, K. S. ^a , McRae, G. J., Molina, L. T., Molina, M. J. ^b (2006), "Implementation of a Markov Chain Monte Carlo method to inorganic aerosol modeling of observations from the MCMA-2003 campaign - Part II: Model application to the CENICA, Pedregal and Santa Ana sites", Atmospheric Chemistry and Physics,6(4889-4904
Barnard, J. C., Kassianov, E. L., Ackerman, T. P., Johnson, K. S. ^a , Zuberi, B., Molina, L. T., & Molina, M. J. ^b (2007). "Estimation of a "radiatively correct" black carbon specific absorption during the Mexico City Metropolitan Area (MCMA) 2003 field campaign". Atmospheric Chemistry and Physics, 7(6): 1645-1655.

Table 8. Peer Reviewed Publications from 2006 Work through August 2007.
Johnson, K. S. ^a , Laskin, A. ^c , Jimenez, J. L., Shutthanandan, V., Molina, L. T., Salcedo, D., Dzepina, K., Molina, M. J. ^b , (2008), "Comparative analysis of urban atmospheric aerosol by particle-induced X-ray emission (PIXE), proton elastic scattering analysis (PESA), and aerosol mass spectrometry (AMS)", <i>Environ. Sci. Technol.</i> ,42(17): 6619-6624
Lane, C. D., Petrik, N. G., Orlando, T. M., & Kimmel, G. A. (2007). "Electron-Stimulated Oxidation of Thin Water Films Adsorbed on TiO ₂ (110)". <i>Journal of Physical Chemistry C</i> . 111(44): 16319-16329.
Lane, C. D. ^a , Petrik, N. G. ^c , Orlando, T. M. ^b , & Kimmel, G. A. (2007). "Site-dependent Electron-Stimulated Reactions in Water Films on TiO ₂ (110)". <i>Journal of Chemical Physics</i> . 127(22): 9.
Zhai, H. J., Wang, L. M., Li, S. D. ^a , & Wang, L. S. ^c (2007). "Vibrationally resolved photoelectron spectroscopy of BO ⁻ and BO ₂ ⁻ : A joint experimental and theoretical study". <i>Journal of Physical Chemistry A</i> , 111(6): 1030-1035.
Zhai, H. J., Wang, L., Li, S. ^a , & Wang, L. S. ^c (2007). "Boronyls as Key Structural Units in Boron Oxide Clusters: B(BO) ₂ ⁻ and B(BO) ₃ ⁻ ". <i>Journal of the American Chemical Society</i> . 129(30): 9254-.
Li, S. ^a , Zhai, H. J., Wang, L. S. ^c , (2008), "B-2(BO)(2)(2 ⁻) - Diboronyl diborene: A linear molecule with a triple boron-boron bond", <i>J. Am. Chem. Soc.</i> ,130(8): 2573-2579
Saheb, A. H. ^a , Smith, J. A., Joczowicz, M., Janata, J. ^b , Baer, D. R. ^c , & Engelhard, M. H. (2007). "Controlling Size of Gold Clusters in Polyaniline from Top Down and from Bottom Up". <i>Journal of Electroanalytical Chemistry</i> . 621(2): 238-244.
Thomas, J. L. ^a , Roeselova, M., Dang, L. X. ^c , & Tobias, D. J. (2007). "Molecular dynamics simulations of the solution-air interface of aqueous sodium nitrate". <i>Journal of Physical Chemistry A</i> , 111(16): 3091-3098.
Yu, Y., Ezell, M., Zelenyuk, A. N., Imre, D. G., Alexander, M. L., Ortega, J. V., Thomas, J. L. ^a , Gogna, K., Tobias, D. J., D'Anna, B., Harmon, C. W., Johnson, S., Finlayson-Pitts, B. J. ^b , (2008), "A New Pathway for Oxidation of Alpha-Pinene through Aqueous Nitrate Ion Photochemistry", <i>Environ. Sci. Technol.</i> ,
Yu, Y., Ezell, M. J., Zelenyuk, A. N., Imre, D. G., Alexander, M. L., Ortega, J. V., Thomas, J. L. ^a , Gogna, K., Tobias, D. J., D'Anna, B., Harmon, C. W., Johnson, S., Finlayson-Pitts, B. J. ^b , (2008), "Nitrate Ion Photochemistry at Interfaces: A New Mechanism for Oxidation of alpha-Pinene", <i>Physical Chemistry Chemical Physics</i> . PCCP,10(21): 3063-3071
Jagoda-Cwiklik, B., Wang, X. B., Woo, H.-K., Yang, J., Wang, G. ^a , Zhou, M., Jungwirth, P., Wang, L. S. ^c , (2007), "Microsolvation for the Dicyanamide Anion: [N(CN) ₂] ⁻ (H ₂ O) _n (n=0-12)", <i>J. Phys. Chem. A</i> ,111(32): 7719-7725

^aParticipant; ^bMentor; ^cPNNL Host

Table 9. Presentations/Conference Papers from 2006 Work through August 2007.
Liu, Y., Cain, J. P. ^a , Wang, H. ^b , & Laskin, A. ^c (2006). "A Kinetic Study of the Heterogeneous Reaction of Deliquesced NaCl Particles with Gaseous HNO ₃ Using Novel Experimental Approach". Presented by Yong Liu at AGU Meeting, San Francisco, CA on December 12, 2006
Liu, Y., Cain, J. P. ^a , Wang, H. ^b , & Laskin, A. ^c (2007). "A Kinetic Study of the Heterogeneous Reaction of Deliquesced NaCl Particles with Gaseous HNO ₃ ". Presented by Yong Liu at AAAR 2007 Meeting, Reno, NV on September 25, 2007.
Liu, Y., Gibson, E. R., Cain, J. P. ^a , Wang, H. ^b , Grassian, V. H., Laskin, A. ^c , (2007), "Chemical Transformation of CaCO ₃ Particles by Heterogeneous Reaction with HNO ₃ : Kinetic Measurements Over a Wide Range of Humidity", San Francisco, CA

Table 9. Presentations/Conference Papers from 2006 Work though August 2007.
Baer, D. R. ^b , Tratnyek, P. G., Amonette, J. E., <u>Chun, C. L.</u> ^a , Nachimuthu, P., Nurmi, J., Penn, R. L., Matson, D. W., Linehan, J. C., Qiang, Y., Sharma, A., "Tuning the Properties of Iron Nanoparticles: Doping Effects on Reactivity and Aging". In International Environmental Nanotechnology Conference: Applications and Implications 2008.
Zelenyuk, A., <u>Cuadra-Rodriguez, L. A.</u> ^a , Imre, D., Shimpi, S., & Warey, A. (2006). "The Size and Composition of Individual Ultrafine Diesel Emission Particulate from 2007 Diesel Engines with and without after Treatment". Presented by Alla Zelenyuk at DEER 2006, Detroit, MI on August 21, 2006.
Zelenyuk, A. ^c , <u>Cuadra-Rodriguez, L. A.</u> ^a , Imre, D., Shimpi, S., & Warey, A. (2006). "Comprehensive Characterization of Ultrafine Particulate Emission from 2007 Diesel Engines: PM Size Distribution Loading and Individual Particle Size and Composition". Presented by Alla Zelenyuk at American Geophysical Union Meeting, San Francisco, CA on December 13, 2006.
Zelenyuk, A. ^c , <u>Cuadra-Rodriguez, L. A.</u> ^a , Imre, D., Shimpi, S., & Warey, A. (2007). "Comprehensive Characterization of Ultrafine Particulate Emission from 2007 Diesel Engines with Aftertreatment: PM Size Distribution, Loading and Individual Particle Size and Composition". Presented by Alla Zelenyuk at AAAR Meeting, Reno, NV on September 24, 2007.
Zelenyuk, A. ^c , Imre, D., <u>Cuadra-Rodriguez, L. A.</u> ^a , & Ellison, B. (2007). "Measurements and Interpretation of the Effect of Soluble Organic Surfactants on the Density, Shape and Water Uptake of Hygroscopic Particles". Presented by Alla Zelenyuk at AAAR Meeting, Reno, NV on September 25, 2007.
<u>Chang, C.L.</u> ^a , Shutthanandan, V., Ramanathan, S., (2006), "High-resolution ion scattering studies on oxide-semiconductor interfaces", Cincinnati, OH
<u>Chang, C.L.</u> ^a , Shutthanandan, V., Singhal, S. C., Ramanathan, S., (2007), "In-Situ High-Resolution Ion Scattering Studies on Oxygen Defect Chemistry and Migration Kinetics Across Nanoscale Oxide Hetero-Interfaces", San Francisco, CA
Tratnyek, P. G., Sarathy, V., Nurmi, J., <u>Baer, D. R.</u> ^c , Amonette, J. E., <u>Chun, C. L.</u> ^a , Penn, R. L., Reardon, E. J., "Aging of Iron Nanoparticles in Water: Effects on Structure and Reactivity", In International Environmental Nanotechnology Conference: Applications and Implications 2008.
Weber, T. J., <u>Sundaram, S. K.</u> ^c , Riley, B. J., Addleman, R. S., Fifield, L. S., <u>Dutta, D.</u> ^a , & <u>Moudgil, B. M.</u> ^b (2007). "Targeting Nanomaterials to Cell Surface Receptors: Implications for Defining Relevant Modes of Action and Chronic Toxicity", by Tom Weber at Society of Toxicology, Charlotte, NC on March 25, 2007.
Weber, T. J., <u>Dutta, D.</u> ^a , <u>Sundaram, S. K.</u> ^c , Teeguarden, J. G., Riley, B. J., Fifield, L. S., Jacobs, J. M., Addleman, S., Kaysen, G. A., <u>Moudgil, B. M.</u> ^b , (2007), "Adsorbed Proteins Influence the Biological Activity and Molecular Targeting of Nanomaterials", Seattle, WA
<u>Gomes, D. E.</u> ^a , Lins, R. D., <u>Pascutti, P. G.</u> ^b , Straatsma, T. P., <u>Soares, T. A.</u> ^c , "Molecular Models to Emulate Confinement Effects on the Internal Dynamics of Organophosphorous Hydrolase". In Lecture Notes in Computer Science: Advances in Bioinformatics and Computational Biology, Third Brazilian Symposium on Bioinformatics, BSB 2008, Santo Andra, Brazil, Vol. 5167, p 68-78.
Dessiaterik, Y., <u>Hopkins, R. J.</u> ^a , Tivanski, A., Berkowitz, C. M., <u>Gilles, M. K.</u> ^b , & <u>Laskin, A.</u> ^c (2006). "Chemical Speciation of Sulfur in Marine Cloud Droplets and Particles: 1. Analysis of Individual Particles Using Complementary Microprobe Methods" Presented by Yury Dessiaterik at AGU Fall Meeting, San Francisco, CA on December 13, 2006.
Dessiaterik, Y., <u>Hopkins, R. J.</u> ^a , Tivanski, A., <u>Gilles, M. K.</u> ^b , & <u>Laskin, A.</u> ^c (2006). "Partitioning of Methanesulfonate and Non-Sea-Salt Sulfate in Individual Sea Salt Particles Collected at the Pt. Reyes National Seashore". by Alex Laskin (Invited Speaker) at AirUCI Workshop, Christchurch, New Zealand on December 11, 2006.

Table 9. Presentations/Conference Papers from 2006 Work though August 2007.
Johnson, K. S. ^a , Gonzalez, R. L. ^a , Molina, L. T. ^b , Hopkins, R. J. ^a , Tivanski, A., Gilles, M. K. ^b , Dessiaterik, Y., & Laskin, A. ^c (2007). "Microscopy and Microprobe Studies of Individual Particles Collected During MILAGRO 2006 Study". Presented by Alex Laskin at European Geosciences Union General Assembly 2007, Vienna, Austria on April 18, 2007.
Dessiaterik, Y., Hopkins, R. J. ^a , Tivanski, A., Gilles, M. K. ^b , & Laskin, A. ^c (2007). "Partitioning of Methanesulfonate and Non-Sea-Salt Sulfate in Individual Sea Salt Particles Collected at the Pt. Reyes National Seashore". Presented by Alex Laskin at European Geosciences Union General Assembly 2007, Vienna, Austria on April 19, 2007.
Hopkins, R. J. ^a , Tivanski, A., Dessiaterik, Y., Gaspar, D. J., Gilles, M. K. ^b , & Laskin, A. ^c (2006). "Analysis of Field Collected Individual Atmospheric Particle Using Multi-Analytical Microprobe Methods". Presented by Yury Dessiaterik at AAAR Meeting, St. Paul, MN on September 13, 2006.
Hopkins, R. J. ^a , Tivanski, A., Dessiaterik, Y., Laskin, A. ^c , & Gilles, M. K. ^b 2006. "Chemical Speciation of Sulfur in Marine Cloud Droplets and Particles: 2. Partitioning of Methanesulfonate and Non-Sea Salt Sulfate in Individual Sea Salt Particles". Presented by Yury Dessiaterik at AGU Fall Meeting, San Francisco, CA on December 13, 2006.
Hopkins, R. J. ^a , Dessiaterik, Y., Zaveri, R. A., Berkowitz, C. M., Tivanski, A., Gilles, M. K. ^b , & Laskin, A. ^c (2007). Chemical Speciation of Sulfur in Marine Cloud Droplets and Particles: Quantitative Assessment of Methanesulfonate and Non-Sea Salt Sulfate Partitioning in Individual Sea Salt Particles. Presented by Alex Laskin at AAAR 2007 Conference, Reno, NV on September 25, 2007.
Hopkins, R. J. ^a , Lewis, K. M., Dessiaterik, Y., & Wang, Z. (2007). Diversity of Biomass Burn Aerosols Based on Fuel. Presented by M. K. Gilles at AAAR 2007 Meeting, Reno, NV on September 26, 2007.
Onasch, T. B., Slowik, J. G., Davidovits, P., Herndon, S., Wood, E. A., Canagaratna, M. R., Worsnop, D., Kolb, C. E., Knighton, W. B., Zavala, M. A., Thornhill, D. R., Marr, L., Arnott, W. P., Mazzoleni, C., Dubey, M., Hopkins, R. J. ^a , Gilles, M. K. ^b , Dessiaterik, Y., Laskin, A. ^c , (2007), "Carbonaceous Aerosol Processing in the Mexico City Metropolitan Area", San Francisco, CA
Gilles, M. K. ^b , Hopkins, R. J. ^a , Tivanski, A., Laskin, A. ^c , Dessiaterik, Y., Tyliczszak, T., (2008), "Characterizing Black Carbons and Biomass Burn Particulates: Evidence for Oxygenated Interfaces on Aged Biomass Burn Particulates", New Orleans, LA
Johnson, K. S. ^a , Gonzalez, R. L., Molina, L., Hopkins, R. J., Tivanski, A., Gilles, M. K., Dessiaterik, Y., Laskin, A. ^c , (2006), "Microscopy and Microprobe Studies of Individual Particles Collected During MILAGRO 2006 Study", Vienna, Austria, 2006,
Laskin, J. ^c , Yang, Z., & Lam, C. ^a (2007). "Surface-Induced Dissociation of Even- and Odd-Electron Peptide Ions". Presented by Julia Laskin at Gordon Research Conference on Gaseous Ions: Structures, Energetics & Reactions, Ventura, CA on February 28, 2007.
Petrik, N. G. ^c , Lane, C. D. ^a , Orlando, T. M. ^b , & Kimmel, G. A. (2007). "Electron Stimulated Desorption and Dissociation of Thin Water Films Adsorbed on TiO ₂ (110)". Presented by Nick Petrik at ACS International Conference, Boston, MA on August 20, 2007.
Lee, C. ^a , Wachsman, E. D., Phillpot, S. R., Devanathan, R. ^c , & Sinnott, S. B. ^b (2007). "Chemical Properties of LaFeO ₃ from First Principles Calculations: Implications for Use as SOFC cathodes. Presented by Chan-Woo Lee at 2007 Gordon Research Conference on Solid State Studies in Ceramics", Andover, NH on August 8, 2007.
Lee, C. ^a , Wachsman, E. D., Phillpot, S. R., Devanathan, R. ^c , & Sinnott, S. B. ^b , (2007), "The Effect of Sr and Co Substitutions on the Performance of LaFeO ₃ for Solid Oxide Fuel Cell Cathodes: Predictions of Density Functional Theory Calculations", Boston, MA

Table 9. Presentations/Conference Papers from 2006 Work though August 2007.
<u>Lee, C.</u> ^a , Wachsman, E. D., Phillpot, S. R., Devanathan, R. ^c , & Sinnott, S. B. ^b , (2008), "Examination of the LaFeO3 (010) Surface Using Density Functional Theory and Thermodynamics", Boston, MA.
<u>Li, S.</u> ^a , Fu, L., Wang, C. M. ^c , Lea, S., Arey, B., Engelhard, M., & <u>Cheng, Z.-Y.</u> ^b (2006). Characterization of Microstructure and Composition of Fe-B Nanobars as Biosensor Platform. Paper presented at the MRS Proceedings, Boston, MA.

^aParticipant; ^bMentor; ^cPNNL Host

2007 Follow-up

Work from the summer of 2007 has already produced 25 peer-reviewed publications as well as 3 submitted (Table 10) and 16 presentations (Table 11).

Table 10. Peer Reviewed Publications from 2007.
Petrik, N. G., <u>Kimmel, G. A.</u> ^c , <u>Akin, M. C.</u> ^a (2008), "Electron-Stimulated Reactions and O2 Production in Methanol-Covered Amorphous Solid Water Films", J. Chem. Phys., Submitted
Bateman, A. P. ^a , Walser, M. L., Desyaterik, Y., <u>Laskin, J.</u> ^c , Laskin, A., Nizkorodov, S. A. ^b , (2008), "The effect of solvent on the analysis of secondary organic aerosol using electrospray ionization mass spectrometry", Environ. Sci. Technol.,42(19): 7341
<u>Gupta, S.</u> ^a , <u>Kuchibhatla, S. V. N. T.</u> , Engelhard, M. H., Shutthanandan, V., Nachimuthu, P., Jiang, W., <u>Saraf, L. V.</u> ^c , Thevuthasan, S., <u>Prasad, S.</u> ^b , (2008), "Influence of samaria doping on the resistance of ceria thin films and its implications to the planar oxygen sensing devices", Sensors and Actuators. B, Chemical
Hess, N. J. ^c , <u>Hartman, M. R.</u> ^a , Brown, C. M., Mamontov, E., Karkamkar, A., Heldebrant, D. J., Daemen, L. L., Autrey, T., (2008), "Quasielastic neutron scattering of -NH3 and -BH3 rotational dynamics in orthorhombic ammonia borane", Chem. Phys. Lett.,459(1-6): 85-88
Kwak, J. H., Hu, J. Z., <u>Lukaski, A.</u> ^a , Kim, D. H., Szanyi, J., <u>Peden, C. H. F.</u> ^c , (2008), "Role of pentacoordinated Al3+ ions in the high temperature phase transformation of gamma Al2O3", J. Phys. Chem. C,112(25): 9486-9492
<u>Lower, B. H.</u> ^c , Lins, R. D., <u>Oestreicher, Z. W.</u> ^a , Straatsma, T. P., Hochella Jr, M. F., Shi, L., <u>Lower, S. K.</u> ^b , (2008), "In Vitro Evolution of a Peptide with a Hematite Binding Motif That May Constitute a Natural Metal-Oxide Binding Archetype", Environ. Sci. Technol.,42(10): 3821-3827
<u>Sieker, F.</u> ^a , <u>Straatsma, T. P.</u> ^c , Springer, S., <u>Zacharias, M.</u> ^b , (2008), "Differential tapasin dependence of MHC class I molecules correlates with conformational changes upon peptide dissociation: A molecular dynamics simulation study", Mol. Immunol.,45(14): 3714-3722
<u>Thurber, A.</u> ^a , Reddy, K. M., Shutthanandan, V., Engelhard, M. H., Wang, C., Hays, J., <u>Punnoose, A.</u> ^b , (2007), "Ferromagnetism in chemically synthesized CeO2 nanoparticles by Ni doping", Physical Review B,76(16):
Reddy, K. M., Benson, R., Hays, J., <u>Thurber, A.</u> ^a , Engelhard, M. H., Shutthanandan, V., Hanson, R., Knowlton, W. B., <u>Punnoose, A.</u> ^b , (2007), "On the room-temperature ferromagnetism of Zn1-xCr _x O thin films deposited by reactive co-sputtering", Solar Energy Materials and Solar Cells, 91(15-16): 1496-1502
<u>Punnoose, A.</u> ^b , Reddy, K. M., <u>Thurber, A.</u> ^a , Hays, J., & Engelhard, M. H., (2007), "Novel Magnetic Hydrogen Sensing: A Case Study Using Antiferromagnetic Hematite Nanoparticles.", Nanotechnology,18(16): 165502

Table 10. Peer Reviewed Publications from 2007.
<u>Thurber, A.</u> ^a , Hays, J., Reddy, K. M., Shutthanandan, V., & <u>Punnoose, A.</u> ^b . 2007. (2007), "Fluorine doping in dilute magnetic semiconductor Sn _{1-x} FexO ₂ ", Journal of Materials Science-Materials In Electronics,18(11): 1151-1155
Misra, S. K., Andronenko, S. I., Engelhard, M. H., <u>Thurber, A.</u> ^a , Reddy, K. M., <u>Punnoose, A.</u> ^b (2008), "Role of dopant incorporation on the magnetic properties of Ce _{1-x} NixO ₂ nanoparticles: An electron paramagnetic resonance study", J. Appl. Phys.,103(7): Art. No. 07D122
<u>Wigginton, N. S.</u> ^a , <u>Rosso, K. M.</u> ^c , & <u>Hochella, M. F.</u> ^b (2007), "Mechanisms of electron transfer in two decaheme cytochromes from a metal-reducing bacterium", Journal of Physical Chemistry B,111(44): 12857-12864
<u>Wigginton, N. S.</u> ^a , <u>Rosso, K. M.</u> ^c , Lower, B. H., Shi, L., & <u>Hochella, M. F.</u> ^b 2007. Electron tunneling properties of outer-membrane decaheme cytochromes from Shewanella oneidensis. Geochimica et Cosmochimica Acta, 71(3): 543-555.
<u>Wigginton, N. S.</u> ^a , <u>Rosso, K. M.</u> ^c , M., Shi, L., Lower, B. H., <u>Hochella, M. F.</u> ^b , (2007), "Insights into enzymatic reduction of metal-oxides from single-molecule tunneling studies of multiheme cytochromes", Geochimica Et Cosmochimica Acta,71(15): A1112-A1112
<u>Wigginton, N. S.</u> ^a , <u>Rosso, K. M.</u> ^c , Stack, A. G., <u>Hochella, M. F.</u> ^b , (2008), "Long-Range Electron Tunneling Across Cytochrome-Hematite (α-Fe ₂ O ₃) Interfaces", Journal of Physical Chemistry,
<u>Yu, Z. Q.</u> ^a , Zhang, Y., Wang, C. M., Shutthanandan, V., Lyubinetsky, I., Engelhard, M. H., Saraf, L. V., McCready, D. E., Henager, C. H., Nachimuthu, P., <u>Thevuthasan, S.</u> ^c , (2007), "Synthesis and Characterization of Compositionally Graded Si _{1-x} Gex Layers on Si substrate", Nuclear Instruments and Methods in Physics Research. Section B, Beam Interactions with Materials and Atoms,261(1-2): 723-726
<u>Yu, Z. Q.</u> ^a , Kuchibhatla, S., Engelhard, M. H., Shutthanandan, V., Wang, C. M., Nachimuthu, P., Marina, O. A., Saraf, L. V., <u>Thevuthasan, S.</u> ^c , Seal, S., (2008), "Growth and structure of epitaxial Ce _{0.8} Sm _{0.2} O _{1.9} by oxygen-plasma-assisted molecular beam epitaxy", J. Cryst. Growth,310(10): 2450-2456
<u>Yu, Z. Q.</u> ^a , Kuchibhatla, S., Saraf, L. V., Marina, O. A., Wang, C. M., Engelhard, M. H., Shutthanandan, V., Nachimuthu, P., <u>Thevuthasan, S.</u> ^c , (2008), "Conductivity of oriented samaria-doped ceria thin films grown by oxygen-plasma-assisted molecular beam epitaxy", Electrochem. Solid State Lett.,11(5): B76-B78
Goering, J., Kadossov, E., Burghaus, U., <u>Yu, Z. Q.</u> ^a , <u>Thevuthasan, S.</u> ^c , & Saraf, L. V. (2007). "Adsorption of Iso-/n-butane on an Anatase Thin Film: A Molecular Beam Scattering and TDS Study". Catalysis Letters, 116(1-2): 9-14.
Lyubinetsky, I., <u>Yu, Z. Q.</u> ^a , & Henderson, M. (2007). "Direct Observation of Adsorption Evolution and Bonding Configuration of TMAA on TiO ₂ (110)". Journal of Physical Chemistry C 111(11): 4242-4346.
<u>Yu, Z. Q.</u> ^a , Wang, C. M., Engelhard, M., Nachimuthu, P., McCready, D. E., Lyubinetsky, I., & <u>Thevuthasan, S.</u> ^c (2007). "Epitaxial Growth and Microstructure of Cu ₂ O Nanoparticle/thin Films on SrTiO ₃ (100) ". Nanotechnology 18:Art. No. 115601., 18(115601): doi:10.1088/0957-4484/1018/1011/115601.
Funk, S., Hokkanen, B., Nurkic, T., Goering, J., Kadossov, E., Burghaus, U., A., G., Schmuki, P., <u>Yu, Z. Q.</u> ^a , <u>Thevuthasan, S.</u> ^c , & Saraf, L. V. (2007). "Reactivity Screening of Anatase TiO ₂ Nanotube Arrays and Anatase Thin Films: A Surface Chemistry Point of View". Journal of the American Chemical Society, Submitted .
Thevuthasan, S., Yu, Z., Kuchibhatla, S., Saraf, L. V., Marina, O. A., Shutthanandan, V., Nachimuthu, P., Wang, C. M., (2008), "Oxygen Ion Conductance in Oriented Thin Film Electrolytes", Nature.

Table 10. Peer Reviewed Publications from 2007.
<u>Zink, P.</u> , Yoon, K. J., Pederson, L. R., Pal, U. B., Gopalan, S., (2008), "Defect Chemical Analysis of the Electronic and Ionic Conductivity of Calcium Doped Lanthanum Ferrite", Solid State Ionics, Submitted .

^aParticipant; ^bMentor; ^cPNNL Host

Table 11. Presentations/Conference Papers from 2007
<u>Bateman, A. P.</u> ^a , Walser, M. L., Desyaterik, Y., <u>Laskin, J.</u> ^c , Laskin, A., <u>Nizkorodov, S. A.</u> ^b (2008), "Analysis of Organic Aerosol Constituents using High Resolution ESI-MS: Solvent-Analyte Reactions and Selection of Appropriate Solvents", Presented by Adam Bateman (Invited Speaker) at 235th ACS National Meeting , New Orleans, LA on April 8, 2008.
<u>Gupta, S.</u> ^a , <u>Saraf, L. V.</u> ^c , Nachimuthu, P., Engelhard, M. H., Shutthanandan, V., Thevuthasan, S., & <u>Prasad, S.</u> ^b (2007), "Ceria Nanomonitors For Trace Oxygen Monitoring In Portable System". Presented by Shilpi Gupta at 2007 Micro Nano Breakthrough Conference Registrations, Portland, OR on September 10, 2007.
<u>Gupta, S.</u> ^a , <u>S Saraf, L. V.</u> ^c , Kuchibhatla, S., Engelhard, M. H., Shutthanandan, V., Thevuthasan, S., <u>Prasad, S.</u> ^b , (2008), "Portable Ceria Nanomonitors For High Temperature Trace Oxygen Monitoring", Presented by Shilpi Gupta at LabAutomation 2008, Palm Springs, CA on January 29, 2008.
<u>Gupta, S.</u> ^a , <u>Saraf, L. V.</u> ^c , Kuchibhatla, S., Engelhard, M. H., Nachimuthu, P, Wang, C.M., Shutthanandan, V., Thevuthasan, S., <u>Prasad, S.</u> ^b , (2008) "Portable Ceria Nanomonitors For High Temperature Trace Oxygen Monitoring." Presented by Shilpi Gupta at 2008 MRS Spring Meeting, San Francisco, CA on March 25, 2008.
<u>Gupta, S.</u> ^a , <u>Saraf, L. V.</u> ^c , Kuchibhatla, S., Engelhard, M. H., Nachimuthu, P, Wang, C.M., Shutthanandan, V., Thevuthasan, S., <u>Prasad, S.</u> ^b , 2008. "Portable Ceria Nanomonitors for High Temperature Trace Oxygen Monitoring." Presented by Shilpi Gupta at NSTI Nanotech 2008, Boston, MA on June 4, 2008.
<u>Gupta, S.</u> ^a , Kuchibhatla, S., Engelhard, M. H., Nachimuthu, P., Wang, C. M., Shutthanandan, V., Jiang, W., <u>Saraf, L. V.</u> ^c , Thevuthasan, S., <u>Prasad, S.</u> ^b , (2008), "Synthesis and Characterization of Samaria Doped Ceria Thin Films for Use in Oxygen Gas Sensing", Presented at 2008 Symposium of the Pacific Northwest Chapter of the AVS, Richland, WA on September 18, 2008.
<u>Hess N. J.</u> ^c , Karkamkar, A. J., Parvanov, V. M., Schenter, G. K., Mundy, C. J., Kathmann, S. M., Stowe, A. C., Hartl, M. A., Daemen, L. L., Proffen, T. E. , Brown, C., Mamontov, E., <u>Hartman, M. R.</u> ^a , and Autrey T., (2007)."Neutron Scattering Approaches to the Chemical and Physical Properties of Ammonia-Borane." Presented by Tom Autrey (Invited Speaker) at International Symposium on Materials issues in a Hydrogen Economy, Richmond, VA on November 14, 2007.
<u>Ortiz, S. Y.</u> ^a , Ziolo, R. F., <u>Burton, S. D.</u> ^c , & <u>Espe, M. P.</u> ^b (2007), "Solid-State NMR studies of CdS Nanoparticles". Presented by Sarah Burton at Rocky Mountain Analytical Conference, Breckenridge, CO on July 23, 2007
<u>Saraf, L. V.</u> ^c , <u>Oo, W. M. H.</u> ^a , McCluskey, M. D., Zhu, Z., Wang, C. M., Engelhard, M. H., Shutthanandan, V., Hendricks, C. A., (2008), "Solubility and Secondary Phase Segregation Relationship for Favorable Vs Unfavorable Dopants in Oriented/Epitaxial ZnO Films Grown by MOCVD", Presented by Lax Saraf at 2008 MRS Spring Meeting , San Francisco, CA on March 24, 2008.
<u>Wigginton, N. S.</u> ^a , <u>Rosso, K. M.</u> ^c , Shi, L., Lower, B. H., Hochella, M. F., (2007), "Insights into enzymatic reduction of metal-oxides from single-molecule tunneling studies of multiheme cytochromes", Presented by Nicholas S. Wigginton (Invited Speaker) at Goldschmidt 2007 Conference, Cologne, Germany on August 20, 2007.

Table 11. Presentations/Conference Papers from 2007
Rosso, K. M. ^c , Kerisit, S. N., Valiev, M., Smith, D. M., Deskins, N. A., Yanina, S., <u>Wigginton, N. S.</u> ^a , Straatsma, T. P., Dupuis, M., (2007), "Computational Bioelectrochemistry for Cytochrome-electrode Interfaces" Presented by Kevin Rosso at 234nd ACS National Meeting, Boston, MA on August 21, 2007.
Kuchibhatla, S., <u>Yu, Z. Q.</u> ^a , Nachimuthu, P., Shutthanandan, V., Engelhard, M. H., Saraf, L. V., Seal, S., <u>Thevuthasan, S.</u> ^c , (2007), "Optimizing the Structure and Composition of Hetero-structured Ceria / Zirconia Multilayers through Oxygen Plasma Assisted Molecular Beam Epitaxy", Presented by Satya Kuchibhatla at 54th AVS, Seattle, WA on October 17, 2007.
<u>Yu, Z. Q.</u> ^a Kuchibhatla, S., Saraf, L. V., Marina, O. A., Shutthanandan, V., Nachimuthu, P., Engelhard, M. H., Wang, C. M., <u>Thevuthasan, S.</u> ^c , (2008), "Oxygen Ion Conductance in Oriented Thin Film Electrolytes", Presented by Theva Thevuthasan at 32nd International Conference & Exposition on Advanced Ceramics & Composites, Daytona Beach, FL on January 28, 2008.
Sundaram SK, Kuchibhatla, S., <u>Yu, Z. Q.</u> ^a , Nachimuthu, P., Engelhard, M. H, Shutthanandan, V., <u>Thevuthasan, S.</u> ^c , and Henager, C. H., (2008). "Copper Oxide Nano-clusters: Growth – Morphology – Chemistry." Presented by S. K. Sundaram at PL07-MDT Program Review "Materials Discovery Tool", ETB/Wenatchee River Room, PNNL, WA on August 15, 2008.
Kuchibhatla, S., <u>Yu, Z. Q.</u> ^a , <u>Thevuthasan, S.</u> ^c , Nachimuthu, P., Shutthanandan, V., Wang, C. M., Li, Y., Henager, C. H., Sundaram, S. K., (2008), "Growth and Characterization of Cuprous Oxide Nanoclusters on Strontium Titanate (100) Surface", Presented by Satyanarayana Kuchibhatla (Invited Speaker) at 2008 Symposium of the Pacific Northwest Chapter of the AVS, Richland, WA on September 17, 2008.
<u>Yu, Z. Q.</u> ^a , Kuchibhatla, S., Engelhard, M. H., Wang, C. M., Marina, O. A., Jiang, W., Shutthanandan, V., Nachimuthu, P., Devanathan, R., Saraf, L. V., <u>Thevuthasan, S.</u> ^c , (2008), "Ionic Conductivity of Scandia Doped Zirconia Thin Films Synthesized by Oxygen-Plasma-Assisted Molecular Beam Epitaxy", Presented by Mark H. Engelhard at AVS 55th International Symposium & Exhibition, Boston, MA on October 21, 2008.

^aParticipant; ^bMentor; ^cPNNL Host

Technical Reports

The remainder of this document is devoted to the technical reports provided by each young scientist. As noted above, some of these are single paragraph abstracts and, therefore, have rather limited content. Other reports, however, are nearly complete papers. These documents are “as received,” apart from minor formatting changes in some cases. We have made no effort to edit or evaluate these reports. Given the limited distribution intended for this report, none of the results in these reports should be considered “published” by virtue of appearing here.

**Pacific Northwest National Laboratory
Heriot-Watt University**

Intermolecular Interactions in Ammonia Borane – Hydrogen Systems
Rock Salt and Zinc Blende Structures of Ammonium Borohydride

2008 Summer Research Institute at PNNL
Final Report

Alexander Abramov

Supervisor: Prof. Maciej Gutowski
PNNL Collaborators: Greg Schenter, Shawn Kathmann

**Richland, Washington, USA
September 2008**

Table of Contents

Preface.....	37
I. Intermolecular Interactions in AB-AB, AB-H ₂ , and H ₂ -H ₂ Systems	37
Introduction	37
Methodology	37
Results and Discussion	38
Conclusions	43
II. RS and ZB Structures of NH ₄ BH ₄	43
Introduction	43
Methodology	43
Results and Discussion	45
Conclusions	49
Acknowledgments.....	49
Bibliography	49

Preface

Presented work is splitted into two different and distinct parts. The first part is dedicated to understanding of intermolecular interactions in AB-AB (AB - Ammonia Borane, NH_3BH_3), AB-H₂, and H₂-H₂ systems. This section deals with a subtle issue of weak intermolecular interactions in gas phase. The second part of the work is concentrated on a study of relation between two possible phases, the RS (Rock Salt) and the ZB (Zinc Blende), of ammonium borohydride (NH_4BH_4). This section describes probable mechanism of the phase transformation and tries to estimate relative stabilities of the two phases at different temperature conditions. Each mentioned part composed of subsections. Introduction, which sketches general background information. Methodology, which represents applied computational methods and technics. Results and discussion, which provides main outcomes of the work and their interpretation. Conclusions, which summarizes the results.

I. Intermolecular Interactions in AB-AB, AB-H₂, and H₂-H₂ Systems

Introduction

Theoretical research done at Heriot-Watt University [1], [2] showed that AB might form clathrate compounds with molecular hydrogen being a guest molecule. These compounds have promising hydrogen density along with kinetically easily accessible hydrogen. Several clathrate cages and periodic structures were identified. The study approached limits of state of the art computational methods and hardware capabilities not only because of the size of the clathrate systems, which are naturally big, but also due to the deficiencies of the DFT, which was applied to the systems of that size and which is unable to describe weak intermolecular interactions stabilizing clathrate structures. The research left unanswered the most fundamental question: Are these compounds stabilized by the host-guest interactions? Although there are some promising indications [3] that the host-host and the host-guest interactions in AB systems are stronger than in corresponding water systems, and water is known to form clathrates, it is not considered as a robust evidence of stability of AB clathrates.

Modern high level theoretical methods allow one to compute intermolecular interactions with a great accuracy but they are limited to small systems containing no more than dozen of atoms. This is although enough to construct an intermolecular potential which then can be used for larger simulations requiring much less computational effort and providing comparable precision. The main purpose of the work presented in this section is to accurately describe intermolecular interactions in AB-AB, AB-H₂, and H₂-H₂ systems in order to use produced data to construct corresponding intermolecular potentials.

Methodology

To calculate the interaction energies both supermolecular and perturbational approaches were used. In supermolecular approach [4] interaction energy is represented as:

$$E_{\text{int}} = E_{XY} - (E_X + E_Y),$$

where E_{XY} , E_X , and E_Y are ground-state energies of the complex XY, and of the monomers X and Y.

The ground-state energies were computed at the MP2 [5] and CCSD(T) [6] levels of theory using Dunning type basis-sets aug-cc-pVDZ and aug-cc-pVTZ. Interaction energies were

corrected for BSSE using the counterpoise method. NWChem software package was used for the calculations.

Perturbational methods [7] compute the interaction energy as a sum of physically meaningful contributions:

$$E_{\text{int}} = E_{\text{pol}}^{(1)} + E_{\text{exch}}^{(1)} + E_{\text{ind}}^{(2)} + E_{\text{disp}}^{(2)} + E_{\text{exch}}^{(2)} + \dots,$$

where $E_{\text{pol}}^{(1)}$, $E_{\text{ind}}^{(2)}$, and $E_{\text{disp}}^{(2)}$ are the classical electrostatic interaction energy, classical induction, and quantum mechanical dispersion energies, respectively; $E_{\text{exch}}^{(1,2)}$ are exchange corrections defined by the Symmetry-Adapted Perturbation Theory (SAPT) [8].

For AB dimer the second order SAPT corrections were calculated along with Hartree-Fock correction term (delta HF), so-called hybrid SAPT approach. For AB-H2 and H2 dimer third order SAPT [9] was applied.

Basis-set used for SAPT calculations was 6-311++G** with a mid-band 3322 (stands for 3s3p2d2f) placed in the center of the separation, dimer-centered basis set (DC+BS) approach. The calculations were done using SAPT2006 package with Atmol code as a front-end SCF program.

Results and Discussion

For AB dimer four configurations were considered (Figure 1-Figure 4).

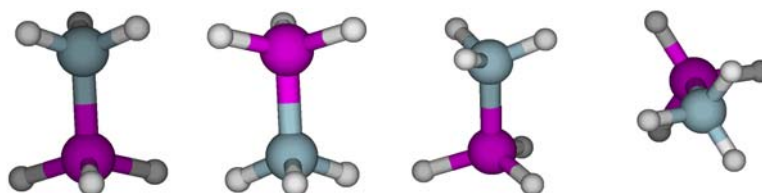


Figure 1: AB dimer, configuration A

Figure 2: AB dimer, configuration B

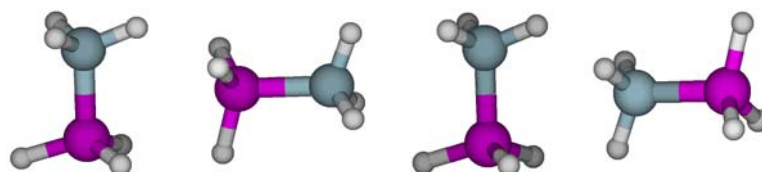


Figure 3: AB dimer, configuration C

Figure 4: AB dimer, configuration D

For AB-H2 (Figure 5-Figure 7) and H2 dimer (Figure 8-Figure 10) three configurations per each system were considered.

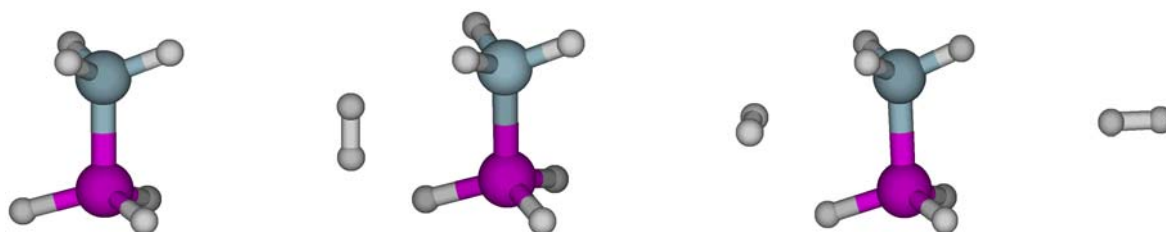


Figure 5: AB-H2, configuration A

Figure 6: AB-H2, configuration B

Figure 7: AB-H2, configuration C



Figure 8: H2 dimer, configuration A

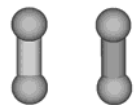


Figure 9: H2 dimer, configuration B



Figure 10: H2 dimer, configuration C

Intermolecular potentials for each considered system and geometrical configuration calculated on the basis of supermolecular approach are presented in Figure 11-Figure 20.

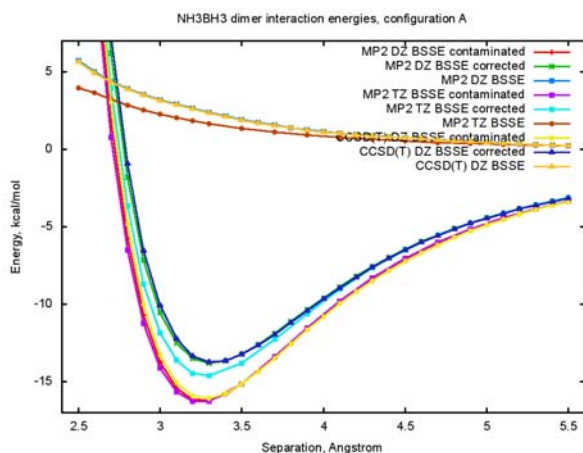


Figure 11: AB dimer, config. A, supermolecular approach

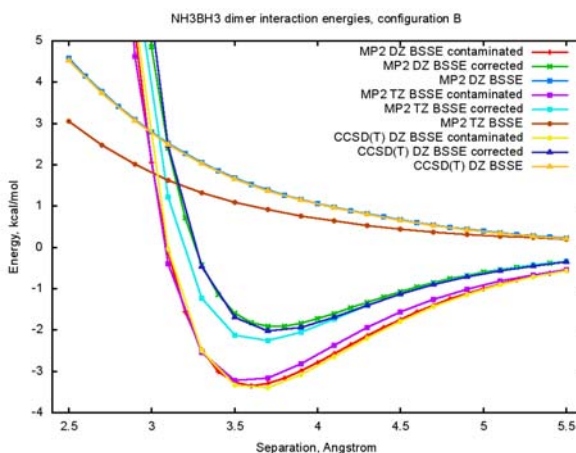


Figure 12: AB dimer, config. B, supermolecular approach

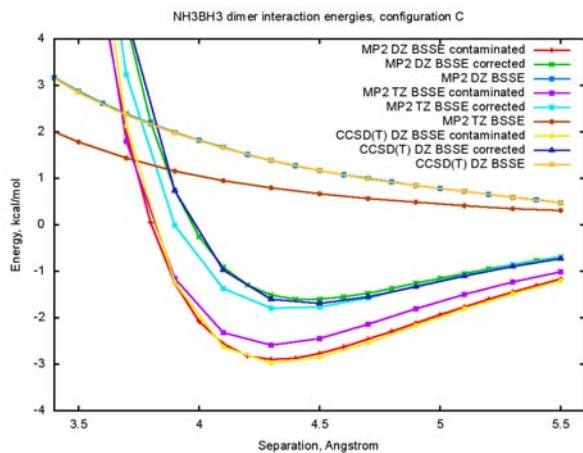


Figure 13: AB dimer, config. C, supermolecular approach

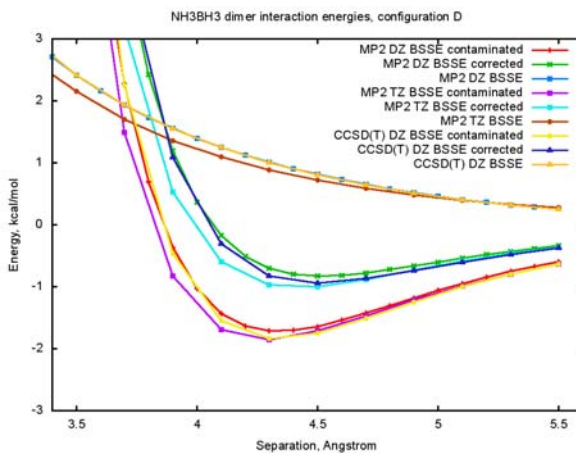


Figure 14: AB dimer, config. D, supermolecular approach

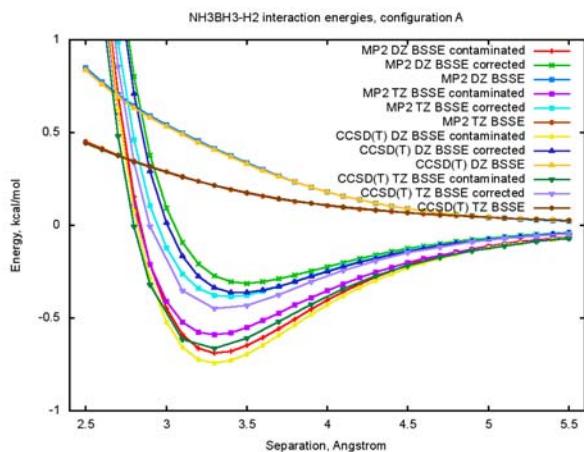


Figure 15: AB-H2, config. A, supermolecular approach

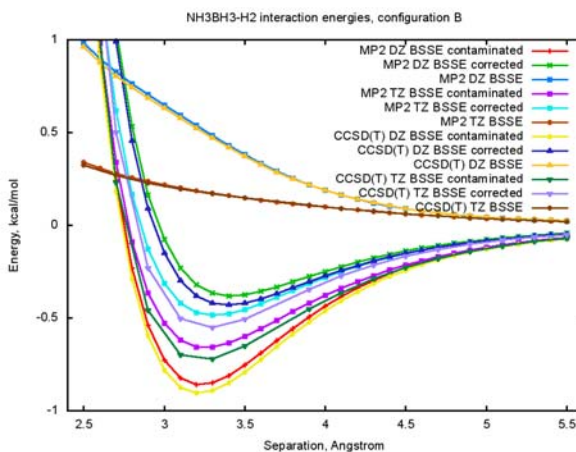


Figure 16: AB-H2, config. B, supermolecular approach

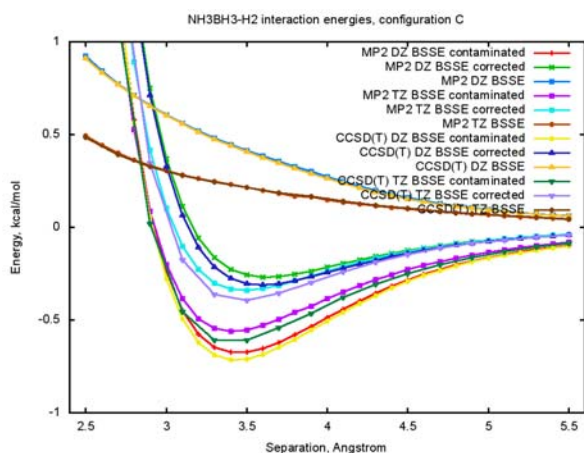


Figure 17: AB-H2, config. C, supermolecular approach

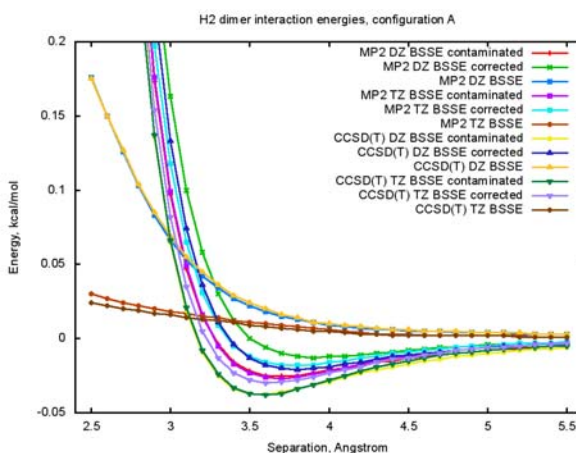


Figure 18: H2 dimer, config. A, supermolecular approach

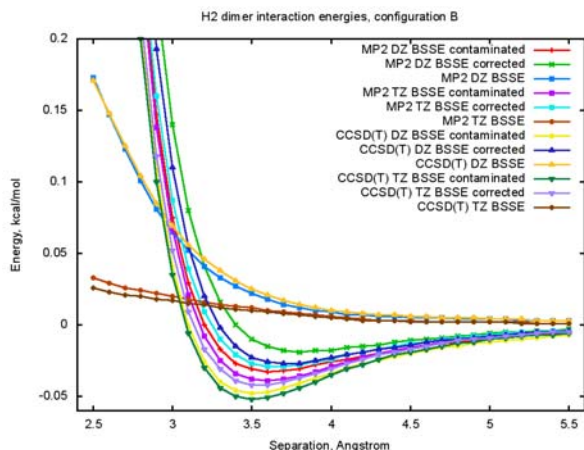


Figure 19: H2 dimer, config. B, supermolecular approach

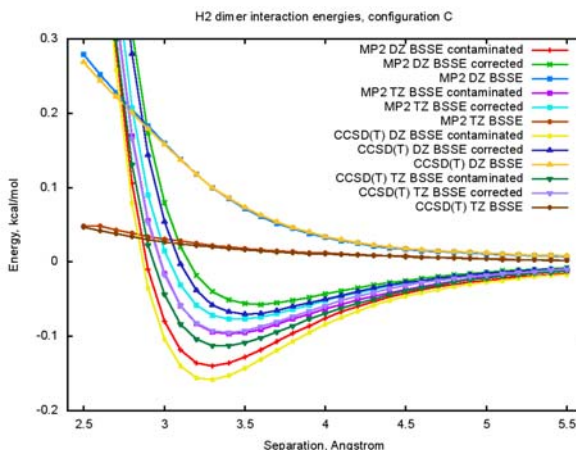


Figure 20: H2 dimer, config. C, supermolecular approach

As expected from high polarity of AB molecule AB dimer shows the strongest interaction energy, around 15 kcal/mol (configuration A), among all studied systems. Drastic reduction in interaction energy occurs when hydrogen is introduced to the system. The strongest interaction energy for the system AB-H2 is by two orders of magnitude smaller than for the

AB dimer and takes the value in the range of 0.5 kcal/mol (configuration B). Hydrogen dimer exhibits the lowest interaction energy about 0.1 kcal/mol (configuration C).

Effect of the basis-set size and level of theory becomes more and more important when interactions get weaker. If in case of AB dimer reasonably good description may be achieved at the MP2/DZ level of theory then in case of the systems involving hydrogen the CCSD(T)/TZ gives tens of percent improvement in comparison with the lower levels of theory.

Intermolecular potentials for each considered system and geometrical configuration calculated on the basis of the perturbational approach and their comparison with the supermolecular approach are presented in Figure 21-Figure 30.

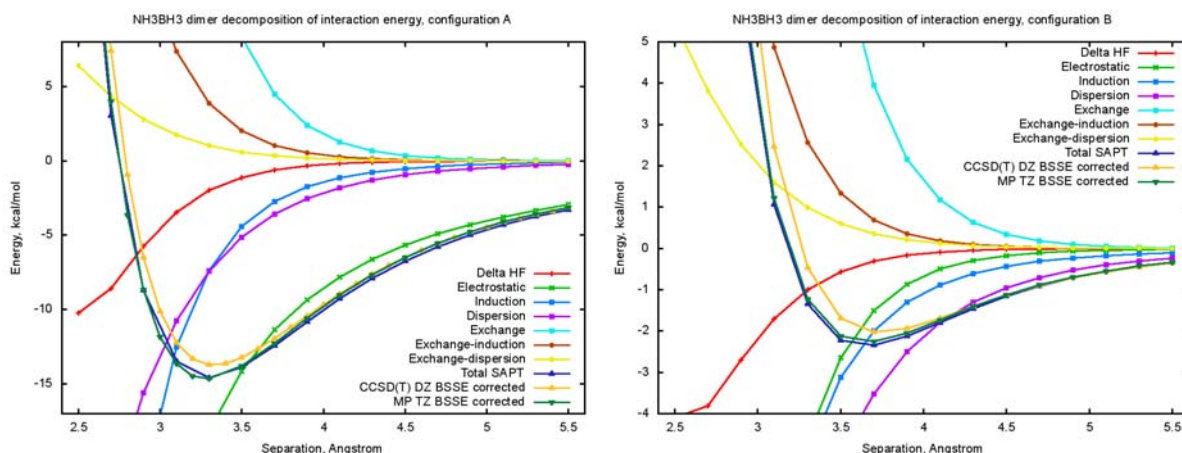


Figure 21: AB dimer, config. A, perturbational approach
 Figure 22: AB dimer, config. B, perturbational approach

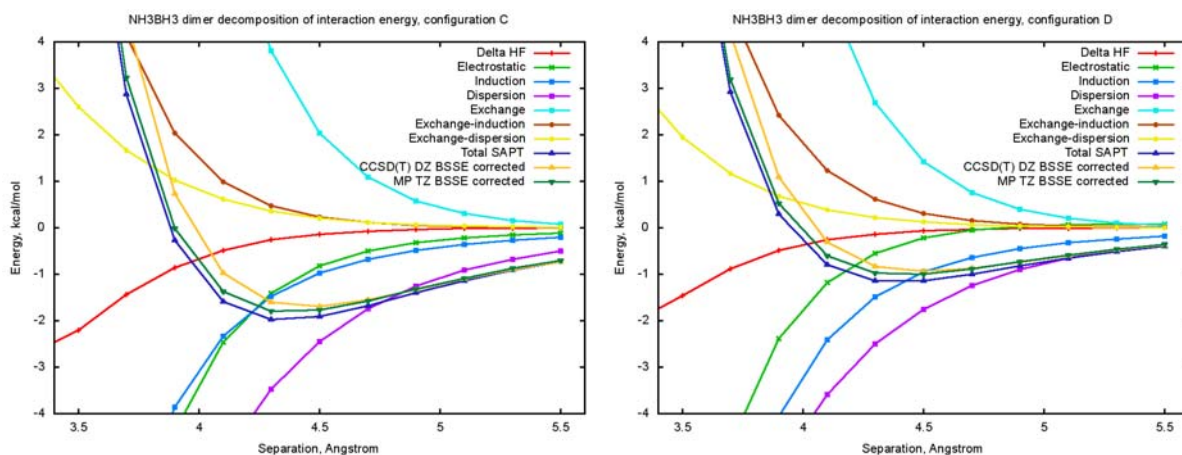


Figure 23: AB dimer, config. C, perturbational approach
 Figure 24: AB dimer, config. D, perturbational approach

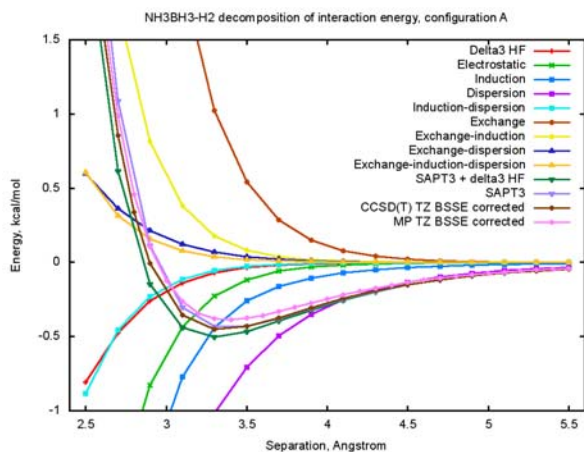


Figure 25: AB-H2, config. A, perturbational approach

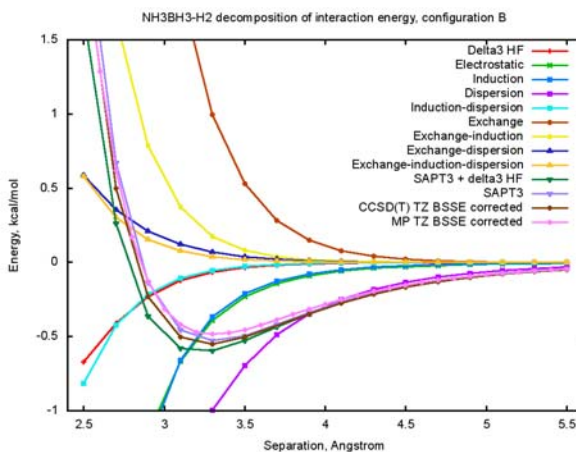


Figure 26: AB-H2, config. B, perturbational approach

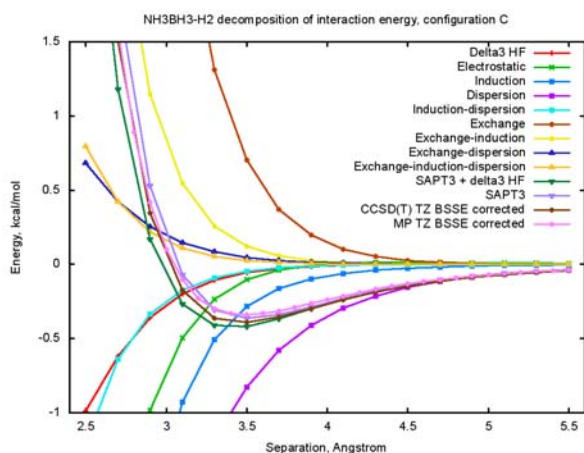


Figure 27: AB-H2, config. C, perturbational approach

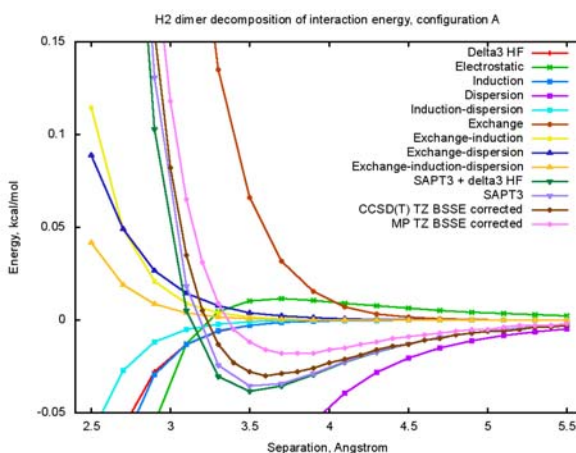


Figure 28: H2 dimer, config. A, perturbational approach

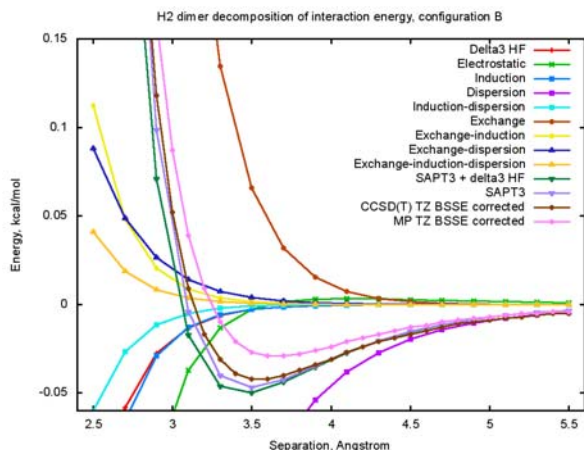


Figure 29: H2 dimer, config. B, perturbational approach

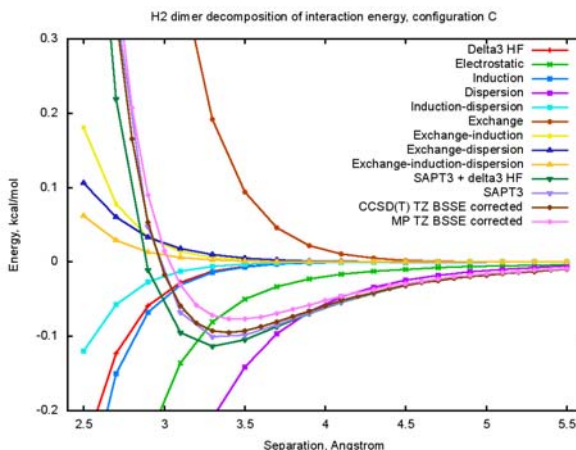


Figure 30: H2 dimer, config. C, perturbational approach

For AB dimer the SAPT results are in an agreement with the MP2/TZ level of theory. For the AB-H2 system the SAPT reproduces dispersion part of the intermolecular potential as accurate as at the CCSD(T)/TZ level of theory, and the repulsive wall as at the MP2/TZ level of theory. For H2 dimer, the interaction energy for configuration C is almost

equivalent to that calculated at the CCSD(T)/TZ level of theory, for configurations A and B there is some overestimation of the binding in comparison with the CCSD(T)/TZ level of theory. To very large extent attractive interactions in the considered systems are determined by the dispersion type of interactions. The noticeable exception is AB dimer configuration A where the electrostatic component is the dominant type of the interaction energy.

Conclusions

Interaction energies for three molecular systems AB-AB, AB-H₂, and H₂-H₂ in several different configurations were calculated at MP2/DZ, MP2/TZ, CCSD(T)/DZ, and CCSD(T)/TZ levels of theory. Decompositions of the interaction energies were obtained within the framework of the SAPT. Satisfactory agreement between supermolecular and perturbational approaches was demonstrated. The dispersion type of the interactions was found to be the dominant for most of the considered systems. The future work will be the construction of the intermolecular potentials, applicable to larger simulations, out of the acquired data.

II. RS and ZB Structures of NH₄BH₄

Introduction

Recently NH_xBH_x (x=2...4) compounds attracted attention of researchers [10], [11] struggling with hydrogen storage problem because of their high hydrogen content. Ammonium borohydride (NH₄BH₄) is among the most interesting materials not only because of its extremely high hydrogen capacity but also due to the fact that upon its dehydrogenation one might form ammonia borane (NH₃BH₃) which was recognized as a strongest candidate to be used as a practical hydrogen storage medium [12]. In spite of importance of ammonium borohydride there is no clear understanding of its structure. There was an attempt to refine the structure from ab-initio calculations (study done by Maciej Gutowski at PNNL) which showed that the ZB is the most stable structure in terms of the ground state electronic energy but an experimental work (study done by Nancy Hess at PNNL) observed the RS structure only over a wide temperature range. To resolve the contradiction theoretical study accounting for thermal corrections is required. The aim of the work presented in this section is to propose a possible phase transformation mechanism, to estimate the energy barrier of the phase transformation, and to identify the most stable phase of NH₄BH₄ from theoretically obtained free energies.

Methodology

To define the phase transformation mechanism the RS and the ZB phases of NH₄BH₄ were represented by unit cells with close geometrical parameters including lattice vectors (a, b, and c), angles between vectors (alpha, beta, and gamma), and fractional coordinates of all atoms. To simplify the task only primitive cells containing one NH₄ and one BH₄ groups were considered. A linear transformation from the set of parameters describing the ZB structure to the set of parameters describing the RS structure was then taken as a possible phase transformation mechanism. This can be illustrated as follows. Let us say that we want to have X coordinate of an atom of a phase which is exactly half a way from the ZB to the RS, that would be given by:

$$X_{0.5} = X_{ZB} + (X_{RS} - X_{ZB}) \cdot 0.5.$$

The energy barrier of the phase transformation was estimated by optimization of the intermediate structures obtained using above mentioned method with constraints on the lattice vectors and the volume of the cell, and on the volume of the cell only. VASP code was used for optimization. The default kinetic energy cut-off for the plane wave basis set was increased by 30% by setting high precision. The Brillouin zone was sampled with Monkhorst-Pack grid of k-points of the size 9x9x9. Exchange and correlation effects were treated within the GGA approximation using Perdew-Wang 91 exchange-correlation functional. Nuclei potentials and core electrons were described using projector-augmented pseudopotentials.

The free energy was calculated as follows (see, for example, [13]):

$$G(T) = H(T) - T \cdot S(T).$$

For solids, neglecting pV term, the enthalpy can be written as:

$$H(T) = E_0 + E_{vib}(T),$$

where E_0 is the ground state electronic energy. The vibrational enthalpy contribution within the harmonic approximation is given by:

$$E_{vib}(T) = \frac{1}{2} m \int \hbar \omega g(\omega) \coth\left(\frac{\hbar \omega}{2k_B T}\right) d\omega,$$

where T is the temperature, m is the number of degrees of freedom, \hbar is the reduced Planck constant, ω is the vibrational frequencies, $g(\omega)$ is the phonon density of states, and k_B is the Boltzmann constant.

In the limit of zero temperature $E_{vib}(T)$ becomes the zero-point energy:

$$E_{ZPE} = \frac{1}{2} m \int \hbar \omega g(\omega) d\omega.$$

The vibrational entropy within the harmonic approximation is given by:

$$S(T) = mk_B \int g(\omega) \left\{ \left(\frac{\hbar \omega}{2k_B T} \right) \left[\coth\left(\frac{\hbar \omega}{2k_B T} \right) - 1 \right] - \ln \left[1 - \exp\left(-\frac{\hbar \omega}{k_B T} \right) \right] \right\} d\omega.$$

Phonon frequencies were obtained in three different ways, from linear response theory [14], by the Fourier transform of the atomic velocity autocorrelation function, and with the direct method [15], [16] at the Gamma point of the Brillouin zone.

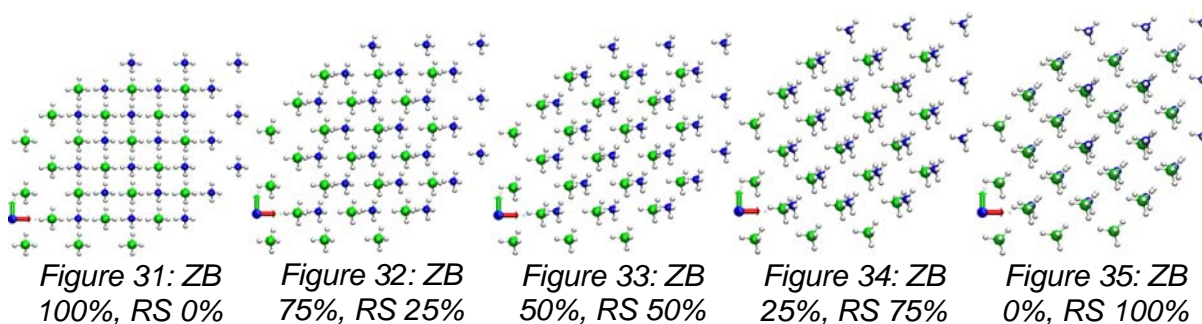
For Linear Response (LR) calculations Quantum Espresso code was used. The dynamical matrices were calculated on a grid of q-vectors 3x3x3. The Brillouin zone was sampled with a mesh of k-points 9x9x9. Exchange and correlation were treated in the GGA of Perdew-Wang 91. Kinetic energy cut-off for the plane wave basis set was set to 70 Ry. Nuclei potentials and core electrons were replaced with ultrasoft pseudopotentials. The structures were relaxed until the forces on atoms were converged to 0.001 Ry/Bohr. Primitive cells were used.

To obtain the atomic velocity autocorrelation function Molecular Dynamics (MD) simulations in the microcanonical (NVE) ensemble with CP2K code were performed. Electron exchange and correlation were treated in the GGA of PBE. The triple-zeta quality basis set was used for 15000 steps of simulations with 0.5 femtosecond time step at 2.5 K. The super cells of the size 3x3x3 were used.

The Gamma point phonon calculations were done with VASP using 0.015 Angstrom displacement to obtain the Hellman-Feynman forces. The Brillouin zone was sampled with a mesh of k-points 9x9x9. Exchange and correlation were treated in the GGA of Perdew-Wang 91. The default kinetic energy cut-off for the plane wave basis set was increased by 30% by setting high precision. Nuclei potentials and core electrons were replaced with projector-augmented pseudopotentials. The structures were relaxed until the forces on atoms were converged to 0.001 eV/Angstrom. Primitive cells were used.

Results and Discussion

ZB to RS phase transformation pathway was constructed in a form of sequence of xyz coordinates using developed awk script. The ZB structure, the RS structure, and some intermediate structures are shown in Figure 31-Figure 35.



The energy profile of the transformation is presented in Figure 36.

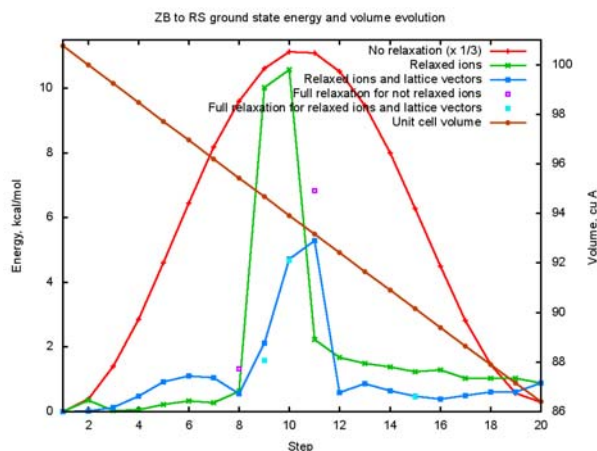


Figure 36: The energy profile of the phase transformation ZB to RS

The upper limit for the energy barrier of the phase transformation is 5 kcal/mol. The value is taken from the energy pathway with the smallest number of constraints, i.e. with relaxed ions and altered during the relaxation lattice vectors. That is necessarily an upper bound as there might be lower energy pathways.

The integrals required to calculate the free energy were coded in awk and the code was tested on orthorhombic phase of AB molecular crystal. The phonon density of states was calculated within the framework of the LR theory, Figure 37. A small negative part of the curve was cut and the curve was renormalized. Good agreement with previously done theoretical [13] and experimental [17] works has been observed, Figure 38.

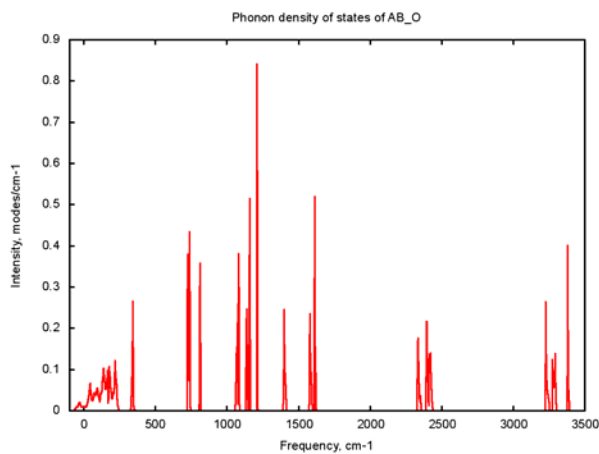


Figure 37: Phonon DOS of orthorhombic phase of AB

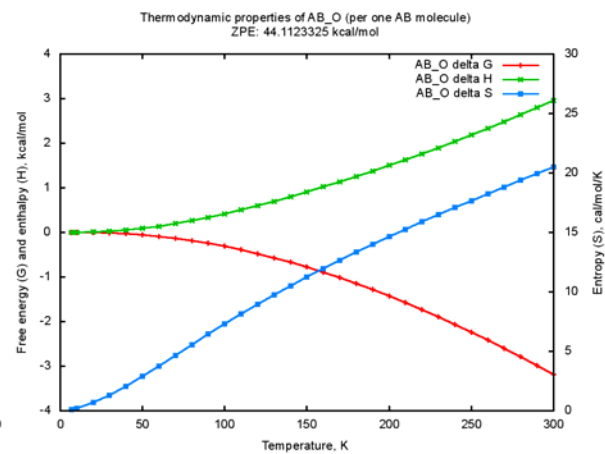


Figure 38: Calculated free energy, enthalpy, and entropy of orthorhombic phase of AB

The phonon DOS of the RS and the ZB structures of NH₄BH₄ obtained using different approaches are shown in Figure 39-Figure 41.

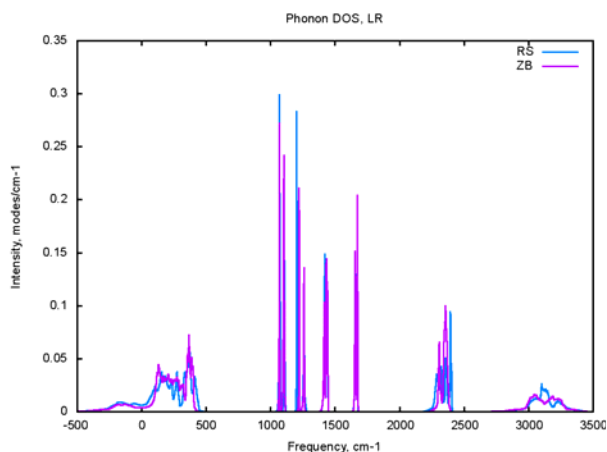


Figure 39: Phonon DOS of the RS and the ZB structures from the LR theory

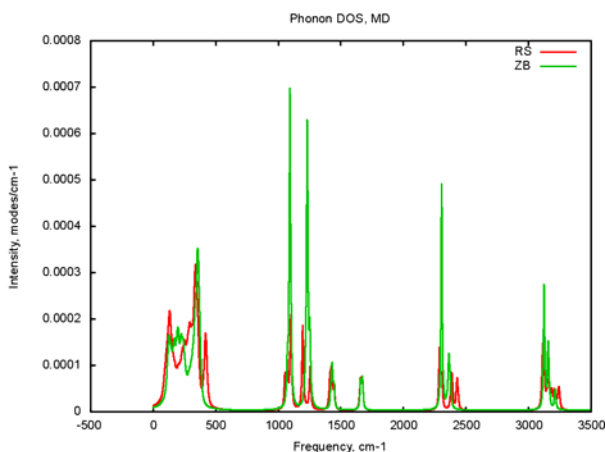


Figure 40: Phonon DOS of the RS and the ZB structures from the MD simulations

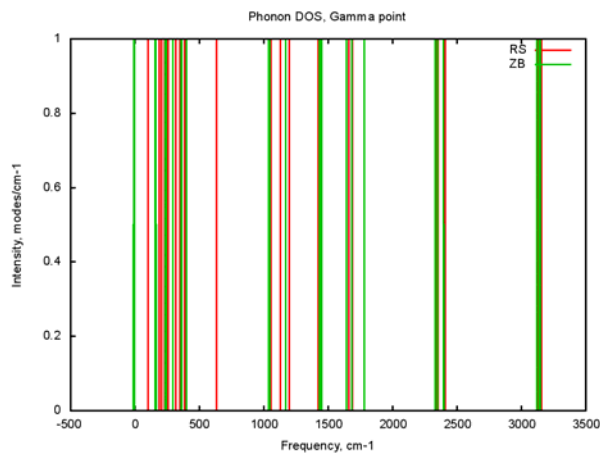


Figure 41: Phonon DOS of the RS and the ZB structures from the direct method

All three methods give very similar positions of the peaks. The only noticeable exception is the peak around 600 cm⁻¹ for the RS structure obtained with the direct method at the

Gamma point. The LR theory provides practically the same phonon DOS for both structures. In case of the MD simulations there is a significant difference in the intensities of the peaks with the ZB intensities being much larger. These intensities although are somewhat meaningless as the only one set of the initial conditions was used and the length of the dynamical trajectory was limited by only 15000 steps. The results from the direct method are the frequencies of the modes, i.e. the positions of the peaks only with the intensities being also arbitrary.

Calculated from the phonon DOS thermodynamic properties are presented in Figure 42-Figure 44. The phonon DOS curves underwent the same treatment as in case of the test system if negative frequencies were present, i.e. the negative part was cut and the curve was renormalized.

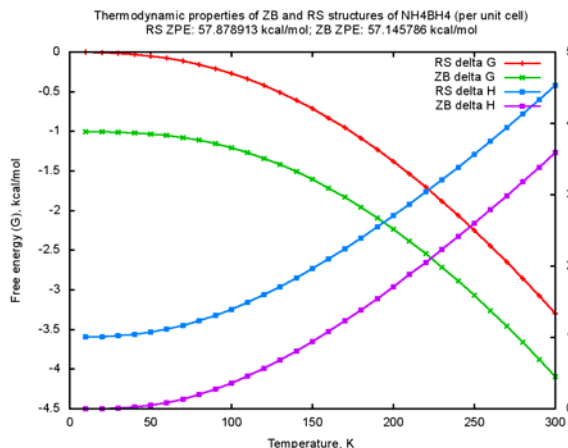


Figure 42: Thermodynamic properties from the LR theory

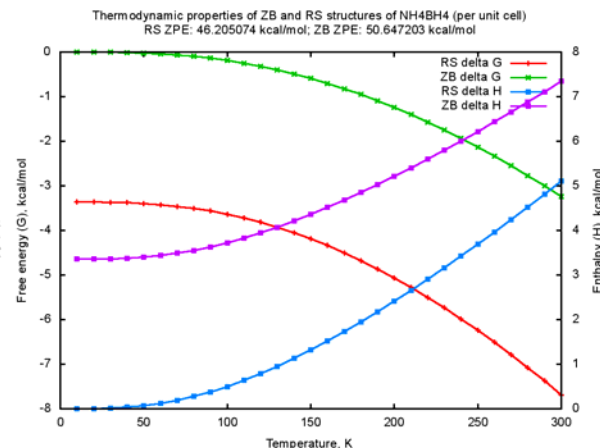


Figure 43: Thermodynamic properties from the MD simulations

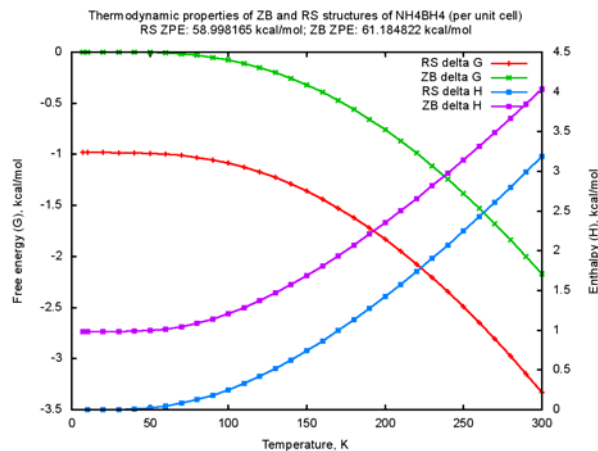


Figure 44: Thermodynamic properties from the direct method

As expected from the similarity of the phonon DOS of the RS and the ZB structures obtained with the LR theory the thermal corrections to the ground state energy are practically equal for both structures. This preserves the difference of about 1 kcal/mol in the free energy over the wide temperature range with the ZB structure being more stable. The outcome from the MD simulations is also expected because of the large intensities of the ZB structure which make it to be less stable. With the intensities being arbitrary the direct method gives the results which are in agreement with the MD results in terms of the most stable structure, which is the RS for the both methods.

The both purely harmonic methods, the LR and the direct method, provided contradictory results. The Gamma point only calculations are of course a rough approximation but its disagreement with the LR theory might be an indication that the harmonic analysis for the RS structure being considered is not suitable. It is known that the RS structure of NH₄BH₄ has a bunch of local minima on a flat potential energy surface. To improve the harmonic results we attempted to find the RS structure in the deepest potential well, ideally the global minimum structure. The spaghetti diagrams constructed from NVT simulations was utilized for that purpose. Let us consider XH₄ group (X is a heavy atom, B or N). At each time step of the simulation an origin of the coordinate system can be chosen to be coincidental with the position of the heavy atom. Having X-H bond to be almost constant during the course of simulations the positions of the hydrogens can be determined by two angles of the spherical coordinate system Theta and Phi. Each hydrogen forms a trajectory in this two dimensional phase space which can be easily visualized. The spaghetti diagrams for the NVT simulation at 70K are shown in Figure 45 and Figure 46.

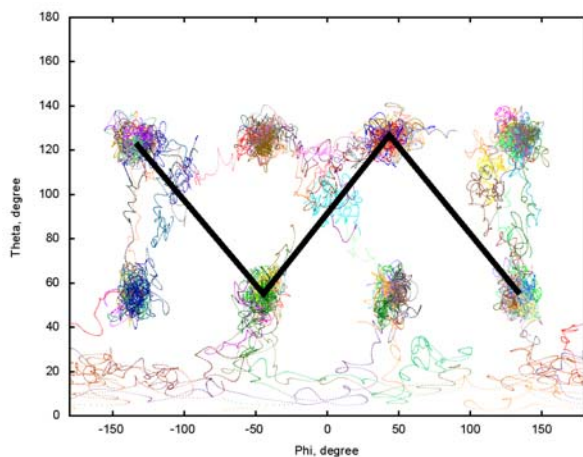


Figure 45: Trajectories of the hydrogens of the BH₄ groups, NVT 70K

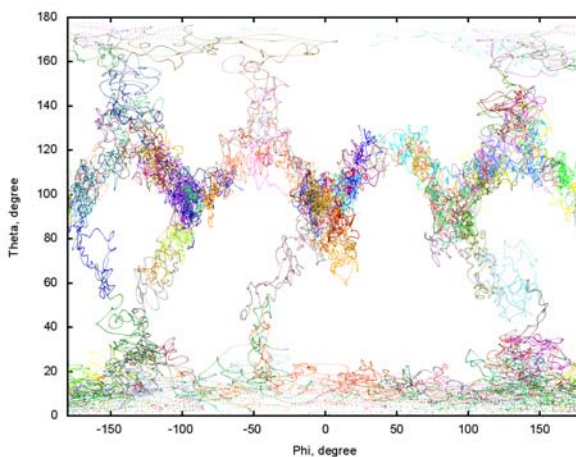


Figure 46: Trajectories of the hydrogens of the NH₄ groups, NVT 70K

Simulations at 70 K were found to provide distinguishable localization of the hydrogens. Temperatures 80 K, 90 K, 110 K, 180 K, and 300 K were also tested. It follows that there are only two preferential orientations of the BH₄ groups (Figure 45), one of them is shown with the zigzag, another one is a reflection of the first one (remaining spots). The hydrogens of the NH₄ groups can also be localized at lower temperature, Figure 47. The RS structure refined in this way is shown in Figure 48.

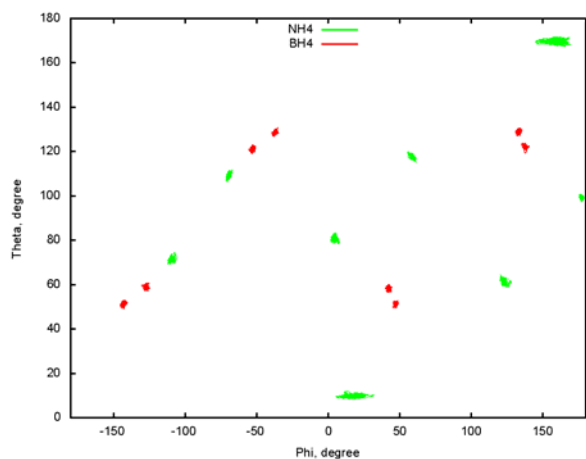


Figure 47: Trajectories of the hydrogens of the BH₄ and the NH₄ groups, NVE 2.5K

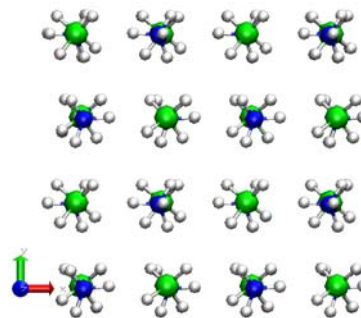


Figure 48: Refined RS structure

Conclusions

The pathway of the phase transformation from the ZB to the RS structure of NH₄BH₄ has been proposed. The upper limit of the energy barrier of the phase transformation has been estimated to be 5 kcal/mol. The script for construction of the phase transformation pathways has been developed and may be applied to analogous problems, for example, a phase transformation from orthorhombic to tetragonal structure of AB molecular crystal.

Phonon DOS of the RS and the ZB structures of NH₄BH₄ have been calculated using three different technics, the LR theory, the MD simulations, and with the direct method at the Gamma point. The script for calculation of the thermodynamic properties from the phonon DOS was developed, tested on AB molecular crystal, and applied to the calculated spectra of the RS and the ZB structures. The harmonic approximation results, the LR and the direct method, were found to provide contradictory conclusions about the stability of the different phases. To improve the results the RS structure was refined with the aid of spaghetti diagrams representing trajectories of the hydrogen atoms over the course of MD simulations. A focus of the future work will be the analysis of the stability of the refined RS structure with respect to the ZB structure on the basis of free energies.

Acknowledgments

I would like to thank Dr. Garold Murdachaew for his valuable advices regarding usage of the SAPT2006 package and for fruitful discussions of the symmetry-adapted perturbation theory.

Bibliography

1. A. Abramov, M. Gutowski, Periodic Structures of Ammonia Borane Clathrates, ScotCHEM Computational Chemistry Symposium, The University of Glasgow, Glasgow, UK, April 2nd, 2008.
2. A. Abramov, M. Gutowski, Ammonia Borane Clathrates as a Basis for Hierarchical Hydrogen Storage, International Symposium on Metal-Hydrogen Systems, University of Iceland, Reykjavik, Iceland, June 24-28th, 2008.
3. M. Gutowski, R. Bachorz, T. Autrey, J. Linehan, *Prepr. Pap.-Am. Chem. Soc., Div. Fuel Chem.*, 2005, **50(2)**, 496-498.
4. L. Piela, *Ideas of Quantum Chemistry*, Elsevier, 2007.
5. C. Moller, M. S. Plesset, *Physical Review*, 1934, **46**, 618-622.
6. R. J. Bartlett, M. Musial, *Reviews of Modern Physics*, 2007, **79(1)**, 291-352.
7. P. Arrighini, *Intermolecular Forces and their Evaluation by Perturbation Theory*, Springer, 1981.
8. B. Jeziorski, R. Moszynski, K. Szalewicz, *Chem. Rev.*, 1994, **94**, 1887-1930.
9. K. Patkowskia, K. Szalewicz, B. Jeziorski, *J. Chem. Phys.*, 2006, **125**, 154107(1)-154107(20).
10. M. Gutowski, T. Autrey, *Prepr. Pap.-Am. Chem. Soc., Div. Fuel Chem.*, 2004, **49(1)**, 275-276.
11. M. H. Matus, K. D. Anderson, D. M. Camaioni, S. T. Autrey, D. A. Dixon, *J. Phys. Chem. A*, 2007, **111**, 4411-4421.
12. F. H. Stephens, V. Pons, R. T. Baker, *Dalton Trans.*, 2007, -, 2613-2626.
13. C. R. Miranda, G. Ceder, *J. Chem. Phys.*, 2007, **126**, 184703(1)-184703(11).
14. P. Giannozzi, S. de Gironcoli, P. Pavone, S. Baroni, *Phys. Rev. B*, 1991, **43(9)**, 7231-7242.
15. S. Wei, M. Y. Chou, *Phys. Rev. Lett.*, 1992, **69**, 2799-2802.

16. G. J. Ackland, M. C. Warren, S. J. Clark, *J. Phys.: Condens. Matter*, 1997, **9**, 7861-7872.
17. G. Wolf, J. Baumann, F. Baitalow, F.P. Hoffmann, *Thermochim. Acta*, 2000, **343**, 19-25.

**Implanting C in TiO₂ and investigate the location of C and
damage/damage recovery in TiO₂ as a function of annealing temperature**

Athavan Nadarajah, Rolf Koenenkamp,
Portland State University, Portland, OR

And

Shutthanandan Vaithiyalingam,
Pacific Northwest National Laboratory,

W.R. Wiley Environmental Molecular Sciences Laboratory, Richland, WA

Abstract:

In the summer research, we seek to tune the band structure of TiO₂ (110) for visible light absorption by substitutional doping of C anion for the O in the lattice. Anion doping demonstrates significantly higher reaction activity in comparison to cation doping. Anion doping produces a new absorption state with the low energy excitation of filled anion-dopant states at the top of the TiO₂ valence band. The challenge in preparing anion doped TiO₂ (110) is placing C in these substitutional sites. Based on the literature works, we are confident that we can place C in the proper lattice location using ion implantation at elevated temperatures. The experiments will provide fundamental insight at the atomic level about the effect of anion dopants on electronic structure and visible light absorption. In particular, we will address the following key issues, such as an effective ion implantation method and the influence of ion implantation on structural properties, experimental investigations of the effects of anion dopants on the electronic structure, and understanding the influence of specific dopants in specific structural environments on photochemistry

Background:

Heterogeneous photocatalysis, involving electron-hole pair formation initiated by band-gap excitation of the semiconductor, is particularly promising at least in two major directions, such as organic molecule activation and water splitting [1]. Photocatalytic materials under light irradiation should generate e⁻/h⁺ pairs with sufficient energy to promote reduction/oxidation chemistry, be stable under reaction conditions, and overlap the solar

spectrum in order to efficiently utilize sunlight [1, 2]. In virtually all above applications, TiO₂-based materials offer the greatest potential [1-3]. However, since TiO₂ has a wide optical band gap of about 3.0eV only the UV fraction of solar light can be utilized. Several approaches have been investigated to modify TiO₂ to better utilize sunlight, including use of organic sensitizers and electronic relays, mixed semiconductor systems, and cation doping [1, 4, 5]. For cation doping (e.g., Cr, Fe, Al), extension of the absorption into the visible has been achieved but often at the expense of decreased reaction activity. Unlike cation-doping, anion doping appears to be exclusively p-type, which should trap holes and free photo-excited electrons for surface reductive chemistry. Numerous studies have been published on anion-doped TiO₂ photocatalysis over last few years since the Science publication in 2001 of visible-light photoactivity on N-doped TiO₂ [6]. The general consensus is that anion doping with N, C or S produces a new absorption state, and the longer wavelength absorption arises from excitation of filled anion-dopant states at the top of the TiO₂ valence band [6-8]. The anion dopants are believed to be substitutional in the TiO₂ lattice [6, 7, 9] based on XPS binding energy comparisons.

Proposed Research:

We propose examining from a fundamental perspective the influence of the ion-beam implantation doping of TiO₂ single crystals on the visible light absorption and photocatalytic activity in a combined approach that employs:

- (1) controlled doping of single crystal substrates via ion beam implantation – placing the dopant at the right lattice location;
- (2) structural, chemical and dopant location characterization using a wide variety of surface and bulk sensitive characterization techniques;
- (3) probing *insitu* photochemistry utilizing UHV surface science methods

1. *Ion beam implantation doping:* The single most important issue contributing to the poor understanding of the fundamentals of heterogeneous photocatalysis is the variance that exists in photocatalyst preparation. The best foundation for addressing this issue is to start with well-characterized model materials, and to place the dopant at the desired depth and proper

lattice location; and in known and controllable quantities. This task will be undertaken utilizing the ion beam implantation for controlled substrate doping. We will prepare suitable samples by implanting single crystal TiO_2 -based materials with selected dopant of C anion. Since the lattice position of the dopant and the sample damage are crucial in these experiments, ion implantation at elevated temperatures is important. Optimized implantation parameters including implantation temperature and dose will be used to place the dopant at the proper site. Longer term efforts will include preparation of more elaborate doped samples involving more than one dopant and in which differently doped layers are intermingled.

2. *Characterization of anion doped TiO_2 single crystal surfaces:* Lattice location of the dopant can be determined using nuclear reactions (NRA) those are specific for C in channeling and random geometries. The chemical state and electronic structure information will be obtained by characterizing the samples using XPS and UPS (X-ray and UV induced Photoelectron Spectroscopy).

3. *UHV photochemistry studies:* we will study the water splitting reaction on doped TiO_2 surface at various reaction stages. The SPM (Scanning Probe Microscopy) will be used to study the water absorption configurations, their formation probabilities, and their correlation with surface defects. The Electron paramagnetic resonance (EPR) will be employed to estimate the concentration of intermediate and precursor states, trapping of light-generated electrons and holes in the bulk and on the surface, and also efficiency of the electron-hole formation and separation.

References:

- [1] M. A. Fox and M. T. Dulay, Chem. Rev. 93 (1993) 341.
- [2] M. Ashokkumar, Int. J. Hydrogen Energy 23 (1998) 427.
- [3] A. J. Bard and M. A. Fox, Acc. Chem. Res. 28 (1995) 141.
- [4] M. Gratzel, Acc. Chem. Res. 14 (1981) 376.
- [5] J. A. Koningstein, J. Photochem. Photobiol. A 90 (1995) 141.
- [6] R. Asahi, T. Morikawa, T. Ohwaki, K. Aoki, and Y. Taga, Science 293 (2001) 269.
- [7] H. Irie, Y. Watanabe, and K. Hashimoto, J. Phys. Chem. B 107 (2003) 5483.

- [8] T. Ohno, M. Akiyoshi, T. Umenayashi, K. Asai, T. Mitsui, and M. Matsumura, *Appl. Catal. A* 265 (2004) 115.
- [9] O. Diwald, T. L. Thompson, E. G. Goralski, S. D. Walck, and J. J. T. Yates, *J. Phys. Chem. B* 108 (2004) 52.

Photochemical Aging of Secondary Organic Aerosol

Adam P. Bateman,¹ Sergey A. Nizkorodov,¹ Alexander Laskin,² and Julia Laskin³

¹ *Department of Chemistry, University of California, Irvine, Irvine, California 92617-2025*

² *Environmental Molecular Sciences Laboratory and* ³*Chemical and Materials Sciences Division, Pacific Northwest National Laboratory, Richland, Washington 99352*

This is a joint report for experiments done by UCI graduate student Adam Bateman and his advisor Sergey Nizkorodov as a part of the 2008 SRI program.

Abstract

The primary goal of this project was to understand the importance of photochemical aging of secondary organic aerosol (SOA) derived from oxidation of selected monoterpenes. SOA was generated in the laboratory by mixing d-limonene and ozone in a reaction chamber, under various relative humidities and exposures to UV-light. The SOA samples were collected as a function of reaction time using a drum-impactor developed at EMSL, and as a function of reaction time and particle size using a MOUDI impactor. Microscopy measurements were performed on size separated limonene SOA. The composition of all d-limonene SOA was analyzed in detail using powerful tools of high-resolution electrospray ionization mass spectrometry (HR-ESI-MS) in Dr. Julia Laskin's and Dr. Alexander Laskin's groups.

In addition, several small experiments were conducted as a precursor to larger projects in the future. Laboratory generated limonene SOA was produced and then collected using a Particle into Liquid Sampler (PILS). This system uses a steam delivery system to collect aerosol particles directly and then collect them in liquid water for further analysis. The water soluble organic carbon (WSOC) compounds can then be analyzed by using HR-ESI-MS. The PILS system also allows for collection of SOA as a function of reaction time. Finally, laboratory generated SOA from the reaction of isoprene and ozone was investigated using HR-ESI-MS.

Introduction

Secondary Organic Aerosol (SOA) particles are a complex mixture of organic compounds with low volatility that are formed from reactions between biogenic compounds (limonene, α -pinene, terpenes...) and atmospheric oxidants (ozone, OH radical, and NO₃ radical). In urban areas, volatile exhaust from fossil fuel combustion serves as the main precursor to SOA formation. Model SOA particles can be made in the laboratory by mixing certain VOC (Volatile Organic Compounds) and ozone in a reaction chamber.

Regardless of the SOA source (lab or ambient) they are routinely analyzed by collecting them on filters and extracting soluble components using sonication into the solvent of choice. Recently, HR-MS-ESI has been used to study laboratory generated aerosol particles as well as field aerosol particle samples. These studies have concluded that the chemical composition of SOA particles is very complex, and that SOA species include various multifunctional organic acids, alcohols, peroxides, and carbonyls. Furthermore, many organic aerosol samples were found to contain oligomeric compounds produced by polymerization of smaller organic molecules within aerosol particles.

Experimental

Aerosol particles were generated by reacting either limonene or isoprene with ozone in a Teflon bag, cyclohexane was added and used as an OH scavenger. UV light was generated using UV-C lamps mounted to a rack surrounding the Teflon reaction chamber. The particles were collected on Teflon tape (Drum Impactor) or aluminum foil (MOUDI) and sonicated in acetonitrile. The particles were extracted directly into water using the PILS system purchased from Brechtel Manufacturing Incorporated (BMI).

All samples were analyzed using a Thermo-Fisher Orbitrap high resolution mass spectrometer at the Environmental Molecular Science Laboratory (EMSL) at the Pacific Northwest National Laboratory (PNNL), in Richland, WA.

Results

We are currently working on analysis of the data we obtained during our trip to EMSL. We expect that results of these measurements will be published in at least two separate publications in 2009. However, some key experimental findings can be summarized as follows:

- The chemical composition of SOA does not significantly change with particle size, i.e., extracts from MOUDI samples at different particle sizes do not show distinct differences in mass spectra.
- The appearance of ESI-MS changes significantly with mass loading of SOA. The ratios of peaks between monomer/dimer and trimer regions vary with concentration of SOA extracts, in a linear fashion. More importantly at low SOA concentrations the ratios are approximately constant. (Fig. 1)
- Time-resolved formation of SOA shows significant trends in ESI-MS analysis. Plots of total peak counts, as well as individual peak intensities show trends versus time. Most show an initial rise and then a leveling off, as equilibriums are established.
- Comparison of mass spectra of SOA generated using dark conditions and humid air or dry air (Fig. 2a) and after UV exposure show slightly different trends in peak intensities as well as overall oxidation. Further analysis is required to generate mechanisms to explain the changes in SOA composition.
- Water soluble SOA extracts are an exciting new direction for our research. Mass spectra from water soluble SOA extracts (Fig. 2b) are significantly different from the organic extracts (Fig. 2a) analyzed in all our previous work. Significant shifts in monomer and dimer regions are present, as well as an absence of many higher MW species as found in the organic extracts.
- Isoprene SOA analyzed using ESI-MS show entirely different spectra from limonene SOA. (Fig. 2c) The absence of distinct regions i.e. monomer/dimer clearly distinguishes the spectra, as well as the presence of many more highly oxidized and small MW species.

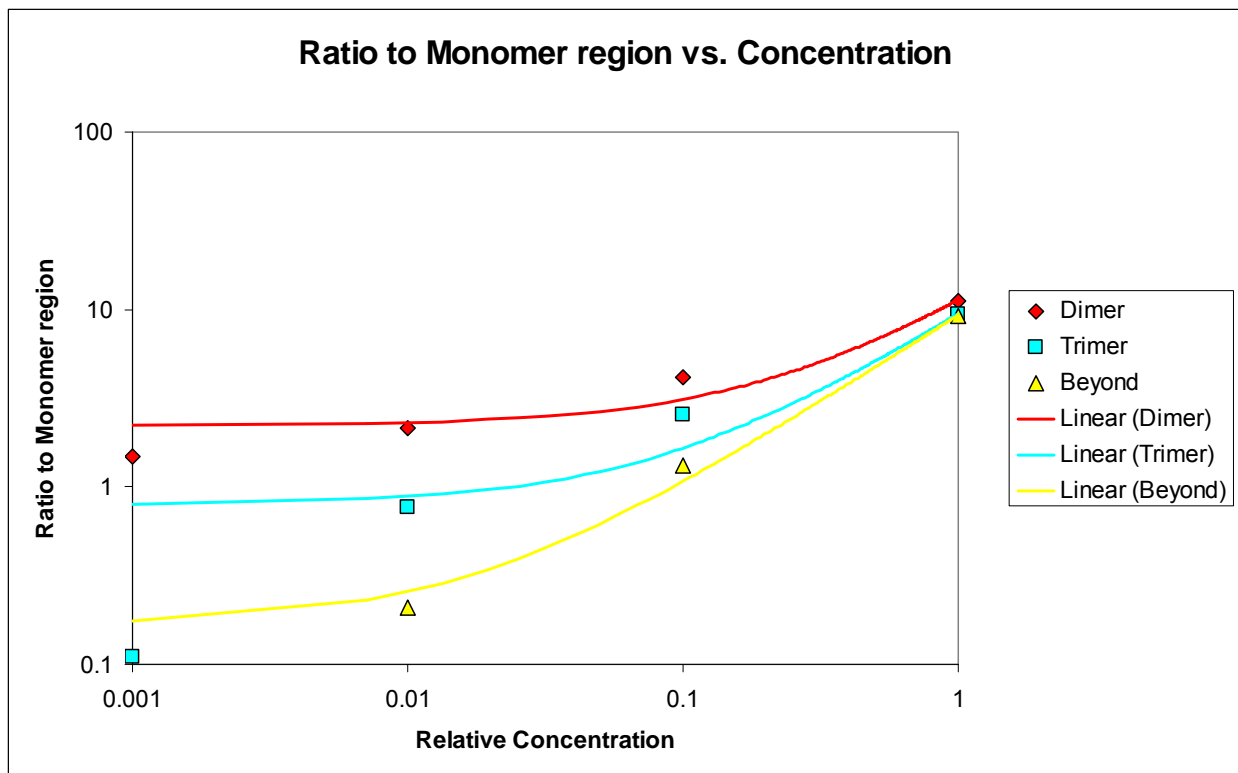


Figure 1. Ratio of all peaks in dimer(300-500 m/z), trimer (500-700 m/z) and further (700-1000 m/z) regions to the monomer region(150-300 m/z) vs. solution concentration.

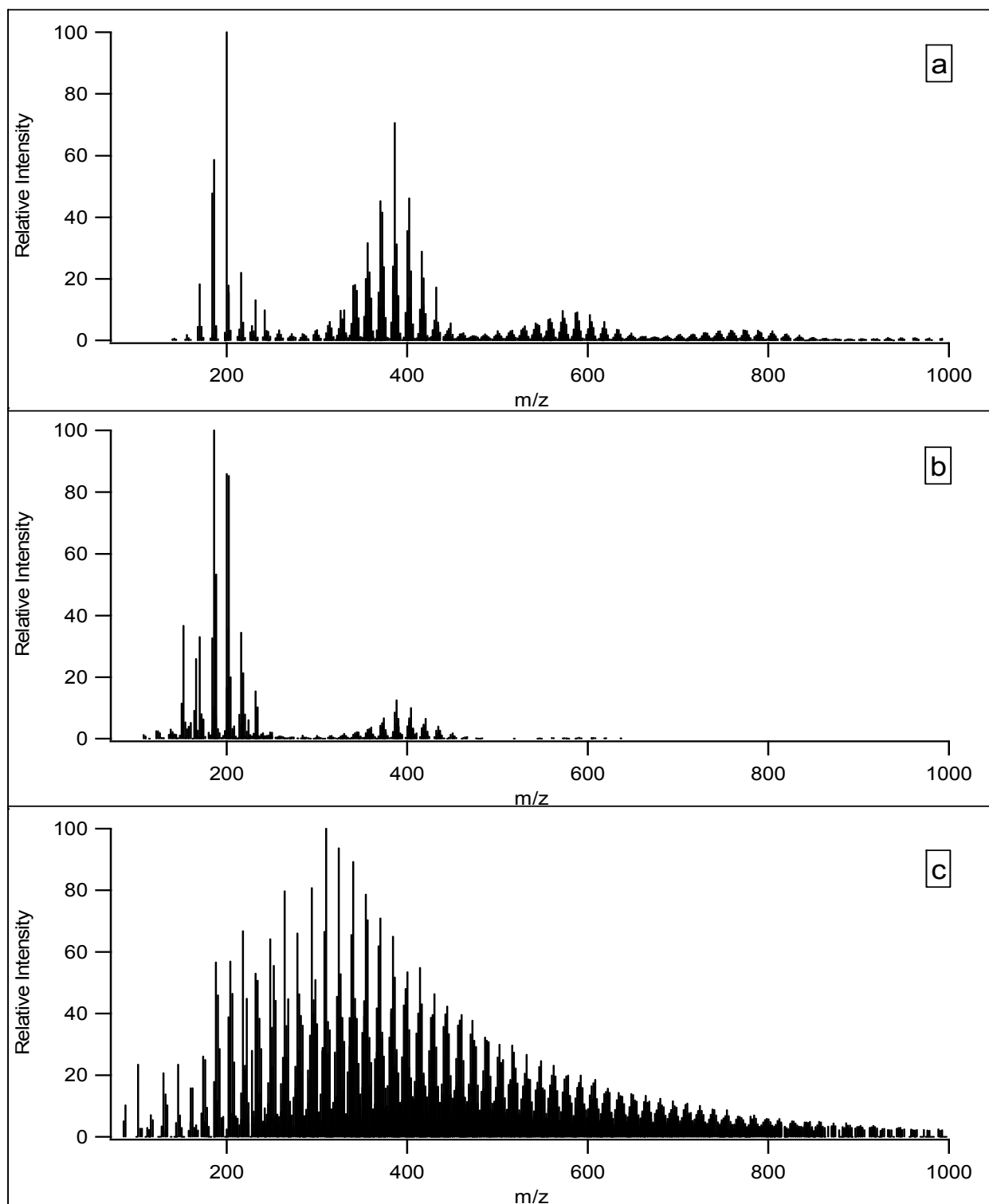


Figure 2. Representative mass spectra for various systems studied. Organic extracts from SOA formed during reaction of limonene and ozone in the dark (a); water soluble extract from SOA formed during the reaction of limonene and ozone in the dark (b); and organic extract from SOA formed during the reaction of isoprene and ozone in the dark (c). All spectra were recorded in the positive ion mode and m/z adjusted to represent the true compounds molecular weight.

Analysis of Ethylene Soot Produced by a Flat Flame Burner

Jeremy Cain, Hai Wang, Alexander Laskin

Soot is a particulate emission formed during high temperature, fuel rich combustion of hydrocarbon fuels. It is composed primarily of black carbon (BC), with small amounts of hydrogen. This particulate is of interest to the atmospheric science community because of its direct (light absorption and scattering) and indirect (cloud formation and heterogeneous reactions) effects on climate. Ideally, research to qualitatively and quantitatively describe these effects would be conducted on emissions from real world sources, e.g., aircraft gas turbines, locomotive and car diesel engines, and automotive gasoline engines. However, due to significant equipment costs and the complexity of the combustion process underlying their operation (e.g., turbulence, multi-component diffusion, and large hydrocarbon fuel structure) it would be difficult to gain any fundamental knowledge that the combustion process variables (e.g., equivalence ratio, C/O ratio, and flame temperature) have on the soot's physical and chemical properties. Thus, a burner that is used for soot modeling, a flat flame pre-mixed burner, may aid in this effort. This combustion device was built and installed at PNNL during a previous SRI appointment.

An experimental setup that utilizes this burner to produce soot and collect these particles is shown in Figure 1. The fuel (C_2H_4), diluent (Ar), and oxidizer (O_2) flow rates are individually controlled by a pressure regulator (not shown) prior to mixing upstream of the burner entrance point. A bed of glass beads and porous sintered brass filter create a spatially uniform reacting mixture issuing from the burner surface and, subsequently, a flat circular disc flame front. A chiller cools the burner by pumping cold water through an annulus near the burner's surface. Soot is produced downstream of the flame front and sampled through a 0.5 mm diameter pinhole in a 1/4" diameter stainless steel tube held in place at a particular height above the burner surface. The flow rate of dry nitrogen through the sampling probe is controlled by a rotometer manifold, and the dilution ratio (dictated by the amount of suction at the pinhole) is monitored by the upstream and downstream pressure measurements given by a u-tube water manometer. Soot particles are deposited on Si_3N_4 substrates attached to various impaction stages, corresponding to different aerodynamic diameters, in a nano-MOUDI (multi-orifice uniform discharge impactor) via jet impingement. Particles as small as $D_{50\%} = 12$ nm may be resolved in the nano-MOUDI. Particle size distribution functions are measured by an online SMPS (scanning mobility particle sizer) system, which consists of a TSI 3080 electrostatic classifier and a 3025A ultrafine charged particle counter.

A first step to characterizing the soot is through its chemical composition. This may be done by micro-FTIR spectroscopy and mass spectrometry. By taking samples at different heights above the burner surface, it may be determined if and to what extent surface reactions (oxidation and growth) have on its composition. IR spectroscopy allows for the determination of functional groups. A sample spectrum is shown in Figure 2. The various peaks correspond to different molecular vibrations attributed to different functional groups. For example, the peaks at 3420, 2960, and 1260 cm^{-1} correspond to O-H (phenol), C-H (aliphatic), and C-O (ether), respectively. Relative amounts of functional groups may be obtained through peak integration. To this extent, comparisons

may be made for different flame heights and temperatures. An example of this is shown in Figure 3.

This spectroscopic study will be expanded in the future to include anthropogenic samples to aid in its assessment of serving as a surrogate. Altering the experimental setup may easily be performed, allowing sampling conditions to be altered (e.g., sampling with dry or humidified air) and soot processing (e.g., post-collection heating) to be performed. This will allow for further manipulations to be made such that laboratory generated soot may resemble anthropogenic samples as close as possible. Furthermore, particles sampled may also be reacted with trace gases in a reaction chamber previously developed and tested at PNNL to allow for determination of these heterogeneous reaction rates.

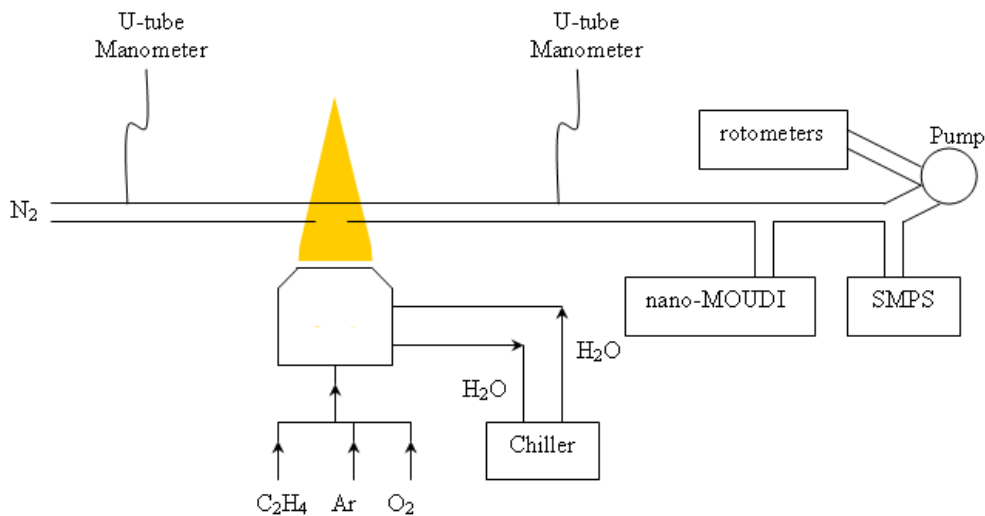


Figure 1 – Experimental setup

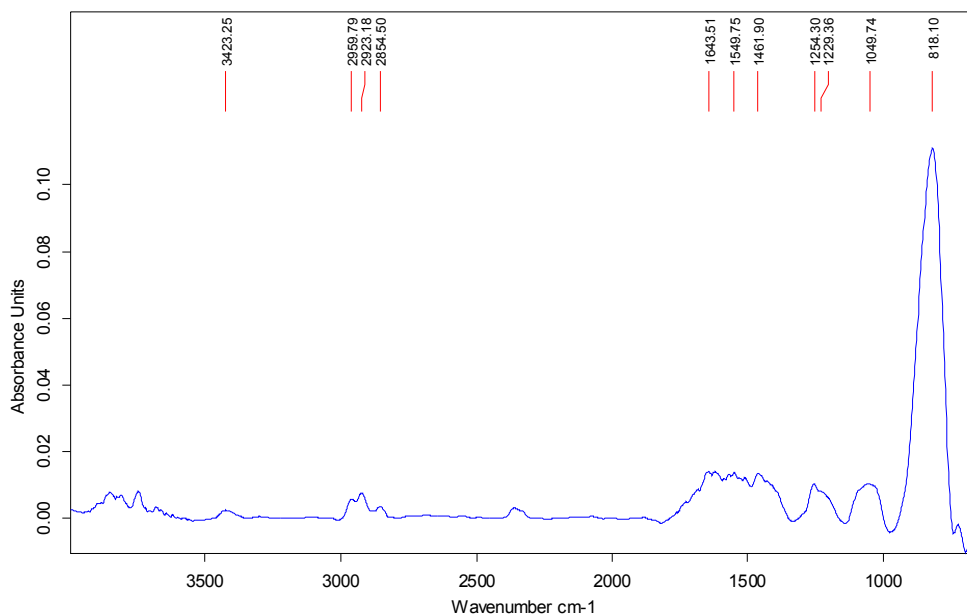


Figure 2 – Sample micro-FTIR spectrum.

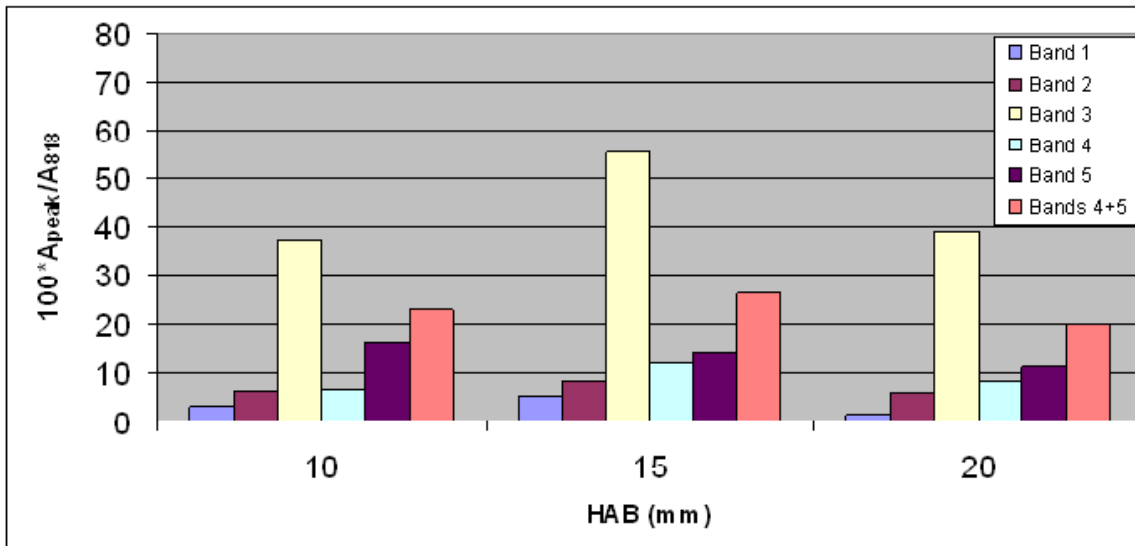


Figure 3 – Band areas, relative to the most prominent peak at 818 cm^{-1} , for 3 different heights above the burner surface (HAB) for a flame with cold gas velocity of 4.5 cm/sec .

Application of in-situ NMR in studying structure and dynamics of condensed phase H-storage materials

Yong Shen Chua¹, S Thomas Autrey², Wendy J Shaw², Abhi Karkamkar², Ping Chen^{1,3}

¹National University of Singapore, Singapore 117542

²Pacific Northwest National Laboratory, Richland, Washington 99354, USA

³Dalian Institute of Chemical Physics, Dalian, China 116023

Lithium amidoborane, also known as Li-AB was synthesized by reacting lithium hydride (LiH) with ammonia borane (AB) in tetrahydrofuran (THF) or dimethoxyethane (glyme). The mixtures of LiH and AB in the solvent were stirred overnight, giving Li-AB and hydrogen gas. Li-AB can also be synthesized by heating up the mixture of LiH + AB in THF at temperature below the boiling point of THF, for instance, 50°C. By increasing the temperature, the reaction in equation 1 can be accomplished in few hours. Hydrogen desorption for the reaction between LiH and AB was monitored by using gas burette at 50°C, proving evolution of 1 equivalent of H₂ to give Li-AB (Figure 1). It is worth mentioning that 158mL of hydrogen gas released correspond to 1 equivalent of hydrogen.

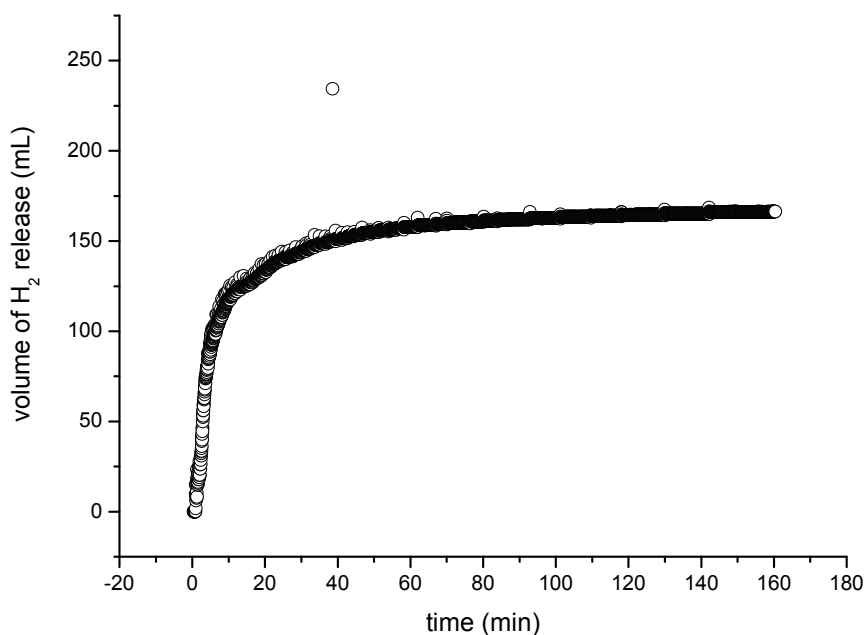


Figure 1: Gas burette measurement on 1LiH + 1 AB, releasing 156 mL of gas (~1 equivalent of H₂).

The product was then characterized by using VARIAN 500MHz NMR spectrometer, ensuring the correct chemical shift in ^{11}B NMR, 21.9 ppm for Li-AB (Figure 2). It is worth mentioning that Li-AB in solvent is unstable. It will slowly decompose to give addition peaks at -8ppm, -19.4ppm and -24ppm.

^{11}B in-situ NMR had been done in a PEEK cell at different temperature, 50°C and 60°C to monitor changes in chemical shift during decomposition of Li-AB. The line shapes of the arrays shown in figure 3 (60°C) demonstrated the decreases of Li-AB concentration with the function of time. At the end of reaction, all the boron species were found precipitate out from the solution, giving no signal to ^{11}B NMR. The insoluble product was then subject to other characterization method, FT-IR and Raman.

Also, ^1H NMR was also obtained on sample before and after the in-situ NMR. From the proton NMR (figure 4), we observed some interesting results. Hydride corresponding peak at ~-1ppm can be found on the sample at room temperature while an unknown peak at 4.5 ppm always appears in great intensity. Therefore, further structural confirmation by other characterization methods are needed to clarify the doubt.

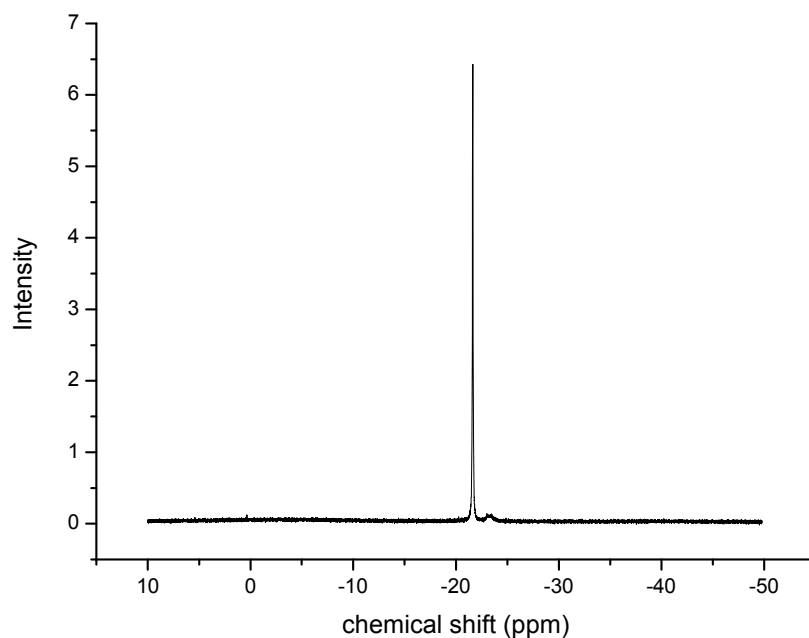


Figure 2: ^{11}B NMR of Li-AB in THF

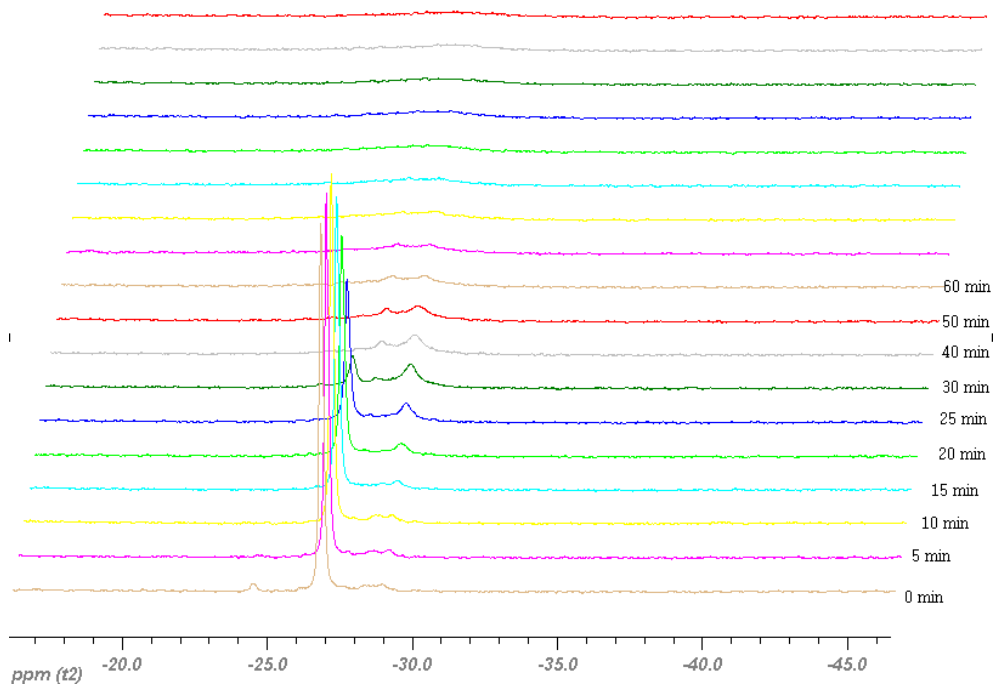


Figure 3: ^{11}B in-situ NMR for Li-AB at 60°C

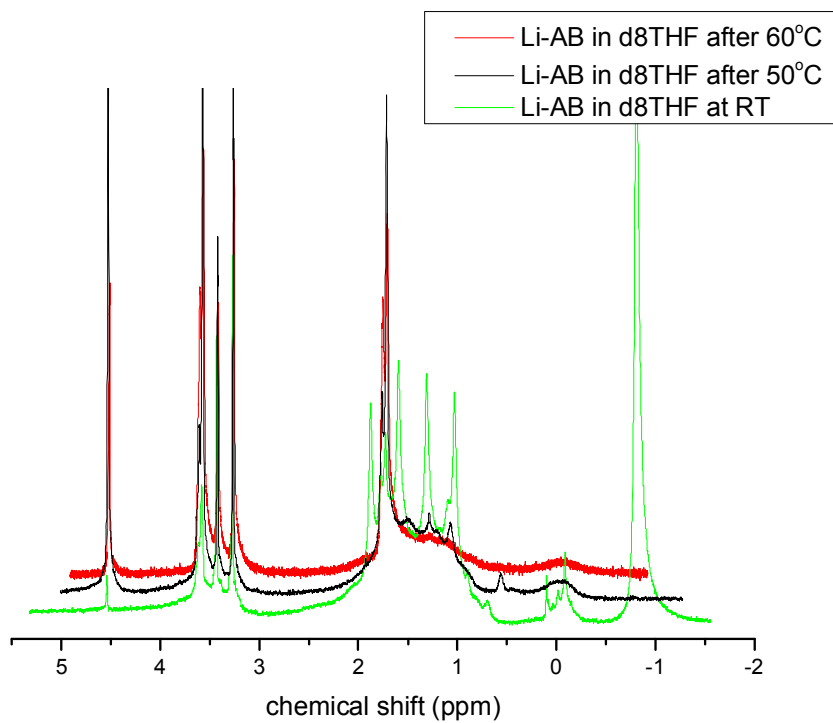


Figure 4: Comparison of ^1H NMR for Li-AB in $d_8\text{THF}$ at room temperature and after in-situ NMR

Heat of reaction in the aforementioned reaction (eq.1), LiH with AB, was also measured by using DSC (Differential Scanning Calorimetry). However, the presence of solvent (THF) resulted in the complication of the heat involved.

Deuterium 2H NMR had also been done on the samples including deuterated AB (NH_3BD_3) on porous material and deuterated Li-AB. Deuterium line shapes of both samples were obtained at room temperature and then decreased further down towards 10K with 10K difference at each interval. Temperature dependence of the deuterium spin-lattice relaxation times, T_1 was also obtained at the same time using inversion recovery pulse sequence technique modified for quadrupolar nuclei. The obtained data can be used to study the molecular motion of the sample. The line shape of the spectra changes with temperature. Deuterated AB on porous material gave only one peak in the H^2 NMR spectra at temperature from 300K to 110K. As the temperature further decreased to 20K, 2 peaks were found, rigid peak and a centre peak which was less rigid. The molecule became rigid at temperature below 20K. The slope of the $\ln T_1$ versus $1/T$ above 250K (before phase transition for centre peak) gives E_a value of 17.01 kJ/mol and 26.83 kJ/mol after the phase transition. Experiment on NH_3BD_3 on porous material should be included for better comparison on the dynamics of BD_3 and ND_3 .

Micro-XRD, X-ray powder diffraction, FT-IR, Raman measurements can be done in the future for more comprehensive understanding of Li-AB decomposition and clear up the puzzles that show up in ^{11}B NMR.

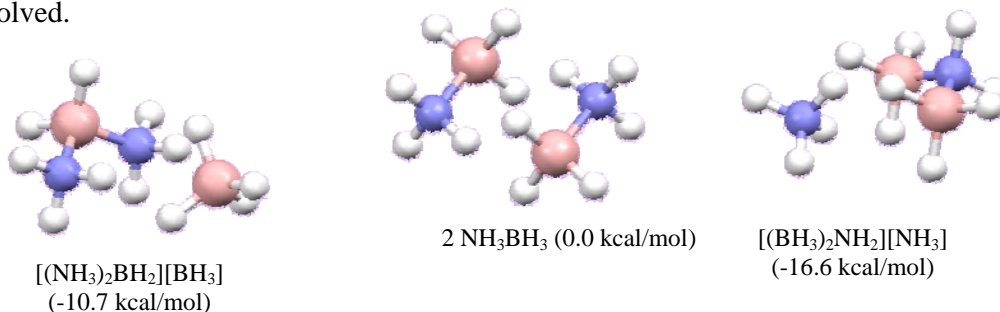
Structure and Energetics of Diammoniate of Diborane: A Computational Study in the Solid State

Michael Edie^{1,2}, Maciej Gutowski^{1,2} and Donald Camaioni²

¹Heriot-Watt University, Chemistry-School of Engineering and Physical Sciences,
Edinburgh EH14 4AS, United Kingdom

²Molecular Interactions & Transactions, Pacific Northwest National Laboratory, PO
Box 999, Richland, WA 99352, USA

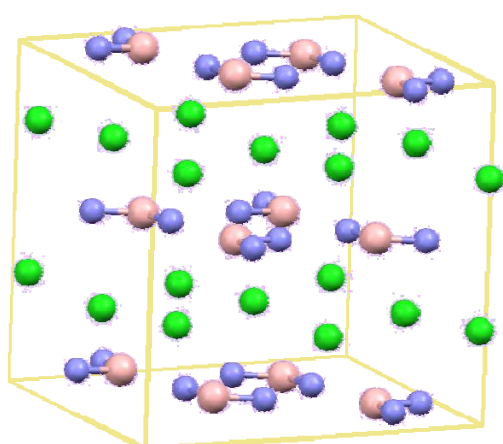
Boron-nitrogen hydrogen (BNH_x) materials display exceptional densities of hydrogen both from a gravimetric and volumetric point of view. The numerous experimental and theoretical studies into the hydrogen storage potential of BNH_x have so far focused predominantly on ammonia borane (AB).¹ For AB though it possesses 19% by weight of hydrogen the release of H₂ is too exothermic and thus regeneration of the depleted material is too challenging for onboard conditions. Moreover the kinetics of hydrogen release for AB is hindered by an induction period lasting approximately 20 minutes (at 100°C) preceding dehydrogenation. Many different strategies, which are aimed to improve the thermodynamic and kinetic performance of AB, have been reported in the literature and while there has been some success, most notable by Autrey and coworkers² and Goldberg et-al,³ such approaches compromise gravimetric and volumetric efficiency, or greatly increasing the overall financial cost of the storage systems. One alternative approach may be to assess alternative forms of BNH₆ that are destabilised relative to AB, be that either thermodynamically, kinetically or both. Such an alternative compound with the same composition as AB is the so-called ionic form diammoniate of diborane (DADB), [NH₃BH₂NH₃]⁺[BH₄]⁻. While DADB was first reported as early as 1958 its molecular structure was the source of much debate.⁴ Early reports by Schlesinger suggested the structural formula [NH₄]⁺[BH₃NH₂BH₃]⁻ coined DBDA. However further analysis by NMR and Raman spectroscopy disproved this though the crystal structure of DADB has never been solved.



Relative stabilities of (AB)₂, DADB, and DBDA at the CCSD(T)/aug-cc-pVTZ level of theory.⁵

Previous theoretical work on the structure and stability of DADB focused on the relative stability of the complexes (AB)₂, DADB, and DBDA in the gas phase.⁵ These findings summarized above were performed at CCSD(T) level of theory and showed that the AB dimer is notably more stable than DADB (-10.7 kcal/mol) and DBDA (-16.6 kcal/mol). While this result is promising from the point of view of improving thermodynamics, it is paramount to understand the role of lattice energies in relative stabilities of these materials in their solid form. The use of electronic

structure calculations such as density-functional theory (DFT) to calculate the energetics and thermodynamic properties of materials is widespread with accuracies dependent of the quality of the density-functional employed. However such calculations require the complete crystal structure of the species under study, calculations involving phases that are uncharacterized crystallographically are further complicated by the selection of the initial guess geometry. The method we have employed to aid in the prediction of the structure of DADB is the so-called database searching method or *Data mining*, where prototype structures are selected from crystallographic databases such as Cambridge Structural Database (CSD) on the basis of chemical or morphological similarities. While the crystal structure of DADB has never been solved our search found one solved data set containing the same unusual complex cation as DADB, but with $[\text{BH}_4]^-$ substituted with Cl^- .⁵ The structure of $[\text{NH}_3\text{BH}_2\text{NH}_3]\text{Cl}$ as observed by Nordman comprised of a orthorhombic unit cell of space group number 64 (Cmca). The conventional orthorhombic cell contains four formula units where layers of $[\text{NH}_3\text{BH}_2\text{NH}_3]^+$ intercalated with layers of Cl^- , the lattice parameters for this structure were $a \approx b = 10.20$ $c = 8.70$.



$[\text{NH}_3\text{BH}_2\text{NH}_3]\text{Cl}$ Structural information

Space Group Cmca(64)

$a = 10.20(\pm 0.04)$

$b = 10.20(\pm 0.06)$

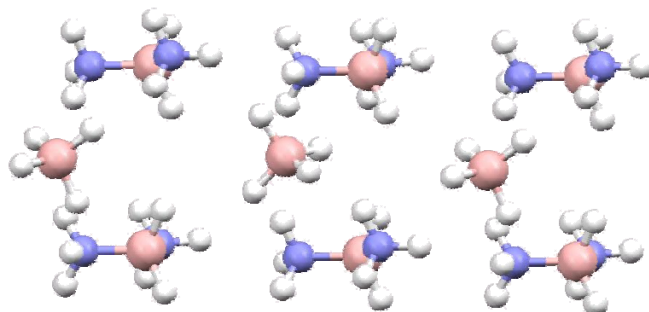
$c = 8.70(\pm 0.04)$

Atomic Position

Center	x	y	z
B	0.212	0.219	0.000
N ₁	0.236	0.064	0.000
N ₂	0.060	0.237	0.000
Cl	0.000	0.000	0.264

Crystal structure and structural information of $[\text{NH}_3\text{BH}_2\text{NH}_3]\text{Cl}$ as reported by Nordman.⁵

Although the monatomic anion Cl^- and the complex BH_4^- have obvious differences in geometry it can be appreciated that effective radius of BH_4^- (2.02\AA) is similar to that of chloride (1.82\AA) and as many chloride salts are isostructural with respect to heavy atom positions to the respective borohydride compounds, we may use $[\text{NH}_3\text{BH}_2\text{NH}_3]\text{Cl}$ as a sound guess structure for DADB. Although the structure of Nordman provides heavy atom positions no coordinates were provided for hydrogen centres. In order to assign hydrogen positions and determine $[\text{BH}_4]^-$ orientation a range of 20 trial structures were optimized with the dominant minima selected. This structure was then globally



Optimized geometry of DADB illustrating the layered structure and BH_4^- orientation.

optimized via simulated annealing within a constant volume regime from 400°K to approximately 20°K. During this process significant rearrangement of the BH_4^- were observed as well as some minor adjustment of the cation. The figure displays a section of the optimised geometry of DADB as prepared from the $[\text{NH}_3\text{BH}_2\text{NH}_3]\text{Cl}$ prototype structure. During optimization of the structure a small contraction of **a** and **b** to 10.15 Å accompanied by a larger expansion of the 12.2 Å in the **c** parameter was observed. Most interestingly the relative stability of DADB in the solid state is only -4.8 kcal/mol less than that of AB in the lowest energy orthorhombic polymorph. Moreover this comparison only takes into account electronic ground state energies and it is conceivable the finite temperature effects may further stabilize DADB relative to AB. While this work gives only approximation of the stability of DADB further work will look at a larger array of prototype structures that may yield lower energy polymorphs. Effects of vibrational contributions to total energy will be considered in order to fully understand the free energy profile of the AB/DADB equilibrium. We will also investigate the kinetics of the transformation of AB into DADB in the solid state as this has been suggested to be an important step in initial hydrogen release of bulk AB. In conclusion it appears from this initial investigation that DADB is of comparable stability to AB in the solid state thus there is no major thermodynamic advantage of the thermolysis of DADB over AB. At this stage it looks unlikely that one may optimize the hydrogen uptake and release thermodynamics of $\text{BNH}_x(x=6)$ by the isomerization alone. However this may be achieved by screening BNH_x or boron-nitrogen based compounds of alternative composition. Such pure BN or composite hydrides may be the key to achieving a fully reversible on-board hydrogen source. This will be the main focus of our further work.

Acknowledgments.

Calculations were performed with the support of the Molecular Science Computing Facility within the William R. Wiley Environmental Molecular Sciences Laboratory and with the in-house developed NWChem and CP2K software packages.

References.

1. F. H. Stephens, V. Pons, T. Baker, *Dalton Trans.*, 2007, 2613
2. A. Gutowska, L. Li, Y. Shin, C. M. Wang, X. S. Li, J. C. Linehan, R. S. Smith, B. D. Kay, B. Schmid, W. Shaw, M. Gutowski and T. Autrey, *Angew. Chem., Int. Ed.*, 2005, **44**, 3578
3. M. C. Denney, V. Pons, T. J. Hebden, D. M. Heinekey and K. I. Goldberg, *J. Am. Chem. Soc.*, 2006, **128**, 12048
4. S. G. Shore, *Dissertation*, University of Michigan, 1958.
5. M. Gutowski, R. Bachorz, T. Autrey, J. Linehan. *Prepr. Pap.-Am. Chem. Soc., Div. Fuel Chem.*, 2005, **50**,496
6. C. E. Nordman and C. R. Peters, *J. Am. Chem. Soc.*, 1959, **81**, 3551

PNNL SUMMER RESEARCH INSTITUTE– 2008

Your Full Name: Razif R. GABDOULLINE
Profession: Research Associate
Phone Number: +49 6221 5451 269
Email Address: razif.gabdoulline@bioquant.uni-heidelberg.de
Institution: University of Heidelberg
Address: BIOQUANT, BQ0018, Im Neuenheimer Feld 267
City, State Zip: Heidelberg, Germany, D-69120
University advisor: Rebecca C. Wade
PNNL advisor: T.P. Straatsma

Dates: **August 11 – September 6**

Title: **Computer simulations on biomolecular systems, using QM/MM, MD and Free Energy methodologies**

Project

The focus of research is on complex enzymatic reactions with the purpose of obtaining a detailed molecular-level characterization and understanding of the reactivity of enzymes related to membrane receptor proteins and to metabolism. These efforts lie on the premise that such an understanding can be obtained through computational modeling and simulations.

NWChem [1] is the computational chemistry software suite developed and maintained by the Molecular Sciences Software Group (MSSG) of the Environmental Molecular Sciences Laboratory at the Pacific Northwest National Laboratory. It utilizes a mixed Hamiltonian quantum mechanical / molecular mechanics (QM/MM) methodology. Fully classical models of the protein guide the simulation of the effects of the long-range domain structure and dynamics of the enzyme on the QM wave function.

Enzymatic reaction steps of metabolic enzyme TPIs will be also modeled, with the purpose of quantifying the differences between the enzymes from different organisms [2-3]. Ab initio quantum mechanical and molecular mechanical calculations of Yeast TPI were already performed [4-5]. It is planned to perform modeling of the catalytic reaction in different TPI-s by means of QM/MM simulations using NWChem software tool at PNL. In the direction of DHAP (dihydroxyacetone phosphate) to GAP (D-glyceraldehyde 3-phosphate) conversion, the transfer of proton from C1 of DHAP to the catalytic base, Glu165, will be simulated as a rate limiting step. In the opposite direction the transfer of proton from C2 of GAP to Glu165 will be modeled. Kinetic data, to be compared with simulations, is available for TPIs from: Yeast (having x-ray structure of TPI-DHAP Michaelis complex 1ney at 1.2 Å resolution), T.Brucei, Chicken, Giardia lamblia and Leishmania Mexicana.

Methods

Homology models of TPIs from different organisms were generated using SwissModel web server [6], known to result in structural models of appropriate quality [3]. A template X-ray structure 1ney [7], chain B was used. Kinetic data to correlate with structures was taken from BRENDA database [8].

Organism	k_{cat} (10^5 min^{-1}) DHAP->GAP	SwissProt ID	Conditions
<i>Trypanosoma brucei</i>	3.1 (2.6-3.7)	TPIS_TRYBB	20°C, 100 mM, pH 7.4
<i>Trypanosoma cruzi</i>	2.7	TPIS_TRYCR	20°C, 100 mM, pH 7.4
<i>Oryctolagus cuniculus</i> muscle	1.86 (1.9-5.1)	TPIS_RABIT	30°C, 50 mM, pH 7.6
<i>Gallus gallus</i> muscle	2.56	TPIS_CHICK	30°C, 100 mM, pH 7.4
<i>Saccharomyces cerevisiae</i>	7.9 (1.4-10)	TPIS_YEAST	25°C, 100 mM, pH 7.6
<i>Leishmania mexicana</i>	2.52 (4.3-2.5)	TPIS_LEIME	25°C, 100 mM, pH 7.6
<i>Plasmodium falciparum</i>	2.68	TPIS_PLAFA	30°C, 50 mM, pH 7.9
<i>Vibrio marinus</i>	4.2	TPIS_VIBMA	10°C, 100 mM, pH 7.6
<i>Escherichia coli</i>	5.4	TPIS_ECOLI	25°C, 100 mM, pH 7.6

PNNL SUMMER RESEARCH INSTITUTE– 2008

<i>Homo Sapiens</i>	2.7	TPIS_HUMAN	25°C, 100 mM, pH 7.6
<i>Giardia lamblia</i>	2.9	TPI1_GIALA	25°C, 100 mM, pH 7.4
<i>Spinacia oleracea</i>	2.7	TPIC_SPIOL	25°C, 100 mM, pH 7.5

For another set of analysis, mutations of triosephosphate isomerase were generated using Swidd-Pdb-Viewer program [6]. The following kinetic data was used

Notation	Mutant	k_{cat} (1/s) GAP->DHAP
000	WT	3500
100	G10S	1700
200	S96P	64
300	S96T	1100
400	E97D	3600
500	E165D	4.3
510	E165D,G10S	14
512	E165D,G10S,S96P	67
513	E165D,G10S,S96T	34
514	E165D,G10S,E97D	25
516	E165D,G10S,V167D	28
517	E165D,G10S,G233R	24
520	E165D,S96P	68
524	E165D,S96P,E97D	40
526	E165D,S96P,V167D	34
530	E165D,S96T	17
534	E165D,S96T,E97D	17
536	E165D,S96T,V167D	12
537	E165D,S96T,G233R	30
540	E165D,E97D	10
546	E165D,E97D,V167D	19
560	E165D,V167D	15
567	E165D,V167D,G233R	29
570	E165D,G233R	8.4
600	V167D	58
700	G233R	1650

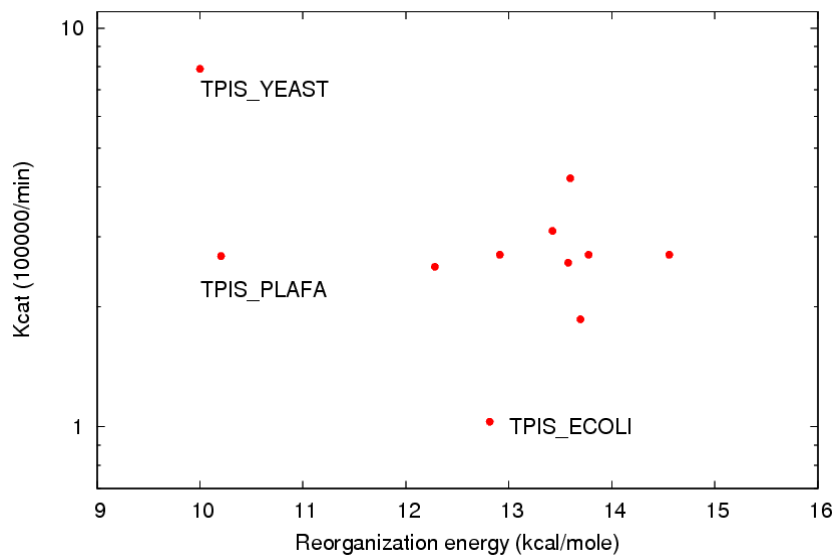
In both cases, only the proton transfer from C2 of GAP to Glu165 (Asp16) was modeled by QM/MM minimization and DFT optimization of QM region using NWChem [1]. QM region was selected to consist of atoms of the substrate GAP and sidechain of Glu165 (Asp165), totaling 25 (22) QM atoms. QM optimization of one system took ca 15*16 CPU*minutes.

Differences in charge (proton) transfer reactions were monitored by calculating solvent polarization energy before and after proton transfer (this is also called as reorganization energy [10]). Charge distribution in reactant and product states were derived by fitting electrostatic potentials.

Reorganization energies were calculated with UHBD [11]. Reorganization energy is the difference between the energy of the product-state charges in the solvent polarization electrostatic potential from the reactant-state charges. The latter potential is calculated as a difference between the electrostatic potentials from the reactant-state charges in the inhomogeneous (low dielectric protein interior and high dielectric solvent) and homogeneous (all over low dielectric) media. Solvent dielectric value was set to 80, and solute (protein) dielectric was 2.

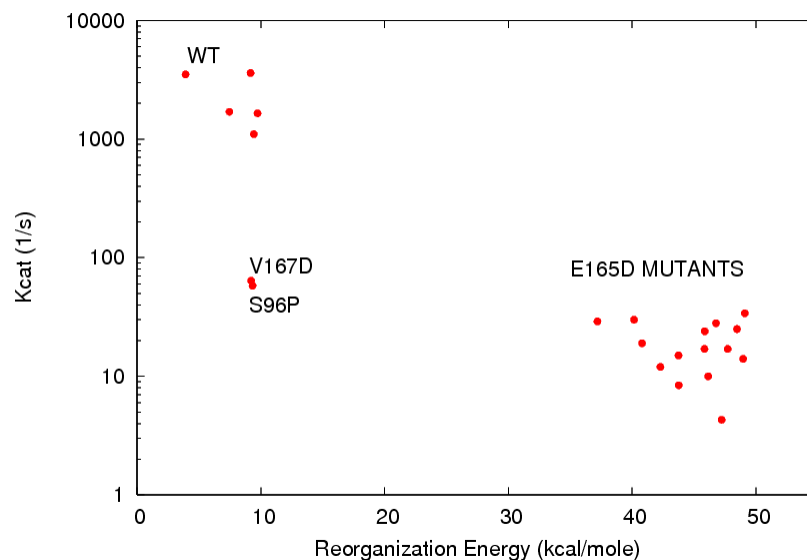
Results

Relation between the calculated reorganization energies and experimentally measured k_{cat} values is shown in Figure 1 (expected correlation is: the reorganization energy is proportional to $-\log(k_{cat})$):



There is a good correspondence between overall range of k_{cat} changes (factor of 8) and spread of reorganization energy (5 kcal/mole). If one takes into account that $\frac{1}{4}$ of reorganization energy is a meaningful estimate for activation energy of charge transfer [10], then these 5 kcal/moles imply $\exp(5/4/0.6)$ (~ 8) times deviation of kinetic constant. High k_{cat} value of TPIS_YEAST corresponds to its low reorganization energy. However, low k_{cat} value of TPIS_ECOLI does not correlate with intermediate value of reorganization energy. Low reorganization energy in case of TPIS_PLAFA does not correspond to intermediate value of its k_{cat} .

Analysis in the case of TPI mutants shows that the same approach is able to explain large k_{cat} changes due to E165D mutation



Other changes are not very well explained; especially, V167D and S96P mutations do not result in large reorganization energy changes, what could be expected from their low k_{cat} values.

Conclusions

Optimization of enzyme structures with QM/MM methods and correlating reorganization energies with k_{cat} parameter changes during charge transfer reactions seems to be a promising approach for quantifying kinetic parameter changes due to sequence modification of enzymes. In the modeling it is needed to rebuild the protein structure and bound substrate before and after reaction. This can be done applying QM/MM methods. QM modeling gives necessary charge distribution before and after reaction and MM modeling allows taking into account the modification of the structure coupled to charge transfer.

More elaborate modeling of reactant and product states may be necessary to quantify changes more accurately. Modeling a saddle point of charge transfer, more extensive minimization of the enzyme structure, selection of larger QM region may increase the accuracy of this approach.

References

- [1] Straatsma TP, Apra E, Windus TL, Dupuis M, et al (2003) NWChem, A Computational Chemistry Package for Parallel Computers, Version 4.5, Pacific Northwest National Laboratory, Richland, Washington 99352-0999, USA
- [2] Stein M, Gabdoulline RR, Wade RC (2007) Bridging from molecular simulation to biochemical networks. *Curr Opin Struct Biol* 17: 166-172.
- [3] Gabdoulline RR, Stein M, Wade RC (2007) qPIPSA: Relating enzymatic kinetic parameters and interaction fields. *BMC Bioinformatics* 8: 373.
- [4] Xiang Y, Warshel A. (2008) Quantifying Free Energy Profiles of Proton Transfer Reactions in Solution and Proteins by Using a Diabatic FDFT Mapping. *J Phys Chem B*. 112(3):1007-15.
- [5] Friesner RA, Guallar V. (2005) Ab initio quantum chemical and mixed quantum mechanics/molecular mechanics (QM/MM) methods for studying enzymatic catalysis. *Annu Rev Phys Chem*. 56:389-427.
- [6] Guex N, Peitsch MC (1997) Swiss-Model and the Swiss-Pdb viewer: An environment for comparative protein modeling. *Electrophoresis* 18:2614-723.
- [7] Jogl G, Rozovsky, Mcdermott AE, Tong L (2003) Optimal alignment for enzymatic proton transfer: Structure of the Michaelis complex of triosephosphate isomerase at 1.2-Å resolution. *PNAS*. 100: 50.
- [8] Schomburg I, Chang A, Ebeling C, Gremse M, Heldt C, Huhn G, Schomburg D (2004) BRENDA, the enzyme database: updates and major new developments. *Nucleic Acids Res*. 32:D431-3.
- [9] Blacklow SC, Liu KD, Knowles JR. (1991) Interdependence of combinations of point mutations of a sluggish triosephosphate isomerase. *Biochemistry* 30:8470-6
- [10] Marcus R.A. (1993) Electron transfer reactions in chemistry. Theory and experiment. *Rev. Mod. Phys.* 65:599-610. (1975) Energetic and dynamical aspects of proton transfer reactions in solution. *Faraday Symp. Chem. Soc.* 10:60-8.
- [11] Madura JD, Briggs JM, Wade RC, Davis ME, Luty BA, Ilin A, Antosiewicz J, Gilson MK, Bagheri B, Scott LR, McCammon JA: (1995) Electrostatics and diffusion of molecules in solution: Simulations with the University of Houston Brownian dynamics program. *Comp. Phys. Comm.* 91:57-95.

**Influence of samaria doping on the resistance of ceria thin films and its implications to
the planar oxygen sensing devices**

S. Gupta¹, S.V.N.T. Kuchibhatla², M.H. Engelhard², V. Shutthanandan², P. Nachimuthu²,
W.Jiang², L.V.Saraf², S.Thevuthasan², S.Prasad^{1,3}

1. Department of Electrical Engineering, Portland State University, Portland, OR 97201, USA

2. EMSL, Pacific Northwest National Laboratory, Richland, WA 99352, USA

3. Department of Electrical Engineering, Arizona State University, Tempe, AZ-85287, USA

***Corresponding Author:**

Shalini Prasad

Dept of Electrical Engineering,

ERC 237, Arizona State University,

Tempe AZ 85287

Email: shalini.prasad.1@asu.edu

**Influence of samaria doping on the resistance of ceria thin films and its implications to
the planar oxygen sensing devices**

S. Gupta¹, S.V.N.T. Kuchibhatla², M.H. Engelhard², V. Shutthanandan², P. Nachimuthu²,
W.Jiang², L.V.Saraf², S.Thevuthasan², S.Prasad^{1,3}

1. Department of Electrical Engineering, Portland State University, Portland, OR 97201, USA

2. EMSL, Pacific Northwest National Laboratory, Richland, WA-99352, USA

3. Department of Electrical Engineering, Arizona State University, Tempe, AZ-85287, USA

Abstract

In order to evaluate and analyze the effect of samarium (Sm) doping on the resistance of cerium oxide, we have grown highly oriented samaria doped ceria (SDC) thin films on single crystal sapphire [Al₂O₃ (0001)] substrates by using oxygen plasma assisted molecular beam epitaxy (OPA-MBE). The films' structure and chemistry were characterized with various *in situ* and *ex situ*, surface and bulk sensitive techniques. Uniform Sm concentration and the oxidation states of the cerium (Ce, +4) and samarium (Sm, +3) have been confirmed by depth profile and X-ray photo electron spectroscopy (XPS), respectively. The doped cubic CeO₂ films were found to have a preferred (111) orientation using high resolution X-ray diffraction (HRXRD). The crystal quality and thickness were analyzed using Rutherford backscattering spectrometry (RBS). The resistance of these films was obtained by two probe measurement capability under various conditions of operating temperature (623 – 973 K) and oxygen pressure (10⁻³ –100 torr). The resistance of the doped ceria films was found to be

significantly lower than that of pure ceria under varying oxygen partial pressure. Based on the resistance values, for the first time, it is proposed that there exists an optimum dopant concentration of 6 atom% Sm to obtain maximum oxygen sensitivity in SDC films. Possible reasons behind various observations have been discussed and the implications to planar oxygen sensors have been outlined.

Keywords: oxygen sensor, ionic conduction, samaria doped ceria, thin films, MBE

1. Introduction

Oxygen sensors have been the subject of enormous interest because of their wide application in vital areas such as automobiles, industries, life sciences and medicine [1]. Oxygen sensors play a key role in pollution control through the automobile engine management by controlling A/F ratio, optimizing industrial boilers and exhaust from steel, cement industries, biological and food processing plants and control of chemical processes [2]. Most of these applications require for the oxygen sensor to operate at elevated temperatures along with the ability to rapidly detect a large dynamic range of the gas concentration varying from trace amount to reasonably high volume percentages.

For oxygen monitoring at elevated temperatures sensors based on potentiometric equilibrium, limiting current amperometry and surface resistance variation have been widely used. Metal oxide semiconductor (MOS) type sensors based on the resistive gas sensing principle have become significantly popular [1-5]. Oxygen sensors based on MOS offer a number of advantages like miniaturization, higher signal to noise ratio and portability over the

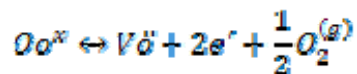
other types of sensors because of the use of nanomaterials and thin films as the active sensing element.

Izu et al. [1, 5-8] have pioneered the technique of using pure and doped oxides for oxygen gas sensing. They have fabricated sensors and reported the kinetic behavior of the oxygen gas sensing by MOS such as ceria in both micro and nanoscale[9]. Rare earth materials such as pure and doped ceria are the main candidates because of their lower activation energy (E_a) which facilitates ionic conductivity at temperatures in the range of 600-800°C[10]. Recently, resistive oxygen gas sensors using cerium oxide have been reported by several teams [3-6, 11]. Ceria has been used as active sensing material for oxygen detection due to its unique ability to lose or gain oxygen in response to the ambient oxygen concentration, which is of great interest to catalysis and solid oxide fuel cells as well [12]. This property of ceria could also be exploited in designing better oxygen gas sensors. The defect concentration and migration govern the oxygen storage and oxygen ion conduction properties in ceria. Replacement of Ce^{4+} with divalent or trivalent cations results in the creation of oxygen vacancies and high oxygen ionic conductivity over extended temperature and oxygen partial pressure ranges [13]. The choice of the dopant is usually advocated by the ability of the dopant to minimize the internal strain of the lattice [14-16]. Dopants such as, hafnia [5], zirconia [7] and yttria [17] were studied with the goal of improving the sensitivity of ceria sensors. Andersson et al. [10] have recently proposed, with the help of quantum-mechanical first-principle studies, that Sm with atomic number 62 is the best dopant for optimizing the conductivity in ceria. Systematic evaluation of the chemistry of the films, effect of crystal structure and the dopant concentration are very limited in the existing sensors literature. Here, we demonstrate the role of Samaria doping in controlling the chemistry and structure of

cerium oxide and the resultant variation in the resistance of the high quality, epitaxial and highly oriented SDC films.

2. Principle of Operation

In general, resistive oxygen sensors operate on the basic principle in which an electrical signal is generated due to oxygen ion diffusion and oxygen ion conduction by hopping through the oxygen vacancies in the sensor material when it is exposed to oxygen. At low and medium temperatures (about 300-500°C) chemisorptions of oxygen at the surface of the oxide leads to the formation of surface oxygen ions [18]. The density of the surface oxygen ions depend on the oxygen partial pressure in the surrounding atmosphere. At higher temperatures (600-1100°C), oxygen ions diffuse in the vacancies. The basic reaction between oxygen molecules in the gas phase, $O_2^{(g)}$, and the oxygen vacancy, V_o , in the bulk can be expressed as:



The material used for oxygen sensing is generally a non-stoichiometric oxide for example an oxygen deficient oxide containing oxygen vacancies. Ceria is the most commonly studied material for the oxygen sensing. Doping of trivalent element such as Sm in ceria film generates more oxygen vacancies in comparison to pure ceria film and, as a result, oxygen ionic conduction significantly increases through the samaria doped ceria films. Since elevated temperatures help the oxygen ions to overcome the activation energy barrier the current through the films increases with annealing temperature. This change in current is directly proportional to a change in the conductivity of the thin film, which can be measured by using the constant voltage method. A constant voltage of 2V was applied in series with

the sample as depicted in figure 1. An electrometer, which was also connected in series with the sample, was used to measure the current change through the sample.

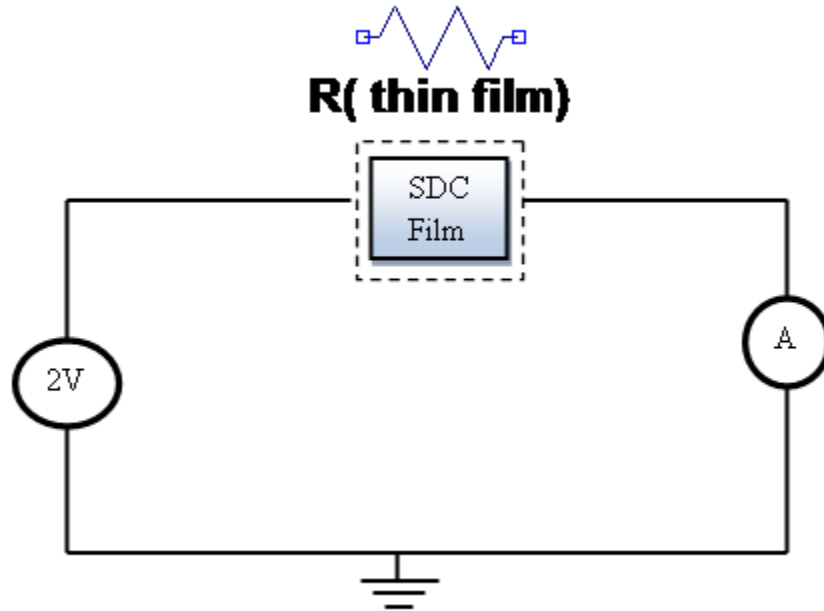


Figure 1: The equivalent circuit of the constant voltage method used to measure the change in the resistance of the SDC films with the change in temperature. R (thin film) is the equivalent resistance of the SDC films.

3. Experimental Details

To study the effect of oxygen diffusion in the SDC films and to test these films for the oxygen sensing, the experimental work contains two main parts: (1) synthesis of the active sensing surface (SDC films) i.e. film growth with chemical and structural characterization and (2) evaluation of electrical properties as a function of temperature and pressure. The details of both are described below:

3.1 Film growth and *in situ* characterization

Growth of ceria films with various dopant concentrations of Sm on sapphire (0001) and *in situ* characterization were carried out in a dual chamber ultrahigh vacuum (UHV) system described in detail elsewhere[19]. The molecular beam epitaxy (MBE) chamber consists of five metal evaporation sources and a UHV compatible electron cyclotron resonance (ECR) oxygen plasma source, as well as reflection high energy electron diffraction (RHEED) for real-time characterization of film growth. High purity cerium (Ce) rods were used as the source material in an e^- beam evaporator. Samarium (Sm) was evaporated from an effusion cell. Growth rate of the films was monitored using quartz crystal oscillators (QCOs). The QCOs were calibrated based on the results from RBS and XPS depth profile analyses.

Al_2O_3 (0001) substrates were ultrasonically cleaned in acetone prior to insertion into the dual-chamber UHV system through a load lock. Once in the MBE chamber, the substrates were cleaned by annealing for several minutes at 650°C in the oxygen plasma operating at 200W under a chamber pressure of $\sim 2 \times 10^{-5}$ Torr of oxygen. The growth of the film was monitored using RHEED measurements which were carried with 15 kV e^- beam during growth. Predetermined quantities of Ce and Sm metal flux were directed at the substrate in activated oxygen plasma. The substrate temperature, Sm and Ce deposition rates and oxygen partial pressure were systematically varied and the resulting films were characterized to establish optimum growth conditions for high quality, epitaxial films [13] with controlled chemistry.

3.2 *Ex situ* structural and chemical characterization

In addition to *in situ* RHEED, the samples were characterized using various *ex situ* surface and bulk sensitive techniques. Rutherford backscattering spectrometry (RBS) experiments were performed on SDC samples in the beam line at Environmental Molecular Sciences laboratory (EMSL) located in Pacific Northwest National Laboratory (PNNL) along random and channeling directions using 2.0MeV He⁺ ions to determine film thickness and crystal quality, respectively. The details of the accelerator facility and the end stations were described previously[20]. The backscattering spectrum was collected using a silicon surface barrier detector at a scattering angle of 150°. The SIMNRA program was used to model the experimental RBS results followed by curve fitting of the experimental data to precisely determine the film thickness and composition. It should be noted that small difference in the atomic numbers of Sm and Ce makes it difficult to resolve them in the RBS spectra.

X-ray photoelectron spectroscopy (XPS) measurements were performed using a Physical Electronics Quantum 2000 Scanning ESCA Microprobe. This system consists of a focused monochromatic Al K α X-ray (1486.7eV) source and a hemispherical section analyzer. The X-ray beam was incident normal to the sample and the emitted photoelectrons were collected at an emission angle of 45° relative to the normal. Wide scan data were collected using pass energy of 117.4eV. High resolution scans were obtained using pass energy of 46.95eV. The XPS spectra were referenced to an energy scale with binding energies for Cu 2p_{3/2} at 932.67±0.05eV and Au 4f at 84.0±0.05eV. Low energy electrons at ~1eV, 21μA and low energy Ar⁺ ions were used to minimize the charging. The depth profile data were collected by sample sputtering using 2kV Ar⁺ ions rastered over a 2mm × 2mm area of

the specimen. The sputter rate for these ion gun conditions was calibrated at 4.4nm/min for a known SiO₂/Si as a reference material.

X-ray diffraction (XRD) measurements were performed using both high resolution and high flux Philips X'pert MRD and MPD diffractometers operating at 45 kV and 40mA with fixed Cu anodes. The analyses of diffraction data were carried out using JADE 6.0 from Materials Data Inc. Glancing-incidence XRD, symmetric 2Theta-Omega scans and x-ray reflectivity (XRR) measurements were used to study the film quality (mono-crystallinity, crystallite size, possible minor phases etc.), crystal orientation and to verify the film thickness measured by the XPS depth profile and RBS, respectively. Experimental observations are discussed in detail in the later portion of the manuscript.

3.3 Experimental test bed for electrical measurements

Schematic of the experimental test bed for the measurement of the current/resistance of the sample as a function of oxygen pressure and operating temperature is presented in Figure 2(a). The experimental test bed was built and customized for testing the oxygen sensing materials within the EMSL at PNNL. The experimental test bed consists of a six inch four-way cross stainless steel chamber, attached with a turbo pumping system and a leak valve to control the oxygen partial pressure in the chamber and ion gauge for pressure measurements. The other ports were used to connect thermocouple, electrical feedthroughs for sample temperature and heater current measurements. The sample was mounted on the top plate of the two-inch heater using inconel (oxidation resistant) clips and the temperature was measured using a thermocouple connected to the back side of this top plate holding the sample. Two electrical leads were mounted on the opposite corners of the sample using silver paste (both electrically and thermally conductive) for the resistance measurements. The signal cables are directly

connected to the computer through an analog to digital converter for automatic data collection. The heater power is manually controlled to obtain desired temperatures during the experiments.

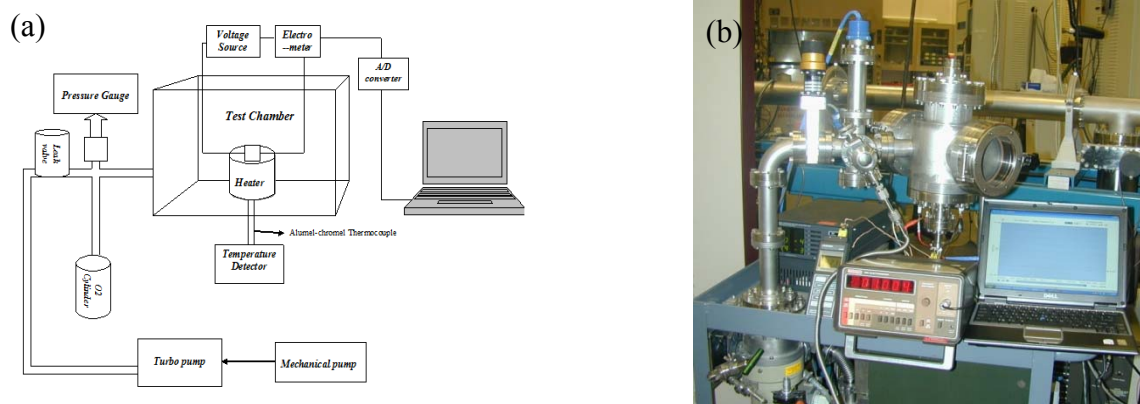


Figure2: (a) Schematic representation of the experimental test bed (b) Experimental test bed constructed at EMSL for testing the samaria doped ceria thin films.

3.4 Electrical characterization

The chamber was first pumped down to 10^{-4} Torr using a mechanical and a turbo pump connected to the chamber. Once the system reached the base pressure the valve connected to turbo pump was closed and the oxygen was introduced through a leak valve to fill the chamber with oxygen. Keeping the pressure constant at 1, 10 and 100 Torr, the operating temperature range was changed from room temperature to 973K with an interval of 25K. At each temperature the sample was maintained at the constant temperature for about 15 minutes for temperature and resistance stabilization. Once the temperature was stabilized the current through the film was measured and this measurement was repeated for each temperature. In addition, the change in current was studied under the vacuum conditions ($\sim 10^{-3}$ Torr) for the purpose of comparison.

4. Results and Discussion

4.1 Active sensing area (SDC film) characterization

The RHEED pattern from the blank sapphire substrate after plasma cleaning is shown in Figure 3(a). This corresponds to a high quality $\text{Al}_2\text{O}_3(0001)$ surface which is essential for epitaxial growth of thin films[19]. As the samaria doped ceria (SDC) film is deposited on the substrate, the RHEED streaks from the clean sapphire surface changed into streaks associated with the ceria (111) as shown in fig 3(b) indicating a well oriented two dimensional growth. The streaks persisted till the end of the film growth indicating that the film followed the two dimensional growth throughout the deposition.

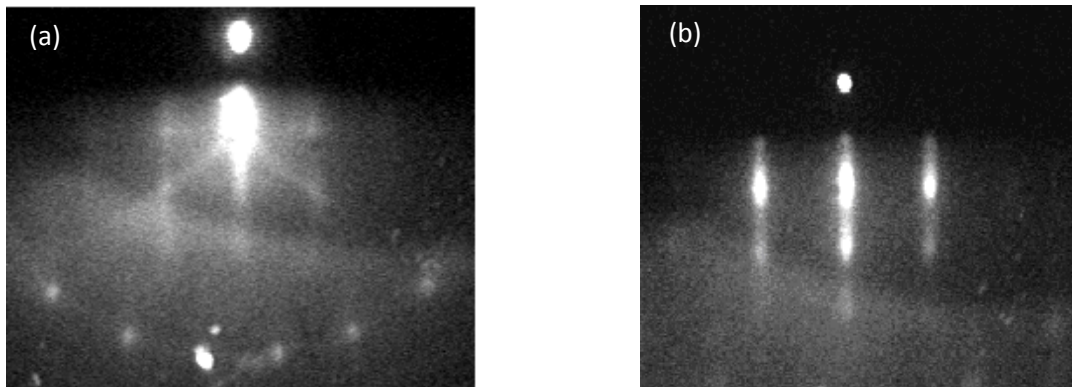


Figure 3: The RHEED patterns of (a) sapphire (0001) substrate after plasma cleaning and before deposition (b) at the end (100 min) of SDC deposition resulting in the film thickness of 110nm. The primary beam energy was 15keV.

A typical high-resolution 2θ - ω scan for the as grown SDC film is presented in Figure 4. The graph clearly demonstrates (006), (009) and (0, 0, 12) reflections from the substrate and (111), (222) and (333) reflections from the ceria film. Presence of only (111), (222) and (333) reflections of ceria clearly indicates that the films are highly oriented in (111) direction

parallel to the substrate basal plane. Any polycrystalline or secondary phases in the film, if existing, are not detectable. This result was also confirmed by high-resolution and GIXRD measurements (data not shown). The film structure is consistent with the fluorite lattice (PDF# - 034 – 0394). Deviation from the epitaxial nature has been observed for films with high dopant concentrations.

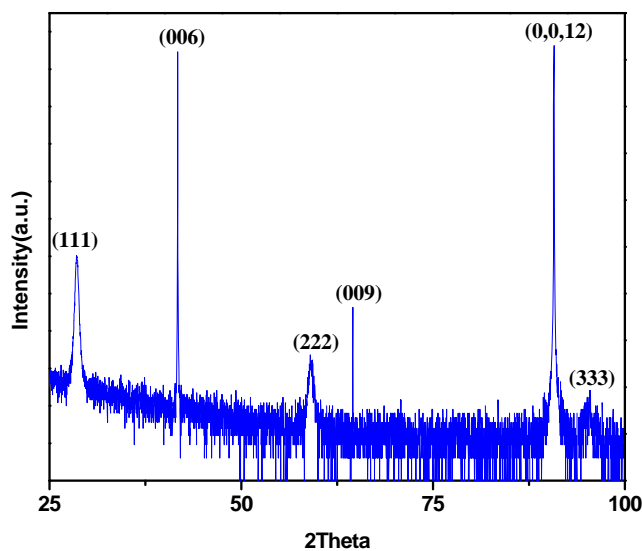
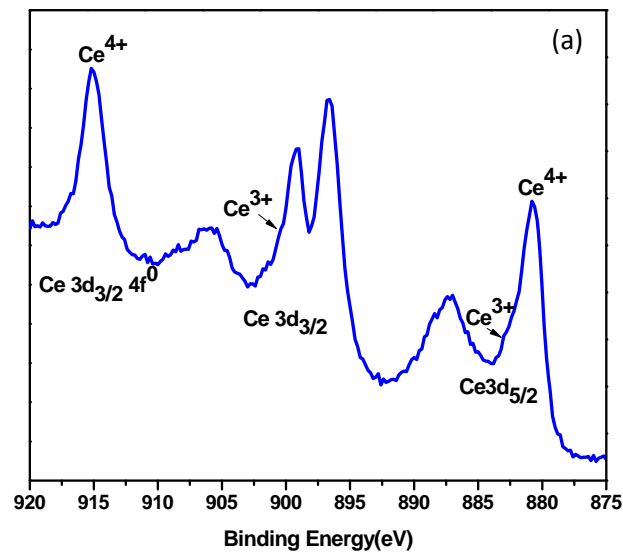


Figure 4: Representative XRD of the samaria doped ceria film on Al_2O_3 . (111), (222), (333) are reflections from the ceria film and (006), (009) and (0,0,12) are reflections from the sapphire substrate

XPS was done to determine the chemical composition, oxidation state of the elements and their distribution in the SDC films. XPS wide scan data (not shown here) have been used to quantify the amount of Sm in the films. The high resolution XPS scans of $\text{Ce}3d$ and $\text{Sm}3d$ core levels collected from a mildly sputtered surface (to remove adsorbed hydrocarbons and other surface contaminants) are shown in the figure 5(a) and 5(b), respectively. The $\text{Ce}3d$

spectrum exhibits complicated features, which are consistent with the results in the literature [[21, 22]]. Except for a small amount of Ce^{3+} signal, as a result of the sputtering, the films are found to be completely oxidized with Ce in the +4 oxidation states and Sm in +3 oxidation states. Thus, in order to maintain the electrical neutrality and structural stability, every two Sm^{3+} ions result in one doubly positive oxygen vacancy. This increase in the oxygen deficient sites can lead to an increase in the oxygen ionic conductivity of the film. No significant changes have been observed in the chemistry of the films before and after the electrical measurements.



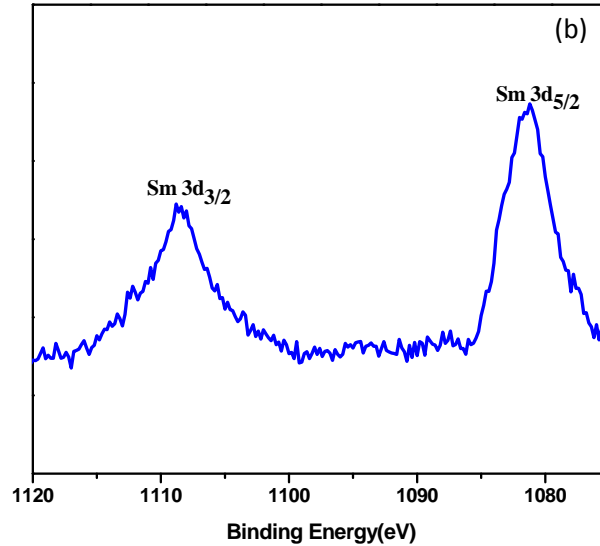


Figure 5: High resolution scan of (a) Ce3d and (b) Sm 3d region confirming the Sm doping in SDC films. Ce and Sm are found in +4 and +3 oxidation states, respectively.

The XPS depth profile of the doped ceria film on the sapphire substrate is presented in figure 6(a). The Ce and Sm profiles clearly indicate uniform elemental distribution. The interface appears to be very sharp within the experimental uncertainties. Aluminum profile clearly shows that there is no major diffusion of Al in to the film or across the film/substrate interface. Thickness of the films was found to be about 110nm for all the samples. The Sm concentration was found to be consistent with the predetermined values from QCOs.

RBS in random and channeling directions was carried out on various samples to verify the crystal quality, interface characteristics and film thickness. The results are shown in Figure 6(b), where arrows are used to indicate the channel numbers for elements Ce, Sm, Al and O. Since the backscattering signals from Sm and Ce overlap, it is difficult to determine the exact Sm concentration in the film based on the RBS data. Ion-channeling experiments (not shown)

confirmed the high quality of the crystal films. The RBS spectrum was simulated using SIMNRA and the concentration of Sm observed in XPS depth profile was used to obtain a fit. Based on the simulation, thickness of the films was determined to be ~110 nm which is consistent with the XPS depth profile data. In addition, this thickness was also confirmed by XRR measurements and model simulation using software BEDE (data not shown). RBS results further clearly demonstrate that there is no inter-diffusion of elements at the film/substrate interface.

In addition to the as-grown films, RBS measurements were carried out on some of the films after the electrical characterization to investigate quality of the films and their interfaces. Identical results (not shown) to those presented in Figure. 6(b) were found, which clearly indicate that there were no significant changes in the film properties during the resistance measurements. XRD analysis was also performed before and after the ionic conductivity measurements. It was discovered that the crystal quality of the film did not change, deteriorate after the thermal annealing at 973 K. This observation is vital because repeated use of the material as an oxygen sensor at high temperatures is strongly desired.

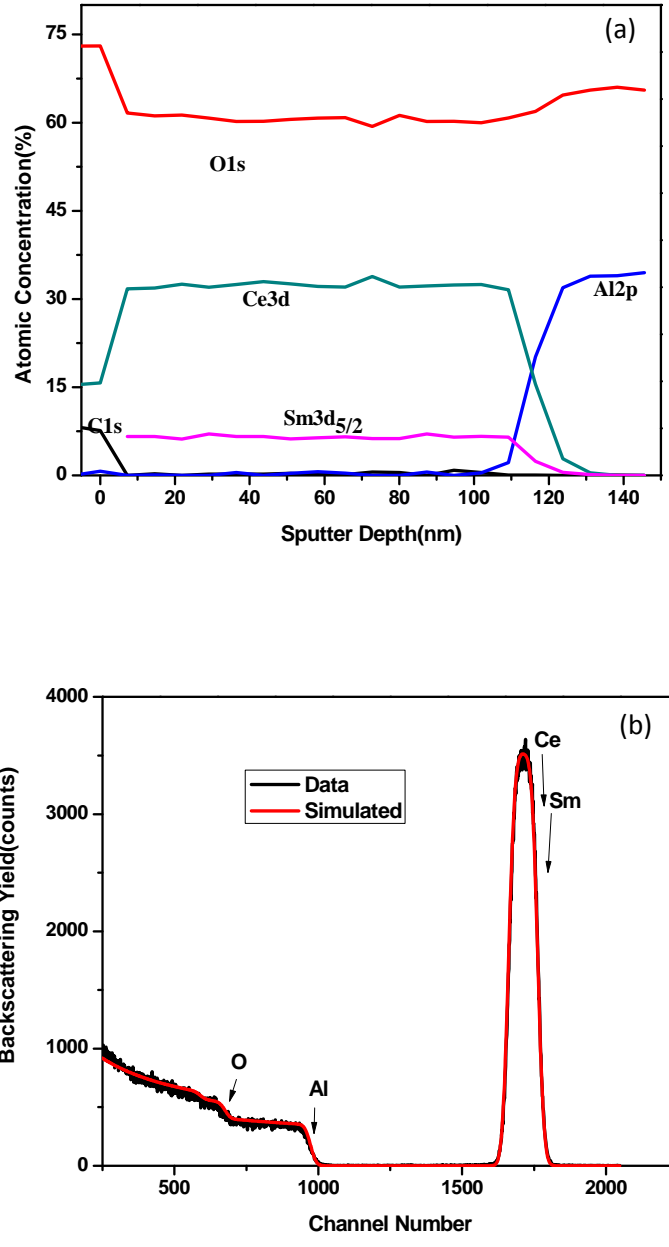


Figure 6: (a) XPS depth profile of SDC thin films on sapphire substrate confirming a uniform concentration of Sm throughout the depth, (b) Random RBS spectrum along with SIMNRA simulated results for highly oriented samria doped ceria films on sapphire (0001). The

incident energy of He^+ beam was 2.04 MeV and the scattering angle was 150° . The thickness of the film was found to be 110 nm and there was no major diffusion in the film.

4.2 Electrical characteristics of the sensing material and the implications

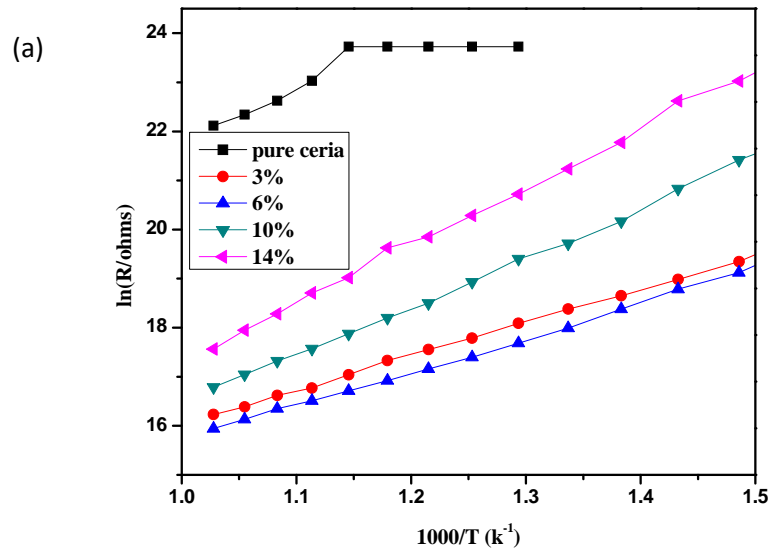
The resistance of all the samples was obtained by measuring the current using the two-probe method under the varying oxygen pressure from 10^{-3} to 100 Torr and the varying operating temperature (room temperature to 973K). Figure 7(a) shows the temperature dependence of the resistance of the SDC thin films with different Sm concentration (0-14 atom %) at 10 Torr of oxygen. The resistance fluctuation was statistically insignificant hence the error bar is omitted in the figure. The resistance of all the samples at the room temperature is infinite and remains in the range of higher $\text{G}\Omega$ until 673K, above which it started decreasing sharply. The resistance of all the samples (pure and samaria doped ceria) from 673K-973K is presented in Table 1. Pure ceria showed higher order of resistance throughout the operating temperature. However, with the Sm doping the resistance for oxygen ion conduction decreased sharply because of the increase in the oxygen deficient sites and hence more frequent hopping from one site to the other. Sm doping of 6 atom% resulted in the smallest electrical resistance. Further increase in the dopant concentration resulted in higher resistance compared to the 6 atom % film, probably due to the loss of epitaxial nature and the structural disorders in the films as reported by Yu et al [23].

In order to further investigate the sensitivity of the film to oxygen, the oxygen partial pressure was varied and the influence on the overall current (resistance) was studied. Figure 7(b) depicts the effect of the oxygen pressure on the current across the SDC film with 10 atom% of Sm doping. The films showed very small current (~ 20 nA) under the vacuum

conditions at 973 K. Although this measurement was done under vacuum conditions with the background pressure of approximately 1×10^{-3} Torr, the measured current could be attributed to the presence of residual oxygen. The current increased linearly with the increase of the oxygen partial pressure, which indicates that more oxygen ions participated in the diffusion process. This response is valid for all the SDC films in this study.

Table1: Change in the resistance of the pure and samaria doped ceria films at 673K and 973K. The oxygen partial pressure was kept at 10 Torr for these measurements.

Sample	Resistance (Ω) @673K	Resistance (Ω) @973K
Pure ceria	Infinite	3.5×10^9
3% SDC	2.5×10^8	1.11×10^7
6% SDC	2.01×10^8	8.38×10^6
10% SDC	2×10^9	1.95×10^7
14% SDC	1×10^{10}	4.2×10^7



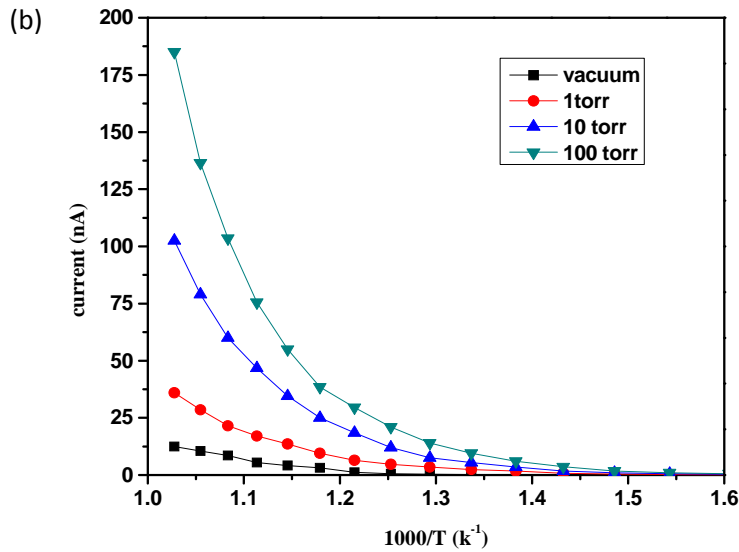


Figure7: (a) Temperature dependence of the resistance of pure and samaria doped ceria thin films at 10 Torr. 6% Sm doped ceria sample shows the smallest resistance at all the allied temperatures. (b) Pressure and temperature dependence of current for the 10 at.% Sm doped ceria thin film. Current increases with the increase of oxygen pressure.

The decrease of the resistance with the Sm doping up to a level of about 6 atom% is attributed to more available oxygen vacancies in the crystal structure, which lead to faster oxygen diffusion through hopping process at the operating temperatures. Pure ceria has very high resistance both at room temperature and at elevated temperatures. Doping ceria with Sm increases the oxygen deficient sites and hence oxygen ion conduction of the film. The oxygen vacancies for the 6 atom% SDC film will be around 1.8×10^{22} /mole. These oxygen vacancies are aligned because of the epitaxial nature of the films which assists a linear diffusion of the oxygen ions in the film and hence the reduction in the activation energy with the increase in the Sm concentration. The increase in the activation energy after 6atom% can be due to the increase in the structural defects with the increase in the dopant concentration

leading to the decrease in the oxygen diffusion. The current determined as a function of Sm concentration at 100 Torr of oxygen pressure and at different temperatures are shown in figure 8. As explained above, the current increases with the increase of the Sm concentration and peaks around 6 atom% and decreases with higher Sm concentrations. Moreover, the increase in temperature enhances the diffusion of oxygen ions and hence the overall resistance decreases with the increase of temperature.

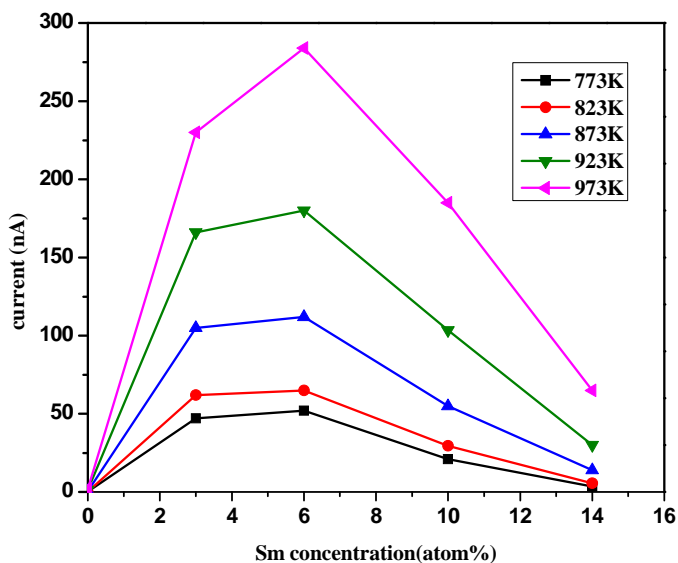


Figure 8: Current through the Sm doped ceria films as a function of Sm concentration for temperatures ranging from 773 to 973 K. The 6 atom% Sm doped sample shows the highest current over the temperature range.

During the conduction through the hopping process oxygen ions need to overcome an energy barrier which is the activation energy for this process. Typically lower activation energies corresponds to lower barrier for the oxygen transport throughout the crystal which will facilitate higher ionic conductivity at lower temperatures. Pure ceria has negligible ionic

conductivity but the ceria doped with the lower valence cations contains intrinsic oxygen vacancies which improves the ionic conductivity and overall reduction in the activation energy. We determined the activation energy from the slope of the lines for $\ln(R)$ vs. $1000/T$ in Figure 7(a) using the Arrhenius equation, where R is the resistance of the sensing material and T is the temperature. The activation energy was determined to be in the range of 0.6-0.9eV for all the doped samples with various Sm concentrations. 3% and 6% Sm doped films showed the lowest activation energy of 0.6eV lower than values reported for the hafnia doped ceria thin films [5] and 14% doped sample has the maximum activation energy of 0.9eV. These values are independent of oxygen pressure in the temperature range. It is therefore concluded that the optimum doping concentration of Sm in CeO_2 is about 6 atom% for oxygen sensor applications.

While finalizing this manuscript, we have come across a publication by De Souza et al, [24]. Authors have systematically shown that the use of “thin film electrolytes” can improve the conductivity but just the use of nanocrystalline materials may not be of a significant advantage. Another interesting observation, that the presence dissolved water in the form of protons and the strain as the origins of enhanced conductivity as opposed to the grain boundaries and complex space charge effects. Our two probe conductivity studies reported in this manuscript, have shown significantly low resistance and low activation energy for the conductivity in the thin films. Hence, we propose that the use of high quality thin films as opposed the thick polycrystalline samples reported in the literature may improve the performance of the planar oxygen sensing devices. Based on the fact that the sensor response is highly dependent on the surface conductivity as a result of the interaction with the oxygen from the sensing environments, use of films with nanometer thickness on an insulating

surface imply that the entire “electrolyte” is effectively used for the sensing purpose. Use of quick and cheaper deposition techniques such as sputtering on substrates with interdigitated electrodes are subject of future investigations.

5.Summary

Epitaxial Sm doped ceria films have been synthesized using oxygen-plasma-assisted MBE on sapphire (0001) substrate and characterized by XPS, XRD and RBS. Ce and Sm in the films are fully oxidized to Ce^{4+} and Sm^{3+} , respectively. The films showed the uniform thickness of about 110nm as confirmed by XPS depth profile, RBS and XRR. The doped cubic CeO_2 films have demonstrated a preferred (111) orientation. The doped samples showed higher conductivity compared to the pure ceria sample at high temperatures with 6atom% as the optimum dopant concentration. The reduction in the resistance for the 6atom% sample is from $2 \times 10^8 \Omega$ at 673K to $9 \times 10^6 \Omega$ at 973K. The activation energies determined from the films demonstrate that the oxygen diffusion process is more complicated in the films with higher dopant in comparison to the film with 6atom% Sm. We propose that the use of high quality thin film electrolytes may enhance the performance of planar oxygen sensors.

Acknowledgments

The work described in this paper was conducted in the Environmental Molecular Sciences Laboratory (EMSL) at Pacific Northwest National Laboratory (PNNL). PNNL is operated by Battelle for the US Department of Energy. EMSL is a national scientific user facility for DOE-BER. SP and SG would also like to thank ONAMI (Oregon Nanoscience and Micro technologies Institute) for the financial support.

References

1. Izu, N., et al., *Development of resistive oxygen sensors based on cerium oxide thick film*. Journal of Electroceramics, 2004. **13**(1-3): p. 703-706.
2. Ramamoorthy, R., P.K. Dutta, and S.A. Akbar, *Oxygen sensors: Materials, methods, designs and applications*. Journal of Materials Science, 2003. **38**: p. 4271-4282.
3. Beie, H.J. and A. Gnörich, *Oxygen gas sensors based on CeO₂ thick and thin films*. Sensors and Actuators B: Chemical, 1991. **4**(3-4): p. 393-399.
4. Gerblinger, J., et al., *High temperature oxygen sensor based on sputtered cerium oxide*. Sensors and Actuators B: Chemical, 1995. **26**(1-3): p. 93-96.
5. Izu, N., et al., *The effect of hafnia doping on the resistance of ceria for use in resistive oxygen sensors*. Sensors and Actuators B: Chemical, 2007. **123**(1): p. 407-412.
6. Izu, N., et al., *The effects of the particle size and crystallite size on the response time for resistive oxygen gas sensor using cerium oxide thick film*. Sensors and Actuators B: Chemical, 2003. **94**(2): p. 222-227.
7. Izu, N., et al., *Resistive oxygen gas sensors based on Ce_{1-x}Zr_xO₂ nano powder prepared using new precipitation method*. Sensors and Actuators B: Chemical, 2005. **108**(1-2): p. 238-243.
8. Izu, N., et al., *Response properties of resistive oxygen sensors using Ce_{1-x}Zr_xO₂ ($x = 0.05, 0.10$) thick films in propane combustion gas*. Sensors and Actuators B: Chemical, 2008. **130**(1): p. 105-109.
9. Izu, N., et al., *Kinetic behavior of resistive oxygen sensor using cerium oxide*. Sensors and Actuators B: Chemical, 2004. **100**(3): p. 411-416.

10. Andersson, D.A., et al., *Optimization of ionic conductivity in doped ceria*. Proceedings of the National Academy of Sciences of the United States of America, 2006. **103**(10): p. 3518-3521.
11. Jasinski, P., T. Suzuki, and H.U. Anderson, *Nanocrystalline undoped ceria oxygen sensor*. Sensors and Actuators B: Chemical, 2003. **95**(1-3): p. 73-77.
12. Koch, K.T. and L.V. Saraf, *Synthesis and Characterization of Pure and Doped Ceria Films by Sol-gel and Sputtering*, in *Journal: Journal of Undergraduate Research; Journal Volume: 4; Other Information: PBD: 1 Dec 2004*. 2004: United States. p. Size: page(s) 84-90.
13. Yu, Z.Q., et al., *Growth and structure of epitaxial Ce_{0.8}Sm_{0.2}O_{1.9} by oxygen-plasma-assisted molecular beam epitaxy*. Journal of Crystal Growth, 2008. **310**(10): p. 2450-2456.
14. Dae-Joon Kim, *Lattice Parameters, Ionic Conductivities, and Solubility Limits in Fluorite-Structure MO₂ Oxide [M = Hf⁴⁺, Zr⁴⁺, Ce⁴⁺, Th⁴⁺, U⁴⁺]* Solid Solutions. Journal of the American Ceramic Society, 1989. **72**(8): p. 1415-1421.
15. Kilner, J.A., *Fast anion transport in solids*. Solid State Ionics, 1983. **8**(3): p. 201-207.
16. Kilner, J.A. and R.J. Brook, *A study of oxygen ion conductivity in doped non-stoichiometric oxides*. Solid State Ionics, 1982. **6**(3): p. 237-252.
17. Fernando M. B. Marques, G.P.W., *Electrical Properties of Ceria-Doped Yttria*. 1991. p. 598-605.
18. Xu, Y. and X. Zhou, *Oxygen sensors based on semiconducting metal oxides: an overview*. Sensors and Actuators B: Chemical, 2000. **65**(1-3): p. 2-4.

19. Chambers, S.A., T.T. Tran, and T.A. Hileman, *Molecular beam homoepitaxial growth of MgO(001)*. J. Mater. Res., 1994. **9**(11): p. 2944-2952
20. Thevuthasan, S., et al., *The ion beam materials analysis laboratory at the environmental molecular sciences laboratory*. Nuclear Instruments and Methods in Physics Research Section A: Accelerators, Spectrometers, Detectors and Associated Equipment, 1999. **420**: p. 81-89.
21. M. A. Henderson, et al., *Redox Properties of Water on the Oxidized and Reduced Surfaces of CeO₂ (111)*. Surface Science 2003. **526**((1-2)): p. 1-18.
22. Kim, Y.J., et al., *Growth and structure of epitaxial Ce_{1-x}Zr_xO₂ thin films on yttria-stabilized zirconia (111)*. Journal of Electron Spectroscopy and Related Phenomena, 2002. **126**(1-3): p. 177-190.
23. Yu, Z.Q., et al., *Conductivity of oriented samaria-doped ceria thin films grown by oxygen-plasma-assisted molecular beam epitaxy*. Electrochemical and Solid State Letters, 2008. **11**(5): p. B76-B78.
24. De Souza, R.A., et al., *Oxygen diffusion in nanocrystalline yttria-stabilized zirconia: the effect of grain boundaries*. Physical Chemistry Chemical Physics, 2008. **10**(15): p. 2067-2072.

**Computational Studies:
Materials for Hydrogen Storage,
Molecular Electronegativities,
Catalytic Properties of Surfaces of WO₃ and ReO₃**

Maciej Gutowski¹, Sotiris Xantheas², Gregory Schenter², Donghai Mei², Donald Cammaioni², Jun Li³

¹ *Chemistry-School of Engineering and Physical Sciences, Heriot-Watt University, Edinburgh, EH14 4AS, United Kingdom*

² *Chemical and Materials Sciences Division, Pacific Northwest National Laboratory, Richland, Washington 99352, U. S. A.*

³ *W. R. Wiley Environmental Molecular Sciences Laboratory, Pacific Northwest National Laboratory, Richland, WA 99352, USA*

During my summer visit at PNNL my work was focused on three topics:

1. Computational studies of materials for hydrogen storage, with the computational work being done primarily by two HWU students, Michael Edie and Alexander Abramov.
2. Development of a new chemical concept of molecular electronegativities, with the computational work done primarily by a HWU student, Alexander Whiteside.
3. Catalytic properties of surfaces of WO₃ and ReO₃, and their heterojunctions, with the computational work done primarily by a HWU student, Sanliang Ling.

Section 1. Computational studies of materials for hydrogen storage

The work was focused on the BN-type materials,¹ in particular ammonia borane (AB), NH₃BH₃, ammonium borohydride (NH₄BH₄), diammoniate of diborane (DADB), (NH₃BH₂NH₃)(BH₄), H-(NH₂BH₂)_n-H oligomers, and substituted molecular compounds based on perhydroborazine, N₃B₃H₁₂.

Calculations were performed on intermolecular interactions in the AB-AB and AB-H₂ complexes. The basis set saturation effects and methodological convergence were explored. In addition to supermolecular MP2, CCSD(T) and DFT calculations the interaction energies were determined using the symmetry-adapted perturbation theory. The results will be used by the PNNL staffs to develop accurate force fields and semiempirical electronic structure methods, which are required in large-scale simulations of hydrogen storage materials based on BN-type compounds.

Our computational studies addressed the problem of crystal structures of ammonium borohydride and diammoniate of diborane. These are important members of the BN-type

family of hydrogen-rich compounds. Even though the materials were synthesized half a century ago, their crystalline structure has not yet been determined.

In the case of ammonium borohydride two structures were considered: the zinc blende (ZB) and rock salt (RS). The ZB structure proved to be the most stable in terms of electronic energies determined at the density functional level of theory. This is the first approximation to the total thermodynamic stability that neglects the effect of zero-point vibrations and thermal contributions to enthalpy and entropy. The RS structure, on the other hand, was suggested by the recent XRD results obtained by our experimental colleagues from PNNL. We have spent much effort on determination of zero-point vibrational energies and thermal contributions to the thermodynamic stability of both phases. In addition, we studied reaction pathways for the ZB \leftrightarrow RS conversions. The upper limit of the energy barrier of the phase transformation has been estimated to be 5 kcal/mol. The zero-point and thermal corrections to thermodynamic stability of both phases were determined using the linear response theory, the MD simulations, and the direct method at the Gamma point. The potentially critical role of anharmonicity was recognized. With the difference in stability of the ZB and RS phases being very small the problem proved to be challenging for theoretical methods and scientifically very fruitful. The problem will be continued on theoretical grounds in close collaboration with our experimental partners.

In the case of diammoniate of diborane, our initial structure was designed based on the experimentally known structure of a similar compound, $(\text{NH}_3\text{BH}_2\text{NH}_3)\text{Cl}$. The initial structure was refined in the course of geometry optimizations started from various initial geometries. Further improvements in stability were accomplished in the course of simulated annealing based on density functional theory forces and energies. In the next step we will simulate the XRD spectrum based on the current most stable structure and we will compare it with the experimental spectrum obtained by our experimental colleagues at PNNL.

The BN-type compounds have high volumetric and gravimetric densities of hydrogen but their utilization as hydrogen storage media is limited by slow kinetics and a too large exothermicity of hydrogen release. We explored whether chemical modifications of the BN-type compounds can alleviate these deficiencies. The experimental results of our colleagues from PNNL indicated that partial substitution of hydrogens with lithium atoms improve kinetics and thermodynamics of hydrogen release. We used a model molecular system, perhydroborazine $\text{N}_3\text{B}_3\text{H}_{12}$, and we explored the effect of substitution of: (i) H(N) hydrogens with lithium atoms, and (ii) some BN pairs with CC pairs. The results indicate that the presence of lithium atoms lowers the kinetic barriers for hydrogen release and suppresses the exothermicity. They also confirmed that partial carbonization of the BN-type materials makes the hydrogen release less exothermic or even slightly endothermic.

We performed computational studies of $\text{H}(\text{NH}_2\text{BH}_2)_n\text{H}$ oligomers, which are possible products from dehydrogenation of ammonia borane and ammonium borohydride. Understanding the kinetics and reaction pathways of formation of these oligomers and their further dehydrogenation is essential for developing BNH_x -based hydrogen storage materials. We have performed density functional and *ab initio* modeling on the energetics and formation of the $\text{H}(\text{NH}_2\text{BH}_2)_n\text{H}$ ($n = 1-4$) oligomers from the NH_3BH_3 monomers and on the subsequent dehydrogenation steps. Through transition state searches and evaluations of the intrinsic reaction coordinates, we have investigated the B-N bond cleavage, the reactions of the NH_3BH_3 molecule with intermediates, dihydrogen release through intra- and intermolecular hydrogen transfer, dehydrocoupling/cyclization of the oligomers, and the dimerization of NH_3BH_3 molecules. The results of our calculations indicate that the $\text{H}(\text{NH}_2\text{BH}_2)_{n+1}\text{H}$ oligomers are likely formed through reactions of the $\text{H}(\text{NH}_2\text{BH}_2)_n\text{H}$ oligomers first with BH_3 followed by reactions with NH_3 and the release of H_2 , where the BH_3 and NH_3 intermediates are formed through dissociation of NH_3BH_3 . We also found that the dimerization of the NH_3BH_3 molecules to form $\text{c}-(\text{NH}_2\text{BH}_2)_2$ is slightly exothermic, with a transition state that leads to the simultaneous release of two H_2 molecules. The dehydrogenations of the oligomers are also exothermic, typically by less than 10 kcal/(mol of H_2), with the largest exothermicity for $n=3$. The transition state search shows that the one-step direct dehydrocoupling cyclization of the oligomers is not a favored pathway because of high activation barriers. The dihydrogen bonding, in which protic (H_N) hydrogens interact with hydridic (H_B) hydrogens, plays a vital role in stabilizing different structures of the reactants, transition states, and products. The dihydrogen interaction within the $-\text{BH}_2(\square^2-\text{H}_2)$ moiety accounts for both the formation mechanisms of the oligomers and for the dehydrogenation of ammonia borane.

Section 2. Molecular electronegativities – development of the concept and first results

Electronegativity is loosely defined as the ability for an atom to attract electrons from its bonding neighbours, or to retain its own. The Pauling² and Mulliken³ scales are limited to atoms, though in many chemical problems it would be handy to use descriptors of functional groups rather than of atoms. We made an effort the extent the concept of Mulliken's electronegativities to functional groups, such as NH_4 and OH and first computational results were obtained. The calculated electronegativity of NH_4 is 1.1. It is much smaller than the electronegativity of the N atom (3.0) and similar to the electronegativity of Na (0.9), which is isoelectronic with NH_4 . The result exposes the role of hydrogen atoms attached to nitrogen. Similarly, the calculated electronegativity of OH is 2.9, which is smaller than the electronegativity of O (3.5) and quite similar to the electronegativity of Br (2.8). The idea of molecular electronegativities seems to be very fruitful and we will continue working on the concept in the ongoing PhD research of Alexander Whiteside.

Section 3. Catalytic properties of surfaces of WO₃ and ReO₃

Bulk tungsten trioxide (WO₃) and rhenium trioxide (ReO₃) have very similar structures. Due to the presences of metal 5d valence band, it turns out that WO₃ is a semiconductor and ReO₃ is a conductor.⁴ This difference in electronic structure sparked our interests in differences in catalytic activity of their surfaces. Comparative studies of hydrogen adsorption in atomic and molecular forms on four similar surfaces which are either based on ReO₃ or WO₃ and are terminated by either ReO₃ or WO₃ surface layer were performed at density functional theory level. For adsorption of atomic hydrogen on these four surfaces, our results showed that hydrogen atoms adsorb on all three sites which have been studied except the W_{5C} site of pure WO₃ surface. In addition the O_{1C} site is the most energetically favorable for all four surfaces. We also found that the termination of WO₃ with a monolayer of ReO₃ could change the surface catalytic activity and support hydrogen adsorption at the metal site which is not doable for WO₃. For adsorption of hydrogen molecule on these surfaces, we found two possible surface states. One is molecular adsorption at the O_{1C} sites, which is more energetically favorable, and the other is dissociative adsorption at the O_{1C} site and at the adjacent O_{2C} site. Transition state searches were performed to identify barriers that separate these two possible surface states. Our studies indicate that changing surface catalytic activities through making interface structures could be a possible way of improving the performances of heterogeneous catalysts, and this possibility should be further explored by theoretical and experimental studies in the future.

Acknowledgements

I would like to thank Drs. Xantheas, Schenter, Mei, Cammaioni, Li, Kathmann, and Jaffe for their hospitality during my 2008 summer stay at PNNL. In addition, I would like to thank PNNL for inviting me through the Summer Research Institute program. The computations were performed using the Molecular Science Computing Facility in the William R. Wiley Environmental Molecular Sciences Laboratory, which is a US Department of Energy national scientific user facility located at PNNL in Richland, Washington.

References

- ¹ Gutowski, M.; Autrey, T. *Chemistry World* **2006**, 3, 44.
- ² Pauling, L. *J. Am. Chem. Soc.* **1932**, 54, 3570.
- ³ Mulliken, R.S. *J. Chem. Phys* **1934**, 2, 782.
- ⁴ Yakovkin I. N.; Gutowski M. *Surf. Sci.* **2007**, 601, 1481.

Investigating Ammonia Borane (NH₃BH₃) nanocomposites in mesoporous silica MCM-41

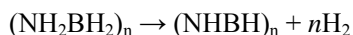
Hyunjeong Kim

Los Alamos National Laboratory

Nancy J. Hess, Wendy J. Shaw, Abhi Karkamkar, and S. Thomas Autrey

Pacific Northwest National Laboratory

Soaring demand for an alternative energy source to hydrocarbon-based fossil fuels continuously stimulates the field of science and R&D to seek for a new way to generate or store energy. A possible use of hydrogen as fuel is in the current spotlight. However, this holds one great material challenge. A material that can safely and efficiently store hydrogen is a vital part for a full realization of the hydrogen fuel economy. However, none of materials available up to date fulfills the requirements for on-board energy storage. Ammonia borane (AB), NH₃BH₃, has attained considerable attention as a potential material for hydrogen storage.¹ This inexpensive, nontoxic, stable molecular crystal is one of few materials that hold high values of both gravimetric and volumetric densities of hydrogen. In crystalline solid, highly polarized AB molecules are held together by molecular dipole-dipole interactions and the attractive interactions between the hydridic hydrogen in BH₃ and proton in NH₃ (Figure 1). The later is called dihydrogen bonding. As heated the AB solid undergoes an orthorhombic to tetragonal phase transition at 225 K and at elevated temperature hydrogen is released by a series of dehydrocoupling reactions:



The first reaction occurs below 373 K and the second occurs above 423 K. Around 12 wt% of hydrogen could be released at ~423 K from this material.²

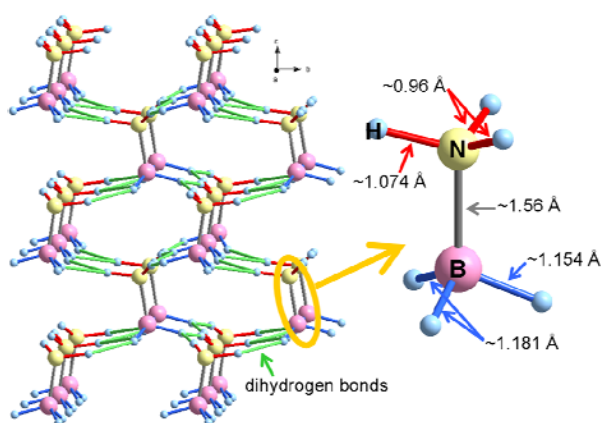


Figure 1. The average crystal structure of neat AB in the orthorhombic phase. Light blue, magenta, and yellow circles represent hydrogen, boron, and nitrogen atoms, respectively. Dihydrogen bonds are indicated by green lines to visualize the dihydrogen bonding network. In the tetragonal phase, AB molecules line up along the *c* axis and hydrogen atoms become heavily disordered.

Current challenges for fuel cell applications of AB are following. Hydrogen is released at rather high temperature after a long induction period and borazine is formed as one of by-products that affect hydrogen purity.³ Many efforts have been made to overcome these obstacles and recently one compelling approach has been reported: nanocomposition of AB by loading AB in a mesoporous silica material.³ Outcome was fascinating. Faster hydrogen desorption was observed at reduced temperature and the formation of borazine was significantly suppressed. Further study shows that dehydrogenation properties were found to be highly dependent on the level of AB loading; neat AB like nature was recovered for high AB loading samples. Even though an improvement was striking, detailed mechanism behind the enhanced properties is still unknown. This is partly because the structural determination of AB inside mesoporous silica is literally difficult. Conventional crystallographic analysis is impossible due to its lack of long-range structural order and transmission electron microscopy (TEM) also fails to locate AB due to its light composed elements compared to its host (SiO₂). Consequently, available structural information is almost none to this day. Therefore the detailed information on how supported AB resides in mesoporous channels and how the dynamics of hydrogen in AB nanocomposites different from one in neat AB is critical for understanding the improved properties and designing new materials with optimal hydrogen storage properties.

Even if the use of mesoporous silica is a popular way to synthesize nanocomposites, it is not trivial to obtain their information such as their structure. Hence to get a whole structural picture and its evolution as a function of temperature, the only way seems to be patching up segments of information from several local structural probing techniques.⁴ We have planned to conduct temperature dependent ²H NMR, ¹²⁹Xe NMR, Raman, and x-ray and neutron atomic pair distribution function experiments on AB loaded MCM-41 sample with the weight ratio of AB:MCM-41=1:2. As the first step, we collected ²H NMR quadrupolar echo spectra of ND₃BH₃ nanocomposites in MCM-41 mesoporous silica over a wide temperature range (Figure 2) in order to study the dynamics of ND₃ side of ND₃BH₃ nanocomposites. Detailed analysis is in progress.

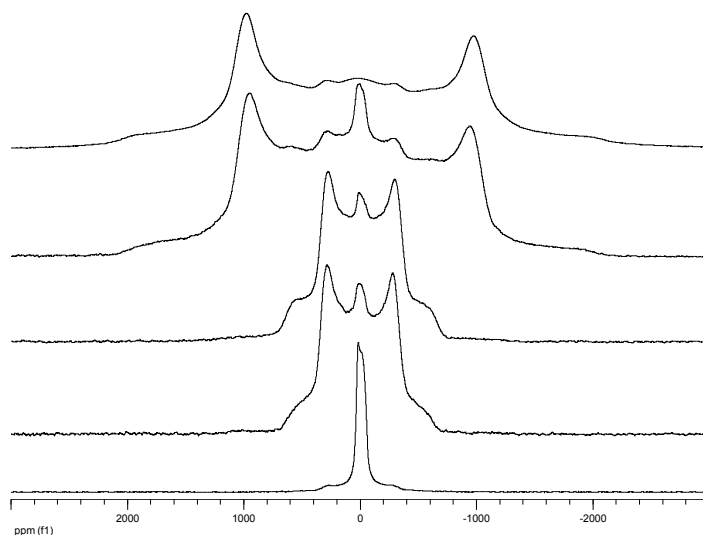


Figure 2 Selective ²H NMR quadrupolar echo spectra of ND₃BH₃ nanocomposites in MCM-41. Data obtained at 5, 29, 83, 211, 270 K (from top to bottom) are shown.

-
- ¹ M. Jacoby, *Chemical & Engineering News* **2008**, 86, 67-70.
- ² Z. Xiong *et al.*, *Nat. Mater.* **2008**, 7, 138-141.
- ³ A. Gutowska *et al.*, *Angew. Chem. Int. Ed.* **2005**, 44, 3578-3582.
- ⁴ S. J. L. Billinge and I. Levin, *Science* **2007**, 316, 561-565.

Hydrogen Adsorption on Surfaces of Pure MO₃ (M=W or Re) and their Interface Structures: A Comparative Study

Sanliang Ling,¹ Donghai Mei,² and Maciej Gutowski¹

¹ Chemistry-School of Engineering and Physical Sciences, Heriot-Watt University, Edinburgh, EH14 4AS, United Kingdom

² Chemical and Materials Sciences Division, Pacific Northwest National Laboratory, Richland, Washington 99352, U. S. A.

Bulk tungsten trioxide (WO₃) and rhenium trioxide (ReO₃) have very similar structures. Due to the presences of metal 5d valence band, it turns out that WO₃ is a semiconductor and ReO₃ is a conductor, which makes them as very promising candidates of heterogeneous catalysts. With the development of modern technology in molecular beam epitaxy, it is possible to combine these two transition metal oxides and make an interface structure between them, which could facilitate even better performance in heterogeneous catalysis. The adsorption of hydrogen in atomic and molecular forms on the (001) surfaces of WO₃, ReO₃ and two different types of interface structures have been studied in a comparative way with *ab initio* calculations at density functional theory level. It is revealed that adsorption of atomic hydrogen at all three different surface sites of four types of surface are exothermic except for the metal site of WO₃ surface. For adsorption of molecular hydrogen on these surfaces, it is found that only molecular adsorption at O_{1C} sites and dissociative adsorption at O_{1C} and O_{2C} sites are energetically favorable, while molecular adsorption at metal site and dissociative adsorption at metal site and O_{2C} site are found to be endothermic. A possible hydrogen desorption pathway from dissociative adsorption at O_{1C} and O_{2C} sites to molecular adsorption at O_{1C} site, and then to dehydration to form desorbed water molecule and surface defect at O_{1C} site is also studied for all four types of surfaces. Our results indicate the formation of surface defects would be possible for some surfaces upon the formation of molecular adsorbed hydrogen at the O_{1C} site.

Introduction

Conductive and narrow bandgap semiconductive transition metal oxides have been known many years for their positive roles in heterogeneous catalysis of various industrial applications.¹ Tungsten trioxide (WO₃) and rhenium trioxide (ReO₃) are widely used in heterogeneous catalysis both as catalysts and supports of catalysts. For example, methanol was found to be molecularly adsorbed to the Lewis acid sites of oxidized WO₃(001) surface and dissociatively adsorbed to the Brønsted base sites of reduced WO₃(001) surface.² High catalytic activities and selectivities for the oxidation of methanol were also found on supported ReO_x surfaces.³ These studies clearly show the promising applications of WO₃ and ReO₃ in heterogeneous catalysis. With the modern technology in

molecular beam epitaxy,⁴ constructing an interface between two structurally similar transition metal oxides becomes possible, and these new types of interface structure might present better performance in heterogeneous catalysis because of the formation of new band structures near Fermi level which contribute most to the catalytic activities of transition metal oxides. As a recent example of such an interface, Chambers et al. grew an epitaxial (0001) superlattices of hematite ($\alpha\text{-Fe}_2\text{O}_3$) and chromia (eskolaite, $\alpha\text{-Cr}_2\text{O}_3$) by oxygen-plasma-assisted molecular beam epitaxy (OPA-MBE) on sapphire ($\alpha\text{-Al}_2\text{O}_3$) substrates,⁵ which showed a remarkable “band-offset noncommutativity”.⁶ Similar phenomenon might also happen in the interface structures which are made with WO_3 and ReO_3 . In this study, we explore this possibility along with comparisons made between pure WO_3 and ReO_3 through hydrogen adsorption to different sites of these surfaces.

It has long been known that hydrogen could form bronze-like structures with WO_3 and ReO_3 . For WO_3 , a fraction of $0 < x < 0.5$ gaseous hydrogen could be adsorbed by bulk WO_3 to form the non-stoichiometric bronze H_xWO_3 , and Berzins et al. found that this adsorption process is even reversible with hydrogen being desorbed in the molecule form with decreasing pressure.⁷ For ReO_3 , Dickens et al. found a fraction of 1.36 at most could be adsorbed by bulk ReO_3 to form cubic bronze $\text{H}_{1.36}\text{ReO}_3$.⁸ Despite these studies, little work was found to concentrate on the hydrogen adsorption on the surfaces of WO_3 and ReO_3 rather than being diffused into the bulk structures. To the best of our knowledge, this is the first DFT investigation of hydrogen adsorption on surfaces of WO_3 and ReO_3 . To make comparisons, hydrogen adsorption on surfaces of two types of interface structures of WO_3 and ReO_3 are also studied. We hope these studies could give us some inspiration on possible roles of pure WO_3 and ReO_3 and their interface structures in selective catalysis of other molecules with industrial applications such as methanol.

This report is organized in the following way. First, we will give our computational details and surface models as well as notations used in this report in the “Computational Details” section. Then we will present our results and discussions in the “Results and Discussions” section. Finally, we will summarize our results and present our conclusions in the “Conclusions” section.

Computational Details

The periodic DFT calculations performed in this study were done with the Vienna Ab initio Simulation Package (VASP).^{9,10} A plane wave basis set with a cutoff energy of 400 eV which was recommended by Ge et al.¹¹ was used to expand the valence electronic wavefunction with valence configurations of all atoms. The Perdew-Burke-Ernzehof (PBE) functional¹² together with ultrasoft pseudopotentials¹³ which were optimized at the same level with the projector augmented wave (PAW) method^{14,15} were used to describe nuclei and core electrons. The ground-state geometries of bulk and surface slabs were obtained by minimizing the change in the total free energy to below 5×10^{-5} eV. A 4-layer surface model with vacuum slab which has approximately the same thickness was used for all surface calculations. A Gaussian type of electronic smearing with a width of 0.1 eV was used to improve convergence of electronic self-consistent field calculations. Spin-polarization was excluded except for calculations of density of states (DOS). For all

calculations, Monkhorst-Pack scheme was used to generate k-points to sample the Brillouin zone, where k-point grids of $9 \times 9 \times 9$, $3 \times 3 \times 1$ and $5 \times 5 \times 1$ were used for bulk energy calculations, surface energy calculations and surface DOS calculations, respectively.

The four surface models of pure WO_3 , ReO_3 and their interface structures which were used in the current study and their respective notations were shown in Figure 1. The notations of surface sites which will be discussed were also shown in Figure 1. As it was revealed by Yakovkin et al.,¹⁶ a polar surface slab with oxygen termination on the top and WO_2 termination in the bottom is not stable, thus a non-stoichiometric surface slab with $c(2 \times 2)\text{O}$ termination was used for all surface calculation. The adsorbate atoms as well as metal and oxygen atoms in the two top layers were relaxed in the calculation, while the two bottom layers were frozen to accelerate the convergence. The geometry optimizations were performed by using a conjugate-gradient or quasi-Newton scheme as implemented in VASP. Transition state search was carried out by using the nudged elastic band (NEB) method^{17,18} with recently implemented climbing image modification.¹⁹

Adsorption energies of hydrogen on different surface sites were calculated by the following equation:

$$E_{ad} = E_{adsorbed_slab} - E_{clean_slab} - E_{H/H_2},$$

where $E_{adsorbed_slab}$ is the total energy of the interacting system of our transition metal oxide surface slab and hydrogen (atoms or molecule), and E_{H/H_2} is the energy of gaseous hydrogen atom or molecule. In the current study, reference energies of -1.11 eV and -6.84 eV were used for gaseous hydrogen atom and molecule, respectively. A negative E_{ad} value indicates the reaction is exothermic and the adsorption is energetically favorable. Unless stated elsewhere, all energies which will be discussed are in kJ/mol.

Results and Discussions

Initial structures of bulk ReO_3 and WO_3 with experimental lattice parameters and coordinates^{20,21} were reoptimized under computational settings mentioned above. The perfect cubic structure of ReO_3 was kept after optimization, and the optimized lattice constant of ReO_3 is 3.764 Å, which is in very good agreement with the experimental value 3.748 Å. For WO_3 , it remained as a monoclinic structure with distorted oxygen positions along the axis after optimization, and the optimized lattice parameters, $a=5.252$ Å, $b=5.043$ Å, $c=7.550$ Å and $\beta=93.210^\circ$, are also in good agreement with the experimental values where $a=5.278$ Å, $b=5.156$ Å, $c=7.664$ Å and $\beta=91.762^\circ$. These lattice parameters were used to construct the surface model as shown in Figure 1. Discussions about surface relaxations and reconstructions could be found in Refs. 11 and 16. To summarize, ReO_3 -based surface slabs remained as cubic cells where oxygen atoms were kept on the axis, while oxygen atoms along z-axis of WO_3 -based surface slabs are less distorted after

optimization. Such phenomenon could be attributed to the adoption of a $c(2 \times 2)O$ surface termination where the terminal oxygen atoms drag the whole surface along the z-axis in two opposite directions which increases the order of atomic arrangements.

I. Adsorption of hydrogen atom

A total of three possible surface sites which might adsorb hydrogen atoms are studied for all four surface models. The adsorption energy of hydrogen for each site of every surface is summarized in Table 1.

From Table 1, we could find that almost all adsorption of hydrogen atoms are exothermic and thus are energetically favorable except for the hydrogen adsorption at the W_{5C} site of pure WO_3 surface which has an adsorption energy of about 41.7 kJ/mol. However, if WO_3 is supported on three layers of ReO_3 which is the case of WRRR, we can find the hydrogen adsorption at the same site could also be energetically favorable with a negative though relatively small adsorption energy of about -48.9 kJ/mol. In this way, we can conclude that indeed the ReO_3 substrate could change the electronic structure of surface WO_3 layer and such an interface structure could have remarkable effect on the catalytic activity of WO_3 as an efficient heterogeneous catalyst. From Table 1, we could also find that the oxygen sites are more energetically favorable than the metal sites as candidates of possible sites which hydrogen atoms adsorb to, and the hydrogen adsorption energies of O_{1C} sites are even higher than the O_{2C} sites by about 60~100 kJ/mol (still with the exception of pure WO_3 surface in which case the two oxygen sites have almost the same adsorption energy of about -265 kJ/mol).

The Bader charge analysis and local density of states (DOS) analysis were also performed in order to get some insights of surface relaxations and reconstructions before and after hydrogen adsorptions of these surfaces as well as components which contribute to the hydrogen adsorptions happened at specific surface sites, see Figure 2 for analysis which was performed for hydrogen adsorptions at three surface sites of pure ReO_3 . From Figure 2, we could find that the hydrogen adsorption is almost localized when hydrogen atom adsorbs to O_{1C} site of ReO_3 surface since little charge transferred to other atoms other than the O_{1C} atom. From the local DOS plotting we could find that the antibonding 2p states of O_{1C} is responsible for the hydrogen adsorption at this site. For hydrogen adsorption at O_{2C} site, it seems that it is not localized as charges from the adsorbed hydrogen atom also transferred to adjacent rhenium atoms other than the bonded O_{2C} atom. This might be resulted from the prominent surface relaxations after hydrogen adsorption at this site. The local DOS plotting of hydrogen adsorption at O_{2C} site showed that a lot of other components might contribute as the change of $O_{2C}(2p)$ states before and after hydrogen adsorption seems to be very small. For hydrogen adsorption at the Re_{5C} site, charge transfer from the Re_{5C} atom to the adsorbed hydrogen atom was observed which indicates the rhenium atom has a bigger electronegativity than the hydrogen atom here. The local DOS plotting showed that the antibonding 5d states of Re_{5C} atom should be responsible for the hydrogen adsorption at the Re_{5C} site. These analyses provide us the clear physical pictures behind the hydrogen adsorptions and could facilitate a better understanding of the mechanism of these adsorptions which will

definitely promote an even more efficient computational/experimental design of similar heterogeneous catalysts in the future.

II. Adsorption of hydrogen molecule

As molecular hydrogen is easier to access than atomic hydrogen and we already know that hydrogen atom favors these surfaces, a fundamental question would be will hydrogen molecule also adsorb on these surfaces? If yes, then how will hydrogen molecule adsorb on these surfaces? To answer these questions, we also studied adsorptions of hydrogen molecules on these four surfaces. As preliminary calculations gave positive adsorption energies for molecular adsorption of hydrogen molecule at one O_{2C} site and dissociative adsorption of hydrogen molecule at two O_{2C} sites on pure ReO_3 surface, only the following cases were considered for adsorption of hydrogen molecule on pure ReO_3 surface as well as other three surfaces: (1) dissociative adsorption at O_{1C} and O_{2C} sites, (2) dissociative adsorption at O_{2C} and Re_{5C} (or W_{5C}) sites, (3) molecular adsorption at Re_{5C} (or W_{5C}) site, and (4) molecular adsorption at O_{1C} site. Adsorption energies of hydrogen molecules at possible sites of four types of surfaces are summarized in Table 2. From Table 2 we could find that there are two possible pathways for hydrogen molecule adsorb on these four types of surfaces we studied: one is the hydrogen molecule molecularly adsorbs at the O_{1C} site (state 1), the second is the hydrogen molecule dissociatively adsorbs at the O_{1C} site and one of its adjacent O_{2C} site (state 2), and from the point of view of adsorption energies, the first pathway is more energetically favorable than the second pathway though the differences are very small for WO_3 supported surfaces. This might be attributed to the large binding energy of H-H single bond and the prominent geometry relaxation in the latter case (state 2) which could lead to smaller adsorption energies in the case of atomic hydrogen adsorption (see Table 1). From Table 2 we could also find that hydrogen molecule doesn't support molecular adsorption at the metal site of which the adsorption energy is almost zero, while for the case of dissociative adsorption at one O_{2C} site and one metal site, our calculation gave positive values for adsorption energies of four types of surface, which might be resulted from the unfavorable geometry relaxations after adsorption. However, one problem came to us as we know the strong H-H single bond might already be broken before interacting with the surfaces. In this way, though the second pathway of adsorption of hydrogen molecule is less energetically favorable than the first one, it is still possible that hydrogen molecule will adsorb to these surfaces in the second pathway in the beginning, then the hydrogen atom which adsorbs at the O_{2C} site will overcome a small transition barrier and transfer to the O_{1C} site which is more energetically favorable. To explore this possibility, nudged elastic band (NEB) calculations were performed to search the transition state (ts1-2) between the optimized geometries of the first possible adsorption pathway and the second possible adsorption pathway for surfaces of pure ReO_3 (see Figure 3 for optimized structures of state 1, state 2 and ts1-2 of pure ReO_3 surface) and pure WO_3 . As another possible process of the first adsorption pathway, dehydration of a water molecule from the surface might happen after the molecular adsorption and thus forms a defect site on the surface (state 3). This possibility is also explored for surfaces of pure ReO_3 and pure WO_3 .

These results including barriers between state 1 and state 2 as well as heats of formation between state 2 and state 3 are summarized in Figure 4. All energies of both two surfaces have been shifted to the respective reference which is the sum of energies of clean surface and gaseous hydrogen molecule (state 0). From Figure 4, we could find for adsorption of hydrogen molecule on pure ReO_3 surface, the most stable surface state is the molecular adsorption (state 1), and the barrier from molecular adsorption (state 1) to dissociative adsorption (state 2) is about 58.4 kJ/mol. This value is even smaller than the heat of formation from molecular adsorption (state 1) to dehydration of water molecule which leads to the formation of surface defect (state 3) by about 30 kJ/mol, which means under the same condition the molecular adsorption would rather transit to dissociative adsorption than be dehydrated. However, for the case of adsorption of hydrogen molecule on pure WO_3 surface, the situation is just opposite, for which the heat of formation from molecular adsorption to dehydration and formation of surface defect is smaller than the transition barrier from molecular adsorption to dissociative adsorption by about 40 kJ/mol, say formation of surface defect would be more possible under the same condition for surface of pure WO_3 . Similar studies about the transition barriers from state 1 to state 2 and heats of formation from state 1 to state 3 for the two surfaces of interface structures will be performed in the future and be compared with the above results of surfaces of pure transition metal oxides to check if there is any possible benefit of making such interface structures for potential applications in heterogeneous catalysis.

Conclusions

Comparative studies of hydrogen adsorption in atomic and molecular forms on four similar surfaces which are either based on ReO_3 or WO_3 and are terminated by either ReO_3 or WO_3 surface layer were performed at density functional theory level. For adsorption of atomic hydrogen on these four surfaces, our results showed hydrogen atoms adsorb on all three sites which have been studied of four surfaces except the W_{5C} site of pure WO_3 surface and O_{1C} site is the most energetically favorable adsorption site for all four surfaces. We also found that terminate the pure WO_3 with a surface layer of ReO_3 could change the surface catalytic activity and support hydrogen adsorption at the metal site which is not doable for surface of pure WO_3 . For adsorption of hydrogen molecule on these surfaces, we found two possible surface states which might support adsorption of hydrogen molecule on these four surfaces, one is molecular adsorption at O_{1C} site which is more energetically favorable and the other is dissociative adsorption at O_{1C} site and one of its adjacent O_{2C} site which is less energetically favorable. Transition state searches were performed to locate the transition states which separate these two possible surface states of adsorption of hydrogen molecules. Compared these results with heats of formation from molecular adsorption to dehydration of a water molecule from the adsorbed surface which leads to formation of surface defect, we conclude that for pure ReO_3 surface, one hydrogen atom moves from its adsorbate O_{1C} atom to the adjacent O_{2C} atom will be more energetically favorable than dehydration of water molecule from the surface, while for pure WO_3 surface, the latter will be energetically favorable. Our studies indicate that changing surface catalytic activities through making interface structures

could be a possible way of improving the performances of heterogeneous catalysts, and this possibility should be further explored by theoretical and experimental studies in the future.

Acknowledgements

We thank Prof. Q. Ge for helpful discussions. S. L. thanks PNNL for providing a fellowship through the Summer Research Institute program. The computations were performed using the Molecular Science Computing Facility in the William R. Wiley Environmental Molecular Sciences Laboratory, which is a US Department of Energy national scientific user facility located at PNNL in Richland, Washington.

References

1. Kung, H. H. *Transition Metal Oxides: Surface Chemistry and Catalysis*; Elsevier Science Publishers B. V.: Amsterdam, **1989**.
2. Ma, S.; Amar, F. G.; Frederick B. G. *J. Phys. Chem. A* **2003**, *107*, 1413-1423.
3. Yuan, Y.; Iwasawa, Y. *J. Phys. Chem. B* **2002**, *106*, 4441-4449.
4. Chambers, S. A. *J. Phys.: Condens. Matter* **2008**, *20*, 264004.
5. Chambers, S. A.; Liang, Y.; Gao, Y. *Phys. Rev. B* **2008**, *61*, 13223.
6. Jaffe J. E.; Dupuis M.; Gutowski M. *Phys. Rev. B* **2004**, *69*, 205106.
7. Berzins A. R.; Sermon P. A. *Nature* **1983**, *303*, 506-508.
8. Dickens P. G.; Weller, M. T. *J. Solid State Chem.* **1983**, *48*, 407-411.
9. Kresse, G.; Hafner, J. *Phys. Rev. B* **1993**, *47*, 558.
10. Kresse, G.; Furthmuller, J. *Comput. Mater. Sci.* **1996**, *6*, 15.
11. Ge, Q.; Gutowski M. Unpublished results.
12. Perdew, J. P.; Burke, K.; Ernzerhof, M. *Phys. Rev. Lett.* **1996**, *77*, 3865.
13. Vanderbilt, D. *Phys. Rev. B* **1990**, *41*, 7892.
14. Blochl, P. E. *Phys. Rev. B* **1994**, *50*, 17953.
15. Hobbs, D.; Kresse, G.; Hafner, J. *Phys. Rev. B* **2000**, *62*, 11556.
16. Yakovkin I. N.; Gutowski M. *Surf. Sci.* **2007**, *601*, 1481-1488.
17. Mills, G.; Jonsson, H.; Schenter, G. K. *Surf. Sci.* **1995**, *324*, 305-337.
18. Henkelman, G.; Jonsson, H. *J. Chem. Phys.* **2000**, *113*, 9978-9985.
19. Henkelman, G.; Uberuaga, B. P.; Jonsson, H. *J. Chem. Phys.* **2000**, *113*, 9901-9904.
20. Schirber, J. E.; Morosin, B. *Phys. Rev. Lett.* **1979**, *42*, 1485-1487.
21. Woodward, P. M.; Sleight, A. W. *J. Solid State Chem.* **1997**, *131*, 9-17.

Table 1. Adsorption energies of hydrogen atom at three different sites of four different surfaces.

surface	adsorption site	E_{ad} (kJ/mol)
RRRR	O _{1C}	-296.25
	O _{2C}	-200.06
	Re _{5C}	-141.52
WWWW	O _{1C}	-266.80
	O _{2C}	-265.09
	W _{5C}	41.69
WRRR	O _{1C}	-278.33
	O _{2C}	-211.21
	W _{5C}	-48.87
RWWW	O _{1C}	-266.82
	O _{2C}	-207.26
	Re _{5C}	-152.30

Table 2. Adsorption energies of hydrogen molecule at four different sites combinations of four different surfaces.

surface	adsorption site	E_{ad} (kJ/mol)
RRRR	$O_{1C} + O_{2C}$	-61.56
	$O_{2C} + Re_{5C}$	56.63
	$Re_{5C} + Re_{5C}$	-2.92
WWWW	$O_{1C} + O_{1C}$	-100.30
	$O_{1C} + O_{2C}$	-29.33
	$O_{2C} + W_{5C}$	147.47
	$W_{5C} + W_{5C}$	1.64
WRRR	$O_{1C} + O_{1C}$	-46.68
	$O_{1C} + O_{2C}$	-42.57
	$O_{2C} + W_{5C}$	130.42
RWWW	$W_{5C} + W_{5C}$	-0.83
	$O_{1C} + O_{1C}$	-106.19
	$O_{1C} + O_{2C}$	-50.30
	$O_{2C} + Re_{5C}$	62.84
RWWW	$Re_{5C} + Re_{5C}$	-2.70
	$O_{1C} + O_{1C}$	-58.78

Figure 1. Sideview of optimized clean (001) surface structures of (a) RRRR: pure ReO_3 , (b) WWWW: pure WO_3 , (c) WRRR: one layer of WO_3 on three layers of cubic ReO_3 , and (d) RWWW, one layer of ReO_3 on three layers of monoclinic WO_3 . Relevant surface sites are also labeled. Color code: White – Hydrogen; Red – Oxygen; Blue – Re; Green – W. Large red spheres represent surface O_{1C} atoms.

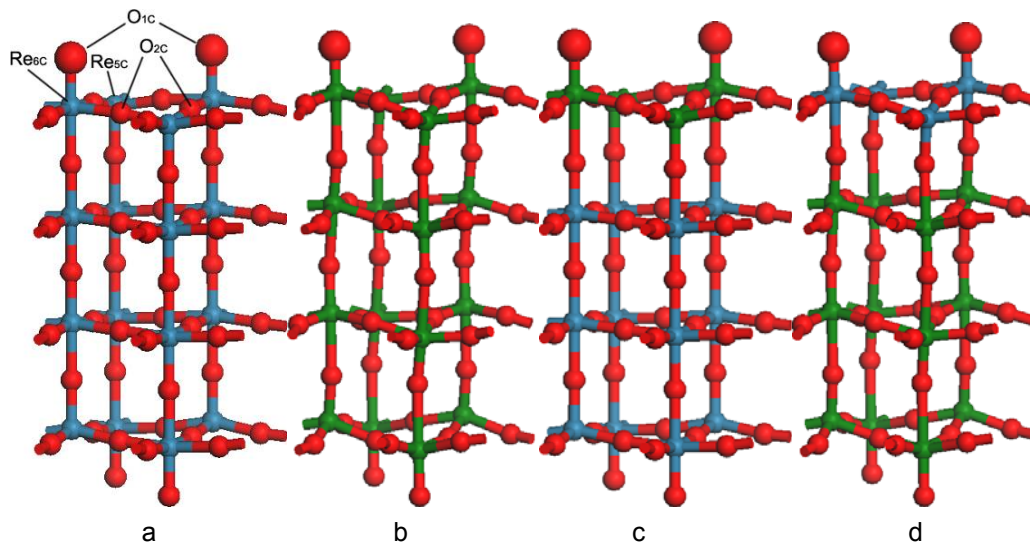


Figure 2. Comparative Bader charge analysis (left) and local DOS analysis (right) of hydrogen adsorption at three different surface sites of pure ReO_3 before and after adsorptions. For Bader charge analysis, charges before and after adsorptions are labeled with numbers in black color (below) and blue color (above), respectively. All local DOS were plotted by aligning at the Fermi level of the corresponding system.

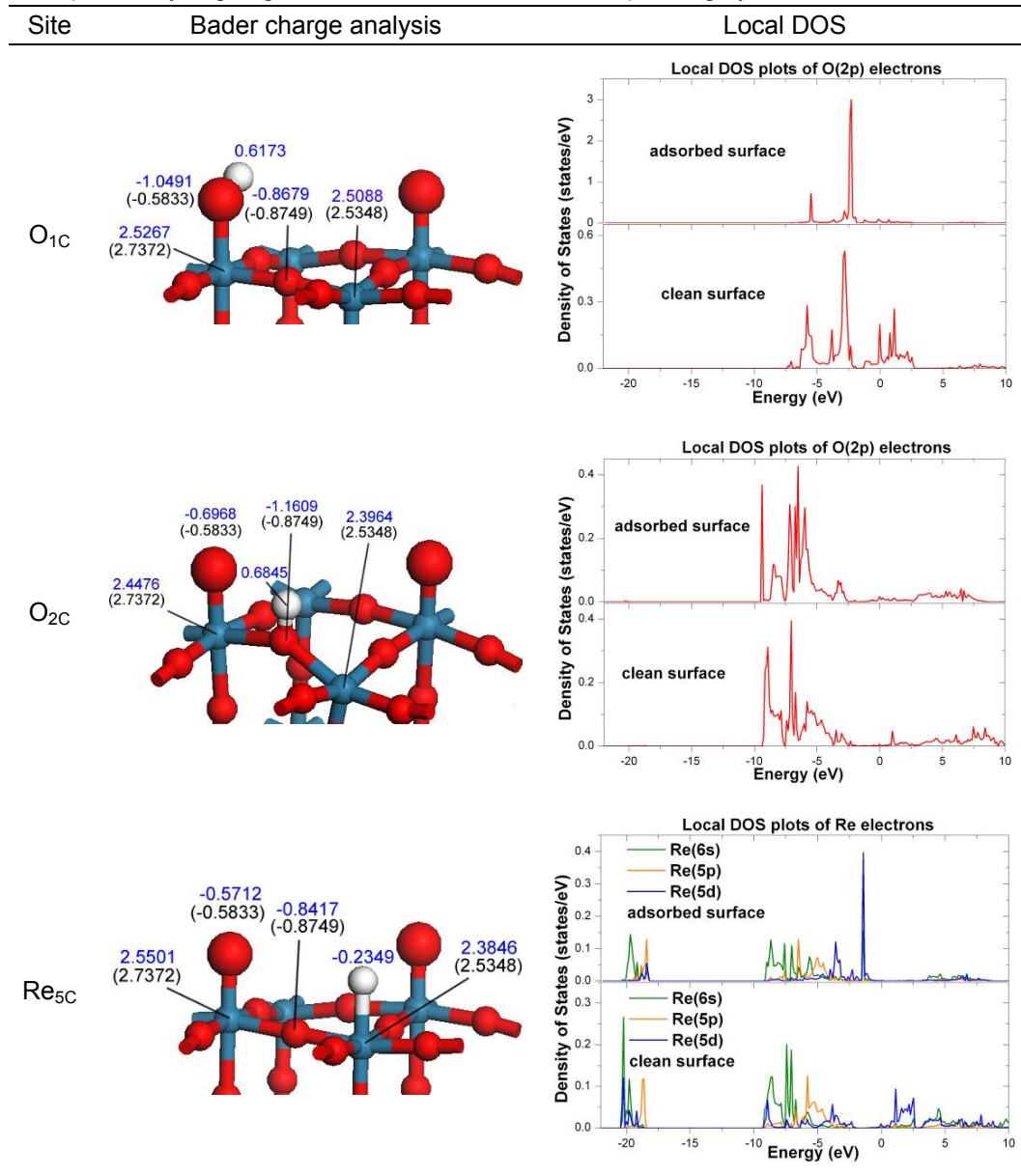


Figure 3. Sideview of optimized geometries of surface states of adsorption of hydrogen molecule on pure ReO_3 surface. Color code is the same with Figure 1. For indications of different states, see “Results and Discussions” section.

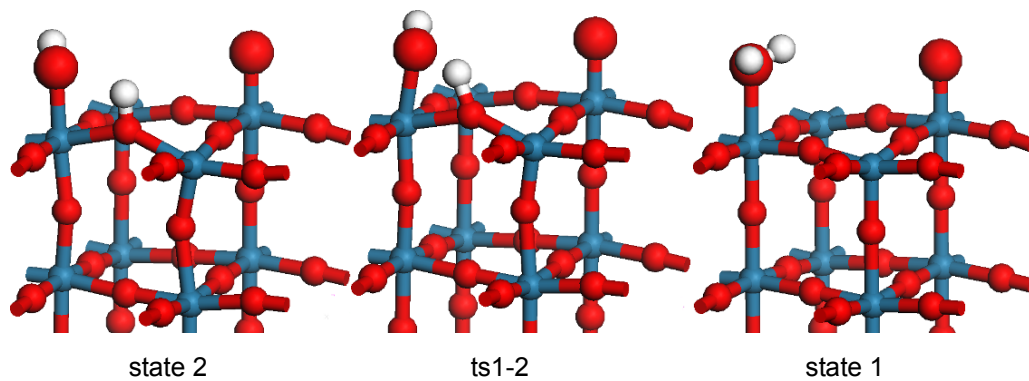
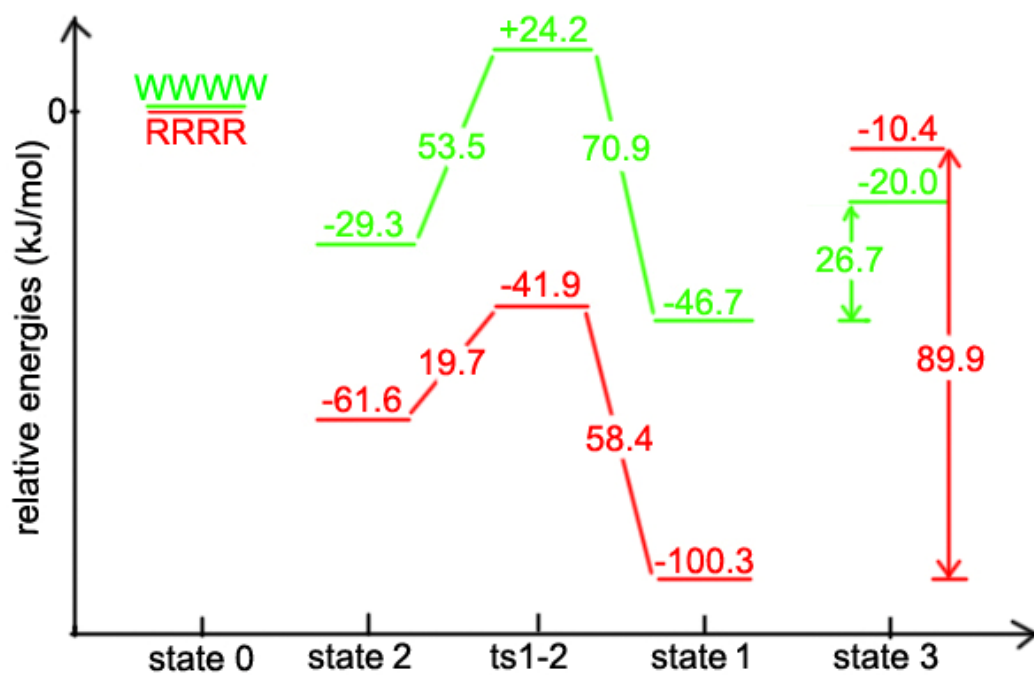


Figure 4. Possible reaction pathways of adsorptions of hydrogen molecule on surfaces of pure ReO_3 (in red) and pure WO_3 (in green). For indications of different states, see “Results and Discussions” section. All energies are in kJ/mol.



Pacific Northwest National Labs Summer Report
Dawei Liu
Mentor Dr. Chongmin Wang and Dr. Jun Liu

This summer, my stay in Pacific Northwest National Labs was focused on three aspects:

1. The learning of Transmission Electron Microscope
2. Fabrication of TiO₂ one dimensional nanostructures which could be used as anode for lithium ion intercalation
3. Study of electrolyte used for lithium ion batteries

1. Transmission Electron Microscope

Under the guidance of Dr. Chongmin Wang, I have mastered the operation of TEM with which nanostructures of various materials could be photographed. Below figures are taken of various nanostructures of different materials:

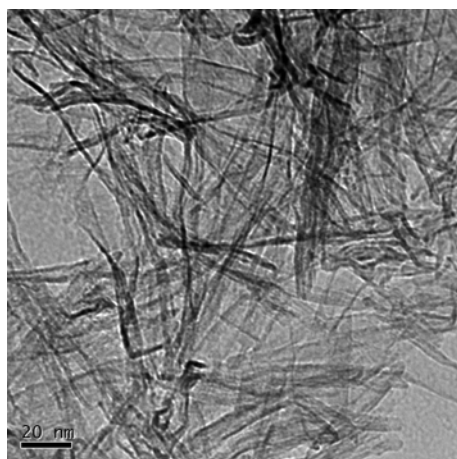


Figure 1. TiO₂ nanotubes

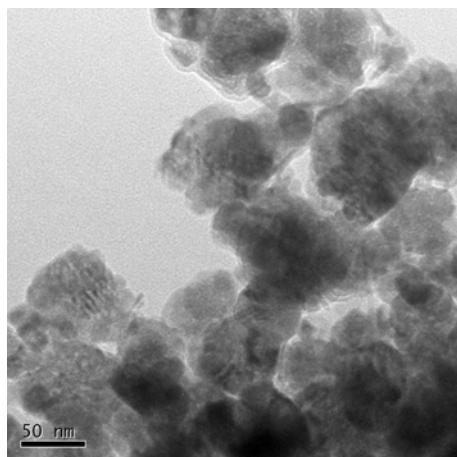


Figure 2. MnO₂ nanoparticles

2. Fabrication of TiO₂ nanowire and nanotube

Under the guidance of Dr. Jun Liu, I have been learning the fabrication of TiO₂ nanowire and nanotubes. The method was through the hydrothermal growth from P25 starting materials. However, this project did not go very well since the hydrothermal growth was very sensitive to conditions. So nanowires were not obtained but only nanoparticles were seen.

3. Electrolyte study

This project was aimed at studying the water absorption ability of different electrolyte in ambient environment. 4 kinds of different electrolyte were studied: BDG, DPG, EDG and PC.

The weight change of the electrolyte after putting the bottled electrolyte in certain moisture was recorded by microbalance and the mass figure was shown in figure 3

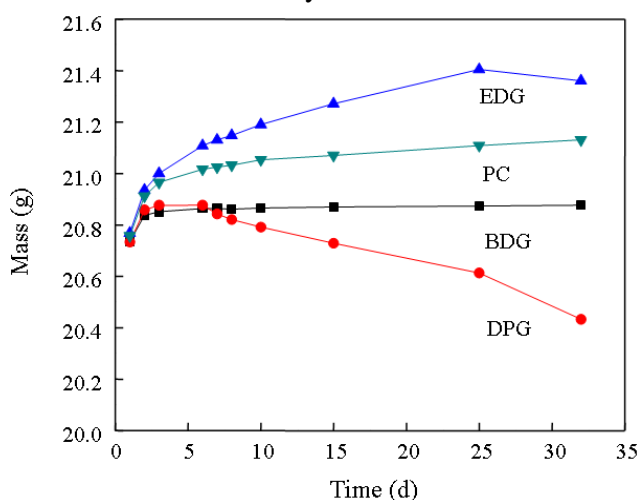


Figure 3. Mass change of different electrolyte

Also, the electrolyte with lithium salts were also studied for the mass change in the same method and the mass change was shown in figure 4

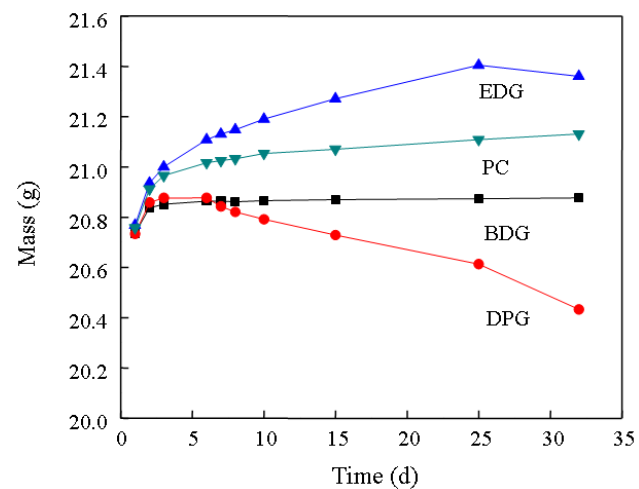


Figure 4. Mass change of different electrolyte with LiF₆ salt

October 2, 2008

Self-consistent polarization density functional theory: Application to Argon

Katie A. Maerzke,[†] Garold Murdachaew,[‡] Christopher J. Mundy,^{‡,*}
Gregory K. Schenter,^{‡,*} and J. Ilja Siepmann[†]

Departments of Chemistry and of Chemical Engineering and Materials Science,
University of Minnesota, Minneapolis, MN 55455
Chemical & Materials Sciences Division,
Pacific Northwest National Laboratory, Richland, WA 99352

Abstract

We present a comprehensive set of results for argon, a case study in weak interactions, using the self-consistent polarization density functional theory (SCP-DFT). With minimal parameterization, SCP-DFT is found to give excellent results for the dimer interaction energy, the second virial coefficient, the liquid structure, and the lattice constant and cohesion energy of the face-centered cubic (fcc) crystal compared to both accurate theoretical and experimental benchmarks. Thus, SCP-DFT holds promise as a fast, efficient, and accurate method for performing *ab initio* dynamics that include additional polarization and dispersion interactions for large, complex systems involving solvation and bond breaking.

[†]University of Minnesota

[‡]Pacific Northwest National Laboratory

*Corresponding authors. Email: chris.mundy@pnl.gov, greg.schenter@pnl.gov

1 Introduction

Accurately describing chemical reactions in the condensed phase remains a significant challenge for molecular simulations, requiring the explicit and computationally expensive treatment of the electrons via a quantum mechanical theory. One popular theory that provides a compromise between speed and accuracy is Kohn-Sham (KS) density functional theory (DFT),^{1,2} which is widely used and implemented in many available software packages. While DFT is in principle exact, a significant deficiency of the current DFT exchange-correlation (XC) functionals is that they are of either local character (local density approximation or LDA) or of semi-local character (generalized-gradient approximation or GGA, with an additional dependence on density gradients). These functionals, requiring charge overlap to result in an interaction, cannot recover the long-range correlation needed to represent the dispersion component which is present even at distances where charge overlap may be negligible.³ Even the newer meta-GGA functionals (with additional dependence on the kinetic-energy density and/or the Laplacian of the density, *i.e.*, TPSS⁴) are still only semi-local. Thus, standard DFT cannot accurately model weak interactions.^{5,6} However, since DFT is essentially parameter free, it holds tremendous promise for describing complex chemical phenomena in hydrogen-bonding fluids where dispersion effects are less important. Examples include simulations exploring different sampling strategies in first-principles simulations of water,⁷ the liquid-vapor interface of methanol,⁸ benzene solvated in water,⁹ and the confinement of water within nanotubes and between graphene sheets.¹⁰ Given the failure of present day XC functionals to capture subtle weak interactions that are known to be present in the aforementioned systems, one must conclude that any good agreement with experiment or more accurate calculations for weakly-bound systems is likely to be accidental. On a positive note, DFT-GGA, by its good description of the molecular electronic density and multipole moments, seems to perform reasonably well for hydrogen-bonded systems such as water near its minimum configurations^{5,6} in which the first-order electrostatic interactions are dominant. Thus, systems in which hydrogen-bonded networks are formed, may be relatively well-represented by DFT XC functionals such as BLYP or PBE,^{5,6,11} but neither performs satisfactorily for the vapor-liquid coexistence curve of water.^{12,13}

The proper description of weak interactions requires a wave function based theory and a careful treatment of the electron correlation. Thus, with a supermolecular approach,¹⁴ one must use MP2 (Möller-Plesset method of second order), or, much better, CCSD(T) (coupled-cluster expansion including single, double, and the non-iterated triple excitations), the most accurate of readily available and affordable su-

permolecular methods, at least for generating potential energy surfaces (PESs) for small- and medium-size systems (see, for example, Bukowski *et al.*¹⁵). Yet another robust approach for studying weakly-bound systems is symmetry-adapted perturbation theory of intermolecular interactions, or SAPT,¹⁶ and its more efficient variant, SAPT(DFT)¹⁷ (see also Hesselmann and Jansen¹⁸). SAPT yields detailed information on the interactions by decomposing the potential into physically interpretable components, and also enables connection with the asymptotic regime and with the properties of the interacting monomers (see, for example, Podeszwa *et al.*¹⁹ for a recent application of SAPT(DFT)). However, the SAPT approach includes a reliance on the many-body expansion and, perhaps more significantly, does not allow the modeling of the breaking or formation of chemical bonds; that is, true chemistry.

Within the efficient DFT, while advances in development of XC functionals are ongoing,³ there are also attempts to improve the existing DFT methodology. The recent overview by Grimme and coworkers²⁰ organizes these attempts into three groups. Workers in the first group attempt to develop or improve DFT XC functionals (GGA or hybrid and/or meta-GGA) for modeling of weak bonds. Here we mention only a few examples and the reader is referred to Grimme *et al.*²⁰ for a more extensive list. These include the GGA XC functionals HCTH,²¹ HCTH120²², B97-1^{21,23}, and the hybrid meta-GGA functionals of Truhlar *et al.* such as M06 and M06-2X.²⁴ The salient feature of the aforementioned methods is that they can, in general, be used within efficient implementations of DFT and can be directly applied to problems concerning chemistry in the condensed phase. If these methods are parameterized to accurate data, they will perform well (although some testing should be done to ensure transferability). However, their inability to recover the physics of the long-range interaction puts these methods at risk of having accidental good agreement with experiment or *ab initio* approaches. Although it is a quite different approach, the attempt by Rothlisberger and coworkers²⁵⁻²⁷ to reproduce weak interactions with standard DFT XC functionals by additional parametrization of effective core potentials (ECPs) for atoms also falls into this category.

Workers in the second and third groups do not rely on error cancelations but rather attempt to add the missing long-range correlation or dispersion component to the DFT functional. Thus, the interaction energy from these approaches should have the correct asymptotic behavior. Those in the second group attempt to add the missing component via an orbital-based or truly nonlocal correlation functional supplement to DFT. Two examples are the vdW-DF approach of the group of Langreth and Lundqvist²⁸ and the similar ACFDT-DFT approach of Harl and Kresse.²⁹ However, these methods may be too expensive to have seen adoption outside the groups which developed them. While these methods hold an advantage in that they do not require parametrization, the accuracy of the potentials obtained with them may be lower

than required. For example, the interaction energy of Ar₂ and Kr₂ given by the vdW-DF approach²⁸ differs substantially³⁰ from accurate calculations; the potential wells for Ar₂ and Kr₂ are too deep by 60% and 40%, respectively, and both are shifted outward by 5%. The error in the well depths is comparable to those of DFT-GGA potentials such as PBE, except that PBE generally makes the well depths too shallow rather than too deep (see Table 1 below). However, the ACFDT-DFT(PBE) approach²⁹ for Ar fcc solid does produce good results (see Table 3 below).

The third group of approaches may be labeled collectively by the term DFT-D. They are based on the HF-D method (see Douketis *et al.*,³¹ Wu *et al.*,⁵ and additional references therein), which is relatively successful for rare gases and other simple systems. In these methods the Hartree-Fock or DFT interaction energy is supplemented by a (damped) long-range dispersion contribution calculated from (possibly pre-determined) long-range dispersion coefficients. DFT-D methods thus require use of DFT XC functionals which behave similarly^{5,32} to HF and have a minimum of attraction (*e.g.*, revised versions of PBE³³ such as revPBE³⁴ or RPBE;³⁵ or, alternatively, BLYP,^{36,37} B3LYP,³⁸ etc.), thus avoiding the possible double-counting of the long-range correlation, as occurs, with *e.g.*, PW91.³⁹ Some groups which have used DFT-D methods are those of Scoles,^{5,32} Elstner^{40,41} (who however supplemented an approximate DFT interaction energy), Wu and Yang,⁴² Grimme,^{20,43} Parrinello,⁴⁴ and Ortmann.⁴⁵ The various implementations of DFT-D differ in which DFT XC functional is used, in how the dispersion coefficients are obtained, in the damping function that is used, and in whether terms past the leading term $-C_6 f(r) r^{-6}$ are included (here, r is the intermonomer separation, $f(r)$ is a damping function, and C_6 is the leading dispersion coefficient; note that inclusion of higher-order coefficients is needed for greater accuracy^{5,32}). The reader is referred to Zimmerli and coworkers⁴⁴ for a comparative study of various DFT-D schemes for approximating the interaction energy of water-benzene. A possible shortcoming of many DFT-D approaches is that the dispersion coefficients are not updated during the course of the simulation and thus will not be consistent with possible changes in electronic structure due to chemical reactions. In addition, atom-atom coefficients are needed to allow for the breaking/formation of bonds and also for the description of intramolecular dispersion interactions present in, *e.g.*, large organic molecules. A possible candidate for a self-consistent, atom-based approach is that of Silvestrelli,⁴⁶ who used DFT with maximally localized Wannier function centers to localize charge density and to compute the effective dispersion. This approach is similar to that of Becke and Johnson,⁴⁷ who demonstrated that the position-dependent dipole moment of the exchange hole can be used to generate dispersion interactions between closed-shell systems.

In this work we present a theory motivated by the need to perform accurate statistical mechanical

sampling and chemistry in the condensed phase. Recently, a self-consistent polarization (SCP) approach in combination with a semi-empirical electronic structure method, implemented by Chang *et al.*,⁴⁸ was used to obtain good results for water clusters. Despite its success, one drawback of the aforementioned approach was the requirement of extensive parametrization. By replacing the semi-empirical method with DFT, which is a more *ab initio* electronic structure method, most of the parametrization is eliminated. The salient feature of SCP-DFT is that it is based on linear response theory,^{49,50} allowing one to simultaneously and self-consistently correct the DFT interaction with auxiliary polarization density, thus recovering the correct classical multipole polarization and polarizabilities. The quantum mechanical treatment of this additional polarization yields the celebrated London dispersion formula. Therefore, with the addition of a single parameter (for atoms), SCP-DFT provides a self-consistent picture of polarization and dispersion and enables one to recover the interaction energy including the dispersion component, which is otherwise completely missing from the local and semi-local XC functionals.

To this end, we performed a comprehensive test of SCP-DFT for argon, a case study in weak interaction. We compare results obtained using SCP-DFT both to experiment and also to those obtained using potentials ranging from a simple Lennard-Jones potential to benchmark-quality, complex many-body potentials which had been obtained by fitting the potential parameters to spectroscopic measurements (the potential of Aziz⁵¹) or to accurate *ab initio* calculations on the dimer (the CCSD(T)/CBS potential of Patkowski *et al.*⁵²) and the trimer (the SAPT three-body potential of Lotrich *et al.*⁵³ and the CCSD(T) calculations of Podeszwa *et al.*⁵⁴). We find that our results for the dimer potential, second virial coefficients, cluster cohesion energies, liquid structure, and fcc solid are in excellent agreement with the benchmarks.

2 Self Consistent Polarization Density Functional Theory

2.1 Definition of the method

The SCP-DFT approach has been implemented within the CP2K package⁵⁵ and is described in detail below. We write the DFT energy functional as

$$E_{\text{DFT}}[\rho_{\text{DFT}}] = T[\rho_{\text{DFT}}] + E_{\text{XC}}[\rho_{\text{DFT}}] + E_{\text{H}}[\rho_{\text{DFT}}], \quad (1)$$

where $T[\rho_{\text{DFT}}]$ and $E_{\text{XC}}[\rho_{\text{DFT}}]$ are kinetic energy and exchange-correlation functionals, respectively, and E_{H} is the Hartree functional,

$$E_{\text{H}}[\rho_{\text{DFT}}] = \int d\mathbf{r}d\mathbf{r}' \frac{\rho_{\text{DFT}}(\mathbf{r})\rho_{\text{DFT}}(\mathbf{r}')}{|\mathbf{r} - \mathbf{r}'|}. \quad (2)$$

We supplement the DFT charge density, ρ_{DFT} , with the SCP charge density, ρ_{SCP} , to construct the total charge density, $\rho = \rho_{\text{DFT}} + \rho_{\text{SCP}}$. Within a Kohn-Sham representation,

$$\rho_{\text{DFT}}(\mathbf{r}) = \sum_A Z_A \delta(\mathbf{r} - \mathbf{r}_A) - \sum_{\gamma, \mu, \nu} P_{\mu\nu}^{\gamma} \phi_{\mu}(\mathbf{r}) \phi_{\nu}(\mathbf{r}), \quad (3)$$

where $P_{\mu\nu}^{\gamma}$ is the density matrix corresponding to spin γ , $\phi_{\mu}(\mathbf{r})$ is an atomic basis set centered on the position \mathbf{r}_{μ} , and Z_A are core charges located at positions \mathbf{r}_A . The SCP density is represented as

$$\rho_{\text{SCP}}(\mathbf{r}) = \sum_{\alpha} c_{\alpha} \chi_{\alpha}(\mathbf{r}), \quad (4)$$

where $\chi_{\alpha}(\mathbf{r})$ are auxiliary basis functions. We supplement the DFT energy functional as

$$E[\rho_{\text{DFT}}, \rho_{\text{SCP}}] = T[\rho_{\text{DFT}}] + E_{\text{XC}}[\rho_{\text{DFT}}] + E_{\text{H}}[\rho_{\text{DFT}}] + E_{\text{DFT-SCP}}^{(e)} + E_{\text{DFT-SCP}}^{(N)} + E_{\text{SCP-SCP}} + E_{\text{SCP}}^{\text{disp}}, \quad (5)$$

where the SCP charge density interacting with the DFT electron density is

$$E_{\text{DFT-SCP}}^{(e)} = - \sum_{\mu, \nu, \alpha} P_{\mu\nu}^T c_{\alpha} (\mu\nu|\alpha) f_{\mu\nu\alpha}, \quad (6)$$

with Coulomb integrals

$$(\mu\nu|\alpha) = \int d\mathbf{r}d\mathbf{r}' \frac{\phi_{\mu}(\mathbf{r}) \phi_{\nu}(\mathbf{r}) \chi_{\alpha}(\mathbf{r}')}{|\mathbf{r} - \mathbf{r}'|}. \quad (7)$$

The SCP charge density interacting with the DFT core density is given by

$$E_{\text{DFT-SCP}}^{(N)} = \sum_{A, \alpha} Z_A c_{\alpha} (A|\alpha) f_{A\alpha}, \quad (8)$$

with Coulomb integrals

$$(A|\alpha) = \int d\mathbf{r}' \frac{\chi_{\alpha}(\mathbf{r}')}{|\mathbf{r}_A - \mathbf{r}'|}. \quad (9)$$

Here $f_{\mu\nu\alpha}$ and $f_{A\alpha}$ are screening functions that damp the Coulomb interactions when they involve auxiliary sites at short distances: $f_{A\alpha} = 0$ when $\mathbf{r}_A = \mathbf{r}_\alpha$ and $f_{\mu\nu\alpha} = 0$ when $\mathbf{r}_\mu = \mathbf{r}_\nu$, $\mathbf{r}_\mu = \mathbf{r}_\alpha$, or $\mathbf{r}_\nu = \mathbf{r}_\alpha$. The SCP-SCP self interaction is given by

$$E_{\text{SCP-SCP}} = \frac{1}{2} \sum_{\alpha,\beta} c_\alpha c_\beta \left\{ \frac{1}{a_\alpha} \delta_{\alpha,\beta} + (\alpha|\beta) f_{\alpha\beta} \right\}, \quad (10)$$

where the Coulomb integral is given by

$$(\alpha|\beta) = \int d\mathbf{r} d\mathbf{r}' \frac{\chi_\alpha(\mathbf{r}) \chi_\beta(\mathbf{r}')}{|\mathbf{r} - \mathbf{r}'|} \quad (11)$$

and $f_{\alpha\beta}$ is a screening function. The generalized polarizability is a_α . A self-consistent expression for the dispersion interaction is

$$E_{\text{SCP}}^{\text{disp}} = -\frac{1}{8} \sum_{\alpha,\beta} \frac{I_\alpha I_\beta}{I_\alpha + I_\beta} a_\alpha a_\beta (\alpha|\beta)^2 f_{\alpha\beta}^2. \quad (12)$$

The self-consistent procedure consists of the two variational conditions,

$$\frac{\delta}{\delta \rho_{\text{DFT}}} E[\rho_{\text{DFT}}, \rho_{\text{SCP}}] = 0 \quad (13)$$

and

$$\frac{\delta}{\delta \rho_{\text{SCP}}} E[\rho_{\text{DFT}}, \rho_{\text{SCP}}] = 0. \quad (14)$$

The DFT charge density is subject to the orthonormality constraint. Explicitly, if the density matrix is represented in terms of the molecular orbitals, $C_{\mu i}^\gamma$,

$$P_{\mu\nu}^\gamma = \sum_i n_i^\gamma C_{\mu i}^\gamma C_{\nu i}^\gamma, \quad (15)$$

where n_i^γ are orbital occupancies, to give

$$\sum_{\mu,\nu} C_{\mu i}^\gamma S_{\mu\nu} C_{\nu j}^\gamma = \delta_{ij} \quad (16)$$

with

$$S_{\mu\nu} = \int d\mathbf{r} \phi_\mu(\mathbf{r}) \phi_\nu(\mathbf{r}). \quad (17)$$

The only constraint on the SCP charge density is that no extra charge is generated (net monomer SCP

moment is zero),

$$\int d\mathbf{r} \rho_{\text{SCP}}(\mathbf{r}) = 0. \quad (18)$$

The variational procedure leads to the standard self-consistent field equations

$$F_{\mu\nu}^{\gamma} C_{\nu i}^{\gamma} = S_{\mu\nu} C_{\nu i}^{\gamma} \varepsilon_i, \quad (19)$$

where the Fock matrix (Kohn-Sham matrix)

$$F_{\mu\nu}^{\gamma} = \frac{\partial}{\partial P_{\mu\nu}^{\gamma}} E[\rho_{\text{DFT}}, \rho_{\text{SCP}}] \quad (20)$$

is decomposed into the unmodified DFT Fock matrix, $F_{\mu\nu}^{\gamma(0)}$, and the perturbation due to SCP, $\Delta F_{\mu\nu}^{\gamma}$,

$$F_{\mu\nu}^{\gamma} = F_{\mu\nu}^{\gamma(0)} + \Delta F_{\mu\nu}^{\gamma}, \quad (21)$$

where

$$\Delta F_{\mu\nu}^{\gamma} = - \sum_{\alpha} c_{\alpha} (\mu\nu|\alpha) f_{\mu\nu\alpha}. \quad (22)$$

In terms of SCP coefficients, c_{α} , the SCP variational expression becomes

$$\frac{\partial}{\partial c_{\alpha}} E[\rho_{\text{DFT}}, \rho_{\text{SCP}}] = 0, \quad (23)$$

or

$$\sum_{\beta} c_{\beta} \left\{ \frac{1}{a_{\alpha}} \delta_{\alpha,\beta} + (\alpha|\beta) f_{\alpha\beta} \right\} - \sum_{\mu,\nu} P_{\mu\nu}^T (\mu\nu|\alpha) f_{\mu\nu\alpha} + \sum_A Z_A (A|\alpha) f_{A\alpha} = 0, \quad (24)$$

leading to the linear response of the SCP coefficients to the external multipole Coulomb field

$$c_{\alpha} = a_{\alpha} \Phi_{\alpha}, \quad (25)$$

where the multipole field is given by

$$\Phi_{\alpha} = - \sum_{\beta} c_{\beta} (\alpha|\beta) f_{\alpha\beta} + \sum_{\mu,\nu} P_{\mu\nu}^T (\mu\nu|\alpha) f_{\mu\nu\alpha} - \sum_A Z_A (A|\alpha) f_{A\alpha}. \quad (26)$$

2.2 Screening Function

We write for the pair screening function

$$f_{\mu\nu} = 1 - e^{-(\sigma^\mu + \sigma^\nu)R_{\mu\nu}} \left(1 + \frac{1}{2} (\sigma^\mu + \sigma^\nu) R_{\mu\nu} \right), \quad (27)$$

where $R_{\mu\nu} = |\mathbf{r}_\mu - \mathbf{r}_\nu|$ and the coefficients σ^μ determine the effective screening length. We will construct triplet screening functions as

$$f_{\mu\nu\alpha} = 1 - (1 - f_{\mu\nu})(1 - f_{\mu\alpha})(1 - f_{\nu\alpha}). \quad (28)$$

In initial implementations, we will take the limit $\sigma^\mu \rightarrow \infty$, giving

$$f_{\mu\nu} = 1 - \delta_{A_\mu, A_\nu}, \quad (29)$$

where A_μ is an atom site label associated with orbital μ . In future work we will consider other forms for this screening and its relation to the parameterization and efficiency of the method.

2.3 Dispersion

To evaluate the expression for the dispersive interaction between two auxiliary charge densities, first consider the energy for an auxiliary charge density in an external multipole field,

$$E = \sum_{\alpha} \left(\frac{c_{\alpha}^2}{2a_{\alpha}} - c_{\alpha}\phi_{\alpha} \right). \quad (30)$$

With $\frac{\partial E}{\partial c_{\alpha}} = 0$,

$$c_{\alpha} = a_{\alpha}\phi_{\alpha}. \quad (31)$$

This represents the response of the auxiliary polarization density matrix, c_{α} , to an external field, ϕ_{α} , where a_{α} is a generalized polarizability. For interacting auxiliary charge densities, the energy is

$$E = \frac{1}{2} \sum_{\alpha, \beta} c_{\alpha} c_{\beta} \left\{ \frac{1}{a_{\alpha}} \delta_{\alpha, \beta} + (\alpha|\beta) f_{\alpha\beta} \right\}. \quad (32)$$

If we consider the interaction as a quantum mechanical perturbation converting density coefficients c_α to quantum mechanical operators \hat{c}_α ,

$$\hat{V} = \sum_{\alpha < \beta} \hat{c}_\alpha \hat{c}_\beta (\alpha|\beta) f_{\alpha\beta}, \quad (33)$$

then a second-order perturbation theory expression for the dispersion energy may be written as

$$\begin{aligned} E^{\text{disp}} &= \sum_{\alpha < \beta} \sum_{\bar{\alpha} < \bar{\beta}} (\alpha|\beta) f_{\alpha\beta} (\bar{\alpha}|\bar{\beta}) f_{\bar{\alpha}\bar{\beta}} \\ &\times \sum_{k \neq 0} \sum_{l \neq 0} \frac{\langle 0|\hat{c}_\alpha|k\rangle \langle 0|\hat{c}_\beta|l\rangle \langle k|\hat{c}_{\bar{\alpha}}|0\rangle \langle l|\hat{c}_{\bar{\beta}}|0\rangle}{E_0^\alpha + E_0^\beta - E_k^\alpha - E_l^\beta}, \end{aligned} \quad (34)$$

where E_k^α denotes an excitation on site α , and α and $\bar{\alpha}$ denote different multipoles on an identical site. In terms of this notation, the multipole dispersion interaction may be written in a ‘‘Casimir-Polder’’ form (the reader is referred to, *e.g.*, the work of Longuet-Higgins⁵⁶ and also of Misquitta *et al.*¹⁷ and additional references therein) as

$$E^{\text{disp}} = -\frac{1}{2\pi} \int_0^\infty d\omega \sum_{\alpha < \beta} \sum_{\bar{\alpha} < \bar{\beta}} a_{\alpha,\bar{\alpha}}(i\omega) a_{\beta,\bar{\beta}}(i\omega) (\alpha|\beta) f_{\alpha\beta} (\bar{\alpha}|\bar{\beta}) f_{\bar{\alpha}\bar{\beta}}, \quad (35)$$

where $a_{\alpha,\bar{\alpha}}(i\omega)$ is a generalized, multipole dynamic polarizability,

$$a_{\alpha,\bar{\alpha}}(\omega) = 2 \sum_{k \neq 0} \frac{E_k^\alpha - E_0^\alpha}{(E_k^\alpha - E_0^\alpha)^2 - \omega^2} \langle 0|\hat{c}_\alpha|k\rangle \langle k|\hat{c}_{\bar{\alpha}}|0\rangle. \quad (36)$$

If it is assumed that

$$a_{\alpha,\bar{\alpha}}(i\omega) = a_\alpha \frac{I_\alpha^2}{I_\alpha^2 + \omega^2} \delta_{\alpha,\bar{\alpha}}, \quad (37)$$

then we recover the generalized, multipole, London dispersion expression that is consistent with the multipole polarizabilities used in eq 12.

3 Computational Details

The DFT and SCP-DFT calculations were performed using the CP2K/Quickstep package^{55,57} in conjunction with the BLYP^{36,37} XC functional and Goedecker-Teter-Hutter-style pseudopotential.^{58–60} Our Ar₂ interaction energy calculations using BLYP revealed that the DZVP basis set gave similar results

to the nearly complete and essentially BSSE-free QZV3P basis set (see Figure 1). The former basis was then used in the majority of the calculations while the latter basis continued to serve as a benchmark.

In CP2K, non-periodic calculations (*i.e.*, cluster calculations) are performed using the non-periodic option with the Martyna-Tuckerman⁶¹ Poisson solver. Alternatively, for uncharged and non-polar systems, it is simple to use periodic boundary conditions (PBC) with a large amount of vacuum to reduce the spurious interactions between images. We found the latter option with a cubic box of side length of 30 Å performed well in terms of lower memory and time requirements. In order to reduce grid effects for our dimer and trimer energy calculations, the energy cutoff used for expansion of the electron density in plane waves was set to a relatively high value of 500 Ry while the SCF energy convergence threshold was tightened to 10^{-8} Hartree/atom. The wave function optimization was performed with the orbital transformation (OT) method using the conjugate gradient (CG) algorithm. For our cluster calculations, the plane wave cutoff was 200 Ry, energy convergence was 10^{-6} Hartree/atom, and convergence of gradient was 4.5×10^{-4} Hartree/Å.

The liquid argon calculations were performed in a supercell containing 96 atoms. The cell parameters of the cubic box containing the sample was chosen to be 16.7 Å, resulting in a density of 1.37 g/mL, which is in reasonable agreement with the density of 1.396 g/mL reported by the CRC Handbook⁶² for liquid argon at its boiling point (87.3 K). The initial configuration was obtained using standard Monte Carlo (MC) in the NpT ensemble with a Lennard-Jones (LJ) argon potential. The LJ parameters for argon, $\sigma = 3.40$ Å and $\epsilon = 114.99$ K, were determined from the precise vapor–liquid equilibrium (VLE) simulations for Lennard-Jonesium by Potoff and Panagiotopoulos⁶³ and the experimental argon VLE data of Michels *et al.*⁶⁴ by taking the appropriate ratios of the critical properties of Lennard-Jonesium to the experimental critical properties of argon, *i.e.* $\epsilon = T_c/T_c^*$ and $\sigma = (\rho_c^*/\rho_c)^{1/3}$. It is important to note here that this parametrization leads to an effective LJ potential that is appropriate for condensed phases and implicitly includes many-body terms and nuclear quantum effects.⁶⁵ A well-equilibrated configuration of LJ argon was used as the starting configuration for a SCP-DFT molecular dynamics (MD) simulation in a periodically replicated cubic cell. The MD simulation was performed in the NVT ensemble using the method of Nosé and Hoover^{66–69} with a time step of 0.5 fs. The system was equilibrated for 10 ps, followed by 25 ps of production for the accumulation of averages. The last 10 ps are presented in our final results. The distance cutoff for the summation of the dispersion contribution to the SCP-DFT energy was 11 Å. The cutoff for the electron density was 200 Ry while the SCF energy convergence threshold was 10^{-6} Hartree/atom. The OT method⁷⁰ with the DIIS minimizer was used in the dynamics calculations for

the optimization of the wave function.

The SCP-DFT calculations on the Ar face-centered cubic (fcc) solid were performed at the Γ -point using a 32 atom supercell. The nearest-neighbor separation, r_{ss} (or equivalently, the lattice parameter $a = \sqrt{2}r_{ss}$), was changed and the cell lattice vectors and atomic positions were likewise scaled as DFT calculations were performed, thus obtaining the cohesion energy per atom as a function of r_{ss} . The cohesion energy per atom is given by $E_{\text{coh}}(r_{ss}) = (E_n(r_{ss}) - nE_1)/n$, where E_n and E_1 are the energies of n atoms and 1 atom, respectively. Due to numerical artifacts associated with a finite charge density grid, and to ensure a smooth cohesion energy curve, it was necessary to compute the reference energy of the argon monomer in the identical supercell, that is, to use the value $E_1(r_{ss})$ in the above equation. The distance cutoff for the summation of the dispersion contribution to the SCP-DFT energy was 11 Å. To ensure accuracy, a density cutoff of 300 Ry was utilized with an SCF energy convergence threshold of 10^{-8} Hartree/atom. Identical results were obtained when a higher density cutoff of 1000 Ry was used. We also confirmed that use of a larger supercell containing 108 atoms gave nearly identical results, ensuring that our cohesion energy is well-converged with respect to cell size and cutoff.

4 Parameterization

As alluded to in Section 1 our choice in developing the SCP-DFT theory is that many of the parameters are determined for us by the choice of XC functional. Thus, in principle, for structureless particles such as argon, the parameterization of the potential should be straightforward. Indeed this is the case. The parameters that must be determined for SCP-DFT are the choice of the auxiliary basis set, and the parameters for the polarizability, a_α , and London dispersion, I_α . In CP2K/QUICKSTEP the basis set is the standard contracted Gaussian basis set. The auxiliary basis sets are of the same form and represent the (unnormalized) density, namely $\sum_i d_{i\alpha} g_i(\mathbf{r})$. Here, d is the contraction coefficient, α is index for the density, and g is a primitive Gaussian function with width determined by a single parameter ζ (in units of $1/\text{Bohr}^2$).

The finite-field approach was used within CP2K to fit the SCP parameter a_α in order to reproduce the accurate static dipole polarizability $\alpha = 11.085 \pm 0.06$ au recently recommended by Lupinetti and Thakkar⁷¹ based on their finite field, large basis set CCSD(T) calculations (with an estimate of the relativistic correction); a theoretical value very close to the experimental one of 11.075 ± 0.006 au.⁶²

The change in energy of a neutral atom in the presence of an applied electric field of strength $F = |\mathbf{F}|$ is given by

$$\Delta E = E(F) - E(0) = \frac{-\alpha F^2}{2!} - \frac{\gamma F^4}{4!} - \dots, \quad (38)$$

where $E(F)$ and $E(0)$ are the field dependent and field-free energies, α is the polarizability and γ is the hyperpolarizability. Ignoring the hyperpolarizability, we have

$$\Delta E = \frac{-\alpha F^2}{2}. \quad (39)$$

We generated fields by placing point charges $\pm Q$ (where Q ranged from 0.1 to 5.0 au) at positions $z = \pm 5$ Å relative to an argon atom at the origin (thus ensuring that the field gradient vanished at the origin). Hence the field at the origin,

$$\mathbf{F}(\mathbf{0}) = -\frac{2Q}{z^2} \hat{\mathbf{z}}, \quad (40)$$

ranged from approximately 0.00224 to 0.112 au. For comparison, Lupinetti and Thakkar⁷¹ used fields ranging from 0.0044 to 0.0176 au.

Since $E(0)$, $E(F)$, and ΔE are all parametrically dependent on the SCP parameters ζ and a_α , we performed calculations for various fixed values of ζ and a_α , each time varying the fields so as to extract α from a least-squares fit of ΔE versus F in eq 39. As ζ increases the argon atom becomes more point-charge-like. Finally we chose a reasonable $\zeta = 0.2$ and only considered p (or dipole) polarization density functions. This choice of ζ reflects our choice of screening function in that in the present study we rely on the natural screening due to the overlap of two overlapping Gaussian charges. For argon this choice of trivial screening allows for a stable theory. However, a more robust choice for the screening parameter will be investigated in future publications. Thus, utilizing only the dipole auxiliary charge density, we fix $a_\alpha = 0.000291$ yielding a polarizability, $\alpha = 11.086 \pm 0.001$ au, which is in very good agreement with the target value of 11.085 au.⁷¹

After fixing ζ and a_α to reproduce the known polarizability, a single parameter for argon, I_α , is needed to reproduce the argon dimer potential of Aziz,⁵¹ which is generally accepted as the most accurate empirical potential. Specifically, we chose $I_\alpha = 3.977$ au to reproduce the interaction energy of the Aziz potential at an interatomic separation of 3.60 Å. The resulting SCP-DFT value of -0.2581 kcal/mol agrees quite nicely with the Aziz value of -0.2579 kcal/mol.

One should be reminded that unlike calculations with LDA or PBE XC functionals,³² the BLYP

argon dimer potential is completely repulsive. This feature actually facilitates the use of the SCP-DFT correction to account for the missing attractive component of the interaction energy.

5 Results

5.1 Dimer potential

We computed the Ar_2 potential over the range $r = 2.10 - 10.0 \text{ \AA}$. Our SCP-DFT potential agrees quite nicely with the Aziz potential,⁵¹ our benchmark empirical potential, in the region of the repulsive wall and the potential well (see top panel of Figure 1). We also compared our results to the highly accurate *ab initio* CCSD(T) with complete basis set limit extrapolation potential of Patkowski *et al.*⁵² (CCSD(T)/CBS), and the effective Lennard-Jones (LJ) potential for argon described above (that is, of course, too repulsive at short separation). The largest discrepancy of the SCP-DFT potential from the benchmarks is in the region of the tail, where it is too negative (see bottom panel of Figure 1). This is related to the fact that the effective leading dispersion coefficient of the SCP-DFT curve, obtained by fitting to its tail, is $C_6^{\text{SCP-DFT}} = 130 \text{ au}$, which is too large compared to the correct value⁷² of 64.691 au . This is likely due to an overcompensation of the SCP-DFT curve for the neglect of higher-order multipoles in the present SCP-DFT model.

Table 1 compares the minimum separations r_e and the binding energies D_e of Ar_2 obtained from different methods to *ab initio* and empirical benchmarks. Upon examining pure DFT, we see that the LDA and PW91 XC functionals overbind the dimer, whereas PBE and revPBE underbind and BLYP is purely repulsive. Of the corrected DFT methods, the DCACP-DFT method²⁶ gives a result that is in good agreement with the MP2 value to which it was fit (basis-set converged MP2, however, overbinds Ar_2). However, we stress that this approach is not physical and cannot reproduce the asymptotic limit of the interaction energy curve. As pointed out in refs,^{5,32} among others, the DFT-D approaches, although justified on physical grounds, require the use of an XC functional that has minimal attraction in order to avoid double-counting. By adding a dispersion correction to PW91, which already overbinds, Ortmann *et al.*⁴⁵ err in this regard. The more complex vdW-DFT²⁸ model also overbinds. The method of Becke and Johnson⁴⁷ underbinds the dimer while that of Silvestrelli⁴⁶ yields a minimum separation r_e is too large by over 0.2 \AA . Our SCP-DFT result, which only has a single parameter, obviously agrees quite well with the

benchmarks. As the LJ potential parameters were determined from VLE properties, it is not surprising that it does not perform as well as the other methods for the dimer.

5.2 Second virial coefficients

The second virial coefficient,⁷³ $B_2(T)$, of a pure substance or mixture depends solely on the two-body intermonomer potential, V_2 . Due to the importance of the virial equation of state in thermal physics, experimental data exists for many substances. This allows one to readily assess the accuracy of model potentials. The second virial coefficients can be expressed as the sum of the classical term and quantum corrections,

$$B_2(T) = B_c(T) + B_q(T). \quad (41)$$

For an atom-atom potential $V_2(r)$,

$$B_c(T) = -2\pi \int_0^\infty dr r^2 [e^{-V_2(r)/k_B T} - 1], \quad (42)$$

where T is the temperature and k_B is Boltzmann's constant. Quantum corrections⁷³ become important at lower temperatures and can be expressed as a series in h^2 , where h is Planck's constant. At the lowest temperature that we considered, 100 K, the first term is sufficient to recover the quantum correction to the virial coefficient of Ar (about $1.50 \text{ cm}^3 \text{ mol}^{-1}$ with various potentials⁵²) to better than $0.01 \text{ cm}^3 \text{ mol}^{-1}$ ^{52,74}. Thus, one can approximate the quantum corrections by their leading term, given by

$$B_q(T) = \frac{h^2}{24\pi m (k_B T)^3} \int_0^\infty dr r^2 e^{-\beta V_2(r)} \left(\frac{dV_2}{dr} \right)^2. \quad (43)$$

For the LJ model potential, the calculation was done using trapezoidal numerical integration over the range 0 to 50 Å with a step size of 0.001 Å. For the SCP-DFT potential, we integrated over the ranges 2.1 to 5 Å and 5 to 10 Å, with step sizes of 0.05 Å and 0.1 Å, respectively. The restricted ranges and larger step sizes were chosen in order to avoid possible numerical artifacts. As a convergence check on the SCP-DFT virial coefficients, we repeated the calculation for the LJ potential using the identical ranges and step sizes. The LJ virial coefficients thus obtained were raised by $9.14 \text{ cm}^3/\text{mol}$ (about 5.7%) at the lowest temperature (100 K) and by $0.89 \text{ cm}^3/\text{mol}$ (about 4.1%) at the highest temperature (1000 K), as compared to the values obtained using the more precise integration presented in Table 2. Thus, it is likely

that our SCP-DFT results presented in Table 2 need to be lowered by similar amounts, and that their disagreement with the benchmarks would slightly increase if the more precise integration were performed (see discussion below). However, such small differences do not affect our overall conclusions.

The virial coefficients are presented in Table 2 and Figure 2. Compared to the experimental data compiled by Dymond and Smith,⁷⁵ and the highly accurate results of the Aziz⁵¹ and CCSD(T)/CBS⁵² potentials, which are in excellent agreement over the entire temperature range, the virial coefficients obtained using the SCP-DFT potential are too negative while the LJ virial coefficients have the opposite problem. These deviations are largest at low temperatures, where the magnitude of the virial coefficient is most dependent on the volume of the potential well. These results could have been predicted from the fact that the overly negative tail for the SCP-DFT potential leads to a volume of the potential well that is too large while the effective LJ potential has a minimum that is too shallow (see Figure 1). Nevertheless, one should be reminded that we have fit our single parameter, I_α , to a single point on the dimer interaction curve. With a single parameter the SCP-DFT potential nearly as well as the effective LJ potential in terms of percent deviation from experiment. This in itself is an accomplishment given that the bare DFT produces a repulsive two-body potential.

5.3 Cluster cohesion energies

As a further test of the transferability of the SCP-DFT potential, we calculated the energies of small argon clusters, containing $n = 2-10$ atoms. The configurations were optimized for the Aziz potential⁵¹ by Naumkin *et al.*,⁷⁶ and are downloadable from the Cambridge Cluster Database.⁷⁷ Our cluster calculations were performed using the LJ, BLYP/DZVP, BLYP/QZV3P, and SCP-DFT potentials. Note that the Aziz potential used by Naumkin and coworkers is strictly a two-body potential, while the LJ potential is an effective two-body potential (*i.e.*, fit to bulk properties), and the BLYP potentials include many-body nonadditive effects. Use of a pure two-body potential in the work of Naumkin *et al.* was justified since the many-body effects in rare gases are known to be small (though significant in the solid, see below). As Figure 3 shows, BLYP without SCP does not form mutually binding clusters. However, it is interesting to note the agreement between BLYP/DZVP and BLYP/QZV3P, which indicates that our choice of the DZVP basis set for the SCP-DFT calculations remains essentially BSSE-free even for clusters larger than a dimer. Moreover, the LJ potential results in clusters which are somewhat underbound, which is not surprising given that the dimer potential is too repulsive, while the SCP-DFT potential yields clusters

which are slightly overbound. The overbinding with SCP-DFT is almost certainly due to an overestimation and wrong sign (and thus attraction rather than repulsion) of the many-body effects with BLYP; further discussion of the problems of BLYP with many-body effects appears below.

5.4 Liquid structure

We also examined whether our excellent agreement with gas phase clusters also holds for the liquid phase by computing the radial distribution function (RDF) at 85 K. Figure 4 shows excellent agreement between the RDF obtained using SCP-DFT with the experimental RDF and the one obtained using the effective LJ potential. Note that whereas the thermodynamics and energetics of liquid argon are quite sensitive⁷⁸ to the many-body effects (see more on the role of the three-body nonadditivity in solid below), the structure of the liquid—and therefore the RDF—is not,⁷⁸ which explains the good agreement of the SCP-DFT RDF with experiment.

5.5 FCC solid and role of three-body nonadditivity

As the final—and more sensitive—test, we used SCP-DFT to obtain the cohesion energy of the fcc argon solid. As with the liquid and the clusters, SCP-DFT calculations were initially performed with BLYP for the DZVP basis set. However, as these results were unsatisfactory (see Figure 5 and Table 3), we decided to perform the same calculations using the more complete QZV3P basis set. Since polarization is zero in the crystal (by symmetry), the dispersion is only determined by the post-processed London dispersion expression and does not enter the total energy through the SCF calculation. Hence calculations for SCP-DFT with BLYP/QZV3P can be performed without re-parameterization. Calculations for BLYP with the QZV3P basis set showed that the BSSE in the crystal is larger than in the clusters, as a comparison of Figures 1 and 5 shows. Replacement of the BLYP/DZVP with the BLYP/QZV3P energies in determination of the SCP-DFT cohesion energies reduces our initial error in the cohesion energy with respect to the Lotrich⁷⁹ (2+3 body)^{51,53} benchmark from a discrepancy of -0.70 kcal/mol (-35% error) for SCP-DFT/DZVP to -0.35 kcal/mol (-17% error) for SCP-DFT/QZV3P (see Table 3).

Given that the initial success of SCP-DFT for the argon clusters and the liquid was better than the above-mentioned 0.35 kcal/mol discrepancy that we obtained for the solid, additional investigation into

the reasons for this discrepancy was necessary in order to understand the limitations of SCP-DFT. To this end, it is important to remember that crystal energetics are more sensitive to many-body effects. Although the many-body effects in rare gas clusters are small, they are known to contribute 3% – 7% to the cohesion energy of rare gas solids (Ne through Xe). The many-body contribution in Ar is about 6%.⁸⁰ For this reason, we examined the leading-order many-body effect, the three-body nonadditivity, defined as

$$V_3 = E(\mathbf{r}_i, \mathbf{r}_j, \mathbf{r}_k) - E(\mathbf{r}_i, \mathbf{r}_j) - E(\mathbf{r}_j, \mathbf{r}_k) - E(\mathbf{r}_i, \mathbf{r}_k) + E(\mathbf{r}_i) + E(\mathbf{r}_j) + E(\mathbf{r}_k) \quad (44)$$

for a trimer, where the energies on the right-hand side of the equation are the total energies of the trimer, the dimers, and the monomers comprising the trimer. Asymptotically, the well-known Axilrod-Teller-Muto^{81,82} triple-dipole dispersion component of the three-body nonadditivity is known to properly represent the three-body nonadditivity of rare-gas trimers, where the standard ATM term for a trimer is given by

$$V_3^{\text{ATM}} = v \frac{(1 + 3 \cos \theta_i \cos \theta_j \cos \theta_k)}{(r_{ij} r_{jk} r_{ik})^3}, \quad (45)$$

and the triangle’s side lengths and angles have their obvious meanings. We used an accurate value of $v = 521.7 \text{ au}$.⁸³

As in Podeszwa *et al.*⁵⁴ we computed the leading-order nonadditive contributions to the interaction energy of argon trimers arranged in an equilateral configuration. These configurations are known to have the largest contributions to the nonadditive part of the cohesion energy of the fcc solid, although the contribution is still quite small. Figure 6 shows that BLYP (with and without SCP) gives a negative value for the three-body nonadditivity of the Ar_3 interaction energy in the region of greatest interest for the solid (3.5 – 4.0 Å), although the trend is correct. The correct result, given by the CCSD(T) curve, and asymptotically by the ATM curve, is positive. This figure also explains why our cluster cohesion energies are more negative than those given by the LJ potential (see Figure 3).

This behavior of BLYP is the opposite of the non-empirical DFT XC functionals (LDA, PBE, TPSS, etc.), where the three-body nonadditivity of rare gases is positive and larger than the true value, as Tkatchenko and von Lilienfeld⁸⁴ have shown. Adding an additional positive ATM term in that situation only makes the error worse, as has been observed.⁸⁴

Since our SCP-DFT model in its present formulation does not account for the many-body dispersion that is missing in BLYP, we are at liberty to add a simple correction in the form of an ATM term.

The ATM contribution to the fcc lattice energy was obtained by performing a three-body sum of Eq. 45 over a (non-periodic) lattice. To obtain a value converged to 0.01 kcal/mol, it was necessary to sum over a lattice of $n = 1372$ atoms. We used a spherical cutoff of $r_{\text{cut}} = 2a$ for all three side lengths, where a is the lattice constant, $a = \sqrt{2}r_{ss}$, and r_{ss} is the nearest-neighbor separation within the lattice. Near the experimental separation, at $r_{ss} = 3.7 \text{ \AA}$ ($r_{\text{cut}} = 10.4 \text{ \AA}$), the ATM contribution is 0.15 kcal/mol, in reasonable agreement with the three-body SAPT contribution of 0.1362 kcal/mol at $r_{ss} = 3.7508 \text{ \AA}$ found in the work of Lotrich and Szalewicz.⁷⁹

To simultaneously correct for the negative three-body contribution coming from BLYP and include the missing many-body dispersion, we determined that we needed to add twice the standard value of the ATM term. This had the effect of reducing the remaining discrepancy relative to the Lotrich⁷⁹ (2+3 body)^{51,53} benchmark from -0.35 to only -0.07 kcal/mol (-3% error). Our final cohesion energy obtained in this manner is labeled SCP-DFT/QZV3P/ATM and agrees quite well with accurate benchmarks. Table 3 compares our results for the minimum separation ($r_{ss,\text{min}}$), the cohesion energy per atom (E_{coh}), and the bulk modulus (B_0) of fcc solid Ar with a wide set of results from the literature. Since the two-body potential provides the most important contribution to the interaction energy for rare gases, the various pure DFT XC functionals perform in an analogous manner as they did for Ar_2 (see Table 1). Of the corrected DFT approaches in the literature, ACFDT with the PBE functional does reasonably well. Our SCP-DFT/QZV3P/ATM result compares very well with the accurate benchmarks. The LJ potential also performs quite well, much better than it did for the dimer, as it was parameterized to bulk properties.

6 Conclusion

Driven by the need to perform accurate statistical mechanical sampling and chemistry in the condensed phase, we have developed an efficient correction to DFT based on linear response theory with the addition of auxiliary polarization functions to account for classical many-body polarization and a self-consistent treatment of two-body dispersion interactions. Moreover, SCP-DFT, as applied to argon, introduces a single undetermined parameter, I_α , which is determined from a single point calculation on the dimer potential energy surface. With this single parameter we are able to reproduce accurate structural, energetic, and thermodynamic quantities in all three phases of argon; a case study in weak interactions. Future work will include calculations of the vapor-liquid equilibria of argon, as well as simulations of

liquid argon under high pressures. Improvements to the current theory are underway and incorporate more polarization functions *i.e.*, *s* and *d* functions, as well as a more rigorous screening function. Although these extensions to the theory are important, we are confident that the formulation presented in this manuscript is sufficient to accurately describe rare gases. Future studies will focus on molecular liquids such as water where DFT in conjunction with BLYP is known to underbind the clusters. Hence, SCP-DFT should be an ideal candidate to describe the subtle interactions giving rise to the correct thermodynamics and spectra in this important and well characterized liquid.

7 Acknowledgements

KAM would like to acknowledge support from the Summer Research Institute at Pacific Northwest National Laboratory (PNNL). The work at the University of Minnesota is supported through research grants from the National Science Foundation (CTS-0553911 and CBET-0756641). We are grateful for the abundant computer resources provided by the National Energy Research Scientific Computing Center, the Minnesota Supercomputing Institute, and the Energy Smart Data Center housed in the Environmental Molecular Sciences Laboratory at PNNL. CJM and GKS would also like to gratefully acknowledge numerous conversations with Juerg Hutter, Joost VandeVondele, and Teodoro Laino. A special thanks to Teodoro Laino for helping with the implementation of the restart capability for the SCP-DFT module in CP2K. GM gratefully acknowledges discussions with Krzysztof Szalewicz. GKS, CJM, and GM are supported by the US Department of Energy's (DOE) Office of Basic Energy Sciences Chemical, Geosciences and Biosciences division. PNNL is operated by Battelle for the US DOE.

Table 1: Argon dimer minimum atom-atom separation r_e and binding energy D_e , as obtained from the literature or by harmonic fits to our results in the region of the minimum. Note that zero-point effects are not included. “n/a” indicates that the curve is repulsive. Results of this work are highlighted in bold font.

method or potential	r_e [Å]	D_e [kcal/mol]
DFT		
LDA ³²	3.42	0.698
PW91 ⁴⁵	3.97	0.318
PBE ³²	4.04	0.137
revPBE ⁴⁶	4.67	0.039
BLYP/QZV3P	n/a	n/a
BLYP/DZVP	n/a	n/a
DFT with corrections		
DCACP-DFT(BLYP) ^{a 26}	3.9	0.23
vdW-DF(revPBE) ^{b 28}	3.9	0.46
DFT-D(PW91) (Ortmann) ⁴⁵	3.97	0.353
DFT-D(B97-1) (Becke) ⁴⁷	3.9	0.240
DFT-D(revPBE) (Silvestrelli) ⁴⁶	4.03	0.274
SCP-DFT	3.788	0.2857
<i>Ab initio</i> calculations and benchmarks		
MP2 ^{c 85}	3.88	0.2253
MP2 ³²	3.77	0.311
CCSD(T)/CBS ⁵²	3.767	0.2838
Empirical calculations and experimental benchmarks		
LJ^d	3.82	0.229
Aziz ⁵¹	3.757	0.2846
Experiment ⁸⁶	3.761	0.284

^avon Lilienfeld *et al.*²⁵ fit the parameters of their optimized effective core potential to reproduce their MP2/aug-cc-pVTZ results.

^bFrom Table IV of Bruch *et al.*⁸⁷

^cA relatively small basis set was used in this work.

^d $r_e = 2^{1/6}\sigma$ and $D_e = -V_{LJ}(r_e)$, but this effective potential implicitly accounts for zero-point effects.

Table 2: Comparison of second virial coefficients (in cm³/mol) at various temperatures (in K).^a

T	Exp ⁷⁵	CCSD(T)/CBS ⁵²	Aziz ^{51,52}	LJ	SCP-DFT
100.0	-183.5 ₁₀	-181.84	-181.98	-159.30	-208.32
150.0	-86.2 ₁₀	-85.81	-85.99	-77.63	-101.30
200.0	-47.4 ₁₀	-47.63	-47.89	-43.29	-58.56
250.0	-27.9 ₁₀	-27.37	-27.70	-24.57	-35.83
300.0	-15.5 ₅	-14.92	-15.30	-12.88	-21.83
400.0	-1.0 ₅	-0.60	-1.03	0.78	-5.67
500.0	7.0 ₅	7.26	6.78	8.37	3.23
600.0	12.0 ₅	12.13	11.62	13.12	8.77
700.0	15.0 ₁₀	15.37	14.85	16.32	12.49
800.0	17.7 ₁₀	17.66	17.12	18.58	15.12
900.0	20.0 ₁₀	19.32	18.77	20.24	17.04
1000.0	22.0 ₁₀	20.56	20.00	21.50	18.49

^a Subscripts indicate uncertainties in the final digits.

Table 3: Argon fcc crystal minimum nearest-neighbor separation $r_{ss,\min}$ (and, equivalently, minimum lattice constant a_{\min}), cohesion energy (per atom) E_{coh} , and bulk modulus B_0 , as obtained from the literature or by harmonic fits to our results in the region of the minimum. B_0 was obtained⁸⁸ as $B_0 = \frac{1}{9cr_{ss,\min}} \frac{\partial^2 E_{\text{coh}}}{\partial r_{ss}^2}(r_{ss,\min})$, where $c = \frac{1}{\sqrt{2}}$ for the fcc crystal. Note that zero-point effects are not included. “n/a” indicates that the curve is repulsive. Final results of this work are highlighted in bold font.

method or potential	$r_{ss,\min}$ [Å]	a_{\min} [Å]	$-E_{\text{coh}}$ [kcal/mol]	B_0 [GPa]
DFT				
LDA ²⁹	3.5	4.9	3.2	–
PW91 ⁴⁵	4.3	6.1	–	0.83
PBE ²⁹	4.2	6.0	0.51	–
BLYP	n/a	n/a	n/a	n/a
DFT with corrections				
ACFDT-LDA ²⁹	3.8	5.4	1.4	–
ACFDT-PBE ²⁹	3.7	5.3	1.9	–
DFT-D(PW91) (Ortmann) ⁴⁵	4.2	6.0	–	0.91
SCP-DFT	3.66	5.17	2.73	6.0
SCP-DFT/QZV3P	3.70	5.24	2.38	3.9
SCP-DFT/QZV3P/ATM	3.75	5.31	2.10	4.5
<i>Ab initio</i> calculations and benchmarks				
LMP2 ⁸⁵	3.68	5.20	2.1354	2.79
CCSD(T) ⁸⁰	3.736	5.284	1.9098	2.72
Lotrich ⁷⁹ (2 body ⁵¹)	3.7508 ^a	5.3044	2.1709	–
Lotrich ⁷⁹ (2+3 body ^{51,53})	3.7508 ^a	5.3044	2.0347	–
Empirical calculations and experimental benchmarks				
LJ (effective 2 body)	3.74	5.29	1.94	3.0
Experiment 1 ⁸⁹	3.7508	5.3044	2.0283 ^b	–
Experiments 2–4 ^{90–92}	3.70 ⁹⁰	5.23 ⁹⁰	2.0507 ⁹¹	2.38 ⁹²

^aLotrich and Szalewicz⁷⁹ presented results at the minimum experimental separation given in ref.⁸⁹

^bThis value has been obtained by subtracting the zero-point effects estimated by Lotrich and Szalewicz.⁷⁹

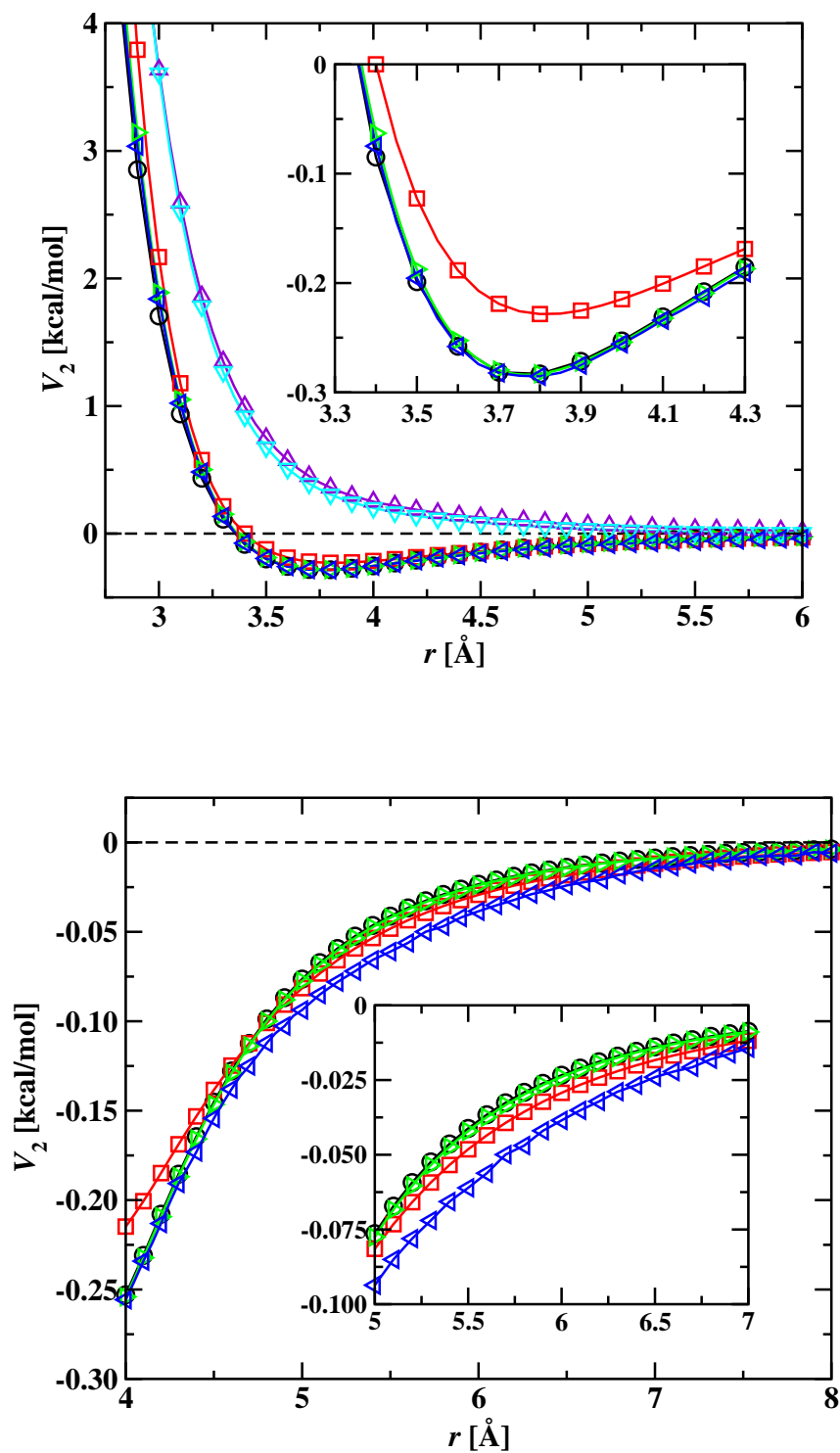


Figure 1: Interatomic potentials for Ar_2 . The top and bottom panels show the whole potential and its tail, respectively. The insets show close-ups. Aziz⁵¹ (black circles), CCSD(T)/CBS⁵² (green right triangles), LJ (red squares), BLYP/QZV3P (purple up triangles), BLYP/DZVP (cyan down triangles), and SCP-DFT (blue left triangles). Lines are shown to guide the eye.

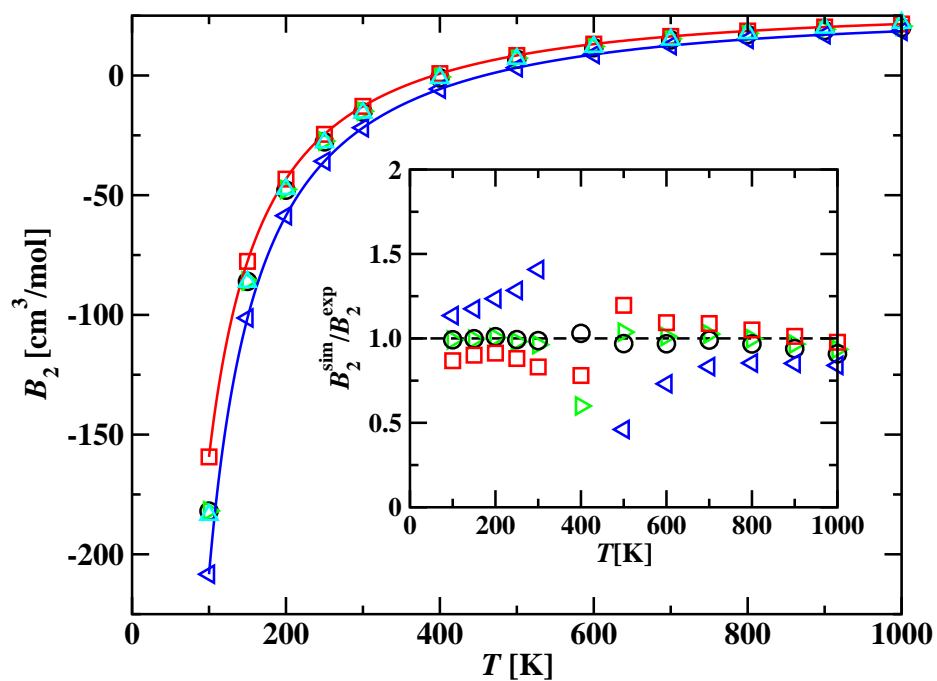


Figure 2: Second virial coefficients of argon. Experiment⁷⁵ (cyan up triangles), Aziz^{51,52} (black circles), CCSD(T)/CBS⁵² (green right triangles), LJ (red squares), and SCP-DFT (blue left triangles). Virial coefficients for the Aziz⁵¹ and CCSD(T)/CBS⁵² potentials were calculated by Patkowski *et al.*⁵² and are taken from Table 5 of that reference. Inset shows a plot of $B_2^{\text{sim}}/B_2^{\text{exp}}$. The largest deviations occur near the Boyle temperature.

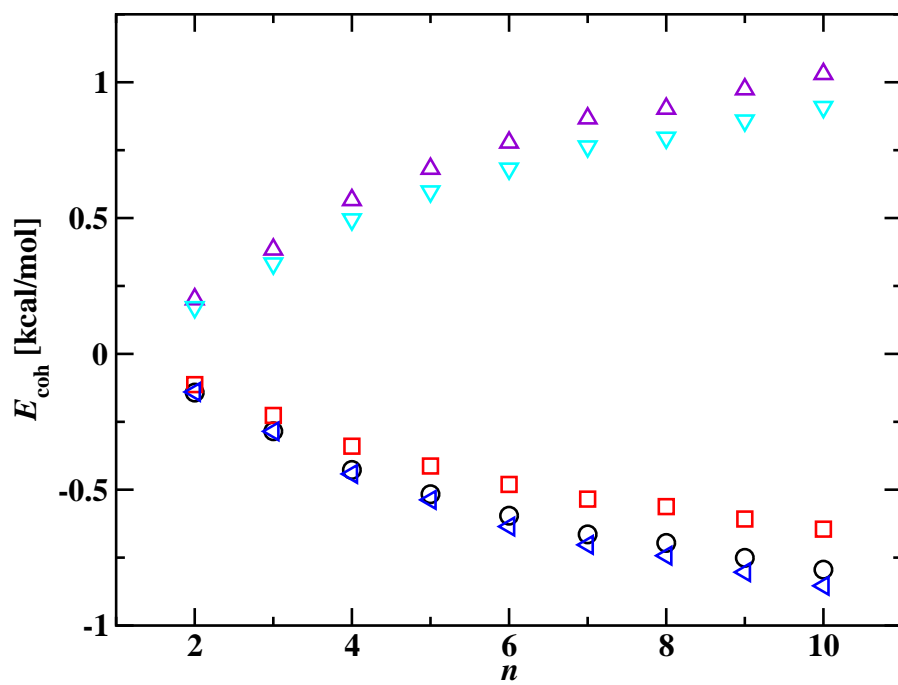


Figure 3: Cohesion energies (per atom) of Ar_n clusters for various cluster sizes n . Aziz⁵¹ (black circles), LJ (red squares), BLYP/QZV3P (purple up triangles), BLYP/DZVP (cyan down triangles), and SCP-DFT (blue left triangles).

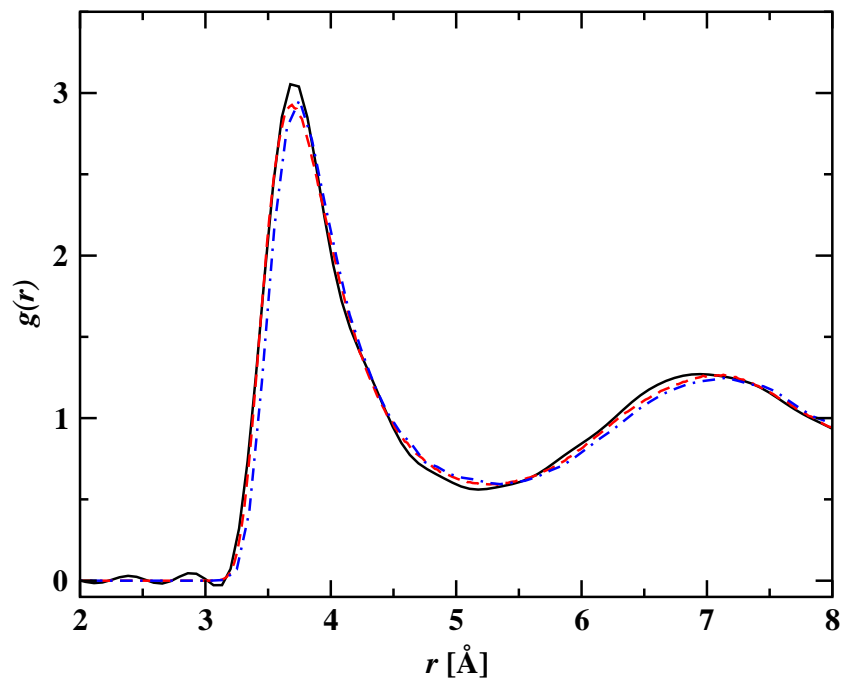


Figure 4: Radial distribution functions of liquid argon at 85 K. Experiment⁹³ (black solid line), LJ (red dashed line), and SCP-DFT (blue dash-dotted line).

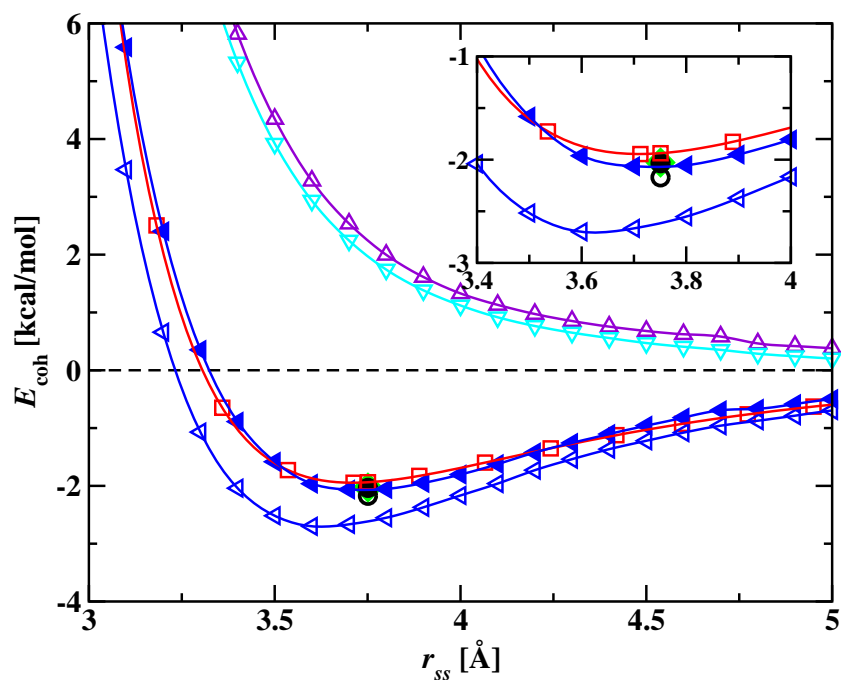


Figure 5: Cohesion energy curves (per atom) of argon fcc solid as a function of nearest-neighbor separation. Note that zero-point effects are not included. Experiment 1⁸⁹ (green diamond), Lotrich⁷⁹ (2 body⁵¹) (black open circle), Lotrich⁷⁹ (2+3 body^{51,53}) (black closed circle), LJ (red squares), BLYP/QZV3P (purple up triangles), BLYP/DZVP (cyan down triangles), SCP-DFT (blue open left triangles), and SCP-DFT/QZV3P/ATM (blue close left triangles). Inset shows a close-up of the minimum region.

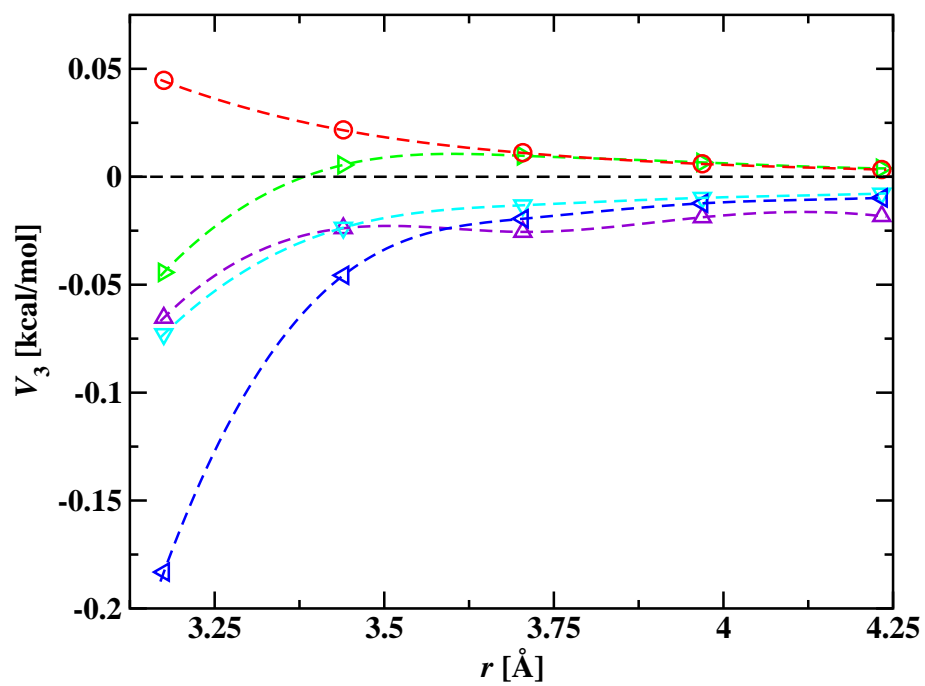


Figure 6: Three-body nonadditive interaction energies of Ar_3 in the equilateral configuration. CCSD(T)⁵⁴ (green right triangles), ATM (red circles), BLYP/QZV3P (purple up triangles), BLYP/DZVP (cyan down triangles), and SCP-DFT (blue left triangles).

References

- [1] Hohenberg, P.; Kohn, W. *Phys. Rev.* **1964**, *136*, B864.
- [2] Kohn, W.; Sham, L. J. *Phys. Rev.* **1965**, *140*, A1133.
- [3] Perdew, J. P.; Ruzsinszky, A.; Tao, J.; Staroverov, V. N.; Scuseria, G. E.; Csonka, G. I. *J. Chem. Phys.* **2005**, *123*, 062201.
- [4] Tao, J. M.; Perdew, J. P.; Staroverov, V. N.; Scuseria, G. E. *Phys. Rev. Lett.* **2003**, *91*, 146401.
- [5] Wu, X.; Vargas, M. C.; Nayak, S.; Lotrich, V.; Scoles, G. *J. Chem. Phys.* **2001**, *115*, 8748.
- [6] Tsuzuki, S.; Lüthi, H. P. *J. Chem. Phys.* **2001**, *114*, 3949.
- [7] Kuo, I.-F. W.; Mundy, C. J.; McGrath, M. J.; Siepmann, J. I.; VandeVondele, J.; Sprik, M.; Hutter, J.; Chen, B.; Klein, M. L.; Mohamed, F.; Krack, M.; Parrinello, M. *J. Phys. Chem. B* **2004**, *108*, 12990.
- [8] Kuo, I.-F. W.; Mundy, C. J.; McGrath, M. J.; Siepmann, J. I. *J. Phys. Chem. C* **2008**, *112*, 15412.
- [9] Allesch, M.; Lightstone, F. C.; Schwegler, E.; Galli, G. *J. Chem. Phys.* **2008**, *128*, 014501.
- [10] Cicero, G.; Grossman, J. C.; Schwegler, E.; Gygi, F.; Galli, G. *J. Am. Chem. Soc.* **2008**, *130*, 1871.
- [11] Sharma, M.; Resta, R.; Car, R. *Phys. Rev. Lett.* **2007**, *98*, 247401.
- [12] McGrath, M. J.; Siepmann, J. I.; Kuo, I.-F. W.; Mundy, C. J. *Mol. Phys.* **2006**, *104*, 3619.
- [13] McGrath, M. J.; Siepmann, J. I.; Kuo, I.-F. W.; Mundy, C. J. *J. Phys. Chem. A* **2006**, *110*, 640.
- [14] Chałasiński, G.; Szczeniński, M. M. *Chem. Rev.* **1994**, *94*, 1723.
- [15] Bukowski, R.; Szalewicz, K.; Groenenboom, G. C.; van der Avoird, A. *Science* **2007**, *315*, 1249.
- [16] Jeziorski, B.; Moszynski, R.; Szalewicz, K. *Chem. Rev.* **1994**, *94*, 1887.
- [17] Misquitta, A. J.; Jeziorski, B.; Szalewicz, K. *Phys. Rev. Lett.* **2003**, *91*, 033201.
- [18] Hesselmann, A.; Jansen, G. *Phys. Rev. Lett.* **2003**, *367*, 778.
- [19] Podeszwa, R.; Rice, B. M.; Szalewicz, K. *Phys. Rev. Lett.* **2008**, *101*, 115503.
- [20] Grimme, S.; Antony, J.; Schwabe, T.; Mück-Lichtenfeld, C. *Org. Biomol. Chem.* **2007**, *5*, 741.
- [21] Hamprecht, F. A.; Cohen, A. J.; Tozer, D. J.; Handy, N. C. *J. Chem. Phys.* **1998**, *109*, 6264.
- [22] Boese, A. D.; Doltsinis, N. L.; Handy, N. C.; Sprik, M. *J. Chem. Phys.* **2000**, *112*, 1670.
- [23] Becke, A. D. *J. Chem. Phys.* **1997**, *107*, 8554.
- [24] Zhao, Y.; Truhlar, D. G. *Theor. Chem. Account.* **2008**, *120*, 215.

- [25] von Lilienfeld, O. A.; Tavernelli, I.; Rothlisberger, U.; Sebastiani, D. *Phys. Rev. Lett.* **2004**, *114*, 153004.
- [26] von Lilienfeld, O. A.; Tavernelli, I.; Rothlisberger, U.; Sebastiani, D. *Phys. Rev. B* **2004**, *71*, 195119.
- [27] Lin, I.-C.; Rothlisberger, U. *Phys. Chem. Chem. Phys.* **2008**, *114*, 2730.
- [28] Dion, M.; Rydberg, H.; Schröder, E.; Langreth, D. C.; Lundqvist, B. I. *Phys. Rev. Lett.* **2004**, *92*, 246401.
- [29] Harl, J.; Kresse, G. *Phys. Rev. B* **2008**, *77*, 045136.
- [30] Podeszwa, R.; Szalewicz, K. *Chem. Phys. Lett.* **2005**, *412*, 412.
- [31] Douketis, C.; Scoles, G.; Marchetti, S.; Zen, M.; Thakkar, A. J. *J. Chem. Phys.* **1982**, *76*, 3057.
- [32] Murdachaew, G.; de Gironcoli, S.; Scoles, G. *J. Phys. Chem. A* **2008**, *112*, 9993.
- [33] Perdew, J. P.; Burke, K.; Ernzerhof, M. *Phys. Rev. Lett.* **1996**, *77*, 3865.
- [34] Zhang, Y.; Yang, W. *Phys. Rev. Lett.* **1998**, *80*, 890.
- [35] Hammer, B.; Hansen, L. B.; Nørskov, J. K. *Phys. Rev. B* **1999**, *59*, 7413.
- [36] Becke, A. D. *Phys. Rev. A* **1988**, *38*, 3098.
- [37] Lee, C.; Yang, W.; Parr, R. G. *Phys. Rev. B* **1988**, *37*, 785.
- [38] Becke, A. D. *J. Chem. Phys.* **1993**, *98*, 5648.
- [39] Perdew, J. P.; Chevary, J. A.; Vosko, S. H.; Jackson, K. A.; Pederson, M. R.; Fiolhais, C. *Phys. Rev. B* **1992**, *46*, 6671.
- [40] Frauenheim, T.; Seifert, G.; Elstner, M.; Hajnal, Z.; Jungnickel, G.; Porezag, D.; Suhai, S.; Scholz, R. *Phys. Stat. Sol. (b)* **2000**, *217*, 41.
- [41] Elstner, M.; Hobza, P.; Frauenheim, T.; Suhai, S.; Kaxiras, E. *J. Chem. Phys.* **2001**, *114*, 5149.
- [42] Wu, Q.; Yang, W. *J. Chem. Phys.* **2002**, *116*, 515.
- [43] Grimme, S. *J. Comput. Chem.* **2004**, *25*, 1463.
- [44] Zimmerli, U.; Parrinello, M.; Koumoutsakos, P. *J. Chem. Phys.* **2004**, *120*, 2693.
- [45] Ortmann, F.; Bechstedt, F.; Schmidt, W. G. *Phys. Rev. B* **2006**, *73*, 205101.
- [46] Silvestrelli, P. L. *Phys. Rev. Lett.* **2008**, *100*, 053002.
- [47] Becke, A. D.; Johnson, E. R. *J. Chem. Phys.* **2006**, *124*, 014104.
- [48] Chang, D. T.; Schenter, G. K.; Garrett, B. C. *J. Chem. Phys.* **2008**, *128*, 164111.
- [49] Tabacchi, G.; Mundy, C. J.; Hutter, J.; Parrinello, M. *J. Chem. Phys.* **2002**, *117*, 1416.

- [50] Tabacchi, G.; Hutter, J.; Mundy, C. J. *J. Chem. Phys.* **2005**, *123*, 074108.
- [51] Aziz, R. A. *J. Chem. Phys.* **1993**, *99*, 4518.
- [52] Patkowski, K.; Murdachaew, G.; Fou, C. M.; Szalewicz, K. *Mol. Phys.* **2005**, *103*, 2031.
- [53] Lotrich, V. F.; Szalewicz, K. *J. Chem. Phys.* **1997**, *106*, 9688.
- [54] Podeszwa, R.; Szalewicz, K. *J. Chem. Phys.* **2007**, *126*, 194101.
- [55] The CP2K developers group.; <http://cp2k.berlios.de/>, 2008.
- [56] Longuet-Higgins, H. C. *Discuss. Faraday Soc.* **1965**, *40*, 7.
- [57] VandeVondele, J.; Krack, M.; Mohamed, F.; Parrinello, M.; Chassaing, T.; Hutter, J. *Comput. Phys. Commun.* **2005**, *167*, 103.
- [58] Goedecker, S.; Teter, M.; Hutter, J. *Phys. Rev. B* **1996**, *54*, 1703.
- [59] Hartwigsen, C.; Goedecker, S.; Hutter, J. *Phys. Rev. B* **1998**, *58*, 3641.
- [60] Krack, M. *Theor. Chem. Acc.* **2005**, *114*, 145.
- [61] Martyna, G. J.; Tuckerman, M. E. *J. Chem. Phys.* **1999**, *110*, 2810.
- [62] In *CRC Handbook of Chemistry and Physics, Internet Version*; Lide, D. R., Ed.; Taylor and Francis: Boca Raton, FL, 87 ed., 2007.
- [63] Potoff, J. J.; Panagiotopoulos, A. Z. *J. Chem. Phys.* **1998**, *109*, 10914.
- [64] Michels, A.; Levelt, J. M.; de Graaff, W. *Physica* **1958**, *24*, 659.
- [65] Siepmann, J. I. In *Forum 2000: Fluid Properties for New Technologies, Connecting Virtual Design with Physical Reality*; Rainwater, J. C., Friend, D. G., Hanley, H. J. M., Harvey, A. H., Holcomb, C. D., Laesecke, A., Magee, J. W., Muzny, C., Eds., Vol. NIST Special Publication 975; NIST: Boulder, 2001; page 110.
- [66] Nosé, S. *J. Chem. Phys.* **1984**, *81*, 511.
- [67] Nosé, S. *Mol. Phys.* **1984**, *52*, 255.
- [68] Hoover, W. G. *Phys. Rev. A* **1986**, *34*, 2499.
- [69] Nosé, S. *Mol. Phys.* **1986**, *57*, 187.
- [70] Hutter, J. V. *J. Chem. Phys.* **2003**, *118*, 4365.
- [71] Lupinetti, C.; Thakkar, A. *J. Chem. Phys.* **2005**, *122*, 044301.
- [72] Kislyakov, I. M. *Opt. Spectrosc.* **1999**, *87*, 357.
- [73] McQuarrie, D. A. *Statistical Mechanics*; University Science Books: New York, 2000.

- [74] Dardi, P. S.; Dahler, J. S. *Theor. Chim. Acta* **1992**, *82*, 117.
- [75] Dymond, J. H.; Smith, E. B. *The Virial Coefficients of Pure Gases and Mixtures: A Critical Compilation*; Oxford University Press: Oxford, 1980.
- [76] Naumkin, F. Y.; Wales, D. J. *Mol. Phys.* **1999**, *96*, 1295.
- [77] Wales, D. J.; Doye, J. P. K.; Dullweber, A.; Hodges, M. P.; Naumkin, F. Y.; Calvo, F.; Hernández-Rojas, J.; Middleton, T. F. *The Cambridge Cluster Database*; <http://www-wales.ch.cam.ac.uk/CCD.html>.
- [78] Bukowski, R.; Szalewicz, K. *J. Chem. Phys.* **2001**, *114*, 9518.
- [79] Lotrich, V. F.; Szalewicz, K. *Phys. Rev. Lett.* **1997**, *79*, 1301.
- [80] Rościszewski, K.; Paulus, B.; Fulde, P.; Stoll, H. *Phys. Rev. B* **1999**, *60*, 7905.
- [81] Axilrod, B. M.; Teller, E. *J. Chem. Phys.* **1943**, *11*, 299.
- [82] Muto, Y. *Proc. Phys. Math. Soc. Jpn.* **1943**, *17*, 629.
- [83] Thakkar, A. J.; Hettema, H.; Wormer, P. E. S. *J. Chem. Phys.* **1992**, *97*, 3252.
- [84] Tkatchenko, A.; von Lilienfeld, O. A. *Phys. Rev. B* **2008**, *78*, 045116.
- [85] Casassa, S.; Halo, M.; Maschio, L. *J. Phys.: Conf. Ser.* **2008**, *117*, 012007.
- [86] Herman, P. R.; LaRocque, P. E.; Stoicheff, B. P. *J. Chem. Phys.* **1988**, *89*, 4535.
- [87] Bruch, L. W.; Diehl, R. D.; Venables, J. A. *Rev. Mod. Phys.* **2007**, *79*, 1381.
- [88] Schwerdtfeger, P.; Gaston, N.; Krawczyk, R. P.; Tonner, R.; Moyano, G. E. *Phys. Rev. B* **2006**, *73*, 064112.
- [89] Tessier, C.; Terlain, A.; Larher, Y. *Physica (Amsterdam)* **1982**, *113A*, 286.
- [90] Peterson, O. G.; Batchelder, D. N.; Simmons, R. O. *Phys. Rev.* **1966**, *150*, 703.
- [91] Schwalbe, L. A.; Crawford, R. K.; Chen, H. H.; Aziz, R. A. *J. Chem. Phys.* **1977**, *66*, 4493.
- [92] Gewurtz, S.; Stoicheff, P. *Phys. Rev. B* **1974**, *10*, 3487.
- [93] Yarnell, J. L.; Katz, M. J.; Wenzel, R. G.; Koenig, S. H. *Phys. Rev. A* **1973**, *7*, 2130.

Micro-Fabrication of: Patterned LCM and LSCF cathodes on YSZ electrolyte and oriented LCM thin-films on single crystals by PLD.

by: Lincoln Miara

Abstract:

Two systems for generating a well-defined solid oxide fuel cell (SOFC) cathode/electrolyte interface were developed in order to facilitate experiments into the fundamental nature of SOFC operation. The first system involved fabricating disks of Ytria-Stabilized zirconia (YSZ) patterned with 20% Ca-doped LaMnO₃ and La_{0.6}Sr_{0.4}Co_{0.2}Fe_{0.8}O₃ (LSCF) with varying triple phase boundary (TPB) lengths but with a constant cathode/electrolyte contact area. Samples were fabricated through a combination of photomicro lithography techniques and DC sputtering. The deposition homogeneity and composition were analyzed with various x-ray techniques such as XRD, SEM, RBS, and XPS. The second system was the growth of heteroepitaxial Ca-doped LaMnO₃ thin films on single crystals of YSZ and Lanthanum aluminate (LAO) by pulsed laser deposition (PLD). Deposition temperature and chamber pressure were varied to try to find optimal growth conditions. The quality of the film was analyzed with X-Ray Diffraction (XRD) and Rutherford Back Scattering (RBS). It was found that at 700°C and 50 mTorr oxygen oriented films of thickness 240Å LCM were grown on LAO and YSZ.

Introduction:

Solid Oxide Fuel Cells (SOFCs) show great promise as power generation devices that operate at high efficiency. However, their deployment into commercial markets has been stilted by high manufacturing costs, sluggish performance, and insufficiently short life spans. Prior work has shown that cathode polarization resistance is one of the most important rate limiting steps in SOFC kinetics. Studies have demonstrated that the resistance is related to the length of the gas-cathode-electrolyte interface, or triple phase boundary (TPB), where the charge transfer reaction $O_2 + 2e^- \rightarrow O_2^-$ occurs. The length of the TPB and thus the connection between microstructure and

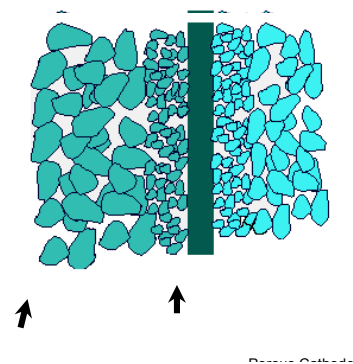


Figure 1: Schematic of a typical screen printed SOFC showing an ill-defined TPB

performance has been difficult to quantify because SOFC devices use porous cathodes (Fig 1). By fabricating a half-cell with a well defined cathode/electrolyte interface, relative effect of geometry on kinetics can be elucidated. Early SOFCs used primarily electronic conducting cathodic materials such as platinum or doped Lanthanum Manganites such as Sr-doped LaMnO₃. Prior work has shown that the

polarization resistance of these materials is directly proportional to the TPB length. Recently, however, there has been increasing interest in the use of cathodes that are mixed electronic and ionic conductors (MIEC). MIECs would allow the oxygen reduction reaction to also take place away from the TPB and thus the polarization resistance would no longer be a direct function only of the TPB length. It is one of the goals of this work to investigate this relationship.

Improvements in SOFC performance have largely followed a trial and error approach. As described above, typical screen printed cells have a large amount of geometrical complexity that convolutes material property assessments, and restricts the ability to develop accurate system models. Thus, the fabrication of heteroepitaxial thin-films of cathode on electrolyte reduces the system to its most fundamental level. Producing accurate models of this system and then building up the complexity will allow for fundamental understanding of the underlying problems with SOFC performance. It is therefore the goal of this work to fabricate epitaxial LCM films on YSZ single crystals.

Methods and Results:

Fabrication of YSZ disks patterned with cathode

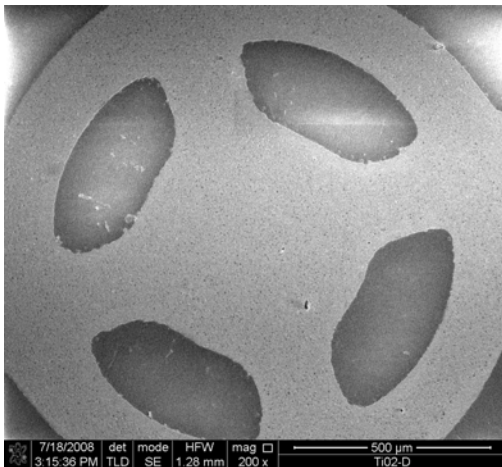


Figure 2: SEM image of deposited LCM cathode on YSZ electrolyte

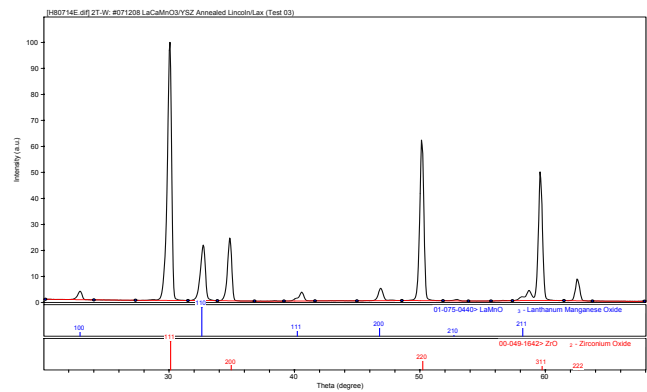


Figure 3: XRD of LCM on YSZ shows the deposited layer is polycrystalline LCM

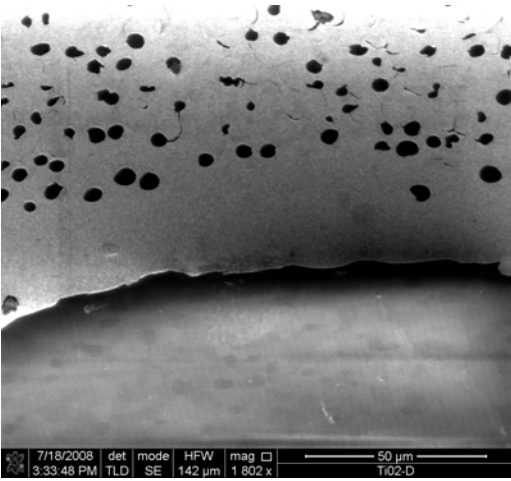


Figure 4: A close SEM image shows porosity in the deposited layer and a somewhat wavy TPB

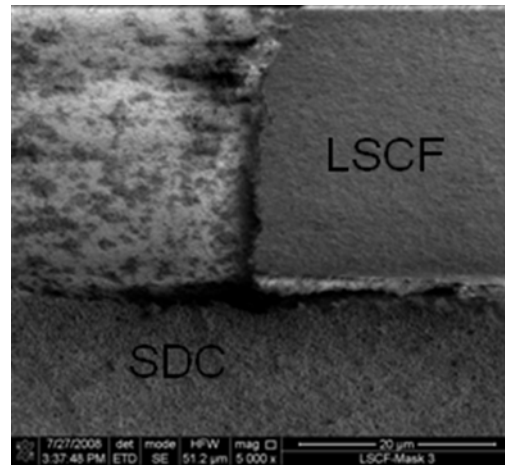


Figure 5: SEM of the LSCF layer deposited on the screen-printed SDC barrier layer. An area where it is cracked off can be seen in the upper left.

Following the method of Radhakrishnan^{1,2}, disks of YSZ (TOSOH – 8Y) were fabricated using standard ceramic powder processing techniques. The powder was pressed uniaxially and then isostatically before being sintered at 1450°C for 5hr in air. The final dimensions of the disks were 22mm in diameter by 2mm thickness. The sintered disks were then polished on one side to a 1μm finish. Half of the samples were then screen-printed with a Samarium-doped Gadolinium (SDC) barrier layer between the LSCF cathode and YSZ electrolyte, to prevent formation of any undesired phases. The screen-printed samples were sintered at 1200°C for 2hrs. After sintering, the SDC layer was 95% dense. In order to obtain the mesh pattern of cathode, the disk was initially coated with positive photoresist Shipley 1818 and was baked at 60°C for 5 min. The sample was then exposed to UV light for 99s using a previously prepared dark field mask with an appropriate mesh pattern. The exposed sample was developed using MF 321 developer for between 30 and 60s, rinsed in DI water, and dried with N₂. Several samples were patterned using different masks, each having the same contact area but different TPB length ranging from 50 cm⁻¹ to 500 cm⁻¹. DC sputtering was performed on the masked substrates. 2” sputter targets of LCM and LSCF were fabricated using standard pressing and sintering techniques. Sputtering was performed at 50 Watts in a 5.5 mTorr 20% O₂ – Ar mixture. Pressure was kept to a minimum to maximize the density of the deposited substrate. The samples were suspended 7” above the target and rotated. Films of 0.5μm thick were deposited at a rate of 1nm/min LCM and 1.5nm/min LSCF. After deposition, the photoresist was removed with acetone. Then a counter electrode of LSM-20 was screen printed onto the YSZ, and finally the prepared samples were annealed at 1100 deg C for 2 hours.

For the LCM samples SEM revealed a continuous layer approximately 0.5 μm thick (Fig 2). XRD was performed on the as deposited and after annealed samples. The as-deposited samples appear to be completely amorphous, however after annealing a single phase emerged with an average crystal size

was 54 +/- 4nm (Fig. 3). Microstructural analysis using SEM revealed that the as deposited layer was porous and not completely dense (Fig. 4). The pores are evenly distributed and of relatively uniform size. Thus, the actual TPB length of each sample was calculated using the length of the mask TPB and the increased TPB length due to the porosity: $l_{TPB} = l_{TPBp}(1+\alpha) + l_{TPBo}$ where $\alpha = l_{TPB}$ increase due to line waviness and $l_{TPBo} = l_{TPB}$ is the baseline TPB introduced due to the presence of pores.

The LSCF cathode did not adhere well to the SDC coated YSZ. On some samples a significant amount of delamination occurred. This could be seen clearly in SEM (Fig. 5). The most probable explanation for this is that the annealing temperature of 1100°C was too high. A significant thermal expansion mismatch between the YSZ and the LSCF caused the LSCF layer to delaminate.

To investigate the relative contributions of the TPB length to polarization resistance, a series of Electrochemical Impedance Spectroscopy (EIS) measurements on the patterned electrode samples will be obtained. The dependence of the polarization resistance on the TPB and the environmental variables, namely temperature and oxygen partial pressure will be elucidated.

Fabrication of thin-films of LCM on single crystal substrates by PLD

In order to grow epitaxial thin-films, there must be good agreement between lattice parameters in the single crystal substrate and the crystal structure of the film to be grown. For the LCM perovskite crystal, there is approximately a 1.5% lattice mismatch with the LAO and 7.5% mismatch with the YSZ. Thus, LAO is a very good match and was used in these experiments as a control, while the 7.5% mismatch made the success of the LCM-YSZ system more challenging. The experiments were designed to first find the optimal growth conditions on LAO and then apply them to the LCM-YSZ system. A literature review found limited work on this system³⁻⁵, so the growth conditions were systematically explored by varying the substrate temperature and the chamber pressure. The single crystal substrates used were 1 cm by 1cm square single crystals of YSZ (100), LAO (100), and Silicon purchased from Crystek Crystals. Figure 6 is a schematic of the PLD setup. A sample holder with up to four substrates was suspended above the target, but arranged off axis. The laser was pulsed at 1 Hz, the chamber pressure was varied between 10 and 50 mTorr oxygen, and the substrates were heated during deposition over a range from 550°C to 800°C. After deposition the samples were annealed at 900°C for 3hrs in an oxygen containing environment. Samples grew at a rate inversely proportional to the substrate heating temperature increasing the temperature from 550°C to 700°C decreased the rate from

11.5 A/min to 7.3 A/min. However, the films appeared to be more oriented at the higher substrate temperature.

Hi-Res XRD was performed on the LCM-LAO (100) sample deposited at 700°C in 50 mTorr of oxygen shows an oriented film; however, the peaks do not correspond to the peaks listed in the PDF database; they are shifted to a substantial degree (Fig. 7). Data collected from RBS show good agreement in composition between the film and target (Fig. 8). After annealing at 900°C for 3hrs, the LCM-YSZ (100) sample also deposited at 700°C in 50 mTorr oxygen showed signs of an oriented phase, but its identity requires further investigation (Fig. 9).

The next step will be to utilize this system to explore the electronic properties of the cathode material, the surface properties of the cathode-gas interface, and how these change under various operating conditions. To examine this, Van der Pauw measurements will be conducted concurrently with XRD measurements. Thus realtime data will be gathered to examine the surface structure and its relationship to the electronic conductivity and their dependence on the temperature and oxygen partial pressure of the system.

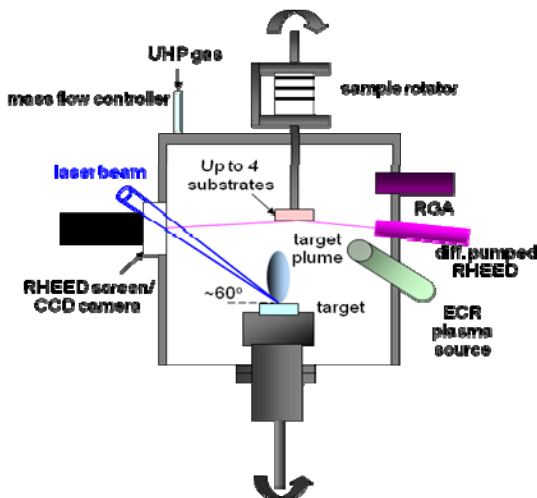


Figure 7: Schematic of PLD setup

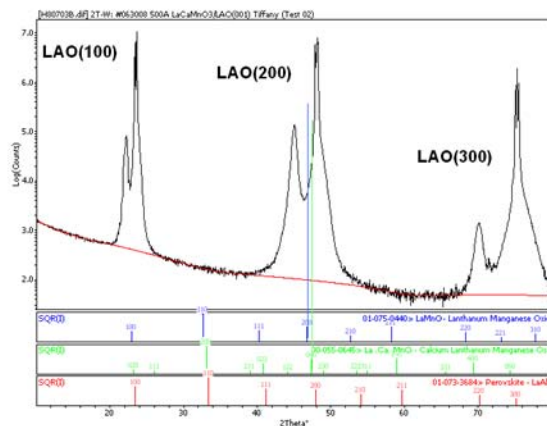


Figure 6: Hi-Res XRD of LCM on LAO (100) evidence of oriented film growth, however the peaks are highly shifted.

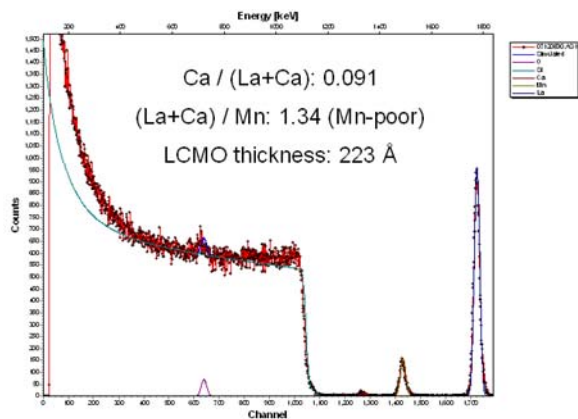


Figure 9: RBS data of LCM on YSZ, the composition of the film is slightly La rich

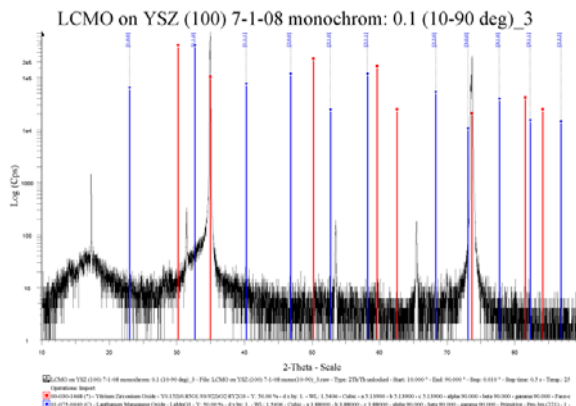


Figure 8: XRD of LCM on YSZ (100) evidence of oriented peaks after annealing but their origin is unknown.

Acknowledgements:

I would very much like to thank Lax Saraf for his mentorship this summer. I would also like to thank Larry Pederson for supporting my work at PNNL. Additionally I would like to thank all of the staff at PNNL who helped me with various parts of the work including: Tiffany Kaspar, Wendy Bennett, Charlie Bonham, and Greg Coffey.

References:

1. Radhakrishnan R, *J. Electrochemical Society*, **152**(1) A210-A218 (2005)
2. Radhakrishnan R, *J. Electrochemical Society*, **152**(5) A927-A936 (2005)
3. Giebeler L et. al. *Chem. Eng. Technol.* 2007, **30**, No. 7, 889-894 2007
4. Huang Q. et. al. *Physical Review B*, Vol 58, No. 5 pg 2684-2691 1998
5. Buch JJU et. al. *J. Phys. D: Appl. Phys.*, **41** (2008) 025406 (10pp)

A High Resolution Mass Spectrometry Study of Organic Particulate Matter Aging in an Urban Environment

Ryan C. Moffet and Mary K. Gilles
Lawrence Berkeley National Laboratory

Nancy A. Marley and Jeffrey S. Gaffney
University of Arkansas at Little Rock

Alexander Laskin and Julia Laskin
Pacific Northwest National Laboratory

Introduction

Organic carbon makes up a large component of submicron atmospheric particulate matter (PM) and it is difficult to measure both qualitatively and quantitatively due to the small size of the aerosol particles and the complexity of the molecules. A more detailed understanding of aerosol organic carbon is necessary for developing models of climate change and visibility in addition to understanding the negative health effects aerosols impart on the human body. Organic carbon (OC) has been found to represent one of the largest components of the submicron aerosol mass in regions with large anthropogenic and biogenic volatile OC (VOC) sources. A large fraction of the aerosol phase OC from the oxidation of gas phase molecules to form low volatility particle phase species. Predicting the character and quantity of the organic matter in the atmosphere requires a mechanistic understanding of OC formation. In order to understand the mechanism behind OC formation, a molecular understanding of the OC as a function of age in the atmosphere is essential. In this current work, a high resolution mass spectrometer equipped with an electrospray ionization source is used to obtain molecular level detail on organic particulate matter from the Mexico City region.

Experimental

High volume filter samples were taken at two sites in the Mexico City Metropolitan area. The T0 and T1 sampling sites at which the filter samples were taken are displayed in the map in Fig. 1. The T0 site was located in a heavily industrialized area while the T1 site was located just outside of the major urban center. Atmospheric modeling studies(1) indicated the afternoon airflow was directed from T0 to T1. Filters were changed twice daily at 12AM and 12PM resulting in two 12 hr samples per day. Samples were collected on quartz fiber filters (Pall Life Sciences, TISSUQUARTZ 2500QAT-UP). Subsamples of the filters were cut off of the main filter, extracted in 1 mL of acetonitrile, and sonicated for 15 min. The extracts were then filtered through quartz fiber syringe filters and diluted by a factor of 10. A blank filter was extracted using sample preparation steps that were identical to those used on the particulate matter filters.

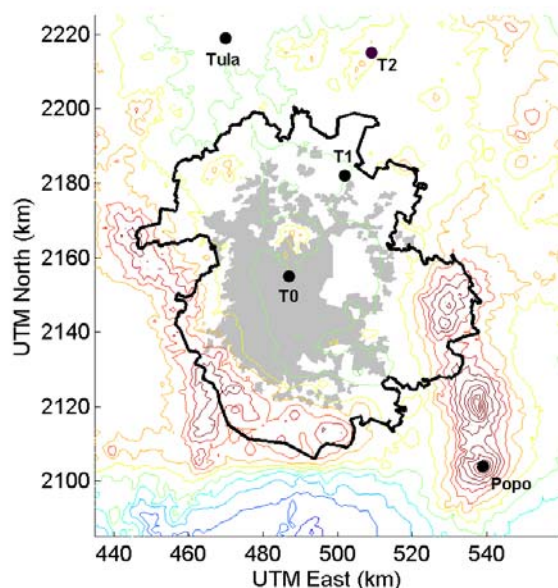


Figure 1. A map of the Mexico City area. The MCMA political border is represented by the black line and the urban area is shaded in grey. The colored lines are terrain contours every 250m. The locations marker with black dots are the T0-T2 sampling sites, Tula refinery, and Popocatepetl (Popo) volcano

The diluted extract was sampled directly into a Finnigan LTQ Orbitrap™ hybrid mass spectrometer with an electrospray ionization source. The sample was directed through a pulled fused silica capillary tip at a flow rate of $1 \mu\text{L min}^{-1}$ and voltage of 3.5 kV. The mass spectra analyzed here were collected in the positive ion mode with a mass resolution ($m/\Delta m$) of 60000 at 400 amu.

The mass spectral data was read into the Decon2LS program available freely from <http://omics.pnl.gov/software/Decon2LS.php>. The Decon2LS program generated a list of all peaks having a signal to noise ratio of greater than 3 and a baseline ratio of greater than 1. The peak lists generated from the particulate matter filter and blank were compared so that common peaks that were 3 times higher in the sample were discarded from the sample peak list. The resulting sample peak list was then grouped according to CH₂ series using the CH₂ mass defect(2); the empirical formula for the lowest mass peak in each CH₂ series was identified using Formula Calculator v1.1. Empirical formulas for higher mass peaks in the CH₂ series were then assigned by adding successive CH₂ groups.

Results

Using the high resolution mass spectrometric results, a molecular level analysis was obtained on PM filter extracts. Electrospray ionization coupled with high resolution mass spectrometry (ESI-HRMS) has the ability to give the empirical formulas for unfragmented (molecular) ions. Because 1000-3000 peaks are obtained for each sample, it is useful to analyze the composition using both graphical and statistical approaches.

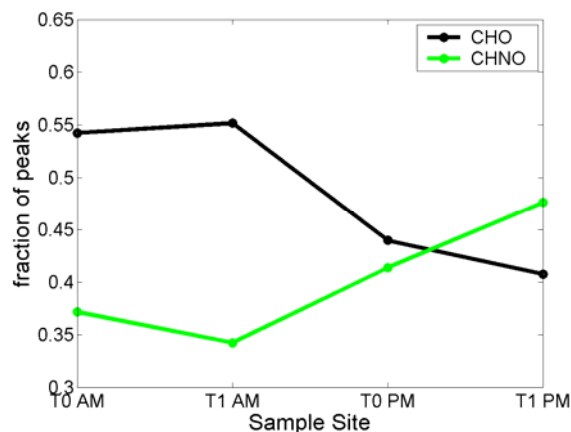


Figure 2. Trend of the two most abundant species at the different sampling sites in Mexico City. The CHO and CHNO types were the most abundant species. The CHNO type was most abundant during the PM hours suggesting that both photochemistry and non-photochemical processes may be responsible for the formation nitrogen containing organic species.

Figure 2 shows the trend of organic PM speciation at the different sampling sites. The fact that CHO species are abundantly present is not surprising; however, a large portion of the peaks were of the CHNO variety. Molecular species having the CHNO empirical formula, mostly organic nitrates, are expected from both photochemical oxidation of gasphase alkanes(3) as well as nighttime oxidation of alkenes by NO_3 (4). Similar day and nighttime reactions are expected occur for VOC species other than these. The increase in CHNO types from the AM to PM samples indicates that the formation of organic nitrates is more important from 12 PM-12 AM than it is from 12 AM to 12 PM. It is possible that most of the nighttime NO_3 chemistry occurs shortly after sunset, and is the cause for the increase organic nitrates in the PM samples. The overall amount of the CHNO species in Mexico City is higher than other studies done in the USA using ESI-HRMS. An ESI-HRMS study carried out in a rural environment indicated a maximum of 25% CHNO species in water-extractable PM(2). The elevated abundance of CHNO species in Mexico City compared the rural USA sites may indicate that organic nitrates are more prevalent in highly polluted environments. This is likely due to higher levels of nitrogen containing gasphase oxidants such as NO , NO_2 , and NO_3 in the polluted urban environment of Mexico City.

To further characterize the changes in molecular species between the different PM samples in Mexico City, speciated molecular weight (MW) distributions were plotted in Fig. 3. The molecular weight distribution is shifted to higher molecular weights from the morning to night samples. Also, a second mode in both of the T1 samples that is not present in the T0 samples also indicates further differences in chemical composition between T1 and T2. The high MW mode in the morning T1 sample was not identified due to the absence of an unambiguous assignment of these ion series at low masses. While the second mode of in the T1 morning sample is not identified, the high MW mode in the T2 sample is composed mostly of CHNO species. Even for the T2 sample there is a higher fraction of unidentified peaks due to the increased ambiguity at higher masses. Finally, it is apparent that a more sulfur containing organics are present in the morning samples. Although small in number, these peaks may be related to the overwhelming presence of aerosol sulfur identified by proton induced x-ray emission (PIXE) on this particular day.

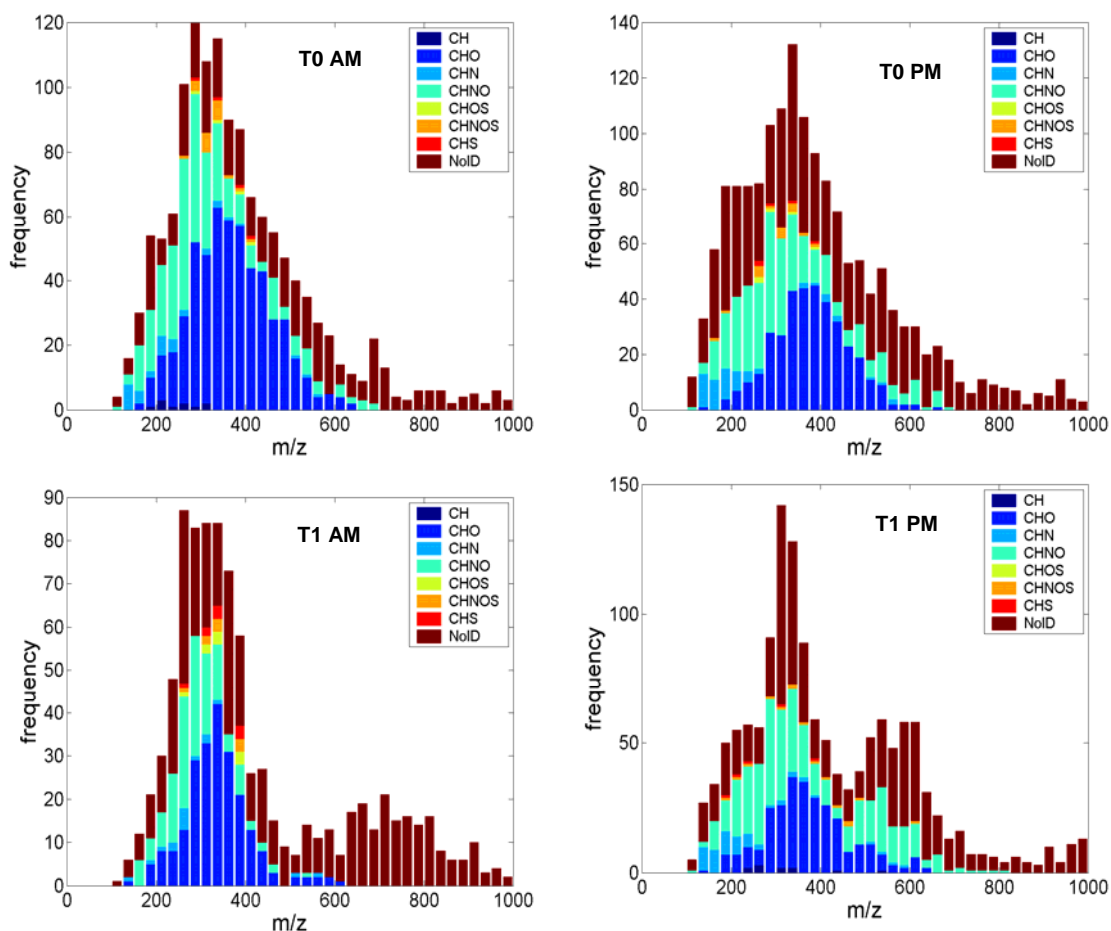


Figure 3. Speciated molecular weight (MW) distributions for the different sampling sites in Mexico City obtained with ESI-HRMS. From AM to PM samples, the molecular weight shifts to higher values. From T0 to T1 samples, a second mode in the MW appears. The CH and CHN Species appear to be constrained to lower MW while the higher MW is mostly made up of CHO and CHNO species. For the T1 AM sample, many of the high MW peaks are not identified.

As organic carbon ages in the atmosphere, changes in the degree of unsaturation may occur due to reaction of double bonds with oxidants or the condensation of longer chain aliphatics into the particle phase due to functionalization (also a result of oxidation). Figure 4. shows how the degree of unsaturation depends on molecular weight (m/z) and sampling site in Mexico City. The graphic in Fig 4. depicts a trend of decreasing unsaturation with m/z due to the addition of CH_2 for the larger molecular weight species. The table overlaid on Fig. 4 shows that the mean % unsaturation decreases and the H/C ratio increases going from the city center in the morning to the peripheral site in the evening. Interestingly, no trend is seen the O/C ratios as was seen in previous airborne studies above Mexico City with online aerosol mass spectrometry(5). However, it should

be noted that the O/C ratio measured above the T0 and T1 sites did not change by a large amount and was in general agreement with the magnitude reported in Fig. 4. However, one must be careful when interpreting these results because ESI is generally not considered to be a quantitative technique on a mass basis; therefore the comparison of O/C ratios with the aerosol mass spectrometry measurements needs to be interpreted with caution.

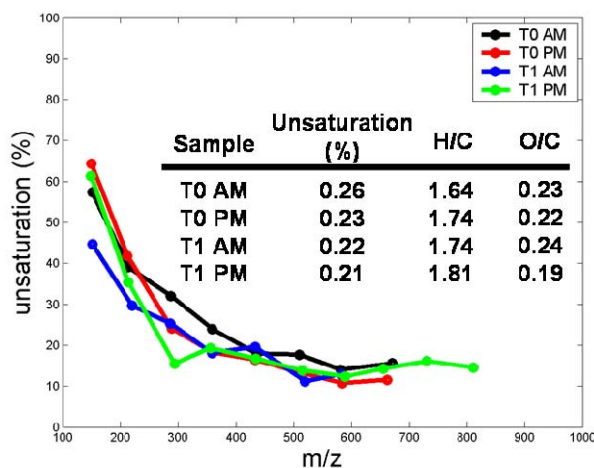


Figure 4. Molecular weight (as m/z) dependence of unsaturation together with a table for the mean value of % unsaturation, H/C ratio and O/C ratio. The % unsaturation goes down with m/z due to the addition of saturated CH₂ groups. These CH₂ additions are also reflected in the H/C and O/C ratios.

The trend of increasing H/C ratio from T0 to T1 is in agreement with microscopic near edge x-ray spectra acquired for these same sites in Mexico City(6). This may indicate that aliphatic molecules that were initially too volatile to be in the particle phase at T0, had functionalized enough to condense into the aerosol phase by the time they reached T1.

Conclusions

In this study, we have used ESI-HRMS to identify organo-nitrates as an important component of particulate matter sampled in Mexico City. The spatial and temporal trends of these organo-nitrates indicate that nighttime NO₃ causes an increased presence of CHNO aerosols in the evening while being ubiquitously present throughout the day as a result of photochemical mechanisms. Furthermore, it was found that the H/C ratio in the organic particulate matter was found to increase from the center of the city to a peripheral site – a result in agreement with x-ray spectroscopy. This indicates that as aerosols age, large aliphatic organic molecules functionalize and partition to the particle phase. These results are currently being compared not only to x-ray spectroscopy techniques, but also to infrared and electron microscopy. These measurements provide essential guidance for the understanding of the most important mechanisms involved in organic aerosol formation in Mexico City.

References

- (1) Doran, J. C.; Barnard, J. C.; Arnott, W. P.; Cary, R.; Coulter, R. L.; Fast, J. D.; Kassianov, E. I.; Kleinman, L.; Laulainen, N. S.; Martin, T. J.; Paredes-Miranda, G.; Pekour, M. S.; Shaw, W. J.; Smith, D. F.; Springston, S. R.; Yu, X. Y. The T1-T2 Study: Evolution of Aerosol Properties Downwind of Mexico City. *Atmos. Chem. Phys.* **2007**, *7*, 1585-1598.
- (2) Wozniak, A. S.; Bauer, J. E.; Sleighter, R. L.; Dickhut, R. M.; Hatcher, P. G. Technical Note: Molecular characterization of aerosol-derived water soluble organics carbon using ultrahigh resolution electrospray ionization Fourier transform ion cyclotron mass spectrometry. *Atmos. Chem. Phys.* **2008**, *8*, 5099-5111.
- (3) Lim, Y. B.; Ziemann, P. J. Products and mechanism of secondary organic aerosol formation from reactions of n-alkanes with OH radicals in the presence of NO_x. *Environmental Science & Technology* **2005**, *39*, 9229-9236.
- (4) Ng, N. L.; Kwan, A. J.; Surratt, J. D.; Chan, A. W. H.; Chhabra, P. S.; Sorooshian, A.; Pye, H. O. T.; Crouse, J. D.; Wennberg, P. O.; Flagan, R. C.; Seinfeld, J. H. Secondary organic aerosol (SOA) formation from reaction of isoprene with nitrate radicals (NO₃). *Atmospheric Chemistry and Physics* **2008**, *8*, 4117-4140.
- (5) DeCarlo, P. F.; Dunlea, E. J.; Kimmel, J. R.; Aiken, A. C.; Sueper, D.; Crouse, J.; Wennberg, P. O.; Emmons, L.; Shinozuka, Y.; Clarke, A.; Zhou, J.; Tomlinson, J.; Collins, D. R.; Knapp, D.; Weinheimer, A. J.; Montzka, D. D.; Campos, T.; Jimenez, J. L. Fast airborne aerosol size and chemistry measurements above Mexico City and Central Mexico during the MILAGRO campaign. *Atmospheric Chemistry and Physics* **2008**, *8*, 4027-4048.
- (6) Moffet, R. C.; Tivanski, A. V.; Hopkins, R. J.; Fast, J. D.; Shutthanandan, V.; Gaffney, J.; Marley, N. A.; Laskin, J.; Laskin, A.; Gilles, M. K. Molecular characterization of carbonaceous aerosol aging in the outflow from Mexico City. *In Preparation* **2008**.

Photoionization of liquid water and aqueous solutions

Babajide Olanrewaju and Thomas Orlando
School of Chemistry and Biochemistry
Georgia Institute of Technology
Atlanta, GA

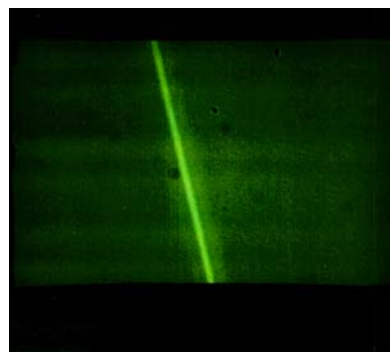
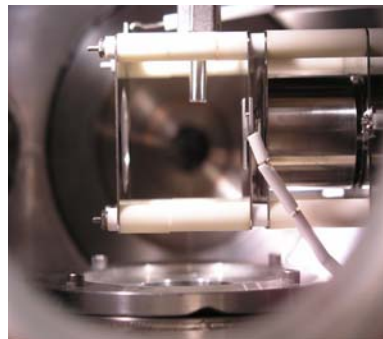
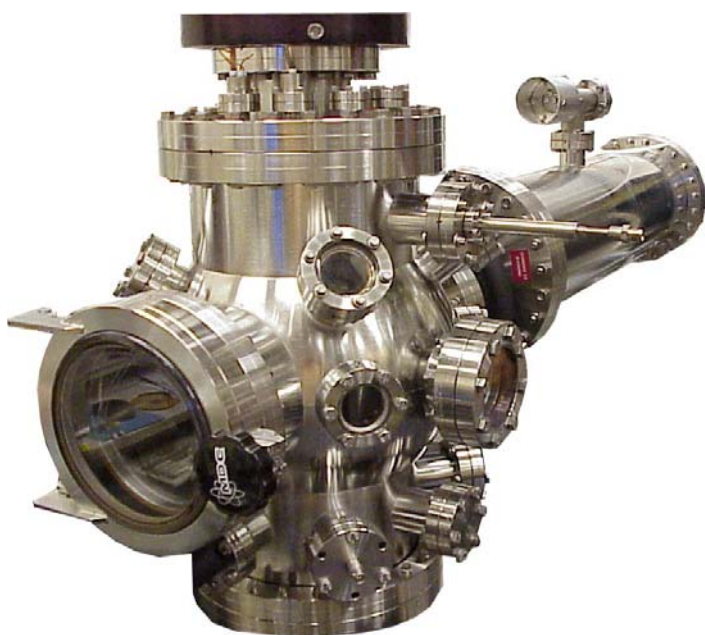
and

Nikolai Petrik and Greg Kimmel
Pacific Northwest National Laboratory
Richland, WA

The advent of liquid jet technique allows the surface of liquid solutions to be investigated in high vacuum environments. Developed by Faubel et al,¹ the liquid jet method, facilitates the direct study of continually renewed liquid surface by traditional surface science techniques such as ultraviolet photoelectron spectroscopy (UPS)² and X-ray spectroscopy (XPS).³ However, despite its importance to wide variety of fields, especially atmospheric chemistry,⁴ very few studies have been done on photoionization of pure water and aqueous solutions. It has been suggested that reactions on surface of liquid aerosol droplets play important role in the marine boundary layer of the atmosphere.⁵ In this research, we planned to investigate in detail the mechanism of cluster ion formation and release of cations from the interface of pure water and aqueous solutions during photoionization.

The experimental system as shown in Figure 1 consist of vacuum chamber equipped with liquid jet assembly mounted on a translational stage, a differentially pumped, 120 cm long R.M Jordan time of flight mass spectrometer and a liquid nitrogen cryotrap for maintaining the pressure in the chamber at 10^{-5} Torr while the liquid jet is running. The jet design has a Shimadzu LC-10A pump designed for high pressure liquid chromatography that delivers solution into the vacuum chamber at a constant set flow rate through a 10 μ m diameter aperture. The flow rate used ranges from 0.15 to 0.5 mL/min. To prevent the nozzle from clogging with small size particles, three in-line filters were used between the solution reservoir and the nozzle. As shown in Figure 1, the diameter of the liquid jet remains stable for approximately 15 mm, beyond which it breaks up into aerosols. The liquid jet is mounted vertically downward on the x-y-z translational stage into the vacuum chamber. Due to evaporative cooling, the liquid jet forms icicles on touching the surface of the liquid nitrogen cyrotrap. A mechanical chopper was attached just above the cyrotrap to help reduce the formation of icicles by slicing the frozen ice.

A 193 nm Excimer laser is used for photoionization of the liquid jet. The laser has a maximum power of ~ 0.55 mJ/pulse with a shot to shot variation of about 10 to 50 μ J/pulse. The laser beam is focused on the liquid jet which is positioned geometrically in the middle of the chamber, between the repeller and the extractor plates of the time of flight (TOF) mass spectrometer. Different parts of the liquid jet can be effectively sampled by moving the translation stages of both the laser optics and the liquid jet. Pure water and aqueous solutions of sodium hydroxide were studied at concentration ranging from 10^{-5} M to 5×10^{-4} M (corrosion from the inline filters and metal parts of the liquid jet assembly prevent studies of higher concentration, reconstruction with Teflon to prevent corrosion is being designed).



Liquid jet at ~15mm
from the nozzle

Figure 1. Liquid jet chamber with a differentially pumped time of flight mass spectrometer. The liquid jet streams downward into a liquid nitrogen trap. The 193 nm-ArF excimer laser intersects the liquid jet in the center of the chamber between the repeller and extraction plate as shown above. Also shown is a stable liquid jet at 15 mm away from nozzle.

Photoionization of pure water produced protonated water clusters of the form $H^+(H_2O)_n$ ($n=1 - 6$) as shown in Figure 2. Preliminary laser power dependence measurement (not shown) shows a threshold at $\sim 140 \mu J$. This is consistent with the Kondow model⁶ that predicts a threshold at which the positive ion formed during photoionization gained enough columbic repulsion that exceed its solvation energy. When the ion is being ejected, several water molecules are sticking to it, and as a result, protonated water clusters are produced. A detail study is required to understand the complexity of hydronium (H_3O^+) and it is excluded from this study. (Attempt to get cluster distributions resulted in an unresolved portion of the time of flight mass spectra from 1 amu to about 20 amu.)

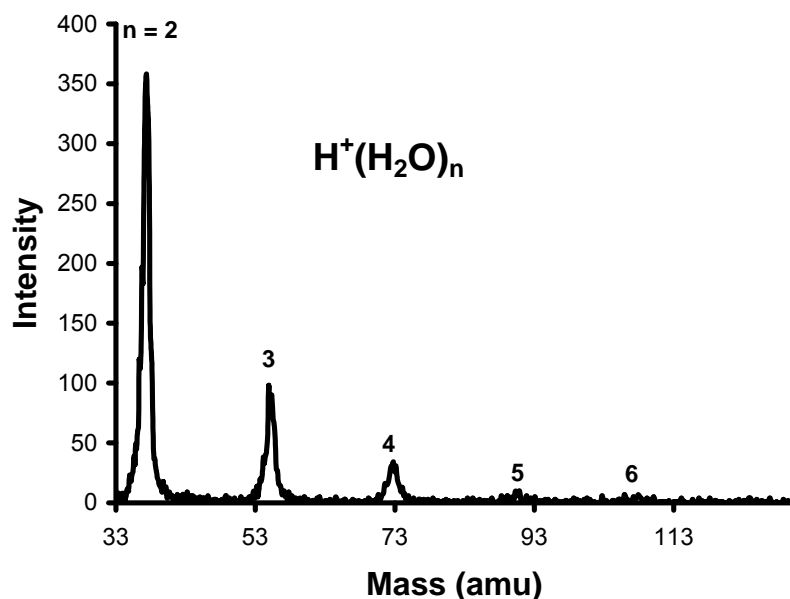


Figure 2. Protonated water cluster (n=2 – 6) formed during photoionization of pure water.

In addition to the protonated water clusters, the photoionization of aqueous sodium hydroxide solution produces hydrated sodium ion clusters as shown in Figure 3. The $H^+(H_2O)_n$ dominated lower concentration (10^{-5} and 5×10^{-5} M NaOH), while $Na^+(H_2O)_m$ are seen at higher concentrations (10^{-4} and 5×10^{-4} M NaOH). Corrosion of filters and metal parts of the liquid jet assembly prevented the study of higher concentration as small particle-like contaminants clogged the nozzle frequently. However, within this small range, Sodium ion (Na^+) is observed even at the lowest concentration without its corresponding hydrated clusters. Also, the protonated water clusters get smaller as the sodium hydrated clusters increases.

Inherent problems with the present liquid jet assembly, which includes the use of high surface area in-line filters and metal tubes, increase the frequency of corrosion and subsequently, clogging of the nozzle. A more robust system, with mainly Teflon tubes and small size filters will be constructed. Detail power and concentration dependence measurement of pure water and aqueous solutions (acid, base and salts) is required to provide more insight into the mechanism of water cluster formation during photoionization. The effect of counter ions especially in aqueous salt solution is of main interest in heterogeneous atmospheric chemistry and will be investigated along with HCl and NaOH solutions.

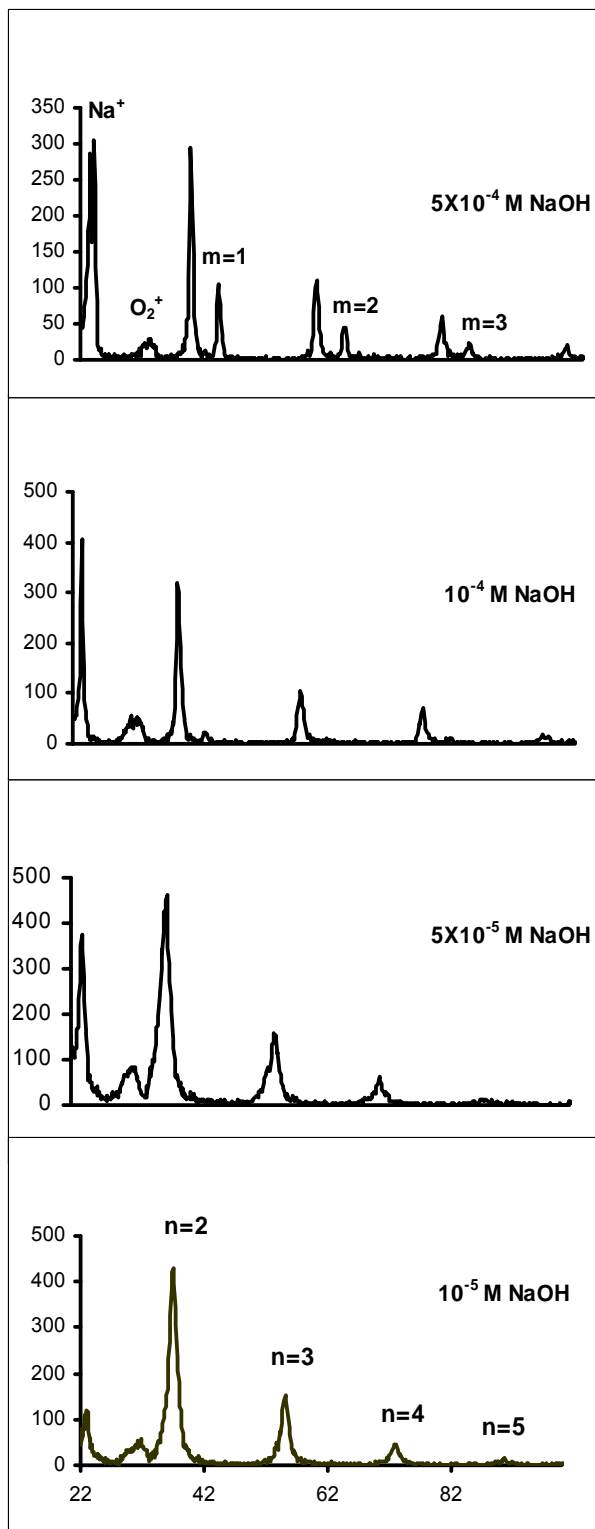


Fig 3. Time of flight spectra obtained during photoionization of NaOH solutions with concentration ranging from 10^{-5} to 5×10^{-4} M; n , m indicate the number of waters in the protonated water clusters and hydrate sodium clusters respectively.

References

- 1) Faubel, M.; Schlemmer, S.; Toennies, J. P. *Z. Phys. D: At., Mol. Clusters* **1998**, 10, 269.
- 2) Winter, B.; Weber, R.; Hertel, I. V.; Faubel, M.; Jungwirth, P.; Brown, E. C.; Bradforth, S.E. *J. Am. Chem. Soc.* **2005**, 127, 7203.
- 3) Winter, B.; Weber, R.; Widdra, W.; Dittmar, M.; Faubel, M.; Hertel I. V. *J. Phys. Chem. A* **2004**, 108, 2625.
- 4) Hunt, S. W.; Roeselova, M.; Wang, W.; Wingen, L.M.; Knipping, E. M.; Tobias, D. J.; Dabdub, D.; Finlayson-Pitts, B.J. *J. Phys. Chem. A* **2004**, 108, 11559.
- 5) Winter, B.; Faubel, M. *Chem. Rev.* **2006**, 106, 1176.
- 6) Kondow, T.; Mafune, F. *Annu. Rev. Phys. Chem.* **2000**, 51, 731.

Effect of ultraviolet photon irradiation on oxygen stoichiometry in ultra-thin zirconia and ceria films

Masaru Tsuchiya and Shriram Ramanathan

Harvard School of Engineering and Applied Sciences, Cambridge, MA

Vaithiyalingam Shutthanandan and Mark H. Engelhard

W.R. Wiley Environmental Molecular Sciences Laboratory, PNNL, Richland, WA

1. Introduction

Recent reports on various oxide systems had revealed functional properties in oxide thin films are extremely sensitive to the subtle change in oxygen stoichiometry. Examples include low leakage current in stoichiometrically controlled gate dielectrics for advanced CMOS devices,¹ blue light emission at room temperature from oxygen deficient SrTiO₃,² significant change in critical current of YBa₂Cu₃O_{7- δ} (YBCO) with small deviation in oxygen stoichiometry³ and so forth. Due to those significant properties changes, there is a growing interest towards precise control of oxygen concentration in thin film oxides.

Among several approaches to manipulate oxygen concentration in oxide thin films, ultraviolet (UV) light irradiation offers an unique route to synthesize oxide thin films at low temperature. The proximity of photon energy to the bond energy of oxygen molecule introduces photochemical reactions that create activated oxygen species, thereby enabling enhanced kinetics of oxygen transport.⁴ This process is effective even at near room temperature, thereby it offers inexpensive, simple and environmentally benign route to tailor oxygen properties in thin film oxides.

At PNNL, we aimed at developing a quantitative understanding on UV film synthesis. Despite numerous reports on structural or functional properties change induced by UV irradiation, to the best of our knowledge, no report was made to quantify stoichiometry change upon UV irradiation. Zirconia and ceria thin films were chosen as a model system for this study, owing to closeness of its bandgap to UV photon energy, fast oxygen transport, and technological importance for various applications such as solid oxide electrolyte, gate dielectrics and catalyst. Also it has been shown that UV acts very effective to introduce significant structural change in those materials. The combination of Rutherford backscattering spectroscopy, Nuclear Reaction Analysis, Proton-induced X-ray Emission as well as x-ray photoelectron spectroscopy was used in this study.

2. Experimental

Thin film zirconia or ceria was prepared at Harvard by using electron beam evaporation and magnetron sputtering at room temperature, then selected samples were exposed to ultraviolet (UV) lamp at room temperature for 15-120 minutes. The resonant radiation emitted from a low pressure Hg lamp, 254 nm (4.98eV) and 185 nm (6.71 eV), produces highly reactive ozone and oxygen radicals. The distance between UV lamp and sample was kept at 2-5 cm during the exposure.

Nuclear reaction analysis (NRA), Rutherford backscattering spectroscopy (RBS) and x-ray photo electron spectroscopy (XPS) were conducted at PNNL. For NRA

measurement the detector was positioned at a backscattering angle of 170° and the deuteron ion beam (d^+) with incident energy of 0.93 MeV was used. For RBS, proton ion beam with incident energy of 2.0 MeV was used in this study.

3. Results and Discussions

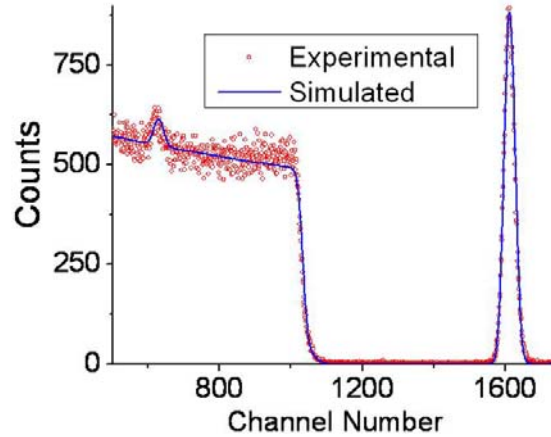


Figure 1: Experimental and simulated Rutherford backscattering spectra of YSZ (~ 38 nm) grown on Si substrate.

Figure 1 shows Rutherford backscattering spectrum of Y-doped zirconia (YDZ) thin film (~ 38 nm) grown on Si substrate. A small bump around channel number 600 corresponds to O in YDZ films, and large peak around channel number 1600 corresponds to the mixture of Zr and Y. The experimental data was successfully fitted by using Zr-Y ratio of $Zr_{0.85}Y_{0.15}$ (or ~ 8 mol% Y_2O_3), indicating cation composition in films are nearly equal to target composition. More detailed analysis was conducted by using proton-induced x-ray emissions (PIXE).

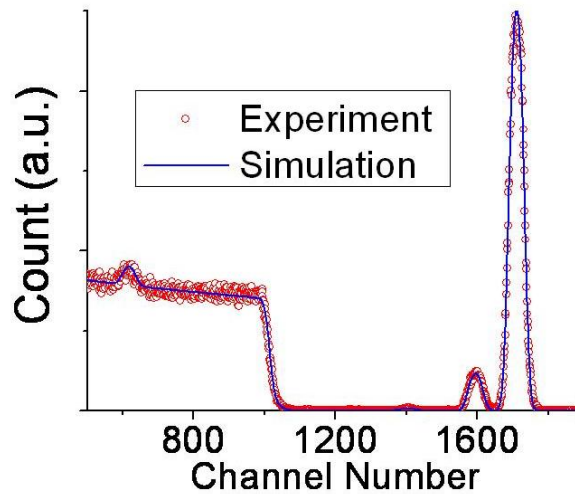


Figure 2: Experimental and simulated Rutherford backscattering spectra of Y-doped Ceria thin films grown on Ge substrate.

Similar spectra were taken for Y-doped Ceria films grown on Ge as shown in Figure 2. A small bump around channel number 600 corresponds to O in Ceria films,

a peak located around channel number 1600 represents Y, and a large peak located around 1700 represents Ce. From these RBS spectra, accurate ratio of Ce and Y in thin film Y-doped Ceria was precisely determined, for example, Ce-Y ratio calculated from the fitting of Fig 2 was $\text{Ce}_{0.85}\text{Y}_{0.15}$, corresponding to $\sim 8\text{mol}\%$ yttria doping.

Unlike the measurement of heavy cation atoms, accurate measurement of light elements (such as oxygen) is not a trivial task. In oxide thin films, the precise understanding on oxygen concentration is critical, because very tiny amount of oxygen non-stoichiometry significantly affects functional properties of oxide thin films. We used $^{16}\text{O}(\text{d,p})^{17}\text{O}$ nuclear reaction to quantify oxygen concentration in thin film zirconia and ceria.

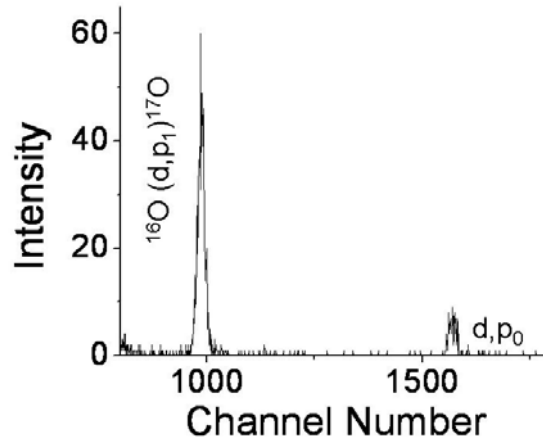


Figure 3: Nuclear reaction analysis (NRA) spectra taken from Y-doped zirconia thin films grown on Ge

Figure 3 shows a typical nuclear reaction analysis (NRA) spectrum taken from Y-doped zirconia thin films ($\sim 48\text{ nm}$) grown on Ge substrates. $^{16}\text{O}(\text{d,p}_1)^{17}\text{O}$ peak located around channel number 985 was used to quantify the oxygen concentration. From detail systematic study, we found that UV photon irradiation increases NRA count oxygen in YDZ films grown by electron-beam evaporation even at room temperature. The result suggests that UV irradiation may be a promising route to control oxygen concentration in oxide thin films at low temperature.

We also used x-ray photoelectron spectroscopy (XPS) to investigate the extent of oxygen stoichiometry change introduced by UV irradiation. The valence state of Ce in ceria is very sensitive to the oxygen stoichiometry (i.e., $\text{Ce}^{3+}/\text{Ce}^{4+}$), thereby we can estimate oxygen concentration in ceria by monitoring Ce valence states. Figure 4 shows the comparison of Ce $3d$ spectrum for UV treated and non-treated ceria thin films at take-off angle of 30° . Development of peaks located around 885.7 eV and 904 eV represents some Ce^{4+} atoms are converted to Ce^{3+} due to oxygen non stoichiometry. Those peaks are very prominent in NO UV films, whereas no apparent peak exists around those energies in UV-treated samples. This implies that UV photon irradiation can introduce changes in valence state of Ce as well as changes in oxygen concentration in ceria thin films.⁵

Overall, we confirmed that UV photon irradiation can effectively introduce oxygen stoichiometry changes in ceria and zirconia thin films at near room

temperature. We anticipate this would be a new route to synthesize oxide thin films with a well-controlled oxygen concentration.

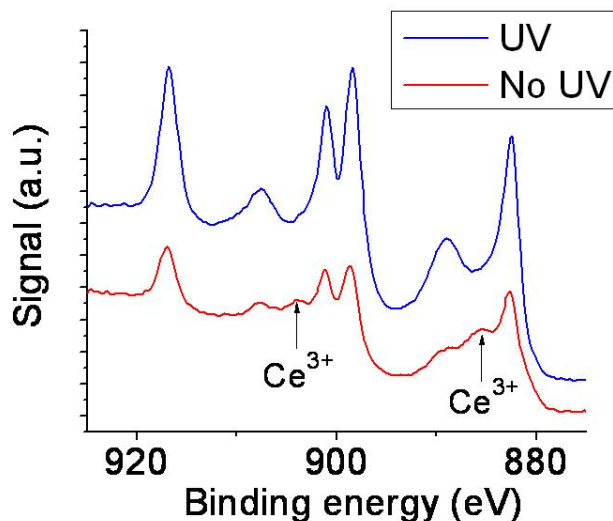


Figure 4: X-ray photoelectron spectroscopy (XPS) of UV and No UV grown ceria thin films

4. Summary

The effect of UV photon irradiation in zirconia and ceria thin films was studied by unique instrumentations available at PNNL this summer. We determined heavy element compositions from Rutherford-backscattering and proton-induced x-ray emission. The concentration of oxygen was measured by nuclear reaction $^{16}\text{O}(\text{d,p})^{17}\text{O}$. The result indicates that UV irradiation slightly increases oxygen concentration in thin film zirconia and ceria thin films. UV induced changes were further studied by x-ray photoelectron spectroscopy (XPS) to evaluate Ce valence state changes upon UV irradiation. Ce^{3+} peaks were consistently less in UV treated films, supporting that UV synthesis can assist oxygen incorporation at near room temperature. This method would be a great route to tailor oxygen stoichiometry in zirconia and ceria thin films.

Reference

1. S. Ramanathan *et. al.*, Applied Physics Letters, **80** (20), 3793 (2002).
2. D. Kan *et. al.*, Nature Materials, **4**, 816 (2005).
3. R. J. Cava *et. al.*, Nature, 329, 423 (1987).
4. H. Okabe, Photochemistry of Small Molecules (Wiley, New York, 1978).
5. M. Tsuchiya *et.al*, manuscript under preparation (2008)..

Introduction

Electronegativity is loosely defined as the ability for an atom to attract electrons from its bonding neighbours, or to retain its own. This can be inferred from the localization of charge on polar bonds. In a C-Cl bond, there is a slight positive charge on C, and a slight negative charge on Cl, indicating that the chlorine atom is attracting the electrons of the covalent bond away from carbon. Chlorine is therefore more electronegative than carbon. Electronegativity is transitive. Therefore if we discover that fluorine is more electronegative than chlorine (as it is in practice) then fluorine is also more electronegative than carbon. From this it may be inferred that a relative scale of electronegativities exists.

From thermochemical data (combustion and formation energies) the energies of individual bonds, for example the C-H bond, can be calculated. It has been postulated that the scheme is additive, i.e. that the energy of a C-H bond is the arithmetic mean of the energies of the C-C and H-H bonds. Linus Pauling noted that polar bonds showed additional strength, presumably arising from the electrostatic interaction. He exploited this non-additive element to create a quantitative scale for electronegativity, reasoning that the polarisation and additional bond strength was commensurate with the difference in electronegativities between the two species, the sign of which could be inferred by the partial charges on the atoms. Pauling's dimensionless thermochemical scale of electronegativity then simply needed an arbitrarily chosen absolute value, setting hydrogen at exactly 2.20. The other elements could then be assigned appropriately.¹

This scale agrees well with the chemical intuition of electronegativity, for example that it should decrease when moving down a column (as the nucleus becomes shielded and covalent radius increases) while increasing across a period (as nuclear charge increases with a far less significant shielding effect).

Mulliken noted two years later² that the electronegativity, as defined by Pauling, is simply a mixing of ionic character into the wavefunction that describes a bond. For example, in a plain covalent C-C bond, there is the obvious $C^0 C^0$ component to the wavefunction, but also a non-zero amount of C^+C^- and C^-C^+ , however as the atoms are identical and therefore have equal electronegativity, the bond is non-polar, and therefore these contributions must be equal. Where these contributions are not equal, the bond is polarised.

Mulliken built on this by observing that the relative energies of these two states, and therefore their contributions to the wavefunction, are related to the electron affinities (E) and ionisation energies (A) of the two atoms. Setting the energy of A^0B^0 as zero, for two atoms A and B of equal electronegativity, bonded as A-B, the contributions of A^+B^- and A^-B^+ to the wavefunction are necessarily equal. Therefore the energy of A^+B^- ($I_A - E_B$) is equal to the energy of A^-B^+ ($I_B - E_A$). If $I_A - E_B = I_B - E_A$, then $I_A + E_A = I_B + E_B$.

If the electronegativities are not equal, then this expression becomes an inequality. If the electronegativity of A is larger, then the contribution of A^-B^+ is greater than A^+B^- ,

therefore $(I_B - E_A) < (I_A - E_B)$, and correspondingly, $(I_A + E_A) > (I_B + E_B)$. Therefore, Mulliken defined $(I_A + E_A)/2$ as the “absolute electronegativity” of an atom A. This scale correlates well with Pauling’s, and may be adjusted to provide similar dimensionless values by a simple formula. Where M is the Mulliken electronegativity in electron volts, and P is the same electronegativity on the Pauling-equivalent dimensionless scale:

$$P = 0.374 M + 0.17$$

Mulliken noted some important caveats. First and foremost is the electronic state of the atom. When bonded, an atom is in a *valence* state, which need not be particularly close to the ground state of the isolated atom. For example, the ground state of chloride in H^+Cl^- , a significant contribution to the HCl molecule, is the singlet, and likewise the ground state of H^+ . For the opposite contribution H^-Cl^+ , the ground states are a singlet and a *triplet*, and (for such light atoms) cannot contribute meaningfully to the overall singlet state of the molecule. Therefore the chlorine must be in a “valence” state for this contribution, an electronic state above the ground state for the free atom which is a singlet and which must also make chemical sense (in this instance).

This subtle issue was addressed more thoroughly by Mulliken in his publication, using a method by Slater to correct for the slightly different energies of the valence states versus the ground states, and chemical/physical intuition to determine which states to use. Suffice to say that the valence state of an atom is intimately linked to its bonding environment, albeit in a manner which makes it intuitive to determine the valence state in question, and which acts as a reminder that electronegativities are not a constant, universal property of the atom, but rather that they vary with the environment. For example it is well-known that the oxidation state of an atom affects its electronegativity – a cation necessarily has a higher electronegativity than the anion. It may be proposed that electronegativities of functional groups or molecular ions will vary less with environment than the electronegativities of the substituent ions.

Many other electronegativity scales have been proposed in the intervening years, either based on the “excess strength” of the bond (e.g. Gordy’s bond order/force constant scheme) or the electronics of the bond (Malone’s dipole-based scheme, Allred and Rochow’s mean valence orbital energy scheme).³ Therefore in addition to providing the chemist with an intuitive sense of the polarisation of the bonds in a molecule, it can provide a quantitative insight into the other properties.

Aims

The electronegativities of *groups* are important in organic chemistry, and continue to be calculated *ad hoc* in order to determine substituent effects in conjugated organic systems or aromatic rings, for example. However to the best of our knowledge rigorous, computationally-determined electronegativities for functional groups and molecular ions have not been produced. Such information would prove useful in making rough predictions of substituent effects, partial charges etc. in many areas of chemistry. It is also hoped that this theoretical study of electronegativity will provide some additional insight into the nature of this property, and how it varies with chemical environment, oxidation state, geometric distortion, etc.

This study aims to computationally predict the Mulliken electronegativities of molecular ions and functional groups, assess the computational approaches needed to predict these values, and discuss the suitability of these values in making useful chemical predictions.

Computational

Calculations were performed using the Gaussian03 code (version C.02). Dunning-type augmented correlation-consistent double- and triple-zeta basis sets were used, with an even tempered set of three additional s and p basis functions added to NH₄ in order to correctly bind the two additional electrons. The exponents of these additional functions form a geometric progression (each exponent is 1/2.5 of the previous exponent) with the most diffuse s and p functions already present in the set. Computations used MP2, CCSD, and CCSD(T) levels of theory, with “tight” SCF convergence and “very tight” geometry optimisation criteria, specifically:

- Force on any degree of freedom must be less than 0.000450 hartrees per bohr or hartrees per radian
- RMS force less than 0.000300 hartrees per bohr or hartrees per radian
- All geometric variables converged to within 0.001800 bohr or radian
- RMS geometric variable convergence within 0.001200 bohr or radian
- SCF energy converged to within 1×10^{-6} hartrees.
- All density matrix elements converged to within 1×10^{-6} hartrees
- RMS density matrix convergence within 1×10^{-8} hartrees

Experimental Mulliken electronegativities are derived from gas-phase spectroscopic measurements of electron affinities and ionisation energies. Therefore these energies can be assumed to be *vertical*, having no geometric relaxation as a result of charge loss or gain. Computational electronegativities which use vertical electron affinities and ionisation energies will therefore be referred to as “vertical electronegativities”.

However, it should be kept in mind that a real functional group or ion will have the opportunity to geometrically relax with the partial charge gained from or lost to its neighbours. Therefore *adiabatic* electronegativities were also calculated.

The issue of valence states was not addressed at this time, but will be revisited in the near future.

Three groups were studied at this time: the atom fluorine, which is a functional group but also an atom and therefore described by existing electronegativity scales; the molecular radical NH_4^0 , which has tetrahedral symmetry and little geometric relaxation on change of charge; and the OH radical, both a functional group and an important chemical entity in its own right.

Results

Table 1: Calculated Mulliken electronegativities (electron volts)

Vertical	MP2 tz	CCSD tz	CCSD(T) dz	CCSD(T) tz
F	10.47624796	10.17891	10.17064	11.27139
OH	7.543838089	7.22768	7.186728	7.351494
NH ₄	2.395972894	2.443993	2.489278	2.503681
Adiabatic				
OH	7.51361713	7.194777	7.156109	7.319278
NH ₄	2.38381757	2.433764	2.476395	2.49129

Table 2: Calculated Mulliken electronegativities (Pauling equivalent dimensionless scale)

Vertical	MP2 tz	CCSD tz	CCSD(T) dz	CCSD(T) tz
F	4.088116739	3.976911	3.973819	4.3855
OH	2.991395445	2.873152	2.857836	2.919459
NH ₄	1.066093862	1.084053	1.10099	1.106377
Adiabatic				
OH	2.980092807	2.860847	2.846385	2.90741
NH ₄	1.061547771	1.080228	1.096172	1.101743

Table 3: Ionisation energies and electron affinities of fluorine (eV)^{4,9}

	MP2	CCSD	CCSD(T) dz	CCSD(T) tz	Experimental
EA	3.640132	3.152406	3.226301	5.427805	3.401189
IE	17.312364	17.20541	17.11498	17.11498	17.42234

Table 4: Ionisation energies and electron affinities of ammonium radical (eV)^{5,6}

	MP2	CCSD	CCSD(T) dz	CCSD(T) tz	Experimental
EA	0.2943428	0.39891611	0.435872	0.458642	0.47
IE	4.4732924	4.468612007	4.516918	4.523938	4.73

Table 5: Ionisation energies and electron affinities of hydroxy radical (eV)⁷⁸

	MP2	CCSD	CCSD(T) dz	CCSD(T) tz	Experimental
EA	2.066726	1.560148	1.627741	1.737136	1.83
IE	12.960508	12.829406	12.68448	12.90142	13.0

Table 6: Geometric parameters of NH₄ with oxidation state

rNH	MP2 tz	CCSD tz	CCSD(T) dz	CCSD(T) tz
0	1.039204	1.037527	1.047469	1.040944
-	1.040813	1.021823	1.048175	1.041357
+	1.021968	1.021823	1.029556	1.023515

Table 7: Geometric parameters of OH with oxidation state

rOH	MP2 tz	CCSD tz	CCSD(T) dz	CCSD(T) tz
0	0.9695243	0.97069735	0.979412	0.973151
-	0.9676043	0.96397084	0.974188	0.96769
+	1.0242444	1.02903382	1.036596	1.031217

For comparison, the literature (experimental) value for the electronegativity of fluorine is 3.98 on the Pauling scale, for nitrogen is 3.04, and for oxygen is 3.44. The Mulliken electronegativities, converted to the dimensionless Pauling scale, are 3.91 for F, 2.90 for N, and 3.41 for oxygen.⁹

Discussion

Adiabatic and vertical electronegativities differ only slightly from each other in these cases, due to the small geometric relaxation seen in these systems. Adiabatic electronegativities are lower than vertical electronegativities in all cases, which is necessary as vertical ionisation energies and electron affinities are higher than the adiabatic.

The electronegativities of the functional groups appear to approach convergence at the CCSD(T) level of theory with a triple-zeta basis set. Of particular note is that the CCSD(T) estimate with a Dunning triple-zeta basis set significantly overestimated the electronegativity of fluorine. This exaggeration is *not* observed with the functional groups, and arises due to a significant stabilisation (ca. 0.9 hartree) for the fluoride anion, but not the other species, at the CCSD(T) level of theory with a triple zeta basis set compared to the double zeta basis set, and the corresponding exaggerated electron affinity. This suggests it is an artefact of the computational scheme. It is not unexpected that the fluorine atom should pose this problem, as extremely large basis sets, or the careful use of diffuse functions, are required to correctly recover the energies for the oxygen and fluorine atoms.¹⁰

Otherwise, the ionisation energies and electron affinities (all adiabatic) proceed well towards convergence and the experimental values, and therefore the behaviour of the electronegativities calculated may be assumed to be caused by the subtleties of Mulliken electronegativities themselves and the omission of many of these considerations (with respect to geometric relaxation, valence states etc.) in this preliminary study.

It should be noted that the electronegativities of NH₄ and OH are calculated to be smaller than those of the nitrogen and oxygen atom, respectively. It is proposed at this stage that this is because the molecular orbitals of the group are higher in energy, larger and consequently more diffuse than the atomic orbitals of the original atom, and that this increase in the apparent atomic radius and energy is not counterbalanced by the additional positive charge of the hydrogen atom.

Conclusions

In spite of the difficulty in benchmarking the computations with fluorine, these results are qualitatively reasonable, and the data involved are in good agreement with experiment, and suggest that a meaningful exploration of electronegativity may be produced with more effort. It is proposed that the electronegativities of groups formed by adding hydrogen atoms to single heavy atoms are necessarily smaller than those of the original atom due to the higher energy and greater diffuseness of the molecular orbitals versus the original atomic orbitals.

Further work

A greater variety of computational methods and basis sets will be used “pin down” the methods and basis sets required to accurately recreate the electronegativities of a broader set of atoms, before continuing to functional groups and molecular ions formed by adding hydrogens, then other heavy atoms, to single heavy atoms. A rigorous program of study will be developed to assess the role of geometric, oxidation state, and valence state effects upon electronegativities.

Acknowledgements

This research was performed at Pacific Northwest National Laboratories (PNL), as part of the Summer Research Institute program, under the supervision of Sotiris S. Xantheas of PNNL and Maciej Gutowski of Heriot Watt University. Some preliminary computations were performed on PNL resources, while the calculations detailed here were performed on the Heriot Watt University computing cluster.

¹ Linus Pauling, JACS vol. 54, pp. 3570 (1932)

² Robert S. Mulliken, J. Chem. Phys vol. 2, pp. 782 (1934)

³ H. O. Pritchard and H.A. Skinner, Chem. Reviews vol. 55, pp. 745 (1955)

⁴ Christophe Blondel, Christian Delsart and Fabienne Goldfarb, J. Phys. B: At. Mol. Opt. Phys. 34 p.281 (2001)

⁵ K. H. Bowen and J.G. Eaton, in *The Structure of Small Molecules and Ions*, edited by R. Naaman and Z. Vager, Plenum, New York, 1987, p.147

⁶ Gregory I. Gellene, David A. Cleary, and Richard F. Porter, J. Chem. Phys. 77, 3471 (1982); DOI:10.1063/1.444291

⁷ P.A. Schulz, R.D. Mead, P.L. Jones, W. C. Lineberger, J. Chem. Phys. 77, 1153 (1982)

⁸ Lide D. R., Ed.; Handbook of Chemistry and Physics, 80th ed.; CRC: Boca Raton, 1999; p 10.

⁹ Mark Winter, Webelements Periodic Table of the Elements, <http://www.webelements.com>, accessed 29 Sept, 2008

¹⁰ F. Sasaki and M. Yoshimine, Phys. Rev. A, vol. 9, p26 (1974)

Calculation of quantum vibrational spectra by means of ab initio Centroid Molecular Dynamics

Tomonori Yamada

Supervisor: Michel Dupuis

Centroid Molecular Dynamics (CMD) is a molecular dynamics simulation method that allows the quantum description of light nuclei in the study of chemical dynamics and rates. It is based on the Feynmann path integral formalism [1] as presented by Schenter et al. [2] for model systems. The goal of my research during the internship was to extend the application of the method to systems for which energies and forces are obtained from quantum chemical electronic structure calculations based on ab initio molecular orbital (MO) theory and the HONDO program. The short term goal of our work is to illustrate the approach to obtain an accurate vibrational spectrum for protonated water dimer $(\text{H}_2\text{O})_2\text{H}^+$ including quantum effects by means of the ab initio CMD. Indeed for this system the proton shared between two H_2O show considerable quantum effect.

The brief theory for CMD is in the following way. The dynamics are generated by Newton's equations of motion,

$$\mathbf{m} \frac{d^2}{dt^2} \mathbf{q}_c(t) = - \frac{d}{d\mathbf{q}_c} V_c(\mathbf{q}_c),$$

where the effective potential energy,

$$V_c(\mathbf{q}_c) = -kT \ln \left[\sqrt{\frac{2\pi\hbar^2}{mkT}} \int Dq(\tau) \delta(\mathbf{q}_c - \tilde{\mathbf{q}}_0) \int_0^{\hbar\beta} d\tau \frac{1}{2} m \left(\frac{dq(\tau)}{d\tau} \right)^2 + V(q(\tau)) \right],$$

is defined so that the quantum statistical partition function is written in a classical form

$$Q = \sqrt{\frac{mkT}{2\pi\hbar^2}} \int d\mathbf{q}_c(\tau) \exp \left[- \frac{V_c(\mathbf{q}_c)}{kT} \right]$$

We coded CMD algorithm for HONDO to calculate potential energies and its gradients based on ab initio MO. The short term goal of our study is to obtain vibrational spectra of H_2O as a test calculation.

This research is ongoing.

[Reference]

[1] R. P. Feynman and A. R. Hibbs, *Quantum Mechanics and Path Integrals* (McGraw-Hill, New York, 1965).

[2] G. K. Schenter, B. C. Garret and G. A. Voth, *J. Chem. Phys.* **113**, 5171 (2000).

